P3HT:PCBM-based organic solar cells : Optimisation of active layer nanostructure and interface properties.

KADEM, Burak Yahya.

P3HT:PCBM-based organic solar cells: optimisation of active layer nanostructure and interface properties

Burak Yahya Kadem

A thesis submitted in partial fulfilment of the requirements of
Sheffield Hallam University
for the degree of Doctor of Philosophy

2017

DECLARATION

I hereby declare that this thesis submitted for the degree of PhD is the result of my own research and that this thesis has not been submitted for higher degree to any other university or institution.

Burak Yahya Kadem

DEDICATION

To my parents, your sacrifices shan't be forgotten
To my beloved wife (Weam), and my children (Huda, Nada and Taha)
without your support and patience throughout my study,
this work would never has seen light

Burak Yahya Kadem

ABSTRACT

Organic solar cells (OSCs) have attracted a significant attention during the last decade due to their simple processability on a flexible substrate as well as scope for large-scale production using role to role technique. Improving the performance of the organic solar cells and their lifetime stability are one of the main challenges faced by researchers in this field. In this thesis, work has been carried out using a blend of Poly(3-hexylthiophene-2,5-diyl) (P3HT) and [6,6]-Phenyl C_{61} butyric acid methyl ester (PCBM) as an active layer in the ratio of (1:1) (P3HT:PCBM). The efficiency and stability of P3HT:PCBM-based solar cells have been examined using different methods and employing novel materials such as1-[N-(2- ethoxyethyl) pent-4-ynamide] -8 (11), 15 (18), 22 (25) - tris -{2-[2-(2-ethoxyethoxy) ethoxy] -1-[2-((2- ethoxyethoxy) - ethoxy) methyl] ethyloxy} phthalocyaninato zinc (II) (ZnPc) to construct a ternary hybrid as the active layer. Controlling the morphology and crystallinity of P3HT:PCBM active layer was carried out using different solvents including chloroform (CF), chlorobenzene (CB) and dichlorobenzene (DCB) and their co-solvents in the ratio of (1:1) to dissolve the P3HT:PCBM blend. Optimum morphology and crystallinity were achieved using a co-solvent made of CB:CF with the obtained solar cell exhibiting the highest performance with PCE reaching 2.73% among other devices prepared using different solvents. Further device performance improvement was observed through optimization of active layer thickness with studied thickness falling in range 65-266 nm. Measurements of the PV characteristics of the investigated OSC devices have revealed optimum performance when active layer thickness was 95 nm with PCE=3.846%. The stability of the P3HT:PCBM-based devices on optimisation of the active layer thickness has shown a decrease in PCE of about 71% over a period of 41 days. Furthermore, P3HT has been blended with different fullerene derivatives ($PC_{60}BM$, $PC_{61}BM$, $PC_{70}BM$ and $PC_{71}BM$) and the active layers were processed using the optimum solvent as well as optimum film's thickness.

These PCBM derivatives have different lower unoccupied molecular level (LUMO) and different higher occupied molecular level (HOMO) positions, which subsequently influence the PV parameters of the OSCs such as the device open circuit voltage (V_{oc}) and its built-in potential (V_{bi}). P3HT:$PC_{61}BM$-based blend has exhibited the highest device performance with PCE reaching 4.2%. Using the above mentioned optimum parameters, the P3HT:PCBM-based devices have been subjected to post-deposition annealing at different temperatures in the range 100-180°C. Efficient device performance was ascribed to P3HT:PCBM layers being subjected to post-deposition heat treatment at 140°C with PCE=5.5%. Device stability as a result of post-deposition heat treatment has also been shown to improve with PCE degrading by about 38% after 55 days.

The use of interfacial layer is found to play a key part in modifying the solar cell performance; using electron transport layer (ETL) such as aluminium tris(8-hydroxyquinoline) (Alq3) as a solution processable layer has contributed in increasing PCE to 4.25%, while, using PEDOT:PSS as a hole transport layer (HTL) doped with metal salts has significantly contributed in increasing PCE to reach 6.82% in device when PEDOT:PSS was doped with LiCl aqueous solution. Stability study for the device based on HTL has shown degradation in the PCE from 6.82% to around 1% over 96 days. Using ETL and HTL simultaneously in a complete device has shown a further enhanced PCE reaching 7%. In a further study, doping the P3HT:PCBM with the novel ZnPc hybrids (SWCNTs and reduced graphene oxide (rGO) are covalently and non-covalently functionalised to ZnPc) with the weight ratio of (1:0.01) has significantly altered the solar cell device properties. The best performance is based on P3HT:PCBM blended with ZnPc-SWCNTs-co bonded as a ternary active layer demonstrating device PCE of 5.3% compared to a reference device based on bare P3HT:PCBM blend with PCE of 3.46%.

ACKNOWLEDGEMENT

Firstly and mainly, I would like to express my appreciation and acknowledgements to my director of study and supervisor Dr. Aseel Hassan, without his support and guidance, this work would not have been possible. Your patience, motivation, interest, and massive knowledge have helped me in all the time of research and writing of this thesis.

I would also like to thank my second supervisor, Prof. I.M. Dharmadasa, for his assistance. Prof. Alexei Nabok, Prof. Wayne Cranton and Dr Heming Wang, your kind support and assistance are gratefully acknowledged.

Great thanks to Dr Tamara Basova and Prof. Mahmut Durmus for their contribution in this research as advisors.

Special thanks to my parents, my wife, my children, and my siblings, for their support, patience and understanding throughout the course of my studies.

I would also like to acknowledge my financial sponsor, the Ministry of Higher Education and Scientific Research in Iraq and University of Babylon, College of Science, Physics Department.

I gratefully acknowledge the Iraqi Cultural Attaché in London for their support during my PhD research.

Finally, I would like to thank my colleagues and friends for making life interesting during many hours underground in the laboratory, especially, Hikemt, Yasin, Ehsan, Maythem, Mohammed, Abdullah, Yaqub, Hisham, Ali, Ali, Hadi, Madugu, Olu, Ojo and Salim. Special thanks are also due to all MERI staff and technicians who were always of assistance.

LIST OF ABBREVIATION

OSCs	Organic solar cells
BHJ	Bulk heterojunctions
ITO	Indium Tin Oxide
P3HT	Poly (3-hexylthiophene)
$PC_{61}BM$	[6,6]-Phenyl C_{61} butyric acid methyl ester
$PC7_1BM$	[6,6]-Phenyl C_{71} butyric acid methyl ester
$PC_{60}BM$	Bis(1-[3-(methoxycarbonyl)propyl]-1-phenyl)-[6,6]C_{62}
$PC_{70}BM$	[6,6]-Phenyl-C_{71}-butyric acid methyl ester
PEDOT:PSS	Poly(3,4-ethylenedioxythiophene)-poly(styrene sulfonate)
Alq3	Tris(8-hydroxyquinoline) aluminium
DIO	1,8-diiodooctane
CB	Chlorobenzene
CF	Chloroform
DCB	Di-chlorobenzene
ZnPc	Zinc phthalocyanine
SWCNTs	Single-walled carbon nanotubes
rGO	Reduced graphene oxide
ZnPc-rGO-co	reduce graphene oxide covalently bonded to ZnPc
ZnPc-rGO-non-co	reduce graphene oxide non-covalently bonded to ZnPc
ZnPc-SWCNTs-co	Single wall carbon nanotube covalently bonded to ZnPc
ZnPc-SWCNTs-non-co	Single wall carbon nanotube non-covalently bonded to ZnPc
PCE	Power conversion efficiency
V_{oc}	Open circuit voltage
FF	Fill factor
J_{sc}	Short circuit current density
HOMO	Higher occupied molecular orbital

LUMO	Lower unoccupied molecular orbital
V_{bi}	Built-in potential
E_F	Fermi levels
E_{Fn}	Fermi level on the n type semiconductor
E_{Fp}	Fermi level on the p-type semiconductor
SCLC	Space-charge-limited conduction
n	Ideality factor
ϕ_B	Barrier height
R_s	Series resistance
R_{sh}	Shunt resistance
L_d	Carrier diffusion length
CT	Charge transfer
D/A	Donor/acceptor
HTL	Hole transport layer
ETL	Electron transport layer
IPCE	Incident Photon to Charge Carrier Efficiency
IQE	Internal quantum efficiency
EQE	External quantum efficiency

LIST OF PUBLICATION

1. **Kadem, B.**, Al-hashimi, M.K. and Hassan, A.K., Energy Procedia, 50 (2014): 237-245.
2. **Kadem, B.** and Hassan, A., Energy Procedia, 74 (2015): 439-445.
3. Kaya, E.N., Basova, T., Polyakov, M., Durmuş, M., **Kadem, B.** and Hassan, A., RSC Advances, 5 (2015) :91855-91862.
4. Basova, T.V., Parkhomenko, R.G., Krasnov, P.O., Igumenov, I.K., **Kadem, B.** and Hassan, A.K., Dyes and Pigments, 122 (2015): 280-285.
5. **Kadem, B.**, Cranton, W. and Hassan, A., Organic Electronics, 24 (2015): 73-79.
6. **Kadem, B.**, Hassan, A. and Cranton, W., Journal of Materials Science: Materials in Electronics, 26 (2015): 3976-3983.
7. **Kadem, B.**, Hassan, A. and Cranton, W., In Proceedings of the 31st European photovoltaic solar energy conference and exhibition, EUPVSEC (2015, Hamburg, Germany).
8. Parkhomenko, R., Sukhikh, A., Klyamer, D., Krasnov, P., Gromilov, S., **Kadem, B.**, Hassan, A. and Basova, T., The Journal of Physical Chemistry C (2016).
9. **Kadem, B.**, Hassan, A. and Cranton, W., AIP Conference Proceedings 1758 (2016): 020006. AIP Publishing.
10. Evyapan, M., **Kadem, B.**, Basova, T.V., Yushina, I.V. and Hassan, A.K., Sensors and Actuators B: Chemical 236 (2016) 605–613.
11. **Kadem, B.**, Hassan, A. & Cranton, W. Journal of Material Science: Material in Electronics, 27 (2016): 7038.
12. Madugu, M.L., Olusola, O.I.O., Echendu, O.K., **Kadem, B.** and Dharmadasa, I.M., Journal of Electronic Materials, 45 (2016): 2710-2717.
13. **Kadem, B.**, Göksel, M., Şenocak, A., Demirbaş, E., Atilla, D., Durmuş, M., Basova, T., Shanmugasundaram, K. and Hassan, A., Polyhedron, 110 (2016):37-45.
14. Basova, T., Parkhomenko, R., Polyakov, M., Gürek, A., Atilla, D., Yuksel, F., Ryabchikova, E., **Kadem, B.** and Hassan, A., Dyes and Pigments, 125 (2016):266.
15. **Kadem, B.**, Hassan, A., Göksel, M., Basova, T., Şenocak, A., Demirbaş, E. and Durmuş, M., RSC Advances, 6 (2016): 93453-93462.
16. **Kadem, B.**, Hassan, A. and Cranton, W., In Proceedings of the 32nd European photovoltaic solar energy conference and exhibition, EUPVSEC (2016, Munich, Germany).
17. **Kadem, B.**, Hassan, A. and Cranton, W., Thin Solid Film, (2017) (Accepted)
18. Maxim S. Polyakov, Tamara V. Basoval, Meltem Göksel, Ahmet Şenocak, Erhan Demirbaş, Mahmut Durmuş, **Burak Kadem**, Aseel Hassan, Synthetic Metals (2017) (Accepted)

CONFERENCES

1. **Kadem B.**, and Hassan A., MERI and BMRC symposium (Dec.2013), Sheffield Hallam University, UK. (Poster)
2. **Kadem B.**, Al-hashimi M. and Hassan A., The International Conference on Technologies and Materials for Renewable Energy, Environment and Sustainability, TMREES14 (April 2014), Beirut-Lebanon. (Oral)
3. **Kadem B.**, and Hassan A., MERI symposium (May.2014), Sheffield Hallam University, UK. (Poster)
4. **Kadem B.**, and Hassan A., UK semiconductor conference (July 2014), Sheffield Hallam University, UK. (Oral)
5. **Kadem B.**, and Hassan A., 16th International Conference on Materials Science and Engineering, (Oct. 2014), Brussels, Belgium. (Oral)
6. **Kadem B.**, and Hassan A., MERI and BMRC symposium (Dec.2014), Sheffield Hallam University, UK. (Poster)
7. **Kadem B.**, Cranton W. and Hassan A., Innovations in Large-Area Electronics Conference (innoLAE) (Feb. 2015), Cambridge, UK. (Poster)
8. **Kadem B.**, and Hassan A., The International Conference on Technologies and Materials for Renewable Energy, Environment and Sustainability, TMREES15 (April 2015), Beirut-Lebanon. (Oral)
9. **Kadem B.**, Hassan A. and Cranton W., 31st European photovoltaic solar energy conference and exhibition (EUPVSEC) (Sep. 2015), Hamburg, Germany. (Oral)
10. **Kadem B.**, Durmuş M., Basova T. and Hassan A., UK semiconductor conference (July 2015), Sheffield Hallam University, UK. (Oral)
11. **Kadem B.**, Durmuş M., Basova T. and Hassan A., UK semiconductor conference (July 2015), Sheffield Hallam University, UK. (Poster)
12. **Kadem B.**, and Hassan A., International Conference on Technologies and Materials for Renewable Energy, Environment and Sustainability, TMREES16 (April 2016), Beirut-Lebanon. (Oral)
13. **Kadem B.**, Hassan A. and Cranton W., 32nd European photovoltaic solar energy conference and exhibition (EUPVSEC) (June. 2016), Munich, Germany. (Poster).
14. **Kadem B.**, and Hassan A., MERI and BMRC symposium (Dec.2016), Sheffield Hallam University, UK. (Poster)

PRIZES AND AWARDS

1. The second paper placing in The International Conference on Technologies and Materials for Renewable Energy, Environment and Sustainability, Lebanon (April 2014).
2. Chair session in 16th International Conference on Materials Science and Engineering, Brussels, Belgium (Oct. 2014).
3. The third poster placing MERI and BMRC symposium/Sheffield Hallam University/UK (May 2015).
4. Award of Excellence in the International Conference on Technologies and Materials for Renewable Energy, Environment and Sustainability, Lebanon (April 2015).
5. Member of Scientific committee in The International Conference on Technologies and Materials for Renewable Energy, Environment and Sustainability, TMREES, Lebanon (2014-2016).
6. Award from the Iraqi Minister of Higher Education and Scientific research as one of the best 20 student in the UK during the PhD study period.

LIST OF FIGURES

LIST OF TABLES

CONTENTS

Chapter 1: Introduction

1.1 General background

Due to the rapid developments in societies and the increase in energy consumption in line with industrial development and climate change, energy demand is considered as one of the major problems that the world community will face [1]. Nowadays, the energy consumption is extremely dependent on fossil fuel resources such as petrol, natural gas and coal. The greatest challenge for the world community is to reduce the fossil fuel consumption specifically by switching partly and gradually to renewable energies, which therefore require major developments in the energy infrastructures. Several projects have been carried out by scientists who have specifically identified renewable energy from different resources such as water, wind, bio-materials and solar radiation [2]. Among all these renewable resources, solar energy draws an increasing research interest [1, 3] mainly because the rate of solar radiation intercepted by the Earth is about 20,000 times greater than the amount of energy consumed by all human being [4]. Additionally, solar resource exceeds all other renewable alternatives, but breakthrough in energy generation remained limited so far because of the high cost and the intermittent nature of solar radiation [2]. Solar energy technologies are experiencing rapid growth and possibly during the next 40 years it will be one of the major global energy providers [2]. The solar radiation comes in the form of electromagnetic radiation of a wide spectrum. The electromagnetic radiation ranges from high-energy (short wavelength) to low-energy (long-wavelength). The solar spectrum covers ultraviolet (UV) radiation ranging from (100-400) nm, the visible radiation ranging from (400-700) nm and the infrared (IR) radiation (700nm and above). The ultraviolet, visible and infrared radiations are significant parts of the solar spectrum which play an important role in global solar energy application including solar thermal and photovoltaic (PV). Fig.1.1 shows the solar spectral irradiance as a function of photon wavelength. The amount of solar radiation incident on a square meter of Earth's atmosphere or Earth's surface is known as irradiance and is measured in watts per square meter ($W.m^{-2}$).

The solar irradiance before entering Earth's atmosphere is about 1,366 $W.m^{-2}$ which is known as air mass zero (AM0) [5] When solar radiation passes through the Earth's atmosphere, the intensity of solar radiation is attenuated by ozone layer (O_3), water molecules, nitrogen molecules, CO_2, and dust. By the time the incoming solar radiation reaches the Earth's surface (sea level), the solar irradiance is reduced to $1000W.m^{-2}$ or $100mW.cm^{-2}$ which is known as air mass 1.5 (AM1.5) (ASTM G-173-03 International standard ISO 9845-1, 1992) is the standard defined for terrestrial use [6].

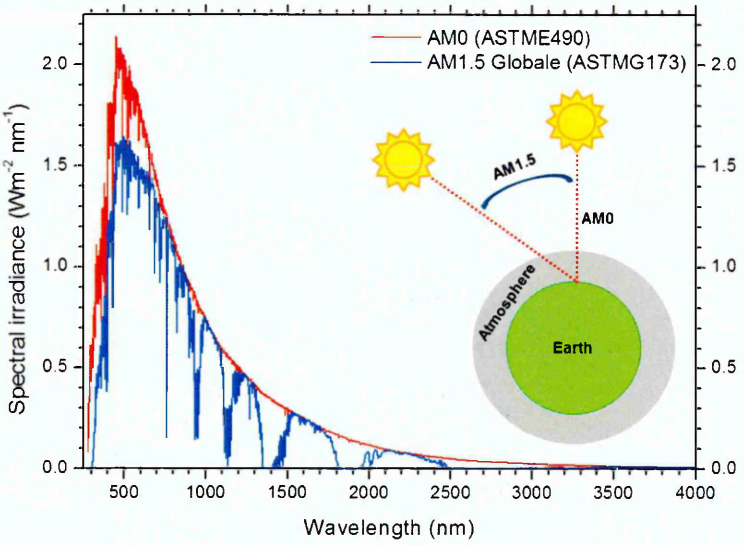

Fig.1.1: The solar spectral irradiance as a function of photon wavelength [6].

Up to date, different types of solar cells have been demonstrated as three different generations; the distinction between these generations is basically in the kind of materials used. The first generation consists of cells prepared by using crystalline silicon (Si) which is doped with Phosphorus (P) or Boron (B) whereas the second generation solar cell is based on semiconductor thin film technology; these include amorphous silicon (a-Si), polycrystalline silicon, copper indium gallium selenide (CIGS) and cadmium telluride (CdTe) based solar cells. The third generation of solar cells is based on a range of new materials, such as organic polymers, small molecules, nanotubes, quantum dots, silicon nanowires, and organic dyes [7].

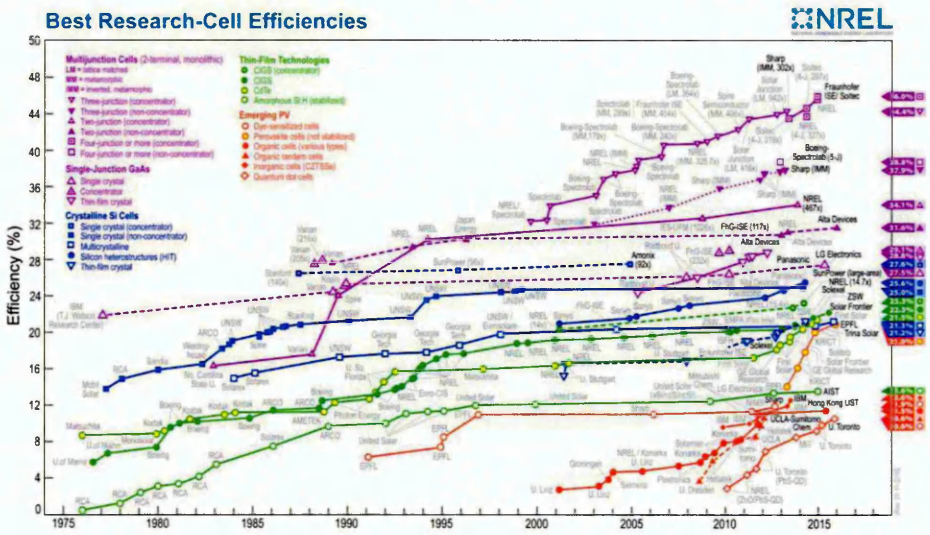

Fig.1.2: Solar cells efficiency table (NREL) [8]

The main parameter used to determine the solar cell performance is the cell power conversion efficiency (PCE). The latter is known as the percentage of the solar energy which is converted by the solar system to an external electrical power. The highest certified efficiency of 46±2.2% for the multi-junction solar cell of GaInP/GaAs and GaInAsP/GaInAs with an active area of 0.0520 cm^2 was developed by Soitec and CEA-Leti, France, together with the Fraunhofer Institute for Solar Energy Systems ISE, Germany and certified by AIS [9, 10]. In general, lower band gap materials are required in order to achieve high-efficiency solar cells. Such materials have the ability to produce more charge carriers and thus increase the photo-generated current as a result of light absorption, which in turn results in higher PV efficiencies. Furthermore, due to the energy distribution of the solar spectrum (see Fig.1.1), 43% of the total spectrum falls within the visible range, therefore the band gap of the semiconducting material plays a critical role in determining the solar cell performance. Fig.1.2 shows the best-certified efficiencies until 2016 including all types of solar cells according to the National Renewable Energy Laboratory (NERL).

1.1.1 First generation solar cell

The first generation solar cell is based on crystalline Si (see Fig.1.3). This generation is dominating the solar cells market by up to 90% of the commercially available cells [11].

The Si-based solar cell has higher efficiency, longer lifetime and stability than the other two generations. One of the main issues with this generation of solar cells is their manufacturing cost; highly pure Si is required to produce this type of solar cell as well as the associated high processing cost. According to Shockley-Queisser limitation, the highest efficiency for the material with indirect energy band gap of 1.1eV (such as Silicon) is found to be 32%; this is because the absorption of light by a material with such band gap corresponds to infrared light [12]. In other words, photons of red, yellow and blue light will all contribute to power production, whereas other wavelengths such as radio waves and microwaves will not. This places an immediate limit on the amount of energy that can be extracted from the sun [12]. Therefore, there is a limitation for the efficiency of the solar cells based on the band gap of the material.

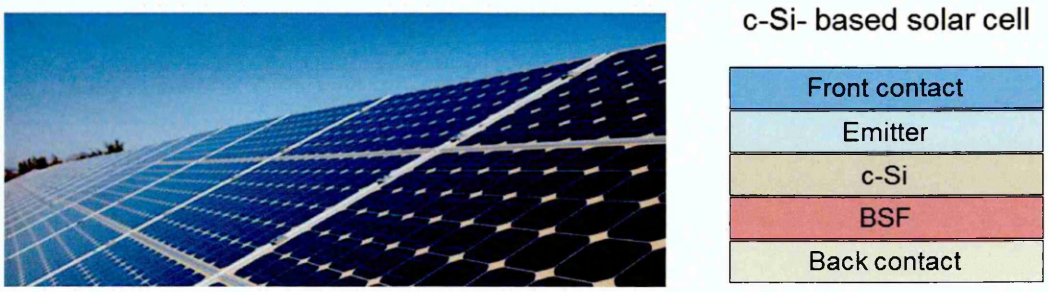

Fig.1.3: First generation solar cell based on crystalline Si

The highest recorded efficiency for crystalline-Si solar cells is 25.6±0.5% according to Panasonic HIT with an active area of 143.7 cm^2; this result has been certified by the Japanese National Institute of Advanced Industrial Science and Technology (NIST) [10, 13]. However, increasing the active area to 778 cm^2 has reduced the efficiency to 22.9±0.6% according to UNSW/Gochermann, a result that has been certified by Sandia test centre [10, 14]. Furthermore, smaller module crystalline-Si solar cells have shown an efficiency of 25.1±0.5% with an active area of 4.01 cm^2 which has been certified in Fraunhofer-Institut für Solare Energiesysteme (FhG-ISE) [10, 15]. Using light concentrator Si solar cell has achieved 27.6%±1.2% with an active area of 1cm^2 under light concentrated of 92.3sun [10, 16].

1.1.2 Second Generation

In order to accommodate new materials and reduce the production cost of solar cells, a significant volume of research has been concentrated on improving and developing cost-effective processes towards producing the second generation of solar cells. The latter encompasses III-V semiconductor cell technologies such as Gallium Arsenide (GaAs), thin film technology such as a-Si based thin film solar cells, Cadmium Telluride/Cadmium Sulfide (CdTe/CdS) solar cells and Copper Indium Gallium Selenide (CIGS) solar cells as demonstrated in Fig.1.4. Alta Devices has recorded the highest certified efficiency of 28.8±0.9% with an active area of 0.9927 cm^2 tested by National Renewable Energy Laboratory (NERL) for thin film GaAs-based solar cell according to the final progress in PV report [10, 17]. On the other hand, an efficiency of 29.1±1.3% has been recorded for a concentrator GaAs-based solar cell with an active area of 0.0505 cm^2 for Fraunhofer ISE [10]. Additionally, CIGS solar cell efficiency has achieved 21.0±0.6% for Solibro tested by Fraunhofer Institute for Solar Energy system (FhG-ISE) with a similar active area [10].

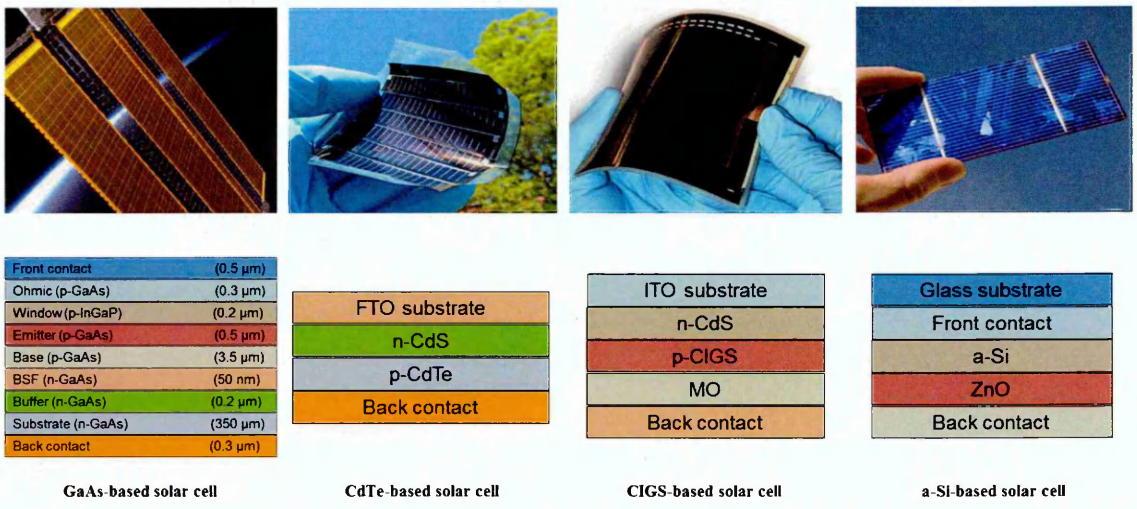

Fig.1.4: Second generation solar cell based on GaAs, CdTe, CIGS and amorphous Si

A significant improvement towards higher efficiency CIGS-based solar cells with PCE of 21.7% with a smaller active area of 0.4972cm^2 has been recorded for Zentrum für Sonnenenergie and Wasserstoff-Forschung (ZSW) [18]. On the other hand, CdTe-based solar cells have achieved 21.0±0.4% efficiency with an active area of 1.0623 cm^2

developed by First Solar and tested by Newport test centre [10]. Further improvement in CdTe solar cells has been reported with an efficiency of 21.5±0.4% by reducing the active area to 0.3455 cm^2 based on First Solar and certified by Newport [10]. On the other hand, an efficiency of 10.2±0.3% has been recorded for a-Si based solar cells with an active area of 1.001cm^2 as tested by Japanese National Institute of Advanced Industrial Science and Technology (AISY) [10, 19]. For the same type of solar cells, TEL Solar, Trubbach Labs have achieved 12.2±0.3% with device active area of 1.4m^2 as certified by European Solar Test Installation (ESTI) [10].

1.1.3 Third Generation

This generation of solar cells is mainly based on a range of new materials, which include conducting polymers, small molecules, nanotubes, quantum dots, silicon nanowires, and organic dyes [7]. The polymer or organic solar cells (OSCs) are mainly fabricated from thin films with a thickness of typically 100-200 nm of organic semiconductors as shown in Fig.1.5 (a) for a mini module organic solar cell. Over the last 20 years, so many different organic materials have been examined to produce the absorber layers including polymers, dyes and small-molecule as p-type semiconductor materials whereas n-type semiconductor materials are mostly carbon-based materials such as fullerene and its derivatives [20]. Their low-cost production as well as the viability of operating using flexible substrates, thus requiring less capital investment, provides them with a significant competitive advantage over the conventional silicon solar cells [21]. OSCs are suitable for large manufacturing such as roll-to-roll printing process (see Fig.1.5 (b)), which potentially leads to low cost and large scale flexible production [22]. Another advantage is ascribed to the diverse and versatile range of materials used, which can offer a wide range of properties including tailored band gap and therefore a varied range of light harvesting efficiency and ability to cover a broad range of the solar spectrum [21]. The relatively low efficiency and stability issues are considered as the main obstacles for this generation of solar cells to compete with the conventional technology. The history of OSCs goes back to 1958 when Kearns and Calvin reported a photo-voltage of 200 mV for magnesium phthalocyanine (MgPc) disks coated with a thin film of air-oxidized tetramethyl p-phenylenediamine (TMϕD) [23].

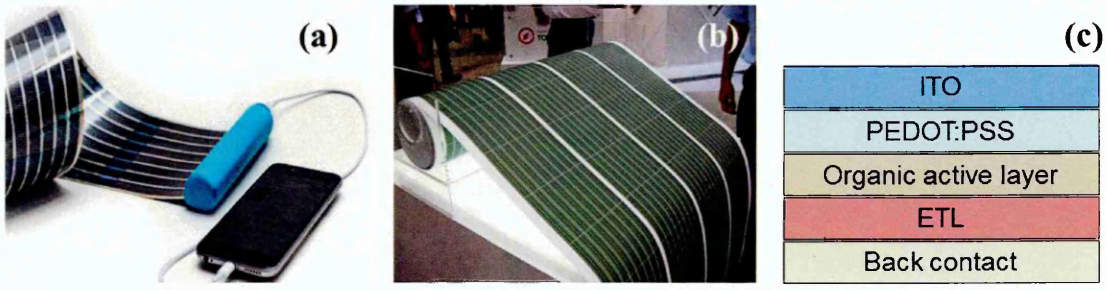

Fig.1.5: Third generation solar cell based on organic materials; (a) Mini module and (b) Large production using roll to roll technology, and (c) Organic solar cell structure

In 1974, Ghosh et al have observed a maximum power conversion efficiency of 0.01% using Al/MgPc/Au cell structure [24]. In 1986, PCE of 1.0% has been achieved by Tang using copper phthalocyanine (CuPc) and a perylene tetracarboxylic derivative and under simulated illumination of AM2 [25]. Since then, significant improvement in OSCs has been achieved through the development of bulk heterojunctions (BHJ), junction engineering and materials purity and control. In 2005, Yang et al [26] have achieved PCE of 4.4% for a OSCs based on a bulk heterojunction of polymer poly (3-hexylthiophene) (P3HT) and methano-fullerene. Since then, P3HT system became a standard in OSCs and acting as a basis for most attempts to commercialise OSCs. In 2013, Hosoya et al [10] have reported an efficiency of 11.0% for OSCs with a cell area of 0.99 cm^2.

Recently, Heliatek R&D teams reached a record conversion efficiency of 13.2% for an OPV multi-junction cell, setting a new world record for the direct conversion of sunlight into electricity using organic photovoltaic (OPV); the latter was independently confirmed by Fraunhofer CSP [27]. The world-record cell is a multi-junction cell combining three different absorbers; each one of them is dedicated to efficiently convert green, red or near-infrared light of the wavelength range between 450 and 950 nm into electricity. These absorber molecules have been developed and are patented by Heliatek. The new record efficiency was measured at simulated AM 1.5 illumination and was confirmed by the Fraunhofer-Center for Silizium-Photovoltaik-CSP in Halle.

According to the latest table of solar cell efficiency, Toshiba has claimed an efficiency as high as 11.2±0.3% with open circuit voltage (V_{oc}) of 0.78V, fill factor (FF) of 74.2% and short circuit current density (J_{sc}) of 19.3mA.cm^{-2} with an active area of about 1cm^2 [10]; the latter efficiency has been certified by AIST for a sub-module measured under the global AM1.5 spectrum (1000 W.m^{-2}) at a temperature of 25°C. Increasing the active area to 26.14cm^2 for a mini-module has resulted in decreasing the efficiency to 9.7±0.3% and decreasing the J_{sc} to 16.47mA.cm^{-2} [10]. For a module with an active area of 802cm^2, Toshiba has reported an efficiency of 8.7±0.3%, V_{oc} of 17.47V, FF of 70.4% and J_{sc} of 0.569A [10, 28]. An efficiency of 10.7% for OSCs based on a series of difluorobenzothiadizole (ffBT) and oligothiophene-based polymers with the oligothiophene unit being quaterthiophene (T4), terthiophene (T3), and bithiophene (T2) was achieved by Hong Kong UST with a cell active area of 0.0429 cm^2 tested by Newport [29]; they have demonstrated that a polymer based on ffBT and T3 with an asymmetric arrangement of alkyl chains assists the fabrication of efficient thick film OSCs without using any processing additives. The higher occupied molecular (HOMO) and the lower unoccupied molecular (LUMO) levels of the polymers have been reduced by reducing the number of thiophene units per repeating unit, and the absorption onsets of the polymer films are also slightly red-shifted. These positive changes contribute to higher V_{oc} and J_{sc} values for the T3 polymer than for the T4 polymers [29].

In the current research, the 3rd generation of solar cell, organic solar cells (OSCs), have been investigated. The main motivation of this research is to produce highly efficient OSC with good stability. OSCs have different advantages such as simple technological processes for devices fabrication, the use of flexible substrates, low cost, and potentially large scale manufacturing. It can include a possibility of tailoring the band gap. Whereas some drawbacks such as short life time, instability, and relatively low efficiency are still under consideration.

1.2 Aims of the research

The principal aim of this research is to investigate strategies and explore venues of improving the performance of organic solar cell based on BHJ of poly (3-hexylthiophene) (P3HT) and [6,6]-Phenyl C_{61} butyric acid methyl ester ($PC_{61}BM$) (P3HT:PCBM). The research programme is firstly focussed on investigating P3HT:PCBM blend properties. The main contribution of this research consists of two parts; firstly, P3HT:PCBM blend being a well-known OSC material, and in order to increase device efficiency, requires a comprehensive understanding of the active layer morphology as well as electron transport properties pertained to the interface properties within the blend itself as well as those related to the metallic charge collecting electrodes. Also, it is essential to understand the morphological and structural properties of P3HT:PCBM active layer by using different solvents and their co-solvents in order to control the active layer morphology and crystallinity. In order to achieve this goal and to attain the highest proposed performance for P3HT:PCBM-based solar cells, the following objectives are to be realised:

1) Optimisation of the P3HT:PCBM active layer parameters using different solvents, different thicknesses, and post-deposition annealing treatment;
2) Using different fullerene derivatives as acceptor in the active layer;
3) Optimisation the hole and electron transport layers;
4) Employing the proposed optimisation parameters and combining them in one device in order to achieve highly efficient solar cell;
5) Investigate the stability of the prepared solar cells.

The second contribution focuses on employing novel hybrids materials based on graphene or single-walled carbon nanotubes (SWCNTs) and zinc phthalocyanine (ZnPc), either covalently or non-covalently functionalized to SWCNTs and reduced graphene oxide (rGO) as additives to the main P3HT:PCBM blend with the aim of enhancing the light harvesting properties, the charge carriers transport properties as well as improving the conductivity of the active layer and therefore the PV properties. The main challenge in this part is to modify the ratio of the carbon-based hybrids and to control the other parameters mentioned earlier to achieve as high as possible PCE.

References

[1] Reddy, P. J. (2012). Solar Power Generation: Technology, New Concepts & Policy. CRC Press.

[2] Panwar, N. L., Kaushik, S. C. & Kothari, S. (2011). Role of renewable energy sources in environmental protection: a review. Renewable and Sustainable Energy Reviews, 15(3), 1513-1524.

[3] Ameri, T., Li, N., & Brabec, C. J. (2013). Highly efficient organic tandem solar cells: a follow up review. Energy & Environmental Science, 6(8), 2390-2413.

[4] http://www.ecoworld.com/energy-fuels/how-much-solar-energy-hits-earth.html

[5] http://rredc.nrel.gov/solar/spectra/am0/

[6] http://rredc.nrel.gov/solar/spectra/am1.5/

[7] Manaf, N., Sheffield Hallam University. Materials Engineering Research Institute, degree granting institution. (2015). Organic/inorganic Hybrid Solar Cells Based on Electroplated CdTe.

[8] http://phys.org/news/2016-02-solar-cell-efficiency-nrel.html

[9] Soitec: New World Record For Solar Cell Efficiency At 46%. (2014, December 02). News Bites - Computing & Information. News Bites - Computing & Information, Dec 2, 2014.

[10] Green, M., Emery, K., Hishikawa, Y., et.al. (2016). Solar cell efficiency tables (version 48). Progress in Photovoltaics: Research and Applications, 24 (7), 905-913.

[11] Krebs, F. C. (Ed.). (2010). Polymeric solar cells: materials, design, manufacture. DEStech Publications, Inc.

[12] Shockley, W., & Queisser, H. J. (1961). Detailed balance limit of efficiency of p-n junction solar cells. Journal of Applied Physics, 32(3), 510-519.

[13] Masuko, K., Shigematsu, M., Hashiguchi, T.,et.al. (2014). Achievement of more than 25% conversion efficiency with crystalline silicon heterojunction solar cell. IEEE Journal of Photovoltaics, 4(6), 1433-1435.

[14] Zhao, J., Wang, A., Yun, F., Zhang, G., Roche, D. M., Wenham, S. R., & Green, M. A. (1997). 20,000 PERL silicon cells for the1996 World Solar Challenge'solar car race. Progress in Photovoltaics, 5, 269-276.

[15] Glunz, S.W., Feldmann, F., Richter, A., et.al., (2015, September), The irresistible charm of a simple current flow pattern 25% with a solar cell featuring a full-area back contact. In Proceedings of the 31st European Photovoltaic Solar Energy Conference and Exhibition (pp. 259-263).

[16] Slade, A., & Garboushian, V. (2005, October). 27.6% efficient silicon concentrator solar cells for mass production. In Technical Digest, 15th International Photovoltaic Science and Engineering Conference, Beijing.

[17] Kayes, B., Nie, H., Twist, R., et.al. (2011). 27.6% Conversion efficiency, a new record for single-junction solar cells under 1 sun illumination. Photovoltaic Specialists Conference (PVSC), 2011 37th IEEE, 000004-000008.

[18] Powalla, M., Jackson, P., Hariskos, D., et.al. (2014, September). CIGS thin-film solar cells with an improved efficiency of 20.8%. In Proc. 29th European Photovoltaic Solar Energy Conference.

[19] Matsui, T., Sai, H., Suezaki, T., et.al. (2013). Development of highly stable and efficient amorphous silicon-based solar cells. In Proc. 28th European Photovoltaic Solar Energy Conference.

[20] Dang, M. T., Hirsch, L., Wantz, G., & Wuest, J. D. (2013). Controlling the morphology and performance of bulk heterojunctions in solar cells. Lessons learned from the benchmark poly (3-hexylthiophene):[6, 6]-phenyl-C61-butyric acid methyl ester system. Chemical reviews, 113(5), 3734-3765.

[21] Mahmoud, A. Y., Zhang, J., Ma, D., et.al. (2013). Thickness dependent enhanced efficiency of polymer solar cells with gold nanorods embedded in the photoactive layer. Solar energy materials and solar cells, 116, 1-8.

[22] Søndergaard, R., Hösel, M., Angmo, D.,et.al. (2012). Roll-to-roll fabrication of polymer solar cells. Materials today, 15(1), 36-49.

[23] Kearns, D., & Calvin, M. (1958). The photovoltaic effect and photoconductivity in laminated organicsystems. Journal of Chemical Physics, 29(UCRL--8441).

[24] Archer, M. D., & Green, M. A. (Eds.). (2014). Clean electricity from photovoltaics (Vol. 4). World Scientific, London.

[25] Tang, C. W. (1986). Two-layer organic photovoltaic cell. Applied Physics Letters, 48(2), 183-185.

[26] Li, G., Shrotriya, V., Huang, J., et.al. (2005). High-efficiency solution processable polymer photovoltaic cells by self-organization of polymer blends. Nature materials, 4(11), 864-868.

[27] Heliatek sets new organic photovoltaic world record efficiency of 13.2%. (2016). Renewable Energy Focus, 17(3), 84-89.

[28] Hosoya, M. O. (2013). Organic thin film photovoltaic modules. 93rd Annual Meeting of the Chemical Society of Japan, (pp. 21-37).

[29] Hu, H., Jiang, K., Yang, G., et.al. (2015). Terthiophene-based D–A polymer with an asymmetric arrangement of alkyl chains that enables efficient polymer solar cells. Journal of the American Chemical Society, 137(44), 14149-14157.

Chapter 2: Theoretical Background

2.1 PN-junction

Diodes and transistors are fundamental devices in the field of solid-state electronics, which form the back bone of complex electronic circuits, including LED and solar cell devices. These devices are based on the formation of PN-junction structures, which consist of two types of semiconducting materials, p-type and n-type, coming into contact, as shown in Fig.2.1. The region which separates the two semiconductors is known as the depletion region or the junction. The latter region is formed as a result of diffusion of some electrons and holes which diffuse across the junction on each side of the junction and eliminate each other's charge. This diffusion of holes and electrons across the junction continues until an equilibrium condition is reached in which a potential difference (usually described as a potential barrier) is formed across the junction, and prevents further charge diffusion. By applying an external voltage, this barrier is either increased or decreased depending on the polarity of the applied voltage (reverse or forward) as illustrated in Fig.2.1 [1]. In the case of applying forward bias, the positive terminal of the DC source is connected to the p-type region and the negative terminal is connected to the n-type region of the junction, as shown in Fig.2.1. This configuration permits the flow of current across the PN-junction, where the holes are repelled by the positive terminal and the electrons by the negative terminal and both will be driven towards the junction leading to the diffusion of excess minority carriers. The potential barrier at the junction is lowered by applying forward bias (V_f) from the equilibrium potential at the junction (V_o) to a smaller value ($V_o - V_f$). Large current flows due to a lower potential barrier across the depletion region thereby allowing more current to flow through the junction. On the other hand, applying reverse bias ($V = -V_r$) the opposite occurs; the potential barrier at the junction becomes higher ($V_o + V_r$) with opposite configuration to that of the forward bias and will thereby prevents the recombination of holes and electrons in the depletion region. The diode current is therefore negligibly small due to increased potential barrier at the junction [2].

The electric field within the depletion region can be assumed from the potential barrier. The potential barrier decreases with a forward bias voltage since the applied electric field opposes the built-in potential. On the application of reverse bias, the potential barrier at the junction is increased by the applied voltage, which is in the same direction as the equilibrium field [3].

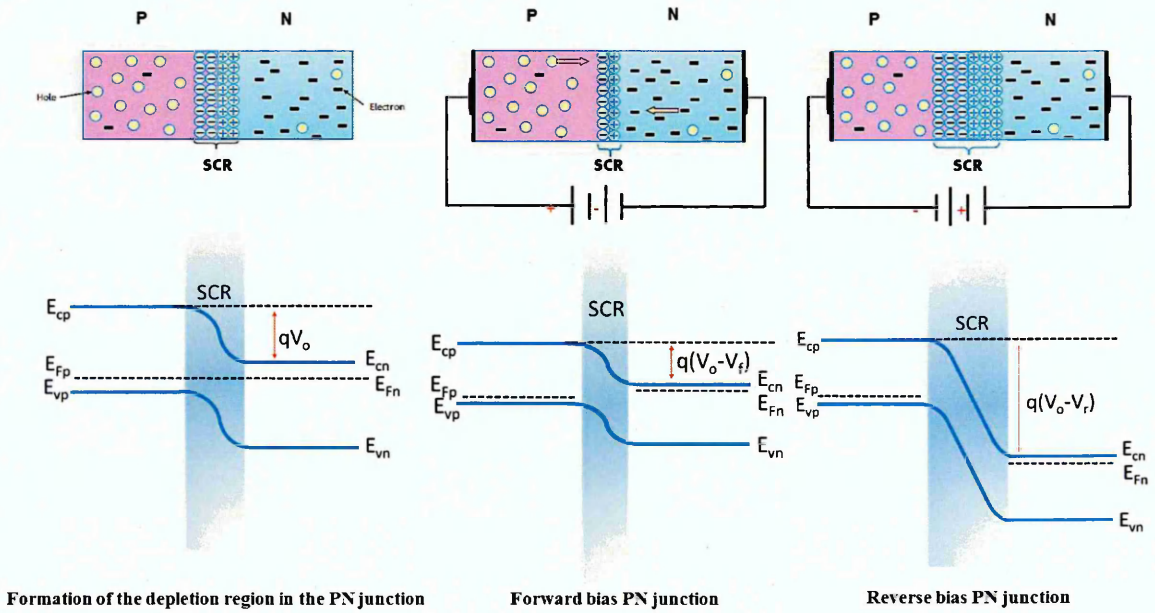

Fig.2.1: The variation of the depletion width of a PN-junction under applying forward and reverse bias

The change in the electric field at the junction is due to the change in the depletion region width (W). The height of the electron energy barrier is simply the electronic charge times the barrier height. Therefore, the bands are separated less under forward bias [$q(V_o-V_f)$] than that at equilibrium, and more under reverse bias [$q(V_o+V_r)$]. Assuming that Fermi level depth inside each neutral region is essentially at the equilibrium value; therefore, the shifting of the energy bands under bias implies a separation of the Fermi levels on either side of the junction. Under forward bias, the Fermi level on the n side (E_{Fn}) is above (E_{Fp}) by the energy (qV_f); for reverse bias, E_{Fp} is qV_r higher than E_{Fn} [3].

2.2 Metal-semiconductor junction

Generally, solar cells require two electric contacts on both sides to collect effectively the photo-generated charge carriers and carrying them to the external circuit. Such contacts are formed as semiconductor/metal (MS) contacts, and are either of ohmic or rectifying nature (Schottky contact) [3,4]. In solar cell devices, the front contact is either a grid to reduce shading effects or transparent electrode to permit incident light passing through it [5]. When a metal with a work function (ϕ_M) is brought into intimate contact with an organic semiconductor with an electron affinity (χ_S), two possible contacts (junction) are formed. The contact could be of ohmic nature; in such a contact, the I-V characteristics exhibit a linear behaviour in both biasing directions [3]. Ideal metal-semiconductor contacts are ohmic when majority carriers provide the charge induced in the semiconductor in aligning the Fermi levels. For instance, when $\phi_m < \phi_s$ ($\phi_m$and ϕ_s are the metal and semiconductor work functions, respectively) for an n-type semiconductor, the Fermi levels are aligned at equilibrium as a result electrons transfer from the metal to the semiconductor. This lowers the potential barrier relative to the metal at equilibrium. In this case, the barrier to electrons flow between the metal and semiconductor is small and can easily be overcome by electrons with applying a small voltage. Similarly, in the case of $\phi_m > \phi_s$ for p-type semiconductor which results in easy flow of holes across the junction. Unlike the rectifying contact, no depletion region occurs in the semiconductor in these cases since the potential differences required aligning the Fermi levels at equilibrium [4]. The metal-semiconductor junction might be rectifying (denoted as Schottky junction) as described in Fig.2.2. In the case of metal/n-type semiconductor contact when $\phi_m > \phi_s$, where the Fermi level in the metal is at a lower potential than in the semiconductor. When the junction is formed between the two materials, Fermi level should line up at the junction and remain flat in the absence of any current. To ensure the continuity of the vacuum level and keep the Fermi level flat, Fermi level must move deeper into the band gap of the semiconductor at the interface region. This involves electrons moving out from the semiconductor to the metal side. Since the metal has enormous electrons density, the metal Fermi level or band profile does not change when a small fraction of electrons are added or taken out [4].

In an ideal Schottky junction, the barrier height (ϕ_B) at the junction defined as the difference between the semiconductor conduction band (LUMO) and the metal Fermi level, and is represented in the following equation [3,4]:

$$\phi_B = \phi_M - \chi_S \tag{2.1}$$

The electrons coming from the semiconductor to the metal face a potential barrier provided by the built-in potential (V_{bi}) of the junction; where V_{bi} is given by the following equation [3,4]:

$$V_{bi} = \phi_M - \phi_S \tag{2.2}$$

The height of V_{bi} can be altered by applying an external bias, as in the case of PN-junction and the junction can rectify [3,4]. Usually, the Schottky barrier height for n or p-type semiconductors depends on the metal and the semiconductor properties [4].

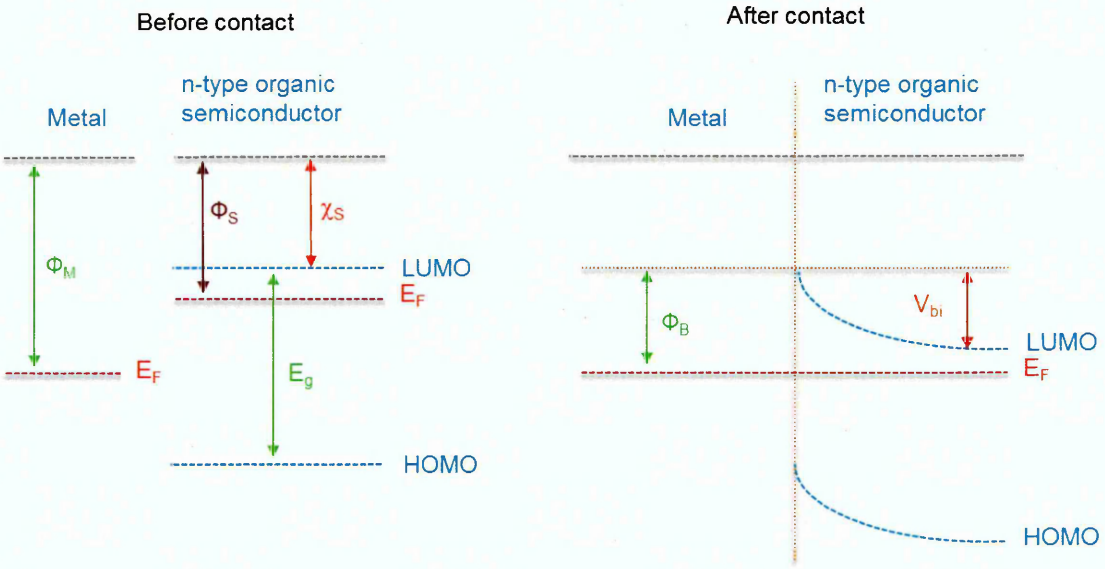

Fig.2.2: Energy level alignments for metal/n-type semiconductor before and after the contact

In the case of a non-ideal surface, the defects region leads to a distribution of electronic levels in the band gap at the interface. If the density of band gap states near the neutral level (ϕ_o) is very large, then the depletion of electrons to the semiconductor does not alter the Fermi level position at the surface and the Fermi level is said to be pinned [4]. The most important and expected mechanism of current flow across the Schottky barrier is due to thermionic emission. In this case, by assuming the absence of tunnelling effect, the electrons that cross the junction must have energies greater than the barrier height at the junction, and therefore, the current is limited by the barrier height [4]. If electrons in the semiconductor are distributed according to Boltzmann statistics, therefore, the density of electrons with energies higher than the barrier height of (V_{bi}-V) is given by:

$$n = n_o \exp\left[-\frac{(V_{bi}-V)}{kT}\right] \tag{2.3}$$

where, V is positive for the forward bias and negative for the reverse bias. n_o is the electron density in the neutral region and n is the electron density across the barrier. n_o is given in terms of the effective density of electrons N_c as:

$$n_o = N_c \exp\left[-\frac{(E_c-E_{Fs})}{kT}\right] \tag{2.4}$$

where barrier height on the metal side is:

$$q\phi_B = qV_{bi} + E_c - E_{Fs} \tag{2.5}$$

Therefore:

$$n = N_c \exp\left[-\frac{(q\phi_B-qV)}{kT}\right] \tag{2.6}$$

If the electrons are considered to be moving randomly, the average flux of electrons imposing on the ϕ_B is approximately ($\frac{Sn}{4}$) where S is the average speed of the electrons. The corresponding current is, therefore:

$$I_{sm} = \frac{qAS}{4} N_c \exp\left[-\frac{q(\phi_B-V)}{kT}\right] \tag{2.7}$$

where A is the device active area. When the applied bias is zero, the current flow from the metal to the semiconductor (I_{sm}) must balance the current flow from the semiconductor to the metal (I_{ms}):

$$I_{ms} = I_{sm} = \frac{qAS}{4} N_c \exp\left[-\frac{q\phi_B}{kT}\right] \tag{2.8}$$

When a voltage (V) is applied, the barrier seen by the electrons from the metal side is unchanged and I_{ms} remains constant ($=I_s$). Therefore, the net current at an applied bias is:

$$I = I_{sm} - I_{ms} = I_s\left[\exp(\frac{qV}{kT}) - 1\right] \tag{2.9}$$

Substituting for the effective conduction band density N_c, then $I_s = I_{sm}$ at $(V = 0)$:

$$I_s = A\left(\frac{m^* qk^2}{2\pi^2\hbar^3}\right) T^2 \exp\left[-\frac{q\phi_B}{kT}\right] \tag{2.10}$$

The quantity $(\frac{m^* qk^2}{2\pi^2\hbar^3})$ is called Richardson constant and is denoted by A*, therefore, equ.2.11 becomes [4, 6, 7]:

$$I_s = AA^* T^2 \exp\left[-\frac{q\phi_B}{kT}\right] \tag{2.11}$$

Most practical Schottky barriers show deviation from ideal thermionic emission behaviour. A dimensionless parameter called the ideality factor (n) is usually included in the I-V relationship to take into account non-ideal diode behaviour, represented by the following equation [8,9]:

$$I = I_s\left[\exp(\frac{qV}{nkT}) - 1\right] \tag{2.12}$$

For sufficient forward bias ($V \gg kT/q$), n and ϕ_B can be determined through the following relations, respectively [7]:

$$n = \frac{q}{kT}\left(\frac{dV}{d\ln I}\right) \tag{2.13}$$

$$\phi_B = \frac{kT}{q} \ln\left(\frac{AA^*T^2}{J_s}\right) \quad (2.14)$$

Cheung and Cheung [10] have developed another method to determine n and ϕ_B values by considering the series resistance (R_s); R_s is an important factor that has a significant effect on the electrical properties of a diode, and therefore when R_s is taken into consideration the I-V relation is described by the following equation [10, 11]:

$$I = I_s \exp\left[\frac{q(V-IR_s)}{nkT} - 1\right] \quad (2.15)$$

where IR_S is the voltage drop across the series resistance of the device.

2.3 Capacitance-Voltage characteristics

In many applications of PN-junction structures, the capacitance is a limiting factor. The junction capacitance of a diode is easy to visualise from the charge distribution in the depletion region. The uncompensated acceptor ions on the p-side provide a negative charge and equal positive charge results from the ionised donor in the n-side of the depletion region [3], where the depletion region width in equilibrium is expressed by the following equation [3]:

$$W = \sqrt{\frac{2\epsilon V_o}{q}\left(\frac{N_a+N_d}{N_aN_d}\right)} \quad (2.16)$$

where N_a represents the acceptor concentration in the semiconductor and N_d is the donor concentration. Under applied bias, W must be altered by the barrier height; W is described by the following equation [3]:

$$W = \sqrt{\frac{2\epsilon(V_o-V)}{q}\left(\frac{N_a+N_d}{N_aN_d}\right)} \quad (2.17)$$

Herein, the applied bias can be either positive or negative to account to forward (V_f) or reverse (V_r) bias, respectively.

The width of the depletion region is increased by applying a reverse bias and is decreased by applying a forward bias as depicted in Fig.2.1. Generally, Mott–Schottky analysis is applied to capacitance-voltage measurements which are known as a simple method to determine several important parameters of Schottky or p-n junctions, such as the built-in potential (V_{bi}), the doping density, the position of Quasi-Fermi level within the band gap (E_F) and the barrier height (ϕ_B) [12]. The linear region of the ($1/C^2$ versus V) plot indicates the Schottky barrier formation at the metal/semiconductor interface which can also be used to estimate the doping density (N_a) as in the following equation [13]:

$$N_a = -\frac{2}{q\epsilon A}\left[\frac{dC^{-2}}{dV}\right]^{-1} \quad (2.18)$$

Another important parameter is the position of Fermi level (E_F) within the band gap which could also be estimated using the following equation [14]:

$$E_F = \frac{KT}{q} \ln\left(\frac{N_v}{N_a}\right) \quad (2.19)$$

Furthermore, ϕ_B can also be determined from the C-V measurements using the following equation [15]:

$$\phi_B = V_{bi} + E_F \quad (2.20)$$

2.4 Space charge limited theory

Since the main focus of this research is in organic materials which typically have low density and mobility of charge carriers, we need to discuss in more details the mechanism of space charge limited conductivity (SCLC). SCLC is similar to the transport conduction of electrons in a vacuum diode. The current density-voltage (J-V) characteristic of a vacuum diode is ruled by the Child's law. In a solid material, such as thin films, SCLC is produced by the injection of charge carriers at an ohmic contact. A typical J-V characteristic plotted in a log-log scale for SCLC is shown in Fig.2.3.

The space charge limited conduction (SCLC) current has a noticeable effect on the electrical properties of semiconductors and insulators because they are normally characterised with a low density of free carriers. Very large effects can be produced by the use of ohmic contacts, which facilitates injection of charges into the thin film. The character and magnitude of SCLC effects are determined largely by the presence of localised states, which can trap and store charges in equilibrium with the free charge. If an electron-injecting contact is applied to a perfect trap-free thin film, electrons will travel from the metal into the conduction band of the thin film and form a space charge [16]. The presence of traps generally reduces the current by capturing most of the injected carriers. As the injection level (applied voltage) is raised, all the traps will eventually become filled and the current will rise sharply back to the trap free value (see Fig.2.3). For trap-free semiconductors, such current is predicted to exhibit a quadratic dependence on the applied voltage, as described by Mott and Gurney [16]. However, early data [17, 18] exhibited an initial slow rise followed by a sharp power-law rise. Rose [18] has viewed the slow rise in current as a function of applied voltage as an Ohmic current which is ascribed to the intrinsic carriers whereas the sharp rise in current is attributed to the injected carriers which are trapped by deep-level defects. Injected carriers get trapped and generate a pushback voltage until all traps are filled (trap-filled limit or TFL); at the TFL, the pushback voltage is overcome and the current rises sharply (see Fig.2.3).

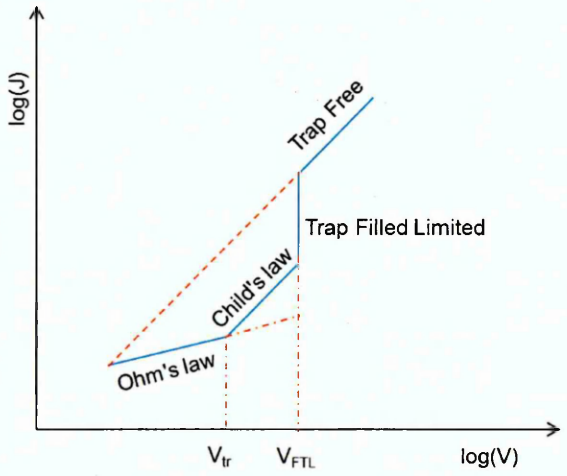

Fig.2.3: Double scale of J-V characteristics represents SCLC

The Mott-Gurney limit is approached at higher voltages when the traps have no further effect. Interesting features of the J-V characteristic are limited within a "triangle" in the logJ-logV curve bounded by three limiting curves: Ohm's law (JαV), Child's law (JαV^2), and a trap-filled-limit (TFL) curve which has a voltage threshold and an enormously steep current rise [19]. Generally, at low applied voltage, charge transport is ascribed to ohm's law (JαV), and it is represented by the following equation [20]:

$$J=pq\mu \frac{V}{d} \tag{2. 21}$$

where p is the hole concentration, μ is the mobility, V is the applied voltage and d is the active layer thickness. At the second region when Child's law (JαV^2) dominates, charge transport can be ascribed to trap-controlled space charge limited conduction (SCLC) with traps located at a single energy level inside the band gap; this mechanism is represented by the following equation [13]:

$$J_{TFL}=\frac{9}{8}\epsilon\epsilon_0\theta\mu \frac{V^2}{d^3} \tag{2. 22}$$

where ϵ is the dielectric constant of the polymer, ϵ_0=8.854 $\times 10^{-12}$ F/m is the permittivity of free space and θ is the trap-limiting factor, which represents the ratio of free to trapped charges and is given by [20]:

$$\theta = (\frac{N_v}{N_t})\exp(\frac{E_t}{kT}) \tag{2. 23}$$

where N_t is the trap concentration at energy level E_t and N_v is the effective density of states in the semiconductor [21]. At higher applied voltage range when the gradient becomes very steep, the J-V characteristics can be associated with trap filling limit beyond which trap-filled SCLC (TSCLC) mechanism is observed. This is evident by the onset of trap-free space charge limited conductivity (TFSCLC) and the J-V dependence is described by Child's law [22]:

$$J = \frac{9}{8}\epsilon\epsilon_0\mu \frac{V^2}{d^3} \tag{2. 24}$$

This happens when the injected carriers from the electrodes exceed the thermally generated carriers and there are no traps in the space charge region or all traps are filled and the current density increases quadratically with the applied voltage [13]. Using the data of this region (TFSCLC) in the logJ-logV dependence, the charge carrier mobility in the active layer can be estimated by plotting J vs. V^2/d^3 (see equ.2.24). Usually, charge carrier mobility in organic thin films is very low, mainly due to structural disorder in the films [23]. This approach of mobility measurements will be used in this work for evaluation of charge carriers' mobilities of the organic layers.

2.5 Solar cell characterisation

It is well known that solar cells operate without an external power supply and relies on the optical power to generate current and voltage. In the solar cell conversion, it is important to note that photons that have energy hν smaller than the semiconductor bandgap (E_g) will not produce electron-hole pairs. On the other hand, photons with energies greater than E_g will produce electron-hole pairs, regardless of how large the difference between the two energies is ($h\nu$-E_g) [4]. This difference in energy is simply dissipated as heat. Therefore, solar cell efficiency depends critically on how the semiconductor band gap (E_g) matches the solar energy spectra. To calculate the parameters of a solar cell, the equivalent circuit of a solar cell shown in Fig.2.4(a) is considered. Under open circuit condition, where I=0, this gives [4]:

$$I = 0 = I_L - I_s\left[\exp\left(\frac{q(V-IR_S)}{nkT}\right) - 1\right] \tag{2.25}$$

The open circuit voltage (V_{oc}) is derived from eq. 2.28 as shown in the following equation [4, 24]:

$$V_{oc} = \frac{nkT}{q}\ln\left(1 + \frac{I_L}{I_s}\right) + IR_S \tag{2.26}$$

Furthermore, V_{oc} could also be determined as a function of the quasi Femi level E_F using the following relation [25]:

$$V_{oc} = \frac{E_{Fn} - E_{FP}}{q} \tag{2.27}$$

where E_{Fn} and E_{Fp} are the quasi-Fermi levels of electrons and holes under open circuit condition. Under short circuit condition:

$$I = I_L = I_{sc} \tag{2.28}$$

where I_{sc} is the short circuit current. A plot of the measured I-V characteristics represents the superposition of the solar cell diode under illumination as shown in Fig.2.4(b). The parameters of V_{max} and I_{max} are defined as voltage and current values which deliver the maximum power (P_{max}) as illustrated in Fig.2.4(b). The power conversion efficiency (PCE) of solar cells is defined as the ratio of the output electric power to the input optical power. When the solar cell is operating under maximum power conditions, PCE is defined as follows [4, 26]:

$$PCE = \frac{P_{max}}{P_{in}} \times 100\% = \frac{I_{max}V_{max}}{P_{in}} \times 100\% \tag{2.29}$$

The fill factor of a solar cell is the ratio of the solar cell out power output ($V_{max} \times I_{max}$) to its ideal power ($V_{oc} \times I_{sc}$) [26]:

$$FF = \frac{I_{max}V_{max}}{I_{sc}V_{oc}} \tag{2.30}$$

This is a key parameter in evaluating the performance of solar cells, where an ideal solar cell would have a FF value of 100%, however, a typical commercial solar cell have a value of 70% or little larger. This significance of this parameter will be discussed in further detail in section 2.5.3.

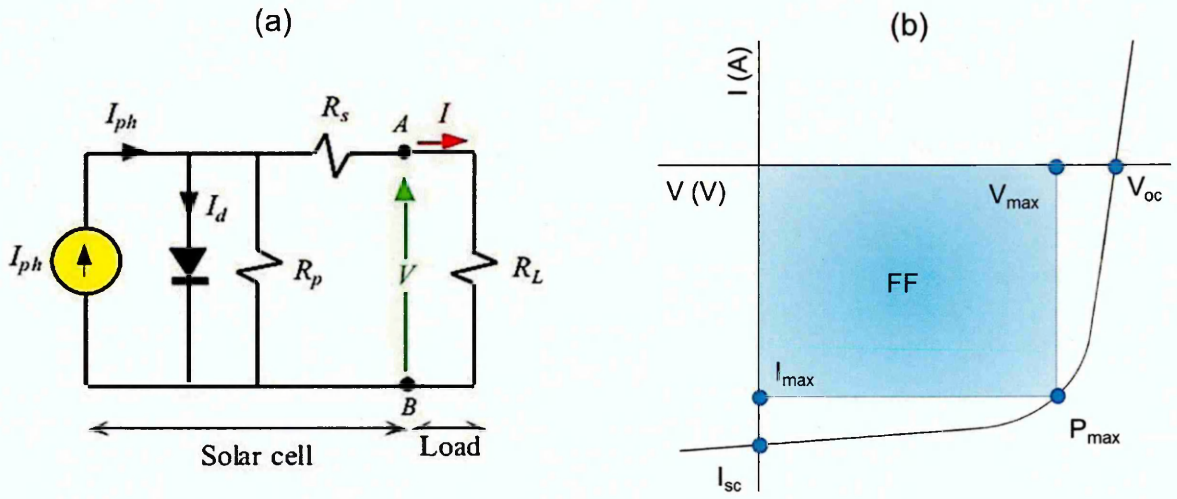

Fig.2.4: (a) equivalent circuit of a solar cell and (b) I-V curve for the solar cell under illumination

2.5.1 Open circuit voltage

In the organic solar cell, excitons are generated when light is absorbed by the organic active layer, and those will be separated into holes and electrons at the donor/acceptor interface within the active layer. These charge carriers will be forced to drift to their respective electrode under the internal electric field whereby they provide power to an external circuit [27]. Under open-circuit condition and stable illumination, the generated carriers will accumulate on both electrodes, creating a voltage difference, which cancels out the built-in potential (V_{bi}). At this point, no clear current occurs inside the device because the charge carriers' generation and recombination rates are exactly balanced. Therefore, the device is under the quasi-equilibrium condition and the voltage difference between the cathode and the anode represents V_{oc}. The latter is known as the maximum output voltage provided by a solar cell [27]. A direct relation holds between V_{bi}, V_{oc} and the Fermi level (E_F) because of the energy level alignment.

2.5.2 Short circuit current density

The current provided by a solar cell plays an important role in determining the final performance of the solar cell. Increasing the current can noticeably increase the PCE of the solar cell. Several parameters affect the production of high current within the solar cell,

such as, the light absorbing material (active layer). This layer has the ability to convert light to charge carriers as described earlier in this chapter and therefore provide current to the external load. Four different processes are expected to take place to ensure high current density and hence high PCE; these are [28]:

1- Absorption of photons from incident light by employing an appropriate absorbing material, taking into consideration the light absorption properties of the material, the band gap and the energy level alignment of donor/acceptor molecules in the case of organic solar cells [29].
2- Generation of charge carriers (holes and electrons); in the case of OSCs excitons are generated due to light absorption and subsequently conversion of these excited state into free negative- and free positive-charge carrier pairs.
3- Charge transport mechanism drives the free charge carriers to the respective electrode by the aid of the internal electric field.
4- Finally, the free carriers will be collected by properly selected electrodes, which are mainly ruled by engineering the contact between the electrodes and the active layer.

If any one of these routes is hindered, poor PV performance is expected. Therefore, in order to obtain high current, a proper choice should be made regarding the absorbing material with an appropriate bandgap. Moreover, it is essential that the blend morphology should be controlled towards achieving a nanoscale interpenetrated networks, which therefore facilitates charge carriers separation and transportation where the exciton diffusion length for the organic system is typically as high as 10-20nm as in the case of P3HT:PCBM blends as an example [30, 31]. It is more common to use the short-circuit current density (J_{sc} in $mA.cm^{-2}$) instead of the short-circuit current to express the magnitude of the solar cell current due to the significant effects of the cell active area on the photogenerated current. Furthermore, the current density highly depends on the power of the incident light source standardised to the AM1.5 spectral irradiance.

2.5.3 Series and shunt resistance

The series resistance (R_s) and shunt resistance (R_{sh}) are effective parameters which influence the solar cell behaviour. Fig. 2.4(a) depicts the widely used equivalent circuit solar cell model. It deconstructs the solar cell J-V behaviour into four constituent parts: a photocurrent source, diode, series resistance (R_s) and shunt resistance (R_{sh}). The photocurrent source (I_{ph}) is simply the result of converting absorbed photons to free charge by the solar cell, the diode represents electron-hole recombination at the p-n junction, R_s accounts for the internal resistance of the cell to current flow, and R_{sh} models leakage current through the cells (e.g., via pinholes). Mathematically this model is represented by the following relation [32]:

$$I = I_L - I_s\left[e^{q(v-IR_s)/nkT} - 1\right] - \frac{V-IR_s}{R_{sh}} \tag{2.32}$$

Shen and co-authors have argued that a dark I-V characteristic is an efficient method to determine the R_s using equ. 2.35 [33]. On the other hand, R_{sh} represents cell leakages, under dark conditions when the photocurrent is zero. When $R_{sh}\rightarrow\infty$ the shunt current approaches zero which is desirable, since it is a parasitic current. In optimized solar cells, including OSCs, the shunt current is often negligible [32], therefore it could be presumed that R_{sh} is large enough to ignor the last term in eq. 2.32. Therfore, the dark I-V characterisitics can be presented in equ.2.25. Therefore, at higher applied voltage when $I>>I_o$, equ 2.25 becomes:

$$I\frac{dV}{dI} = IR_s + \frac{nkT}{q} \tag{2.33}$$

Using the latter equation, R_s could be extracted from the slope at the high current region of $I(dV/dI)$ vs. I plot as shown in Fig.2.6(A). Moreover, the determination of R_{sh} and R_s from the illuminated J-V curves by using the slope as shown in Fig.2.6(B)

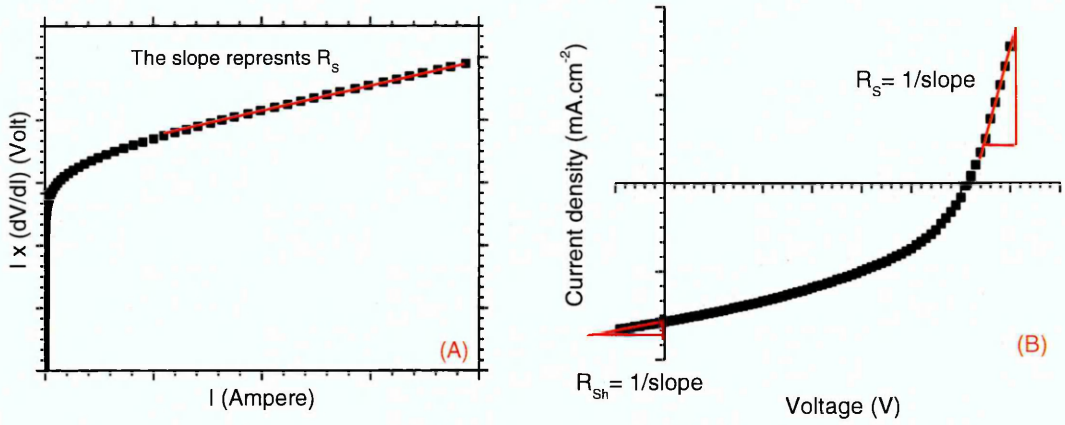

Fig.2.5: (A) The dark J-V relation as represented in equation 2.37 to calculate Rs, and (B) Determination of Rs and Rsh from the J-V curves.

2.5.4 Fill Factor

It has been shown earlier that the solar cell fill factor (FF) is a key parameter, which determines the maximum power (P_{max}) extracted from a solar cell in conjunction with V_{oc} and J_{sc}. Graphically, FF is represented as the largest rectangular area fitted in the J-V curve as shown in Fig.2.4(b). FF indicates in general how the photo-generated carriers are extracted out of solar cell device with an ideal value of 100% (see Fig.2.5 (a)). It is well known that the FF represents the efficiency of charge carrier collection before they recombine inside the cell, which basically depends on the charge carrier's mobility, built-in potential and the carrier recombination rate [34]. The maximum FF values reported for inorganic solar cells is about 90% while in OSCs the FF value is typically in the range of 50–70% [35-38]. Among several other factors, the fill factor is mainly determined by the series resistance (R_s) and shunt resistance (R_{sh}) of the solar cell. The series resistance of the solar cell mainly results from charge carriers' movement through the device and the resistance occurring at the contact between the electrodes and the active layer, as well as the resistance of the two electrodes themselves. R_s has a significant effect on the FF, while extremely high values of R_s leads to a reduction in J_{sc}. A high FF requires large shunt resistance (R_{sh}) to prevent leakage current, as well as lower R_s (see Fig.2.5(b)) [39]. For high R_{sh} and R_s, the FF is reduced as shown in Fig.2.5(c). While, in the case of low R_s and R_{sh}, the FF is represented in Fig.2.5(d).

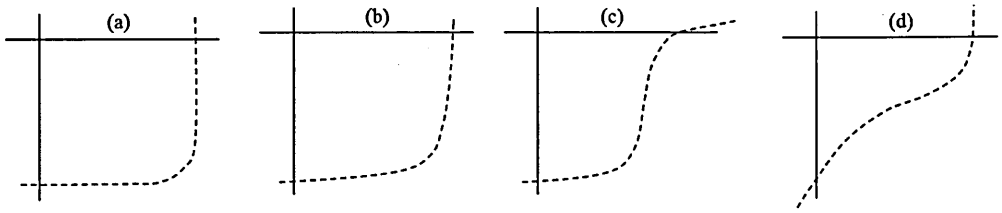

Fig.2.6: J-V characteristics of a solar cell with different FF; (a) ideal FF, (b) FF with high R_{sh} and low R_s, (c) FF with high R_s and high R_{sh}, and (d) FF with low R_{sh} and R_s

In OSCS, the improvement in FF and the device performance could only occur once the photo-generated carriers are extracted without recombination loss. Hence FF of the solar cell is limited by the carrier diffusion length (L_d) for both electrons and holes; the latter is described by the following equation [40]:

$$L_d = \mu\tau E \tag{2.31}$$

where μ is the charge carrier mobility, τ is the carrier recombination lifetime and E is the electrical field. Due to poor carrier mobility in organic materials and high recombination rate, which hinder the efficient collection of photogenerated carriers in OSCs, it is essential to develop a method to solve this issue. Ray and Alam [34] have shown that FF of the OSCs made produced using low-mobility materials can be enhanced up to 80% by introducing a "fixed charge layer" at the donor/acceptor interfaces to minimise the interfacial recombination. This could be achieved by increasing the charge carrier mobility of the organic semiconducting layer. Chu et.al. [41] have verified that controlling the polymer nanoscale structure and increasing the crystallinity of the organic phase-separation of P3HT:PCBM by thermal treatment have resulted in efficient OSCs with PCE of ≈3.8%. The improvement in J_{sc} and FF after solvent annealing with thermal treatment compared to a reference device without treatment is ascribed to increased absorption in the red region of the spectrum and improved charge transfer properties.

References

[1] Sze, S., & Ng, K. (2007). Physics of semiconductor devices (3rd ed.). Hoboken, N.J.: Wiley-Interscience.

[2] R.K. Rajput, "Chapter 4," in A course in electrical engineering materials, India, University science press, 2009, pp. 223-225.

[3] Streetman, B., & Banerjee, S. (2010). Solid-state electronic devices (6th ed., Prentice Hall series in solid state physical electronics). Upper Saddle River, N.J.: Pearson Prentice Hall.

[4] Singh, J. (2001). Semiconductor devices: Basic principles. New York: Wiley.

[5] Dharmadasa, I. (2012). Advances in Thin-Film Solar Cells. Pan Stanford.

[6] Güllü, Ö., Aydoğan, Ş., & Türüt, A. (2012). High barrier Schottky diode with organic interlayer. Solid State Communications, 152(5), 381-385.

[7] Liu, C., Xu, Y., & Noh, Y. Y. (2015). Contact engineering in organic field-effect transistors. Materials Today, 18(2), 79-96.

[8] Shah, M., Sayyad, M. H., Karimov, K. S., & Wahab, F. (2010). Electrical characterization of the ITO/NiPc/PEDOT: PSS junction diode. Journal of Physics D: Applied Physics, 43(40), 405104.

[9] Mohammed, M., Li, Z., Cui, J., & Chen, T. P. (2012). Junction investigation of graphene/silicon Schottky diodes. Nanoscale research letters, 7(1), 1-6.

[10] Cheung, S. K., & Cheung, N. W. (1986). Extraction of Schottky diode parameters from forward current-voltage characteristics. Applied Physics Letters, 49(2), 85-87.

[11] Yakuphanoglu, F., & Anand, R. S. (2010). Charge transport properties of an organic solar cell. Synthetic Metals, 160(21), 2250-2254.

[12] Şimşir, N., Şafak, H., Yüksel, Ö. F., & Kuş, M. (2012). Investigation of current–voltage and capacitance–voltage characteristics of Ag/perylene-monoimide/n-GaAs Schottky diode. Current Applied Physics, 12(6), 1510-1514.

[13] Gunduz, B., Yahia, I. S., & Yakuphanoglu, F. (2012). Electrical and photoconductivity properties of p-Si/P3HT/Al and p-Si/P3HT: MEH-PPV/Al organic devices: Comparison study. Microelectronic Engineering, 98, 41-57.

[14] Ruan, C. H., & Lin, Y. J. (2013). High Schottky barrier height of Au contact on Si-nanowire arrays with sulfide treatment. Journal of Applied Physics, 114(14), 143710.

[15] Khurelbaatar, Z., Shim, K. H., Cho, J., Hong, H., Reddy, V. R., & Choi, C. J. (2015). Temperature Dependent Current-Voltage and Capacitance-Voltage Characteristics of an Au/n-Type Si Schottky Barrier Diode Modified Using a PEDOT: PSS Interlayer. Materials Transactions, 56(1), 10-16.

[16] N. F. Mott & R.W. Gurney, Electronic Processes in Ionic Crystals (Oxford University Press, London, 1940).

[17] Smith, R. W., & Rose, A. (1955). Space-charge-limited currents in single crystals of cadmium sulfide. Physical Review, 97(6), 1531.

[18] Rose, A. (1955). Space-charge-limited currents in solids. Physical Review, 97(6), 1538-1544.

[19] Lampert, M. A. (1956). Simplified theory of space-charge-limited currents in an insulator with traps. Physical Review, 103(6), 1648-1656.

[20] El-Nahass, M. M., & El-Rahman, K. A. (2007). Investigation of electrical conductivity in Schottky-barrier devices based on nickel phthalocyanine thin films. Journal of Alloys and Compounds, 430(1), 194-199.

[21] Osiris, W. G., Farag, A. A. M., & Yahia, I. S. (2011). Extraction of the device parameters of Al/P 3 OT/ITO organic Schottky diode using J–V and C–V characteristics. Synthetic Metals, 161(11), 1079-1087.

[22] Apaydın, D. H., Yıldız, D. E., Cirpan, A., & Toppare, L. (2013). Optimizing the organic solar cell efficiency: role of the active layer thickness. Solar Energy Materials and Solar Cells, 113, 100-105.

[23] Shen, Y., Li, K., Majumdar, N., et.al. (2011). Bulk and contact resistance in P3HT: PCBM heterojunction solar cells. Solar Energy Materials and Solar Cells, 95(8), 2314-2317.

[24] Elumalai, N. K., & Uddin, A. (2016). Open circuit voltage of organic solar cells: an in-depth review. Energy & Environmental Science, 9(2), 391-410.

[25] Li, H., Zhang, Z. G., Li, Y., & Wang, J. (2012). Tunable open-circuit voltage in ternary organic solar cells. Applied Physics Letters, 101(16), 163302.

[26] Yue, G., Wu, J., Xiao, Y., et.al. (2011). Flexible dye-sensitized solar cell based on PCBM/P3HT heterojunction. Chinese Science Bulletin, 56(3), 325-330.

[27] Qi, B., & Wang, J. (2012). Open-circuit voltage in organic solar cells. Journal of Materials Chemistry, 22(46), 24315-24325.

[28] S. J. Fonash, (2010). Solar Cell Device Physics, 2nd Ed. Academic Press is an imprint of Elsevier.

[29] Sun, Y., Liu, J., Ding, Y., & Han, Y. (2013). Decreasing the aggregation of PCBM in P3HT/PCBM blend films by cooling the solution. Colloids and Surfaces A: Physicochemical and Engineering Aspects, 421, 135-141.

[30] Kim, Y.S., Lee, Y., Kim, J.K., et.al. (2010). Effect of solvents on the performance and morphology of polymer photovoltaic devices. Current Applied Physics, 10(4), 985-989.

[31] Liu, J., Shao, S., Wang, H., et.al. (2010). The mechanisms for introduction of n-dodecylthiol to modify the P3HT/PCBM morphology. Organic Electronics, 11(5), 775-783.

[32] Servaites, J. D., Ratner, M. A., & Marks, T. J. (2011). Organic solar cells: a new look at traditional models. Energy & Environmental Science, 4(11), 4410-4422.

[33] Shen, Y., Li, K., Majumdar, N., Campbell, J. C., & Gupta, M. C. (2011). Bulk and contact resistance in P3HT: PCBM heterojunction solar cells. Solar Energy Materials and Solar Cells, 95(8), 2314-2317.

[34] Ray, B., & Alam, M. A. (2012, June). Achieving fill factor above 80% in organic solar cells by charged interface. In Photovoltaic Specialists Conference (PVSC), Volume 2, 2012 IEEE 38th (pp. 1-8). IEEE.

[35] Qi, B., & Wang, J. (2013). Fill factor in organic solar cells. Physical Chemistry Chemical Physics, 15(23), 8972-8982.

[36] Peng, Y., Zhang, L., & Andrew, T. L. (2014). High open-circuit voltage, high fill factor single-junction organic solar cells. Applied Physics Letters, 105(8), 083304.

[37] Meng, D., Sun, D., Zhong, C., et.al. (2015). High-performance solution-processed non-fullerene organic solar cells based on selenophene-containing perylene bisimide acceptor. Journal of the American Chemical Society, 138(1), 375-380.

[38] Liang, Y., Xu, Z., Xia, J., et.al. (2010). For the bright future—bulk heterojunction polymer solar cells with power conversion efficiency of 7.4%. Advanced Materials, 22(20).

[39] Hoppea, H., & Sariciftci, N. S. (2004). Organic solar cells: An overview. J. Mater. Res, 19(7), 1925.

[40] Ma, W., Yang, C., Gong, X., et.al. (2005). Thermally stable, efficient polymer solar cells with nanoscale control of the interpenetrating network morphology. Advanced Functional Materials, 15(10), 1617-1622.

[41] Chu, C. W., Yang, H., Hou, W. J., et.al. (2008). Control of the nanoscale crystallinity and phase separation in polymer solar cells. Applied Physics Letters, 92(10), 103306.

Chapter 3: Organic solar cells

3.1. Organic solar cell configurations

Organic solar cell (OSC) consists of different configurations, such as single-junction and tandem structures. The single-junction solar cells are either of inverted type structure as shown in Fig.3.1(a) or a conventional structure (Fig.3.1(b)); both structures are similar in principle while the tandem structure has different mechanism.

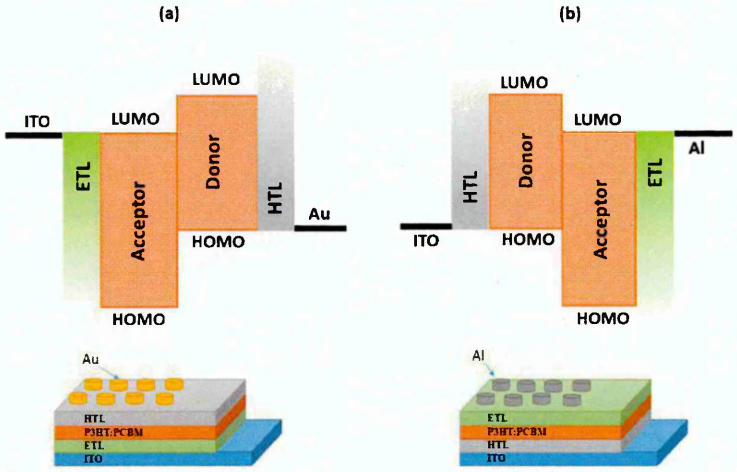

Fig.3.1: The main structures of OSCs; (a) inverted structure and (b) conventional structure

Generally speaking, organic materials have a small dielectric constant and the absorption characteristics are governed by Frenkel-excitons with binding energy around 0.3 eV and a lifetime of the order of ns [1]. A critical step in the operation of a photovoltaic device is the charge separation of the excited electron-hole pairs (excitons) created upon photon absorption. This charge separation occurs at the donor/acceptor interface [2]. A schematic description of the electronic structure of a donor/acceptor blend is illustrated in Fig.3.2. The offset of the electronic levels, the highest occupied molecular level (HOMO) and the lowest unoccupied molecular level (LUMO) of the donor and acceptor, is the main requirement to induce exciton dissociation.

The voltage provided by the solar cells is known as the open circuit voltage (V_{oc}) which is limited by the difference between the LUMO of the acceptor and the HOMO of the donor materials [3] as shown in Fig.3.3. Due to the properties of the organic semiconductors, OSCs are facing several limitations. Although Shockley and Queisser limitation has considered the spectral losses, and thus gives the solar cell a peak theoretical efficiency of 48% with band gap materials of 1.1eV, materials with lower band gaps are thought to exhibit a decrease in V_{oc} while materials with higher band gaps than 1.1 eV are limited by a decreased J_{sc}. The theoretical maximum efficiency decreases to 30% by taking into account the effects of blackbody radiation and radiative/non-radiative recombination of charge carriers [4]. Therefore, for mono-junction organic solar cells with a donor band gap of 1.5 eV, an efficiency of approximately 11% could be achieved according to the assumption made by Ameri and co-authors [5] considering a loss of 0.6 eV in V_{oc} (accounting for the minimum required LUMO level offset and contact losses), taking into account absorption/internal quantum efficiency (IQE) limitations (assuming EQE of 65%) and charge carrier transport losses (assuming FF of 65%).

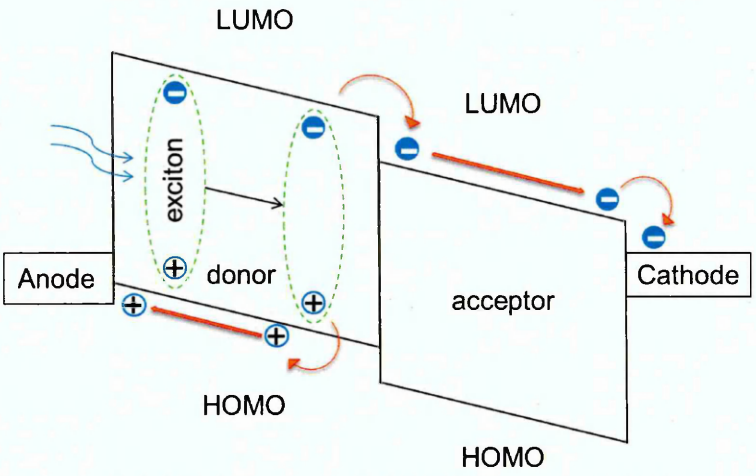

Fig.3.2: A schematic description of the electronic structure of a donor/acceptor blend; exciton generation, separation and collection in organic solar cells

To make high-performance OSCs ready for the market, significant research and development are required. In this respect, various strategies are under investigation at different levels of development. Among these strategies, the well-known model of tandem solar cells is one of the most encouraging approaches to tackle the main losses in single junction OSCs and improve the device performance [5]. Tandem solar cell tackle simultaneously absorption and thermal losses by absorbing the higher energy photons in a wide band gap based cell (higher voltage and lower photocurrent) and the lower energy photons in a smaller band gap based cell (lower voltage and higher photocurrent) [5]. Furthermore, different structures are also considered to improve the OSCs performance; these are bilayer and bulk heterojunction structures.

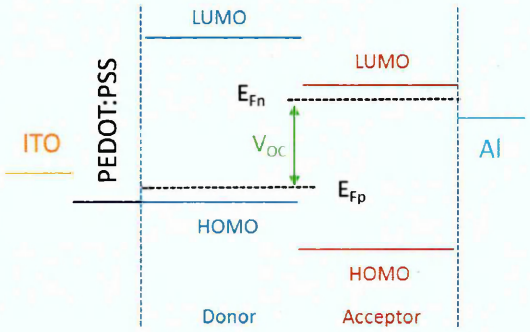

Fig.3.3: Determination of V_{oc} by the donor/acceptor energy level alignment

3.1.1. Bilayer heterojunction

In a bilayer heterojunction, the charge separation occurs at the planar donor/acceptor interface as shown in Fig.3.4(a) [6,7]. The bilayer structure is sandwiched between two electrodes which match the donor HOMO and the acceptor LUMO for effective extraction of the corresponding charge carries. It is well-known that the formation of the classical PN junction requires doped semiconductors with free charge carriers to form the electric field in the depletion region. In the bilayer structure, the charge transfer between the un-doped donor and acceptor materials is correlated to the differences in the ionisation energy and electron affinity of the materials. Upon photon absorption in the donor site, excitons are generated and once they reached the donor/acceptor interface the electron is excited from the HOMO to the LUMO (S^0-S^1) levels [8].

Afterwards, the electron is transferred to the LUMO of the acceptor. This charge photo-induced transfer only happens under light illumination. The main advantage of the bilayer structure is the monomolecular charge transport; after the excitons are dissociated at the interface, the holes travel through the donor material and the electrons through the acceptor material. Therefore, holes and electrons are efficiently separated from each other which in turn reduce the charge carrier's recombination where the latter occurs due to the presence of traps. Moreover, the photocurrent is linearly depending on the light intensity and high fill factor can be achieved [6,7,9].

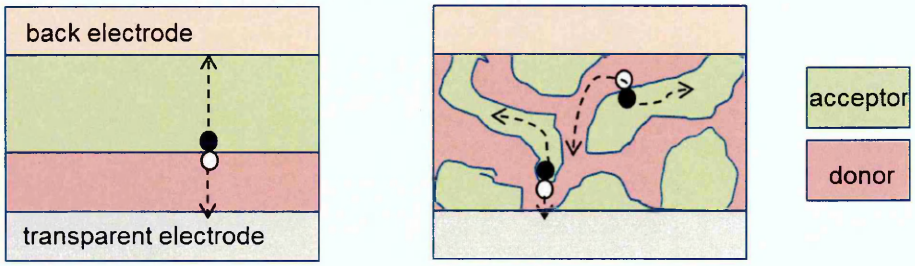

Fig.3.4: Organic solar cell structures; (a) bilayer structure and (b) bulk heterojunction structure

3.1.2. Bulk heterojunction structure

The main principle of bulk heterojunction (BHJ) is through the intimate mixing of the donor and acceptor materials together so that each donor/acceptor interface is within a distance less than the diffusion length of the generated exciton [8]. Fig.3.4(b) shows the bulk heterojunction OSC structure. The BHJ device is similar to the bilayer device with respect to the Donor/acceptor concept, but it shows a largely increased interfacial area where charge separation occurs. Ideally, all excitons are dissociated due to the interface distribution throughout the BHJ within their lifetime; therefore, no loss due to too small exciton diffusion lengths is expected. This results in reducing the recombination due to the percolation pathways for the hole and electron transporting phases to the contacts [10]. In other words, the donor and acceptor phases have to form a continuous and interpenetrating network. Consequently, BHJ devices are considerably sensitive to the nanoscale morphology within the blend.

3.2. Operation principles of OSCs

Once absorption of a photon occurs, an electron in the organic semiconductor is excited from the HOMO to the LUMO energy level (see Fig.3.1). This is similar to exciting an electron in the inorganic semiconductor from the valence to the conduction band. Nevertheless, due to the low dielectric constant and localised electron and hole wave-functions in the organic semiconductors [11], strong coulomb attraction exists between the electron and hole pairs and the resulting pairs are called excitons as shown in Fig.3.1 [12]. Generally, absorption coefficient in organic materials is high ($\sim 10^5 cm^{-1}$) [13]. The active layer thickness plays an important role in the solar cell performance; thicker active layer results in higher absorption intensity; however, thickness affects the bulk resistance, whereby resistance increases in thicker films and therefore limiting the charge carrier transport [14,15]. To achieve improved light absorption using thin films with an optimal film thickness of several hundred nanometers, it is necessary to reduce the transport time for the charge carriers to reach the electrodes [16].

The main concern with the organic materials is the large band gap and the small absorption spectral range, which results in low absorption efficiency in the long wavelength region. It has been reported that ~77% of the solar light is absorbed by materials with a band gap of 1.1Ev [17], whereas the benchmark material of OSCs, P3HT, has a band gap of 1.9eV and most of the other organic materials have ~2 eV [8]. P3HT has the possibility to harvest up to 22.4% of the available photons giving a maximum theoretical current density of $14.3 mAcm^{-2}$ (Note that this may increase if the polymer is applied in a bulk heterojunction device, due to the absorption of the acceptor, i.e. PCBM) [18]. In reality, most OSCs are not efficiently capable of harvesting the light energy below 350-400 nm due to absorption in the substrate and front electrodes (i.e. glass, ITO) but fortunately, this part of the spectrum contains very little intensity [18]. In organic materials, excitons are normally localised as Frenkel or charge transfer (CT) excitons, whereas they are delocalized as Wannier excitons in crystalline silicon [19]. Fig.3.5 shows the different excitons in organic and inorganic semiconductors. The Frenkel exciton in the donor may relax to the CT exciton at the donor/acceptor interface while the electron moves to the acceptor LUMO level (see Fig.3.6).

In this case, phonons are released due to molecular vibrational energy. Further release of phonons causes the CT exciton to dissociate into free charge carriers. Excitons could reach the interface within its lifetime and diffusion length, which are limited by the active layer thickness [20].

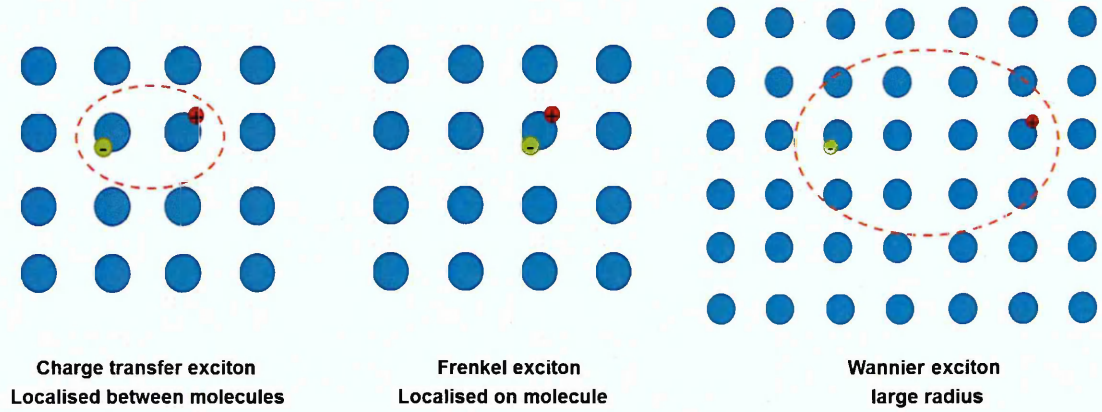

Fig.3.5: The different types of excitons; Frenkel, charge transfer and Wannier excitons

Therefore, organic materials having a long exciton diffusion length and high carrier mobility are desirable for improving PCE. Furthermore the PCE and diffusion length are strongly dependent on the molecular stacking in the active layer [6]. Finally, to complete the OSC operation, the charge carriers will be extracted via two selective contacts [21]; Transparent Indium Tin Oxide (ITO) electrode is usually used in OSC fabrication, as it is suitable to match the HOMO of the conjugated polymer as the hole collecting electrode. Furthermore, ITO is commonly modified by the hole transport layer Poly(3,4-ethylenedioxythiophene)-poly(styrene sulfonate) known as PEDOT:PSS. On the other side of the device, evaporated aluminium (Al) electrode acts as the electron collecting contact, which typically matches the LUMO of the acceptor or the electron transport layer [21]. Using the chemical potentials of electrons and holes (quasi Fermi levels of the doped phases), a gradient is formed in a donor-acceptor junction. This gradient is determined by the difference between the HOMO level of the donor (quasi Fermi level of the holes) and the LUMO level of the acceptor (quasi Fermi level of the electrons), which in turn determines the open circuit voltage (V_{oc}) as depicted in Fig.3.3 [22].

OSCs have received significant attention during the last few decades due to their low cost processing which is compatible with flexible substrates, high throughput and thus requires less capital investment [23]. As has been mentioned in chapter one, OSCs are diverse and versatile, and can offer wide range of properties including tailored band gap and thus varied range of light harvesting efficiency covering a broad range of the solar spectrum. In many organic solar cell devices, polymers have been used as essential parts of their structure (main matrix). For instance, conjugated polymers are often participated as electron donors in the active layer of OSCs and it assists as hole conductors within the donor/acceptor blend [24]. Furthermore, conjugated polymers such as poly (3-hexylthiophene) (P3HT) and fullerenes such as (6,6)-phenyl-C61 butyric acid methyl ester ($PC_{61}BM$) are usually mixed together to form a bulk heterojunctions (BHJ) structure.

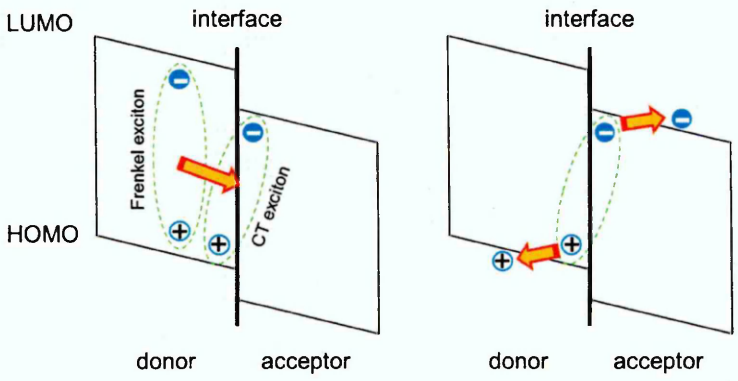

Fig.3.6: Dissociation of excitons into free electrons and holes

The concept of BHJ has been introduced to address the limited exciton diffusion length in OSCs, which had been a problem for previous organic solar cells [25,26]. In a BHJ structure, an interpenetrating network between the donor and acceptor domains with large interfacial areas for efficient exciton dissociation is desired. Heeger and co-workers [26] have introduced the first BHJ structure for polymer:fullerene blends, which has been employed to overcome the early carriers recombination in OSCs. Moreover, BHJ system is used to enhance the charge transfer across a donor-acceptor interface. The power conversion efficiency in bilayer heterojunction devices is limited by charge separation, which takes place at the donor/acceptor (D/A) interface only [26]. Consequently, the photo-

generated excitons produced far from the D/A interface in a bilayer device recombine before reaching the interface. Although charges are separated efficiently at the D/A interface, the conversion efficiency is restricted by the carrier's collection efficiency [26]. Therefore, BHJ with an interpenetrating network of D/A blend is essential for organic photovoltaic applications [27]. To achieve a large interfacial area within a BHJ system, controlling the blend morphology is desirable [10]. Several reviews have been dedicated to the progress made in the field of organic solar cells performance [28-34]. The mechanism of BHJ is mainly described in four step [34] as shown in Fig.3.7(a):

I. Light absorption and generation of Frenkel excitons (highly localized, tightly bound electron-hole pairs)
II. Excitons diffusion to the D/A interfaces
III. Excitons dissociation at the interface leading to creating CT states followed by dissociation into free charge carriers
IV. Charge transport and collection.
V. Charge recombination

There are two key mechanisms of carriers' recombination in OSCs as illustrated in Fig.3.7: geminate pair (see Fig.3.7(b)) and bimolecular recombination (see Fig.3.7(b)) [35]. An electron-hole pair initially undergoes dissociation at the interface of donor (with positive charge) and acceptor (with negative charge) materials regions, but the pair typically remains bound at the interface due to the electron-hole Columbic attraction, i.e. the geminate pair binding energy. In order to proceed to the electrodes, the two charge carriers must therefore overcome this barrier. There are three competing processes at this moment: complete dissociation of the geminate pair (i.e., overcoming the Columbic barrier), relaxation of the initial Franck–Condon vibrational energy in the geminate pair, and recombination at the D/A interface. Later on, after the geminate pair has completely dissociated into free charge carriers, the bimolecular recombination might occur (see Fig.3.7(b)) either by directly (electrons and holes colliding) or via recombination centres (impurities and defects). In OSCs, the photocurrent yield is typically reduced due to geminate pair recombination [35].

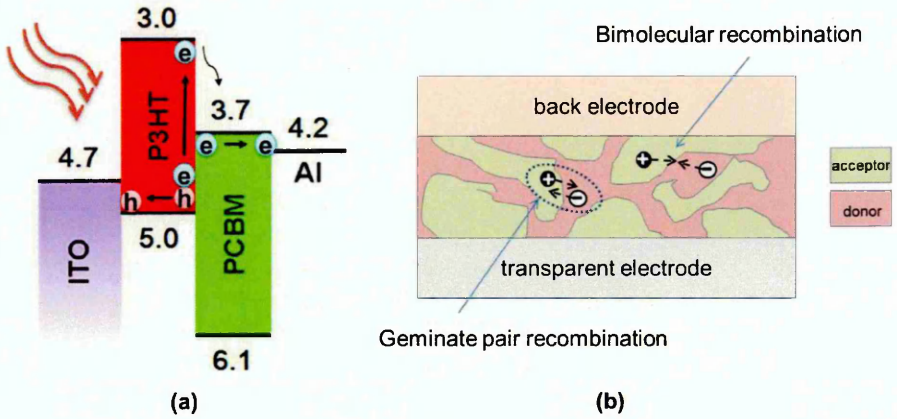

Fig.3.7: (a) Events of generation exciton and dissociated to electron hole pair (b) Geminate pair dissociation and bimolecular recombination loss mechanisms in OPVs

3.3. Materials used in organic solar cells

3.3.1. Early development of donor materials

Generally, the conjugated polymer represents the main matrix of the BHJ blend. Several phases of developing donor polymers have been carried out, among them, three early classes of polymers are worthy of discussion [34] (see Fig.3.8):

I. Poly(phenylenevinylene) (PPV) derivatives such as MEH-PPV

II. Poly[2-methoxy-5-(3,7-dimethyloctyloxy)]- 1,4-phenylenevinylene (MDMO-PPV)

III. Poly- (thiophene) derivatives, mainly poly(3-hexylthiophene) (P3HT)

In 1995, Heeger and co-authors [26] have announced the first BHJ OSCs based on a donor material Poly[2-methoxy-5-(2-ethylhexyloxy)-1,4-phenylenevinylene] (MEH-PV) mixed with an acceptor material ($PC_{61}BM$) with PCE of 1%. This approach has motivated other researchers to develop new PPV polymer derivatives such as Poly[2-methoxy-5-(3′,7′-dimethyloctyloxy)-1,4-phenylenevinylene] (MDMO-PPV) with better processability; PCE of 3% has been recorded for the first time based on this polymer blend [36]. This improvement in PCE was due to enhanced light harvesting, charge transfer and enhanced active layer morphology [36].

Furthermore, the interaction between the π-conjugated polymer and fullerene as well as polymer interchain interactions might result in the improvement of the blend's morphology and hence resulting in enhanced device performance [37]. Controlling the morphology modifies the energy levels of the polymer via modification of the side chain or introducing substituents on the polymer backbone [37]. Reynolds and co-workers [38] reported the introduction of cyano groups (−CN) to the vinylene moiety of PPV polymers cyano-substituted poly[2,5-bis(dodecyloxy)-p-phenylenevinylene] (CNPPV). The electron-withdrawing CN group has shifted down both the HOMO and LUMO levels by 0.5 eV without changing the band gap (2.1 eV). A LUMO level of -3.8 eV has been measured for the polymer CNPPV, which is very well matched to the LUMO level of the acceptor ($PC_{61}BM$) [38].

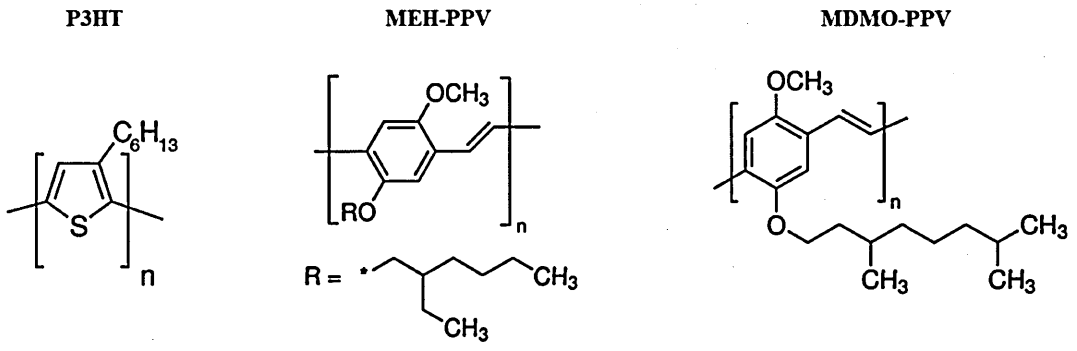

Fig.3.8: The three early class polymers, P3HT, MEH-PPV and MDMO-PPV.

Moreover, they also have revealed that replacement of the dialkoxybenzene unit to more electron-rich dialkoxy thiophene units raised the HOMO level of CNPPV with a slight variation in the LUMO level of CNPPV, resulting in a narrower band gap. Even though, PPV-based polymers have been the main materials used at the early stage of OSCs research, their large band gaps (>2 eV) and low photocurrent hindered any further developments. Research attention rapidly shifted to polythiophene polymers, particularly P3HT [39,40].

3.3.2. Poly (3-hexylthiophene) (P3HT)

It could be said that P3HT is one of the well-known π-conjugated polymers. It has attracted significant attention due to its outstanding properties including solution processability, excellent electronic properties, relatively high charge mobility (10^{-4}-10^{-1} cm^2 V^{-1} s^{-1}), excellent environmental stability and a strong trend towards creating a self-organized thin film that facilitates charge transport [41-44]. P3HT has a band gap of about 1.9 eV, and can be further reduced by increasing the quinoidal character in the polymer [45,46]. Generally, P3HT-based OSCs exhibit high external quantum efficiency (EQE), which is defined as the number of the measured charge carriers generated per photon incident on the device. EQE can reach as high as 88% and PCE reach >5% after modifications, such as increasing the polymer's regioregularity and use of thermal or vapour annealing during device fabrication [34, 47-49].

The regioregularity of the P3HT chains plays an important role in the fabrication of OSCs. Three different regioregularities of P3HT have been discussed by Mauer and co-authors [50]. They have investigated the effects of regioregularity on the charge transport in regiorandom, medium regioregular and very high regioregular P3HT. Firstly, the absorption spectra of the pristine P3HT have shown typical features for the medium and very high regioregular P3HT which indicate that P3HT has exhibited lamella structure, whereas the regiorandom P3HT has shown very disordered and featureless absorption spectra. In P3HT:PCBM blend, the electrons and holes mobilities are found to be similar in the case of very high regioregular P3HT-based devices and the charge transport is, therefore, balanced. However, devices prepared using both medium and very high regioregular P3HT have exhibited similar PCE of 2.5%, suggesting that very high regioregularity might not substantially increase the structural order and charge carrier transport within P3HT:PCBM blends [50]. The degree of regioregularity is well-known to improve the optical [51] and charge transport properties [52] of pristine P3HT films. The degree of regioregularity is defined as the percentage of monomers adopting a head-to-tail (H-T) arrangement instead of head-to-head (H-H) [49]. The regioregularity of the P3HT chains has a tendency to stack into planar arrangements known as 'lamella structure', which are usually oriented perpendicular to the substrate (see Fig.3.9).

The P3HT regioregularity indicates the degree of the crystallinity with a perfect alternation of alkyl and non-alkyl sites on the thiophene rings. Basically, it might lead to the formation of head-to-tail (H-T), head-to-head (H-H), and tail-to-tail (T-T) isomers (see Fig.3.9) [53,54]. Fig.3.9 (a) shows the molecular structure of P3HT and Fig.3.9 (b, c, d, and e) show the ordering coupling structure of P3HT with H-T to H-T, H-H to T-H, H-H to H-H and T-T to H-T, respectively. Preferably, P3HT organised in head-tail to the head-tail orientation as shown in Fig.3.9 (f) offers a higher degree of crystallinity related to the lamella structure with two different orientations, edge-on and face-on, as shown in Fig.3.9 (g and h), respectively [55,56]. The edge-on orientation is the structure where the side chains are perpendicular to the substrate for high H-T regioregularity and low molecular weight whereas in the plane-on orientation the side chains are parallel to the substrate for low regioregularity and high molecular weight [55,56].

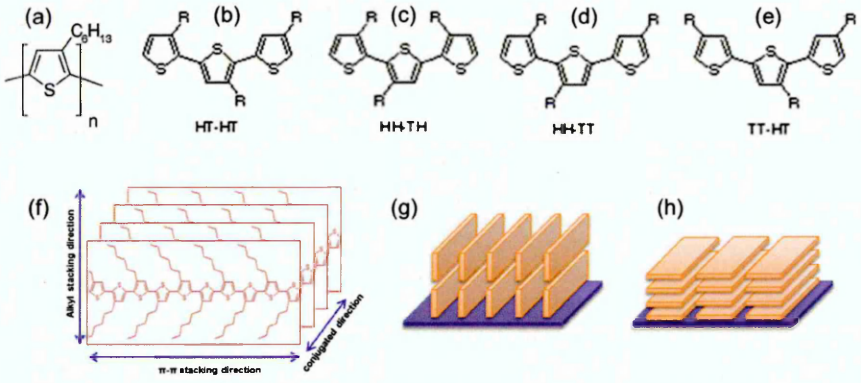

Fig.3.9: (a) poly(3-alkylthiophene) (P3HT), (b) HT-HT, (c) HH-TH, (d) HH-TT, (e) TT-HT, (f) a schematic of interdigitation of regioregular P3HT chains forming lamellar structures, (g) edge-on arrangement and (f) plane-on orientation of P3HT with respect to a surface

The ratio of thiophene units in the conjugated polymer with H-T orientation is known as the degree of H-T regioregularity. This ratio has a significant impact on the P3HT properties and therefore their behaviour in the molecular devices. For instance, highly regioregular H-T oriented P3HT has high crystallinity, high hole mobility and an extended absorption range up to 650 nm which shows that regioregular H-T P3HT has more extended conjugation than regiorandom P3HT.

Several observations have addressed the orientation of the P3HT-based thin film. As an example, Fell and co-authors have detected for the first time a molecules arrangement in P3HT film which have oriented with their side chains parallel to the substrate [57]. DeLongchamp and co-workers have studied the relation between the P3HT molecules orientation with respect to the substrate as a result of varying spin coating speed [58]. P3HT is subjected to different evaporation rates of the used solvent, which was shown to depend on the rotation speed of spin coating. The edge-on orientation is achieved by slower rotation and thus slower evaporation rate throughout the deposition. This type of orientation has resulted in a higher charge carriers' mobility due to the preferential molecular ordering via π-stacking of the polymer chains. The partial overlap between π-orbitals supports the charge transfer between P3HT chains [58].

3.3.3. Other polymers used in OSCs

Recently, new π-conjugated polymers with the capability of increasing V_{oc} have been used. However, increasing V_{oc} requires several approaches such as controlling the energy levels of these new materials as they may reduce J_{sc} due to the potential drop at the heterojunction interfaces [59]. Fig.3.10 shows a number of donor materials that have been used in OSCs. One of the new polymers that have been designed for OSCs is (Poly[N-9′-heptadecanyl-2,7-carbazole-alt-5,5-(4′,7′-di-2-thienyl-2′,1′,3′-benzothiadiazole)],Poly[[9-(1-octylnonyl)-9H-carbazole-2,7-diyl]-2,5-thiophenediyl-2,1,3-benzothiadiazole-4,7-diyl-2,5-thiophenediyl] which is known as PCDTBT. When this polymer is blended with a suitable electron acceptor such as PCBM, a PCE with values higher than P3HT-based devices has been recorded [60,61]. The higher PCE is attributed to a closer alignment of molecular orbital energy levels between the donor and acceptor, leading to higher V_{oc}. Moreover, PCDTBT has a low band gap of 1.8 eV compared to P3HT which also improves the light harvesting at longer wavelengths [62]. While the polymer P3HT is a semi-crystalline material, PCDTBT is a largely amorphous polymer and is characterised by weak intermolecular interaction resulting from π-π stacking between the conjugated backbones [63]. Several investigations have been carried out using PCDTBT as a donor material in OSCs [64-71] One of the most interesting results for PCDTBT-based OSCs has been reported by Heeger and co-authors [60]; they have reported a highly efficient OSCs

employing PCDTBT:$PC_{70}BM$ blend and using a simple processing method to produce the active layer with a thickness of 80 nm. Even without the use of thermal annealing or any additives to the active layer their OSC has recorded a PCE of 6.1%, with J_{sc} of 10.6 $mA.cm^{-2}$, V_{oc} of 0.88V and FF of 66% under AM1.5 G irradiation of 100 $mW.cm^{-2}$ [60]. They have reported internal quantum efficiency (IQE) of about 100% suggesting that all the photons have been absorbed, separated to charge carriers and collected at their respective electrodes. A recent report from nature scientific reports reveals that PCDTBT-based OSCs have shown a one year lifetime of operation under "real-world conditions" [70].

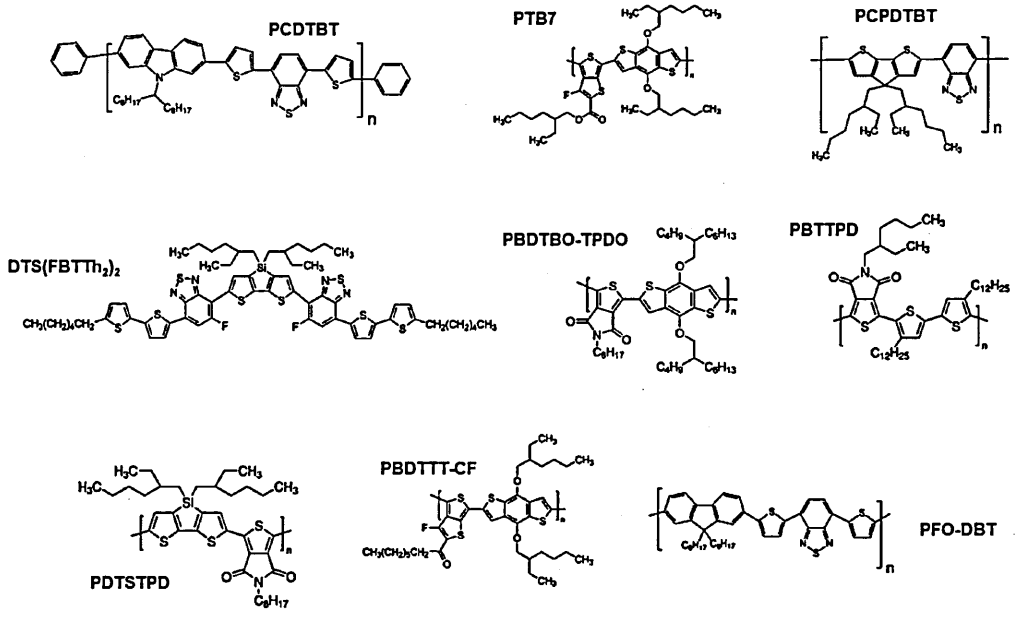

Fig.3.10: A number of polymers used in OSCs with different HOMO and LUMO level positions

A stable device has been fabricated using PCDTBT:$PC_{71}BM$ blend as an active layer from three different solvents and the final device was encapsulated with an epoxy glue and glass slides. The findings have revealed that the edge of the device has degraded faster than the centre part of the device which has been attributed to the access of water and oxygen through the encapsulation epoxy, leading to photo-oxidation of the active layer [70]. PCDTBT:$PC_{71}BM$ based OSCs have shown better solubility using chloroform:chlorobenzene co-solvents with a ratio of 1:1 [72], which in turn have resulted

in PCE as high as 6.82%. The improvement in the FF and J_{sc} were correlated to the formation of nanoscale phase separation and well-connected percolation pathways for both phase-separated materials (donor and acceptor) [73]. The latter observation is in agreement with the observed increase in charge carriers' mobility due to the favourable domain size which also leads to an increase in short circuit current [72]. It has also been suggested that increased surface roughness provides further advantage in enhancing light multiple reflection when passing through the active layer leading to improved light absorption and thus increased J_{sc} [72]. The effects of different solvents (chloroform, chlorobenzene and dichlorobenzene) as well as different blend ratios of the PCDTBT:$PC_{71}BM$ blend prepared by spin coating and their effects on the morphology and subsequently on OSCs performance have been investigated [74].

Different surface morphologies based on the blend ratio and the used solvents have been observed. Best device performance was associated with active layers prepared using dichlorobenzene solvent and an optimum blend ratio of 1:4 with V_{oc} of 0.9V, J_{sc} of 8.41mA.cm^{-2}, FF of 55%, and PCE of 4.15%. The variation in J_{sc} due to the used solvents was obvious with the lowest value recorded for the chloroform-based device and the highest for the dichlorobenzene-based device. This variation is due to the improved nanoscale morphology and good interpenetrating network in the dichlorobenzene-based device [75]. Moreover, using spray coating method to prepare PCDTBT:$PC_{71}BM$ active layer has been carried out [75]. A direct relationship between the active layer's morphology and device performance has been established after optimising different parameters such as the nozzle to substrate distance, choice of used solvent and different weight ratios which directly influence the active layer thickness [75]. Smoother surface has been obtained for PCDTBT bare film, increasing PCBM ratio in the blend has resulted in uniformly dispersed aggregates within PCDTBT matrix. The results have revealed that chloroform and dichlorobenzene provide the optimum co-solvents to achieve PCE of 5.8% [75]. In 2013, Chang and co-workers [76] have reported that the introduction of P3HT within PCPDTBT:$PC_{61}BM$ system has altered the optoelectronic properties of the layer, as was evaluated by measuring the absorption spectra and charge carrier mobility.

The addition of 1 wt% of P3HT in PCPDTBT:$PC_{61}BM$ blend was shown to induce a significant increase in the photoabsorption intensity in the wavelength range from 450 to 650 nm, which was attributed to light absorption by the main chain of P3HT and intermolecular π-π stacking therein. Hence, an increase in the photocurrent is expected [77]. The change in the blend morphology has indicated favourable phase separation with proper domain size after adding 1%wt of P3HT to PCPDTBT:$PC_{61}BM$ blend. This in turn facilitates charge transport [78], and consequently increases PCE from 2.9% to 3.4%, while FF has increased from 51.6% to 54.3%, with a slight increase in J_{sc} from 9.5mA.cm^{-2} to 10.2mA.cm^{-2} while V_{oc} remained unchanged at 0.61V.

Poly[2,6-(4,4-bis(2-ethylhexyl)-4H-cyclopenta[2,1-b;3,4-b']dithiophene)-alt-4,7-(2,1,3-benzothiadiazole)] which is well-known as PCPDTBT, is a low band gap polymer used as an alternative to P3HT in OSCs [79-83] It has an optical band gap E_g of 1.4eV, thus it is more suitable candidate as light-harvesting materials compared to the state of art P3HT in OSCs [84]. In addition, electrochemical studies specify that PCPDTBT has appropriate deep HOMO/LUMO levels that result in a high V_{oc} in OSCs, when fullerene derivatives are used as electron acceptor [84]. In 2006, Mühlbacher and co-workers [85] have reported PCPDTBT polymer as a novel low donor material with improved charge-transport properties as well as appropriate electronic energy levels and good processability. The performance of the PCPDTBT-based device has revealed an EQE limited to 38% which is due to the morphology induced loss mechanisms. Overcoming these deficiencies could results in PCE over 7% for PCPDTBT-based device [85]. Another approach of enhancing OSCs is the incorporation of low band gap polymer (PCPDTBT) into the P3HT:PCBM blend with different ratios of 0%, 5%, 10% and 20% [77]. The light harvesting of a P3HT:PCBM blend is extended into the near IR region by adding PCPDTBT to the blend, which results in higher photocurrent densities after adding low band gap material to P3HT:PCBM blend. Enhancing the photosensitivity of the ternary blend is due to the efficient photoinduced charge transfer, where the transfer of a positive charge from PCPDTBT to P3HT is dominant; PCPDTBT acts as the sensitizer and P3HT as the charge transporting matrix [77].

An optical modelling by Albrecht and co-authors has proposed that using PCPDTBT:$PC_{71}BM$ BHJ in an inverted device architecture is advantageous, because of the favourable optical field distribution, when compared to conventional device architecture [80]. It has been shown that the incorporation of a few volume percent of alkane dithiols as a processing additives into the PCPDTBT:$PC_{71}BM$ active layer solution can increase the efficiency of conventional OPV devices from 2.8% to 5.5% [86]. This improvement has been attributed to the improved morphology due to the additives, however, no increase in the hole mobility has resulted from these additives. In addition, no crystalline phase has been observed for the PCPDTBT: $PC_{71}BM$ films either with or without dithiol processing [86]. Lee and co-authors [87] have also shown that such enhancement in the device performance is due to controlling the active layer morphology by controlling the solubility of the fullerene component within the BHJ layer using high boiling point processing additives. The latter is thought to rearrange the D/A networks, which influences the charge separation, recombination and charge transport [88].

Another low band gap polymer which has been recently used in OSCs applications is Poly({4,8-bis[(2-ethylhexyl)oxy]benzo[1,2-b:4,5-b']dithiophene-2,6-diyl}{3-fluoro-2-[(2-ethylhexyl) carbonyl] thieno [3,4-b]thiophenediyl}) (PTB7) [89-93] Foster and co-authors [94] have reported a certified efficiency of about 10% based on a single-junction device with PTB7:$PC_{71}BM$ as an active layer. This has been achieved by employing the low band gap polymer PTB7 with a deep HOMO level correlated with a reduced tail state density below the LUMO level of the electron acceptor and the disorder degree of the blend [94]. Zhou and co-authors [95] have achieved ~8% efficiency for PTB7:$PC_{70}BM$-based OSCs via methanol treatment. Such treatment has resulted in an increase in V_{bi} across the device by about 100mV, which is similar in magnitude when Ca/Al used as a cathode in OSCs. This increase in V_{bi} is thought to cause an increase of the V_{oc} as a result of methanol treatment [95,96]. Impedance measurements has confirmed that such treatment has induced a passivation of surface traps, a lowered series resistance, an increased hole mobility, an increased charge extraction and a reduced charge recombination due to the high V_{bi} and/or reduction of trap density [95].

Increasing the charge generation rate and the electron mobility as well as decreasing the recombination rate have been observed in PTB7:PCBM-based solar cells [97]. This has been attributed to the addition of solvent additive 1,8-diiodooctane (DIO) to the blend, which has caused an increase in PCE of PTB7:PCBM-based solar cell by almost three times from 3.3% to 9.1%, while an increase in FF from 49.7% to 71.5% and J_{sc} from 8.5 to 17.1 mA cm^{-2} was observed [97]. The latter enhancements have been associated with improving blend morphology after adding DIO compared to the blend without DIO treatment which has shown a clear large clusters of fullerene embedded within PTB7 matrix, resulting in a smaller effective interface area between PTB7 and PCBM components [98].

Chen and co-workers [99] have demonstrated high-performance single-junction OSCs with efficiency over 10% by employing a patterning structure to increase the light absorption correlated with optimum charge extraction. This approach was found to be advantageous and compatible for large-area, flexible, and low-cost electronic devices. The enhancement in the light harvesting in the patterned nanostructured OSCs has achieved 18% increase in J_{sc} from 16.51mA.cm^{-2} to 19.47mA.cm^{-2} and an improved PCE from 8.46% to 10.1%. This was ascribed to the increase in light trapping with broad spectral response; the performance enhancement is also explained by the self-enhanced absorption by including the pattern-induced anti-reflection, light scattering as well as surface plasmonic resonance and minimized recombination possibility [99]. Several other polymers have been investigated as donor materials in OSCs system; Table 3.1 and Table 3.2 illustrate some of these polymers and their photovoltaic performance.

Table 3. 1: PV characteristics for different donor/acceptor blends used in OSCs

Active layer	V_{oc} (V)	J_{sc} (mA.cm^{-2})	FF %	PCE %	Ref.
P-DTS(FBTTH$_2$)$_2$:PC$_{71}$BM	0.711	12.63	59.74	5.4	[100]
PID2:PC$_{71}$BM	0.86	5.29	44.3	2.01	[101]
DTffBT:PCBM	0.91	12.2	56.5	6.26	[102]
DTPyT:PCBM	0.85	12.8	58.1	6.3	[102]
P3HT$_{75}$-*co*-EHT$_{25}$:PCBM	0.675	7.96	59	3.16	[103]
PBTADN:PC$_{71}$BM	0.83	6.9	53.1	3	[104]
PDPP3T:PCBM	0.67	8.82	67.07	3.96	[105]
PBDT-TS1:PC$_{71}$BM	0.81	15.66	62.56	7.89	[106]
PBDTTPD:ICBA	1.09	5.1	48	2.7	[107]
PBDTTPD:PCBM	0.94	11.2	69	7.3	[107]
CuPc/C60	0.49	3.6	62	1.1	[108]
PBDTTT-C:PC$_{60}$BM	0.75	11.49	55	4.76	[109]
P3HT:ICBA	0.84	10.61	72.7	6.48	[110]
P3HT:PC$_{61}$BM	0.55	13.78	54	4.1	[111]
P3HT:PC$_{61}$BM	0.62	10.88	67	4.52	[112]
PTB7:PC$_{71}$BM	0.74	14.5	68.97	7.4	[89]

Table 3. 2: A list of polymers studied and summarised in Table 3.1 with their full name

Abbreviations	Materials' names
p-DTS(FBTTH2)2	7,7-(4,4-bis(2-Ethylhexyl)-4H-silolo[3,2-b:4,5-b′]dithiophene-2,6-diyl)bis(6-fluoro-4-(5′-hexyl-[2,2′-bithiophen]-5-yl)benzo-[c] [1,2,5]thiadiazole)
PID2	poly-3-oxothieno[3,4-d]isothiazole-1,1-dioxide/benzodithiophene
(DTffBT)	poly-(benzodithiophene–dithienyldifluorobenzothiadiazole)
(DTPyT).	poly(benzodithiophene–dithienylthiadiazolopyridine)
(P3HT75-co-EHT25)	poly(3-hexylthiophene-co-3-(2-ethylhexyl)thiophene)
(PBTADN)	poly((5,5-E- α-((2-thienyl)methylene)-2-thiopheneacetonitrile)-alt-2,6-[(1,5-didecyloxy)naphthalene]))
PDPP3T	poly[{2,5-bis(2-hexyldecyl)-2,3,5,6-tetrahydro-3,6-dioxopyrrolo[3,4-c]pyrrole-1,4-diyl}- alt -{[2,2':5',2''-terthiophene]-5,5''-diyl}]
PBDT-TS1	benzodithiophene (BDT)-thieno[3,4-b]thiophene (TT) backbone,
PBDTTPD	(poly[[5-(2-ethylhexyl)-5,6-dihydro-4,6-dioxo-4H-thieno[3,4-c]pyrrole-1,3-diyl][4,8-bis[(2-ethylhexyl)oxy]benzo[1,2-b:4,5-b′]dithiophene-2,6-diyl]])
CuPc	Copper phthalocyanine
ZnPc	Zinc phthalocyanine

3.4. Carbon-based materials in organic solar cells

Throughout the human history, carbon materials played a significant role mainly in the field of energy production. There are however a few drawbacks in using carbon-based materials as energy source, mainly due to the release of carbon dioxide, which results in adverse greenhouse effect [113]. In addition, carbon materials such as coal and fossil fuel are non-renewable sources. During the last 50 years, renewable and green energy technologies such as solar cells and fuel cells have been developed with the use of carbon nanomaterials including fullerene, carbon nanotubes (CNTs) and graphene due to their remarkable mechanical, electrical, optical and thermal properties [114]. Specifically, fullerene derivatives are still the best electron acceptor in organic solar cells; CNT and graphene are promising candidates of the next-generation of transparent conductive films in solar cells [113]. Fig.3.11 shows the three different carbon-based materials used in renewable energy field.

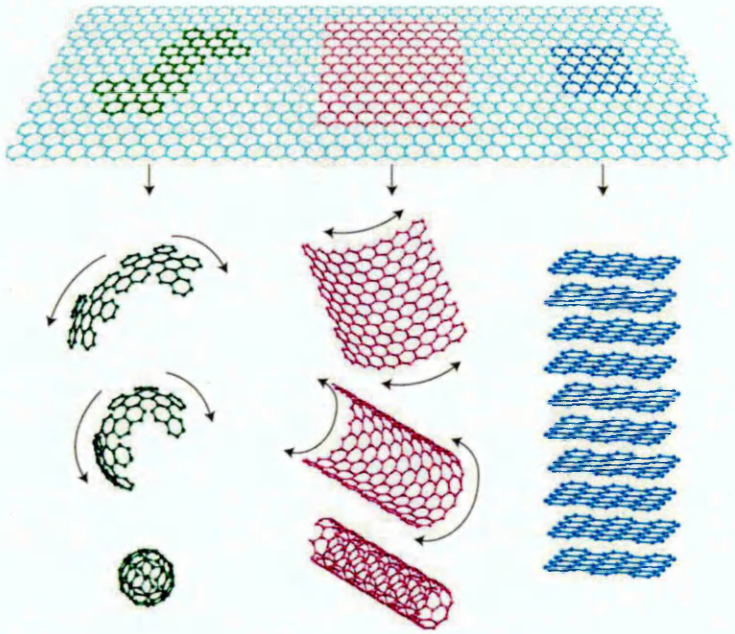

Fig.3.11: Mother of all graphitic forms. Graphene is a 2D building material for carbon materials of all other dimensionalities. It can be wrapped up into 0D buckyballs, rolled into 1D nanotubes or stacked into 3D graphite.

3.4.1. Graphene

Graphene, a single layer of carbon atoms bonded together in a honeycomb crystal lattice, is the fundamental structure in the carbon world. As shown in Fig3.11, graphene is the mother of all graphitic forms including Fullerene, SWCNT and Graphite [115]. Generally, graphene is a single carbon layer of graphite structure, while reduced graphene oxide is prepared from reduction of graphene oxide by thermal, chemical or electrical treatments. So in the reduced graphene oxide there is always some defects and even though we try to reduce the graphene oxide, there are still some oxygen functional groups in or on the reduced graphene oxide surface [115]. One of the main uses of graphene film is replacing PEDOT:PSS in the OSCs as HTL [116,117]. However, the low electrical conductivity of (GO) film results in high series resistance when it is used as HTL. In order to increase the charge carrier transport, butylamine-modified GO sheets have been used to reduce the recombination effect in the organic active layer [118]. To enhance the electrical conductivity of HTL in OSCs and reduce the series resistance, sulfated GO has been used to produce a PCE of 4.37% [119]. The strong acidic groups ($-SO_3H$) in the carbon basal plane of GO sheet and $-COOH$ groups at the edges enhance the doping effect of the donor polymer. Recently, GO has been discovered with an appropriate energy level alignment, high solubility and good film-forming property, which make it suitable for hole extraction [120]. In general, such GO nanoribbons have been synthesised by unzipping SWCNTs using $KMnO_4$ as the oxidant in a concentrated H_2SO_4. The produced GO has been also used to enhance the photovoltaic performance as both electron and hole transport layers [121].

3.4.2. Carbon nanotubes

Carbon nanotubes (CNTs) have been widely studied for transparent conductive electrodes [122]. Carbon nanotubes (CNTs), which are carbons with a cylindrical nanostructure, have unusual properties, which are valuable for nanotechnology, electronics, optics and other fields of materials science and technology. Owing to the material's exceptional strength and stiffness, nanotubes have been constructed with aspect ratio (length-to-diameter ratio) of up to 132,000,000:1 [123], significantly larger than any other material. Thin film of CNTs has a high surface area (about 1600 $m^2 g^{-1}$) and excellent electron-accepting properties [124].

In OSCs, CNTs can attractively fit the requirement of a wide conductive network as well as offer a remarkable opportunity for exciton dissociation. For these reasons, CNTs are expected to get a prominent position in electro- and photoactive nanocomposites in association with semiconducting polymers [125]. An improvement in PCE and FF has been reported for P3HT:PCBM-based OSC by the insertion CNTs in the electron transporting layer (TiO_2) [126]. PCE of 3% and FF of ~61% have been associated with the addition of 0.1%wt SWCNTs concentration to TiO_2 in comparison with PCE of ~1.6% and FF of ~42% for the pure TiO_2 based device. The 0.1%wt single-walled carbon nanotubes (SWCNTs) concentration was found to be the optimum concentration as increasing its value above that has reduced PCE to ~1.2%. Similar performance has been reported for Multi-walled carbon nanotubes (MWCNTs) [126]. These improvements have mostly been attributed to the intrinsic physical and chemical properties of CNTs such as high surface area, electron-accepting properties and excellent carrier mobility [126].

Polythiophene and carbon nanotubes (CNTs) are considered as a strong candidate hybrid material for photovoltaic applications because SWNTs acts as an electron acceptor and/or as electron transportation paths [124]. The electrical conductivity of such hybrids could be explained by the percolation theory; by gradually increasing the conducting filler content (CNTs) within the main polymer matrix, conduction behaviour of the final composite is altered. The electrical conductivity of such composite might increase several times due to the generation of conducting network or continuous electron paths [127]. It has been shown that the dispersion of functionalized SWCNTs in the photoactive layer has resulted in an improved efficiency of OSCs with PCE reaching 3.02% using a 0.3wt% concentration of SWCNTs with an improvement of about 10% over the reference device [128]. The performance enhancement by incorporating functionalized SWCNTs is mainly attributed to the extension of excitons dissociation area and improved charge carriers transfer across the active layer [128, 129]. As an example, MWCNTs have been added to the polythieno[3,4-b]thiophene/benzodithiophene/$PC_{71}BM$ active layer to achieve a high PCE of 8.6%. This enhancement has been attributed to the extra exciton dissociation centres and efficient charge transport channels by the aid of CNTs network [130].

3.4.3. Fullerenes

In polymer bulk heterojunction (BHJ) solar cells the electron accepting materials have similar influence as that of the electron donor polymers. Up to date, fullerene based material such as [6,6]-phenyl-C-61-butyricacid methyl ester (PCBM) is the most studied electron acceptor material for solution processed OSCs. The offset between the energy levels of the donor and acceptor in the BHJ system determines the open circuit voltage of the device as discussed earlier in section 2.5.1. The up shifted LUMO level of a fullerene derivative such as ICBA compared to PCBM has resulted in a higher open circuit voltage (V_{oc}) after blending with P3HT [131]. Generally, PCBM and its derivatives have a low absorption coefficient in the visible spectral range which in turn results in low contribution in the photogeneration process [132]. It has however significant effects on the OSC electrical parameters such as V_{oc} as well as the interface properties at the organic semiconductor/metal junction [133].

In a published study, we have investigated the effects of fullerene ratio of both PCBM and Indene-C60 Bisadduct (ICBA) which were varied in the range of 1-3 in the P3HT-based solar cells under ambient environment [134]. The absorption spectra have shown a decrease in the intensities by increasing the fullerene ratio and the peaks have exhibited a blue shift, which have been attributed to the reduction in the interchain interaction between P3HT molecules. Moreover, a strong reduction in the crystallinity of the P3HT-based films has been observed by increasing the ratio of fullerene within the blend, where the fullerene molecules are thought to interrupt the P3HT crystallinity during the film growth [134]. Another study has been carried out using different fullerene derivatives, where each fullerene has different HOMO and LUMO energy levels which in turn results in different V_{oc} value [135]. The best device performance based on $PC_{61}BM$ has resulted in PCE of 4.2%, FF of 62%, V_{oc} of 0.65V and J_{sc} of 10.4 $mA.cm^{-2}$ [135].

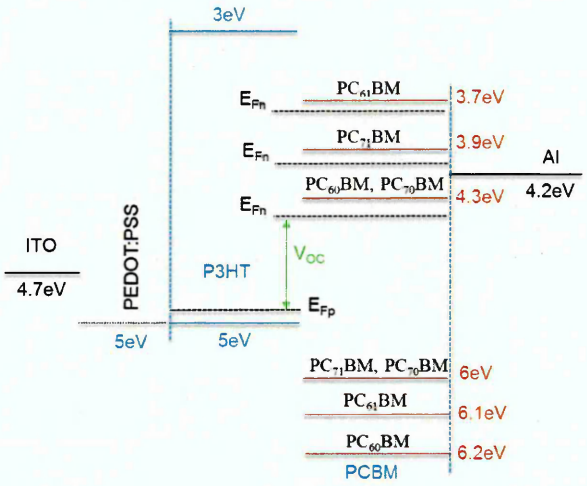

Fig.3.12: Energy level alignment of different fullerene; the values of ITO, PEDOT:PSS, P3HT, $PC_{71}BM$ and $PC_{61}BM$ were cited from Sigma-Aldrich. $PC_{60}BM$ [136], and $PC_{70}BM$ are cited from the literature [137]

Fig.3.12 shows an example of different fullerenes included in a conventional structure of P3HT:PCBM-based solar cell. Different barrier heights at the metal/organic interface have been evaluated using both I-V and C-V measurements [134]. Small variations in the estimated values from I-V and C-V measurements were attributed to the excess capacitance and inhomogeneity of barrier heights [138]. The organic/metal interface barrier varies with the BHJ blend arrangement, depending on which fullerene is used, which leads to the formation of different cathode/PCBM interface properties [139]. Yakuphanoglu and co-workers [140] have studied the inhomogeneity of Schottky barrier in organic solar cells. The interfacial states at the organic/metal interface affect the barrier height, charge extraction and the carrier transport inside the acceptor/donor blends, which therefore determines the overall performance of OSCs [139,141]. In general, the surface disorder of the active layer induces extra energy levels into the band gap, where this is thought to control the charge transport properties in the organic blend [142].

3.5. Optimisation of OSCs' performance

OSCs in general suffer from low power conversion efficiency and limited time stability, and in order to overcome these essential difficulties several device processing and engineering aspects have to be considered when OSCs are designed. These aspects have direct impact on the performance and final output of these devices. The following sections describe some of these areas of development OSCs and supported by some examples.

3.5.1. The use of different solvents

The effects of solvents used to fabricate the organic active layers have received significant attention [10, 143-148], as they have a direct influence on the active layer's morphology and structure and therefore OSCs performance. Higher PCE could be achieved by optimising the active layer's fabrication process, such as using different solvents with different evaporation rates [51] to enhance the formation of a nanoscale interpenetrating network. The latter is resulted in high interfacial area which assists the exciton dissociation efficiency as well as the ordered stacking structure of the polymer chains and thereby enhances the charge carrier mobility [149]. The effects of the solvent type on the morphology and crystallinity of the P3HT:PCBM blend have been discussed by Motaung and co-workers [149].

P3HT:PCBM films prepared using non-aromatic solvents have shown an improvement in the absorption intensity. This enhancement specifies that an improvement in the chain ordering and morphology of P3HT have been realized using the non-aromatic solvents [52]. Different solvents and their co-solvents with different evaporation rates have been used to control the surface composition of P3HT:PCBM organic active layer [150]. High boiling point solvents such as tetralin, chloronaphthalene and acetophenone, have been mixed with chlorobenzene. Using co-solvents with higher boiling point than the initial solvent as well as with better PCBM solubility assists the PCBM molecules to diffuse upwards after the initial solvent has evaporated. The slow evaporation process of film formation provides enough time for PCBM to diffuse upwards during the evaporation of the second solvent [150] (see Fig.3.13).

With the solvents having similar evaporation rate, the PCBM molecules has lower concentration at the surface of the P3HT:PCBM film whereas in the case of co-solvents with different evaporation rates has shown a better composition on the film surface which indicates that the co-solvents have induced better distribution of both donor and acceptor and therefore better interpenetrating network exist [150]. Jang and co-authors [151] have investigated the optical, morphological and electrical properties of P3HT:PCBM blended by different solvents. They have shown that the purity and the type of mixed solvents have significant effects on the device performance. J_{sc} has improved from 5.5 $mA.cm^{-2}$ in Toluene solvent to 10.4 $mA.cm^{-2}$ in dichlorobenzene:chlorobenzene co-solvent with an increase in FF from 31% to 45.5% and PCE from 1% to 2.9% whereas V_{oc} has remained unchanged around 0.6V. This improvement in the device performance by the aid of co-solvents has been attributed to the rougher surface, enhancement in the light absorption and the improvement in the crystalline structure of the active layer. Reisdorffer and co-authors [10] have pointed out the use of co-solvents of chlorobenzene:toluene with different ratios on the morphology and structure of the P3HT-based blends; these two solvents have been selected due to their close boiling points and different polarities. They have revealed that the key factors are the PCBM solubility and distribution within the organic blend [152,153].

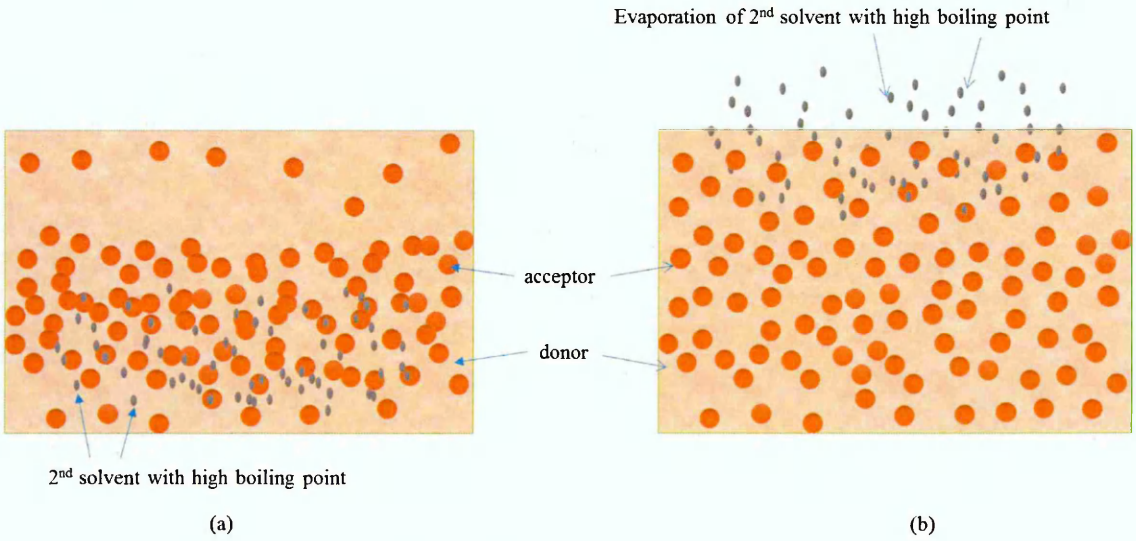

Fig.3.13: Using co-solvents with two different boiling points to control the active layer morphology

3.5.2. Employing different interlayers

In BHJ organic solar cells, open circuit voltage is mainly determined by the difference between the LUMO of the acceptor and the HOMO of the donor, provided that an Ohmic contact is created between the active layer and both cathode and anode electrodes [34]. The Ohmic contact can be established by choosing the anode electrode with work function higher than the HOMO of the donor and the cathode electrode with work function lower than the LUMO of the acceptor [154]. On the other hand, the formation of a Schottky barrier with any of the contacts (cathode and/or anode) can significantly reduce V_{oc} [34]. In this section, different HTL and ETL have been illustrated in order to give brief information about their importance. Transparent conducting electrodes have been investigated comprehensively due to their variety of application in display and in photovoltaic devices [155]. One of the most attracted electron transport layer in photovoltaic devices is ZnO thin film, due to its promising properties such as stability, wide band gap, high optical transmittance, electrical conduction, and low material cost, (Eg= 3.3 eV) [156-159]. Compared to TiO_2 semiconductor as an electron transport layer, ZnO has higher electron mobility that can result in a lower series resistance in the OSC device [160]. Furthermore, the method of fabrication of ZnO films is simpler than that of TiO_2, which is important for industrial applications [161]. For both materials however, a high-temperature annealing is often required to in order to achieve good electronic properties. This treatment step hinders the use of ZnO thin films on flexible substrates and low-cost roll-to-roll processes [162]. Therefore, interest is growing in developing low-temperature growth methods to obtain high quality ZnO layers [163]. Nowadays, Al-doped ZnO (AZO) is widely used as a conductive substrate in OSCs [164-166] as an alternative to ITO conductive substrate, which has some stability issues [167], or to modify the ITO electrode to be suitable for electron collection since the energy level of the acceptor (generally PCBM) does not align properly with the ITO energy level in an inverted architecture [168]. A significant improvement in the P3HT:PCBM-based device efficiency of about 14% has been obtained as a result of incorporating Al into ZnO films (AZO) as electron transport layers (ETLs) [168]. This increase is due to improvement in J_{sc} from 10.73 to 11.12 $mAcm^{-2}$ and FF from 53.7% to 60.8%. Doping Al into ZnO layer has resulted in increasing the carrier concentration and conductivity of the electron transport layer (ETL) [168].

The use of an inverted BHJ solar cell has been carried out employing ZnO layer as electron transport layer [169]. The ZnO morphology is found to be a crucial parameter in the inverted OSCs to improve PCE from 2.36 to 2.73 associated with an increase in V_{oc} from 0.6 to 0.65 [169]. The use of a polar solvents such as 2-methoxyethanol or ethanolamine treatment as a surface treatment of ZnO layer has been reported to reduce the barrier height between the ZnO conduction band and the LUMO level of the acceptor and therefore, increase PCE from 6.71% to 8.69% in PTB7:PC_{71}BM-based solar cells [170]. In 2011, Cao group [171] have developed a new alcohol-soluble polymer called "Poly[(9,9-bis(3'-(N,N-dimethylamino)- propyl)-2,7-fluorene)-alt-2,7-(9,9-dioctylfluorene)]" (PFN) which acts as electron selective material. PCEs as high as 9.2% are achieved using inverted OSCs based on PTB7:PC_{71}BM with PFN as ETL [90]. A thin layer of PFN (10 nm) deposited on the ITO surface has contributed to the efficiency enhancement by two times; it has tuned the cathode work function from 4.7eV to 4.1eV which has resulted in higher V_{oc}. Furthermore, it was found to improve the electron collection by establishing an ohmic contact with the active layer [90]. OSC with a PFN/Al cathode has shown PCEs up to 6.07%, which was attributed to the obvious enhancement in J_{sc} and FF, in comparison to devices prepared with Al and Ca/Al cathodes [172]. The existence of PFN as a polymer interfacial layer has decreased the series resistance by establishing better interfacial contacts, resulting in improved electron collection at the cathode and decreased the possibility of hole–electron recombination [172].

It has been argued that organic-organic interface is more favourable interface for charge transport in comparison with the organic-metal interface [173]. Tris(8-hydroxyquinoline) aluminum (Alq3) has frequently been used as ETL in OSCs [174, 178, 179]. Although the Alq3 LUMO level is not fully matched with the active layer, electron transport can take place through damage induced trap states created by the evaporation of hot metal atoms onto the Alq3 surface [175]. Song et al. [176] have ascribed the improved performance in OSC devices using Alq3 layer to its effect as a blocking layer which prevents the cathode atoms from diffusing into the active layer during the evaporation process. Likewise, employing hole transport layer (HTL) is another crucial factor, which influences the performance of OSCs. Poly (3,4-ethylenedioxythiophene) doped with poly(styrene sulfonate), abbreviated as PEDOT:PSS is one of the most promising conductive polymers

due to its simple film processing, high transparency, high conductivity and high stability [177-180]. The PEDOT:PSS films can be influenced by a variety of factors during the drying processing; those include the fraction of solid content, the particle size, the fraction of PSS and the viscosity which could lead to a different morphological and electronic properties [181]. Graphene oxide (GO) is another alternative to PEDOT:PSS as a solution-processable HTL layer [34]. Li and co-workers [116] have used 2nm thick GO as the HTL in P3HT:PCBM-based OSC, which showed comparable PCE to that of OSCs in which PEDOT:PSS was used as the HTL. Murray and co-workers [182] have demonstrated enhancement in device lifetime of PTB7-based OSCs under extended thermal and humid ambient conditions using GO flakes rather than PEDOT:PSS layer. The GO work function has been altered by chlorination process which has resulted in improved energy level matching with the donor polymer PCDTBT and therefore increased PCE from 5.49% for the PEDOT:PSS-based device to 5.59% for the GO-based device and to 6.56% in the Cl-GO -based device [182].

It has been reported that the conductivity of PEDOT:PSS film has dramatically improved from 0.2 $S.cm^{-1}$ to 103 $S.cm^{-1}$ after treating the layer with different organic solvent such as ethanol, dimethylsulfoxide, acetonitrile, or tetra-hydro-furan [183]. This enhancement in conductivity has been ascribed to the preferential solvation of PEDOT:PSS with a co-solvent comprising water and an organic solvent, which solvate the hydrophilic PSS and hydrophobic PEDOT chains, respectively. The co-solvent has induced the phase-separation of the insulator side (PSS) from the conductive side (PEDOT) and resulted in conformational change of the PEDOT chains from being coiled to linear [183]. Conductive PEDOT:PSS layer can assist in enhancing PCE by providing fast charge transfer with small resistance as well as enhanced surface or interface properties [184]. Ko and co-authors [185] have reported a decrease in the resistance of PEDOT:PSS by doping with organic solvents which has resulted in improving organic solar cell performance [186]. Xiao and co-workers [187] have suggested that enhancing the OSCs performance can also be attained via increasing the light absorption within the active layer, which could be achieved by improving light scattering and by obtaining high surface area with solvent-treated PEDOT:PSS [188].

Lastly, improvement of interfacial properties between PEDOT:PSS and the active layer could be another factor that facilitates greater device performance; this was ascribed to the formation of rougher PEDOT:PSS surface for domains of P3HT and PCBM to be better aligned this resulting in enhanced excitons dissociation [189,190]. Polyanilines on the other hand are classical conducting polymers that have been used in several methods and can be easily doped to obtain high conductivity [34]. As an example, poly(styrene sulfonic acid) (PSSA) doped graft copolymer PSSA-g-PANI has been used as the HTL for P3HT:PC61BM-based devices. A 20% enhancement in PCE has been achieved compared to PEDOT:PSS-based device, which has been attributed to the high transparency over the P3HT absorption range and its high conductivity [191]. Self-doped sulfonic acid polyaniline (SPAN) has been used as HTL for inverted P3HT:PC61BM-based OSC [192]. The device based on this HTL has exhibited an improvement in PCE over that with PEDOT:PSS from 3.3% to 3.54% which has been ascribed to higher conductivity and better film quality of SPAN relative to PEDOT:PSS. Zhao and co-authors [193] have applied a water-soluble hydrochloric acid doped polyanilines (HAPAN) as an ultra-thin HTL for highly efficient OSCs. HAPAN work function has aligned well with the used polymers and the transparency was found much higher in comparison to PEDOT:PSS film. A PCE as high as 9% has been achieved for the PBDTTTEFT:$PC_{71}BM$-based device when HAPAN is used as THL. This enhancement has been attributed to the suitable energy levels, high transparency, and low film roughness [193]. The following table shows OSCs performance using different cathode and anode configurations.

Table 3. 3: OSCs performance using different cathode and anode configurations.

Active layer	Anode	Cathode	V_{oc} (V)	J_{sc} ($mA.cm^{-2}$)	FF	PCE (%)	Ref.
P3HT:PCBM	ITO/PEDOT:PSS	Ca/Al	0.61	10.62	0.67	4.37	[51]
P3HT:PCBM	ITO/SPDPA	Ca/Al	0.6	10.33	0.68	4.2	[194]
MDMO-PVP:PCBM	ITO/TFB:$TPDSi_2$	Al	0.89	4.62	0.54	2.23	[195]
P3HT:PCBM	ITO/CNT/PEDOT:PSS	Al	0.59	21	0.51	4.9	[196]
P3HT:PCBM	ITO/CF_3-SAM	LiF/Al	0.6	13.87	0.38	3.15	[197]
P3HT:PCBM	ITO/PTFE	Al	0.52	7.40	0.49	2.27	[198]
P3HT:PCBM	ITO/MoO_3	Ca/Al	0.60	8.94	0.62	3.33	[199]
P3HT:PCBM	ITO/NiO	LiF/Al	0.64	11.30	0.69	5.16	[200]
P3HT:PCBM	ITO/AgO_x/PEDOT:PSS	Ca/Al	0.60	12.70	0.63	4.80	[201]
APFO-5:PCBM	ITO/PEDOT:PSS	PEO/Al	0.90	4.00	0.51	1.84	[202]
P3HT:PCBM	ITO/PEDOT:PSS	F-PCBM/Al	0.57	9.51	0.70	3.79	[203]
P3HT:PCBM	ITO/PEDOT:PSS	TiO_x/Al	0.61	11.10	0.66	5.00	[47]
PCDTBT:$PC_{71}BM$	ITO/PEDOT:PSS	TiO_x/Al	0.88	10.60	0.66	6.10	[60]
P3HT:PCBM	ITO/PEDOT:PSS	TiO_x:Cs/Al	0.58	10.76	0.67	4.20	[204]

3.5.3. Different OSC layers Fabrication conditions

In order to produce an organic solar cell, different conditions should be considered for its fabrication such as choice of temperature of heat treatment, spin coating parameters, blend ratio between the donor and acceptor materials and using complementary materials to enhance the light harvesting properties. Generally, the organic active layers have amorphous nature and relatively low charge carriers' mobility. Therefore, strong temperature dependence has been observed in organic thin films, which directly affects the current density by influencing the electronic transport properties [205]. A reduction in the current density could be observed in the organic active layers by reducing the temperature due to charge trapping effects and the reduction in charge carriers' mobility [206]. Furthermore, the temperature-dependent series resistance has also been observed in organic materials, which directly impacts on the device FF [205]. Motaung and co-authors [207] have investigated the performance and the morphology change in P3HT:PCBM-based OSCs with different temperature treatment. An increase in PCE from 0.79% to 2.88% has been observed corresponding to an increase in the device FF from 0.49 to 0.60 which was the results of heat treatment of the active layer at 150°C. This improvement has been associated with the enhanced interfacial area, increased light absorption and the improved charge transport [208]. The changes in the films' morphology and phase separation between P3HT and PCBM domains with PCBM assuming a needle-like feature has been found to increase with increasing temperature. The light absorption has also improved after thermal annealing corresponding to a quenching in the PL intensity when samples were heat-treated at 150℃. The latter is ascribed to the fact that PCBM is known to quench the PL intensity of P3HT, hence, an increase in the PL intensity suggests a higher phase separation between P3HT and PCBM is taking place [209]. During the annealing treatment, PCBM molecules diffuse away from P3HT chains resulting in a reduced interaction between the two domains, therefore, a recovery of the PL emission of P3HT [207,2010]. Further investigation suggests that thermal treatment affects the morphology and the thermal conductivity of the P3HT, PCBM and their blends [211]. Furthermore, P3HT:PCBM OSCs have shown an increase in PCE from 1.5% to 3.4% after annealing the active layer at 100°C associated with a decrease in the series resistance and an increase in the J_{sc} and V_{oc} [212].

This enhancement has been attributed to improved blend structure and the formation of better-percolated network with improved electron transport [213]. Another type of annealing treatment applied to P3HT:PCBM active layers is the solvent treatment [51]. The suggested approach of solvent annealing is used to improve the organic thin film morphology by controlling the solidification rate during polymer growth. This is also shown to control the self-organization of the polymer chains, leading to better morphology [214]. It has been shown that using proper solvent annealing or thermal annealing followed by solvent annealing results in improving the OSCs based on IDT-difluorobenzothiadiazole-based D-A oligomers with different spatial symmetry core units, different conjugation lengths, and different amounts of electronegative fluorine atoms (4, 6, 8, and 10 fluorine substituted backbone, respectively) [215]. This treatment has led to a significant improvement in the OSC efficiency to 9.1% with a very high FF of 0.76 using medium-sized oligomer BIT6F with the improved morphology. On the other hand, devices prepared from the shortest oligomer BIT4F have exhibited an impressively high FF of 0.77. The change of chain-length has indicated alteration of energy levels, charge transport and the blend morphology, which in turn had a significant influence on the device performance [215].

Xie and co-authors [216] have observed a 0.246V loss in V_{oc} after solvent annealing in (p-DTS(FBTTh$_2$)$_2$):PC$_{71}$BM solar cells which have been recovered by post-annealing treatment. The use of thermal annealing subsequently after solvent annealing has not shown any recovery to the devices V_{oc}. This was ascribed to the small change in the film morphology, crystallinity and absorption properties. However, using post-annealing treatment after all the layers of the device are completely deposited (complete device) has resulted in the recovery of 0.225V to V_{oc} on average [216]. The post-annealing treatment has also resulted in reducing the recombination and increasing the charge collection rate, which is probably originating from good interface contact as well as the low density of defects. Another factor which influences the active layer morphology and therefore the OSC performance is the donor-acceptor blend ratio. Several attempts by Chen and co-authors [217] have been carried out to investigate the effect of the blend ratio correlated with the solvent annealing process on the morphology and the performance of P3HT:PCBM-based OSCs.

The use of different blend ratios of P3HT and PCBM have shown that 1:1 is the optimum ratio for P3HT:PCBM blend with PCE of 3.66%. No significant change has been observed in the V_{oc} due to variation in the blend ratio. This enhancement in OSC efficiency has been attributed to the improved morphology of the BHJ layer using 1:1 ratio under solvent annealing process [218]. However, increasing the ratio from 1:1 of P3HT:PCBM to 2:1 has resulted in increasing the absorption intensity as well as enhancing PCE from 1.42% to 3.09% as demonstrated by Wu and co-workers [219]. They have recommended that any further increase in the P3HT ratio has resulted in reducing PCE which was due to the irregular distribution of P3HT and PCBM within the blend [219]. Further investigation of the BHJ blend ratio has been carried out using P3HT-based OSCs with ICBA and PCBM with a wide range of blending ratio (0-100%) [220]. The results show that there is a significant impact on PL intensity of P3HT pristine film after adding ICBA and/or PCBM which reflects that the excitons have higher possibility to survive and approach the heterojunction interface, and therein dissociate efficiently [220].

Moreover, increasing the acceptor ratio within the blend has resulted in a red shift and less pronounced shoulder due to the increased disorder of P3HT [221]. PCE has experienced different values due to the blend ratio of P3HT with either ICBA or PCBM; the best-performed device is found to be with the acceptor ratio of 41% in the blend; this ratio has demonstrated PCE of 4.325% and 4.5% for P3HT:PCBM and P3HT:ICBA blends, respectively. However, V_{oc} has shown higher value (0.86V) in the case of the ICBA-based device compared to the PCBM-based device (0.62V). Additionally, the use of different composition ratios in a ternary blend OSC has revealed a direct influence on the light harvesting properties of the blend as well further improved the performance of the OSCs [222]. The device V_{oc} has also shown to be influenced due to the presence of two different donors [223] or two different acceptors [224] in such blends. Device performance has exhibited an increase when ICBA has been used instead of PCBM; V_{oc} increased by about 6%, FF in about 40% and J_{sc} in about 28% whereas PCE of 4.7%has been obtained for P3HT:ICBA-based device in comparison to 3.31% for P3HT:PCBM-based device. This increase in the device performance as the ICBA ratio increases within P3HT:PCBM blend is attributed to the energy difference between PCBM and ICBA in about 0.2eV.

Therefore, once the excitons are dissociated at the P3HT/PCBM interface, the electrons drop from the LUMO level of P3HT to the LUMO level of PCBM and because of the LUMO level of ICBA is higher, therefore, less energy is lost and higher V_{oc} is provided with higher ICBA ratio [224]. The ternary blends are also employed to enhance the light harvesting properties of the active layer by using different materials; each material covers a specific range of the solar spectrum [225]. In a ternary blend OSC, an IR sensitizer is basically incorporated into the host blend of a polymer blended with a fullerene derivative. The ternary approach would expand the photon harvesting resulting in higher J_{sc}, therefore, higher PCEs [226]. The incorporation of tetramethyl substituted copper (II) phthalocyanine (CuMePc) nanocrystals into a P3HT:PCBM blend with different weight ratios has resulted in enhancing the device performance to exhibit PCE of 5.3% compared to reference device with PCE of 3.3% [225]. This enhancement in the photovoltaic performance is attributed to the highest carrier mobility and a broader absorption range of the new composite blend [225].

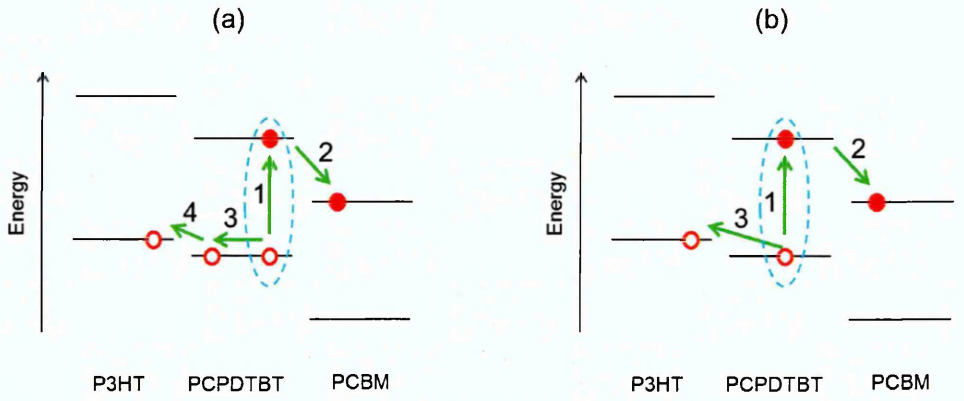

Fig.3.14: The charge separation mechanism in a ternary P3HT:PCPDTBT:PCBM blend (a) with diffusion in PCPDTBT domains, including, (1) Exciton generation in PCPDTBT, (2) Electron transfer from PCPDTBT to PCBM, (3) Hole diffusion to PCPDTBT/P3HT interface, and (4) Hole transfer from PCPDTBT to P3HT; (b) without diffusion in PCPDTBT domains, including, (1) Exciton generation in PCPDTBT (2) Electron transfer from PCPDTBT to PCBM, and (3) Hole transfer from PCPDTBT to P3HT. Reprinted from ref. [227].

To maximise the range of the absorption spectra coverage, copper phthalocyanine (CuPc) has been used in a multilayer device architecture (ITO/PEDOT:PSS/CuPc/P3HT:PCBM/Al) [228]. The incorporation of CuPc layer (~8nm) has extended the light harvesting properties to almost the entire visible range, which in turn resulted in higher J_{sc}. The P3HT:PCBM-based device has exhibited PCE of 3.95%, J_{sc} of 10.61mA.cm^{-2}, V_{oc} of 0.65V and FF of 57.1%, while the CuPc/PCBM-based device has shown a PCE of 0.54%, J_{sc} of 2.3mA.cm^{-2}, V_{oc} of 0.58V and FF of 41.1%. Furthermore, for the multilayer CuPc/P3HT:PCBM-based device, a PCE of 4.13% with J_{sc} of 12.54mA.cm^{-2}, V_{oc} of 0.64V and FF of 51.1% have been achieved. This enhancement on adding a CuPc layer is due to the increase the light harvesting as well as improving the charge transport properties [228]. Using NIR sensitization with a low-band gap polymer (PCPDTBT) in a P3HT:PCBM system has resulted in improving the efficiency to over 4% by adding 30-40% of PCPDTBT to the binary blend, corresponding to an efficiency improvement of 25% compared to the P3HT:PCBM reference device [227]. In this structure, excitons are generated in PCPDTBT and dissociated at the PCPDTBT/PCBM interface followed by electron transfer from PCPDTBT to PCBM. Holes are diffused in the PCPDTBT domains to P3HT/PCPDTBT interface [227,229] Fig.3.14 describes the charge separation mechanism in a ternary blend consisting of P3HT:PCPDTBT:PCBM. Hu and co-authors [230] have used 3% of 1,8-diiodooctane (DIO) additives to the P3HT:PCPDTBT:PCBM (1:0.2:1) ternary blend to reconstruct the microstructure of the active layer blend. This has resulted in 20% higher J_{sc} and 17% enhancement in PCE compared to P3HT:PCBM-based reference device. Overall, ternary solar cells with PCE of 3.33%, J_{sc} of 12.67 mA.cm-^{2}, V_{oc} of 0.55V and FF of 48% have been reported. Controlling the active layer thickness can significantly affect the OSC performance; usually, the diffusion length of excitons in organic materials is low, typically in the range 10-20nm, therefore, thinner active layers are required to prevent charge recombination and thus good charge carriers' extraction is guaranteed [14,231]. A thicker film however is beneficial for increasing light absorption capability of the active layer compared to thinner films; thicker films on the other hand can also increase the series resistance and reduce the charge carriers' mobility [232], whereas thinner films are capable of showing nearly 100% conversion of absorbed photons into collected carriers [60].

To control the active layer thickness, different parameters have been considered, such as using different concentration of donor/acceptor [223], different spin coating parameters [14,234] and controlling the growth time [51]. It has been shown that the correlation between the spin speed and the conjugated plane orientation of P3HT polymer is associated with the variation in the solvent evaporation rate where edge-on orientation of the polymer molecules is obtained at slow spin speed [58]. Additionally, spin coated P3HT film from low-volatility solvents results in more crystalline structure, with more well-organized interchain π-stacking and more preferred edge-on orientation (see Fig.3.15(a)) rather than face-on orientation (see Fig.3.15(b)) in comparison to films prepared from high-volatility solvents [235]. Disordered films on the other hand may result when fast spin speed is used due to the rapid drying process [58]. Based on the processing conditions, P3HT has a lamella structure with 2D conjugated interchain stacking sheets with either a parallel or perpendicular orientation to the substrate (see Fig.3.15) [236]. Two different P3HT molecular orientations have been demonstrated for films prepared by spin coating and casting methods [232]. XRD data has revealed that the casted films have exhibited a normal orientation with the side chain standing perpendicular to the substrate, while spin coated films show orientations in both side chain with respect to the substrate, face-on and edge-on as shown in Fig.3.15.

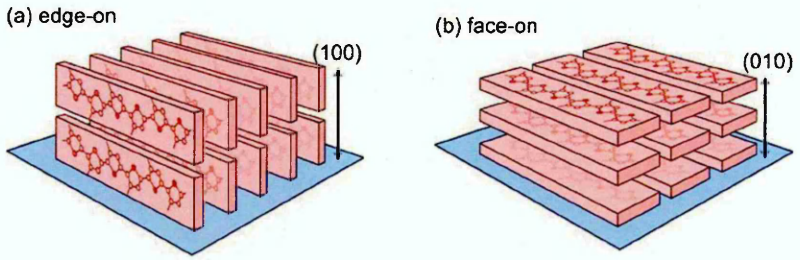

Fig.3.15: (a) Edge-on orientation of P3HT and (b) Face-on orientation of P3HT

3.6. Degradation and stability of organic solar cells

There are still some shortcomings of organic- based PV that need to be addressed before they are commercialized and these include efficiency, lifetime and stability, lifetime falls extensively well behind Si-based solar cells' under outdoor conditions [237]. Generally, degradation in OSCs performance arises due to different reasons such as diffusion of oxygen, water, interlayer and electrode particles into active the layer or due to degradation of interfaces and active layer materials. Furthermore, it might occur due to some morphological variations and/or macroscopic changes such as formation of particles, delamination, cracks and bubbles [238]. In fact, two or more of these mechanisms might take place at the same time while others might happen during the solar cells operation or even during storage time. Some of these mechanisms occur almost immediately after device preparation and others a bit slower, therefore, it is a challenging task to identify the overall performance deterioration of OSCs' to identify degradation mechanisms and thus find a solution [238]. As was mentioned earlier, the interpenetrated network morphology of the active layer is found to extremely affect the device stability, as this morphology efficiently influences the charge generation, transport and collection [239]. Several research groups have thoroughly analysed external parameters such as the relative concentration of the donor and acceptor, the choice of the solvent [37], thermal annealing [48] and solvent annealing procedures [51] in order to optimise the organic active layer morphology for high efficiency solar cells. The donor-acceptor blend might exhibit macro-phase separation between the blend components, which is larger than the excitons diffusion length, when the OSCs are exposed to sunlight for a long period of time. The formation of large PCBM aggregates have been reported after a prolonged thermal annealing, which has effectively deteriorated the device performance [240] Using high boiling point solvent additives such as 1,8-diiodooctane (DIO) in the preparation of (DTS($PTTh_2$)$_2$):$PC_{70}BM$ active layer has shown PCE of 6.7% [241]. Although these additives increase PCE, they reduce the device stability by forming a more unstable morphology of the active layer [242-244]. It has been reported that using DIO in PTB7:$PC_{71}BM$-based solar cell has resulted in preserving 61% and 39% of the original PCEs for devices without and with DIO treatment, respectively [244]. They have shown that the large aggregations of $PC_{71}BM$ as a result of DIO treatment supported the device degradation by interrupting the film's morphology and preventing the

interpenetrating networks to happen [244]. Furthermore, the use of PEDOT:PSS layer has a direct influence on the device stability as it is a water-based material and the diffusion of water into the active layer can damage the low work function of the metal electrode as an oxidation agent [245]; furthermore, the water can move the $PC_{71}BM$, and therefore, induces excessive aggregation [244]. OSC degradation has been further studied by Ngo and co-workers [246] using P3HT:PCBM blends prepared by spin and spray coating methods. The spray coated P3HT:PCBM-based devices has degraded faster than the active layers produced by spin coating, which has been attributed to oxygen trapping in the devices as the spray coated layers have been prepared in ambient atmosphere, whereas the spin-coated layers were prepared in an inert nitrogen atmosphere [246]. Recently, Lima and co-authors [247] have reported an outdoor stability analyses of P3HT:$PC_{60}BM$-based OSCs for more than 900 h, which has revealed higher stability for devices fabricated with the aqueous solution-processed V_2O_5 instead of PEDOT:PSS film as hole transport layer. In PEDOT:PSS-based device, 40% of the initial PCE has been maintained after 900 h, while V_2O_5-based device has maintained around 80% of its initial performance after the same period of time. The observed changes in the device FF are attributed to the reduced interfacial charge transfer efficiency between the different layers, the degradation of the active layer, or the increase of the recombination processes [247]. The strongest change was observed in the short circuit current density due to the increase of internal resistance as a result of the degradation of the electron transport layers, the electron donor, or due to the reduction of the transparency of any layer or interface, which is thought to reduce the amount of light entering the cell [247]. It has been reported that air stable OSCs could be achieved by employing a solution based metal oxide between the active layer and the metal cathode as a buffer layer [237]. For example, a solution based titanium dioxide (TiO_2) with a thickness less than 30nm has been used successfully to reduce the physical and chemical damages in the device [47]. The TiO_2 layer was employed as an effective barrier for oxygen penetration to maintain the device stability in the ambient atmosphere. However, Foe and co-authors [248] have reported that the PCE, J_{sc} and FF of the device have dropped by about 25%, 16% and 11% after 70 days of storage, respectively, while V_{oc} remains quite stable after the same period of time.

References

[1] Frenkel, J. (1931). On the transformation of light into heat in solids. I. Physical Review, 37(1), 17.

[2] Brédas, J. L., Beljonne, D., Coropceanu, V., & Cornil, J. (2004). Charge-transfer and energy-transfer processes in π-conjugated oligomers and polymers: a molecular picture. Chemical Reviews, 104(11), 4971-5004.

[3] Qi, B., & Wang, J. (2012). Open-circuit voltage in organic solar cells. Journal of Materials Chemistry, 22(46), 24315-24325.

[4] Shockley, W., & Queisser, H. J. (1961). Detailed balance limit of efficiency of p-n junction solar cells. Journal of applied physics, 32(3), 510-519.

[5] Ameri, T., Li, N., & Brabec, C. J. (2013). Highly efficient organic tandem solar cells: a follow up review. Energy & Environmental Science, 6(8), 2390-2413.

[6] Peumans, P., Yakimov, A., & Forrest, S. R. (2003). Small molecular weight organic thin-film photodetectors and solar cells. Journal of Applied Physics, 93(7), 3693-3723.

[7] Rostalski, J., & Meissner, D. (2000). Photocurrent spectroscopy for the investigation of charge carrier generation and transport mechanisms in organic p/n-junction solar cells. Solar Energy Materials and Solar Cells, 63(1), 37-47.

[8] Hoppe, H., & Sariciftci, N. S. (2004). Organic solar cells: An overview. J. Mater. Res, 19(7), 1925.

[9] Sariciftci, N. S., Braun, D., Zhang, C., et.al. (1993). Semiconducting polymer-buckminsterfullerene heterojunctions: Diodes, photodiodes, and photovoltaic cells. Applied physics letters, 62(6), 585-587.

[10] Reisdorffer, F., Haas, O., Le Rendu, P., & Nguyen, T. P. (2012). Co-solvent effects on the morphology of P3HT: PCBM thin films. Synthetic Metals, 161(23), 2544-2548.

[11] Gregg, B. A., & Hanna, M. C. (2003). Comparing organic to inorganic photovoltaic cells: Theory, experiment, and simulation. Journal of Applied Physics, 93(6), 3605-3614.

[12] Mayer, A. C., Scully, S. R., Hardin, B. E., et.al. (2007). Polymer-based solar cells. Materials today, 10(11), 28-33.

[13] W. Brütting, " Introduction to the physics of organic semiconductors," in Physics of organic semiconductors, KGaA, Weinheim, Wiely-VCH Verleg GmbH& Co., 2006, pp. 1-14.

[14] Kadem, B., Hassan, A., & Cranton, W. Performance optimization of P3HT: PCBM solar cells by controlling active layer thickness. In Proceedings of the 31st European photovoltaic solar energy conference and exhibition, EUPVSEC (2015, Hamburg, Germany).

[15] Mozer, A. J., & Sariciftci, N. S. (2006). Conjugated polymer photovoltaic devices and materials. Comptes Rendus Chimie, 9(5), 568-577.

[16] Coakley, K. M., & McGehee, M. D. (2004). Conjugated polymer photovoltaic cells. Chemistry of materials, 16(23), 4533-4542.

[17] Nunzi, J. M. (2002). Organic photovoltaic materials and devices. Comptes Rendus Physique, 3(4), 523-542.

[18] Bundgaard, E., & Krebs, F. C. (2007). Low band gap polymers for organic photovoltaics. Solar Energy Materials and Solar Cells, 91(11), 954-985.

[19] Haskal, E. I., Shen, Z., Burrows, P. E., & Forrest, S. R. (1995). Excitons and exciton confinement in crystalline organic thin films grown by organic molecular-beam deposition. Physical Review B, 51(7), 4449.

[20] Li, K., Shen, Y., Majumdar, N., et.al. (2010). Determination of free polaron lifetime in organic bulk heterojunction solar cells by transient time analysis. Journal of Applied Physics, 108(8), 084511.

[21] Yu, P., Mencaraglia, D., Darga, A., et.al. (2010). Investigation of electric charge transport in conjugated polymer P3HT: PCBM solar cell with temperature dependent current and capacitance measurements. physica status solidi (c), 7(3-4), 1000-1004.

[22] Yue, G., Wu, J., Xiao, et.al. (2011). Flexible dye-sensitized solar cell based on PCBM/P3HT heterojunction. Chinese Science Bulletin, 56(3), 325-330.

[23] Mahmoud, A. Y., Zhang, J., Ma, D.,et.al. (2013). Thickness dependent enhanced efficiency of polymer solar cells with gold nanorods embedded in the photoactive layer. Solar energy materials and solar cells, 116, 1-8.

[24] Benanti, T. L., & Venkataraman, D. (2006). Organic solar cells: an overview focusing on active layer morphology. Photosynthesis research, 87(1), 73-81.

[25] Halls, J. J. M., Walsh, C. A., Greenham, N. C., et.al. (1995). Efficient photodiodes from interpenetrating polymer networks.

[26] Yu, G., Gao, J., Hummelen, J. C., et.al. (1995). Polymer photovoltiac cells: Enhanced efficiencies via a network of internal donor-acceptor heterojunctions. Science, 270(5243), 1789.

[27] N. S. &. H. A. J. Sariciftci.Washington DC: U.S./ Patent and Trademark Office. Patent 5,331,183., 1994.

[28] C. J. Brabec, "Organic photovoltaics: technology and market," Solar energy materials and solar cells, 83(2), pp. 273-292., 2004.

[29] Blom, P. W., Mihailetchi, V. D., Koster, L. J. A., & Markov, D. E. (2007). Device physics of polymer: fullerene bulk heterojunction solar cells. Advanced Materials, 19(12), 1551-1566.

[30] Pivrikas, A., Sariciftci, N. S., Juška, G., & Österbacka, R. (2007). A review of charge transport and recombination in polymer/fullerene organic solar cells. Progress in Photovoltaics: Research and Applications, 15(8), 677-696.

[31] Dennler, G., Scharber, M. C., & Brabec, C. J. (2009). Polymer-Fullerene bulk-heterojunction solar cells. Advanced Materials, 21(13), 1323-1338.

[32] Ameri, T., Dennler, G., Lungenschmied, C., & Brabec, C. J. (2009). Organic tandem solar cells: a review. Energy & Environmental Science, 2(4), 347-363.

[33] Helgesen, M., Søndergaard, R., & Krebs, F. C. (2010). Advanced materials and processes for polymer solar cell devices. Journal of Materials Chemistry, 20(1), 36-60.

[34] Lu, L., Zheng, T., Wu, Q., et.al. (2015). Recent advances in bulk heterojunction polymer solar cells. Chemical Reviews, 115(23), 12666-12731.

[35] Servaites, J. D., Ratner, M. A., & Marks, T. J. (2011). Organic solar cells: a new look at traditional models. Energy & Environmental Science, 4(11), 4410-4422.

[36] Wienk, M. M., Kroon, J. M., Verhees, W. J., et.al. (2003). Efficient methano [70] fullerene/MDMO-PPV bulk heterojunction photovoltaic cells. Angewandte Chemie, 115(29), 3493-3497.

[37] Shaheen, S. E., Brabec, C. J., Sariciftci, N. S., et.al. (2001). 2.5% efficient organic plastic solar cells. Applied Physics Letters, 78(6), 841-843.

[38] Thompson, B. C., Kim, Y. G., McCarley, T. D., & Reynolds, J. R. (2006). Soluble narrow band gap and blue propylenedioxythiophene-cyanovinylene polymers as multifunctional materials for photovoltaic and electrochromic applications. Journal of the American Chemical Society, 128(39), 12714-12725.

[39] Schilinsky, P., Waldauf, C., & Brabec, C. J. (2002). Recombination and loss analysis in polythiophene based bulk heterojunction photodetectors. Applied Physics Letters, 81(20), 3885-3887.

[40] Padinger, F., Rittberger, R. S., & Sariciftci, N. S. (2003). Effects of postproduction treatment on plastic solar cells. Advanced Functional Materials, 13(1), 85-88.

[41] Kiriy, A., Senkovskyy, V., & Sommer, M. (2011). Kumada Catalyst-Transfer Polycondensation: Mechanism, Opportunities, and Challenges. Macromolecular rapid communications, 32(19), 1503-1517.

[42] Zhao, D. W., Kyaw, A. K. K., & Sun, X. W. (2011). Organic Solar Cells with Inverted and Tandem Structures. In Energy Efficiency and Renewable Energy Through Nanotechnology (pp. 115-170). Springer London.

[43] Lin, Y. H., Tsai, Y. T., Wu, C. C., et.al. (2012). Comparative study of spectral and morphological properties of blends of P3HT with PCBM and ICBA. Organic Electronics, 13(11), 2333-2341.

[44] Li, Y., Yue, G., Chen, X., et.al. (2013). Application of poly (3, 4-ethylenedioxythiophene): polystyrenesulfonate in polymer heterojunction solar cells. Journal of Materials Science, 48(9), 3528-3534.

[45] Holliday, S., Ashraf, R. S., Wadsworth, A., et.al. (2016). High-efficiency and air-stable P3HT-based polymer solar cells with a new non-fullerene acceptor. Nature communications, 7.

[46] Roncali, J. (2007). Molecular engineering of the band gap of π-conjugated systems: Facing technological applications. Macromolecular Rapid Communications, 28(17), 1761-1775.

[47] Kim, J. Y., Kim, S. H., Lee, H. H., et.al. (2006). New Architecture for high-efficiency polymer photovoltaic cells using solution-based titanium oxide as an optical spacer. Advanced materials, 18(5), 572-576.

[48] Ma, W., Yang, C., Gong, X., et.al. (2005). Thermally stable, efficient polymer solar cells with nanoscale control of the interpenetrating network morphology. Advanced Functional Materials, 15(10), 1617-1622.

[49] Kim, Y., Cook, S., Tuladhar, S. M., et.al. (2006). A strong regioregularity effect in self-organizing conjugated polymer films and high-efficiency polythiophene: fullerene solar cells. Nature materials, 5(3), 197-203.

[50] Mauer, R., Kastler, M., & Laquai, F. (2010). The impact of polymer regioregularity on charge transport and efficiency of P3HT: PCBM photovoltaic devices. Advanced Functional Materials, 20(13), 2085-2092.

[51] Li, G., Shrotriya, V., Huang, J., et.al. (2005). High-efficiency solution processable polymer photovoltaic cells by self-organization of polymer blends. Nature materials, 4(11), 864-868.

[52] Brown, P. J., Thomas, D. S., Köhler, A., et.al. (2003). Effect of interchain interactions on the absorption and emission of poly (3-hexylthiophene). Physical Review B, 67(6), 064203.

[53] McCullough, R. D., Lowe, R. D., Jayaraman, M., & Anderson, D. L. (1993). Design, synthesis, and control of conducting polymer architectures: structurally homogeneous poly (3-alkylthiophenes). The Journal of Organic Chemistry, 58(4), 904-912.

[54] Chen, T. A., Wu, X., & Rieke, R. D. (1995). Regiocontrolled synthesis of poly (3-alkylthiophenes) mediated by Rieke zinc: their characterization and solid-state properties. Journal of the American Chemical Society, 117(1), 233-244.

[55] Zhokhavets, U., Erb, T., Hoppe, H., et.al. (2006). Effect of annealing of poly (3-hexylthiophene)/fullerene bulk heterojunction composites on structural and optical properties. Thin Solid Films, 496(2), 679-682.

[56] Park, J. H., Kim, J. S., Lee, J. H.,et.al. (2009). Effect of annealing solvent solubility on the performance of poly (3-hexylthiophene)/methanofullerene solar cells. The Journal of Physical Chemistry C, 113(40), 17579-17584.

[57] Fell, H. J., Samuelsen, E. J., Als-Nielsen, J., et.al. (1995). Unexpected orientational effects in spin-cast, sub-micron layers of poly (alkylthiophene) s: A diffraction study with synchrotron radiation. Solid state communications, 94(10), 843-846.

[58] DeLongchamp, D. M., Vogel, B. M., Jung, Y., et.al. (2005). Variations in semiconducting polymer microstructure and hole mobility with spin-coating speed. Chemistry of materials, 17(23), 5610-5612.

[59] Boland, P., Lee, K., & Namkoong, G. (2010). Device optimization in PCPDTBT: PCBM plastic solar cells. Solar Energy Materials and Solar Cells, 94(5), 915-920.

[60] Park, S. H., Roy, A., Beaupre, S., et.al. (2009). Bulk heterojunction solar cells with internal quantum efficiency approaching 100&percnt. Nature photonics, 3(5), 297-302.

[61] Chu, T. Y., Alem, S., Tsang, S. W., et.al. (2011). Morphology control in polycarbazole based bulk heterojunction solar cells and its impact on device performance. Applied Physics Letters, 98(25), 253301.

[62] Wang, T., Pearson, A. J., Dunbar, A. D., et.al. (2012). Correlating structure with function in thermally annealed PCDTBT: PC70BM photovoltaic blends. Advanced Functional Materials, 22(7), 1399-1408.

[63] Staniec, P. A., Parnell, A. J., Dunbar, A. D., et.al. (2011). The nanoscale morphology of a PCDTBT: PCBM photovoltaic blend. Advanced Energy Materials, 1(4), 499-504.

[64] Seo, J. H., Gutacker, A., Sun, Y., et.al. (2011). Improved high-efficiency organic solar cells via incorporation of a conjugated polyelectrolyte interlayer. Journal of the American Chemical Society, 133(22), 8416-8419.

[65] Moon, J. S., Jo, J., & Heeger, A. J. (2012). Nanomorphology of PCDTBT: PC70BM bulk heterojunction solar cells. Advanced Energy Materials, 2(3), 304-308.

[66] Liu, J., Shao, S., Fang, G., et.al. (2012). High-Efficiency Inverted Polymer Solar Cells with Transparent and Work-Function Tunable MoO3-Al Composite Film as Cathode Buffer Layer. Advanced Materials, 24(20), 2774-2779.

[67] Clarke, T. M., Peet, J., Nattestad, A., et.al. (2012). Charge carrier mobility, bimolecular recombination and trapping in polycarbazole copolymer: fullerene (PCDTBT: PCBM) bulk heterojunction solar cells. Organic Electronics, 13(11), 2639-2646.

[68] Gusain, A., Chauhan, A. K., Jha, P., et.al. (2015, June). Efficiency enhancement in PCDTBT: PCBM solar cells using graphene nanosheets. In SOLID STATE PHYSICS: Proceedings of the 59th DAE Solid State Physics Symposium 2014 (Vol. 1665, No. 1, p. 050122). AIP Publishing.

[69] Li, Z., Chiu, K. H., Ashraf, R. S., et.al. (2015). Toward Improved Lifetimes of Organic Solar Cells under Thermal Stress: Substrate-Dependent Morphological Stability of PCDTBT: PCBM Films and Devices. Scientific reports, 5.

[70] Zhang, Y., Bovill, E., Kingsley, J., et.al. (2016). PCDTBT based solar cells: one year of operation under real-world conditions. Scientific reports, 6.

[71] Sharma, V., Singh, V., Arora, M., et.al. (2016). Degradation analysis of PCDTBT: PC 71 BM organic solar cells-an insight. Current Applied Physics, 16(3), 273-277.

[72] Yang, S., Zhang, Y., Jiang, T., et.al. (2014). Enhancing the power conversion efficiency of PCDTBT: PC71BM polymer solar cells using a mixture of solvents. Chinese Science Bulletin, 59(3), 297-300.

[73] Marsh, R. A., Hodgkiss, J. M., Albert-Seifried, S., & Friend, R. H. (2010). Effect of annealing on P3HT: PCBM charge transfer and nanoscale morphology probed by ultrafast spectroscopy. Nano letters, 10(3), 923-930.

[74] Shin, P. K., Kumar, P., Kumar, A., et.al. (2014). Effects of organic solvents for composite active layer of PCDTBT/PC71BM on characteristics of organic solar cell devices. International journal of photoenergy, 2014.

[75] Kannappan, S., Palanisamy, K., Tatsugi, J., et.al. (2013). Fabrication and characterizations of PCDTBT: PC71BM bulk heterojunction solar cell using air brush coating method. Journal of Materials Science, 48(6), 2308-2317.

[76] Chang, S. Y., Liao, H. C., Shao, Y. T., et.al. (2013). Enhancing the efficiency of low band gap conducting polymer bulk heterojunction solar cells using P3HT as a morphology control agent. Journal of Materials Chemistry A, 1(7), 2447-2452.

[77] Koppe, M., Egelhaaf, H. J., Dennler, G., et.al. (2010). Near IR sensitization of organic bulk heterojunction solar cells: towards optimization of the spectral response of organic solar cells. Advanced Functional Materials, 20(2), 338-346.

[78] Braun, C. L. (1984). Electric field assisted dissociation of charge transfer states as a mechanism of photocarrier production. The Journal of chemical physics, 80(9), 4157-4161.

[79] Jamieson, F. C., Agostinelli, T., Azimi, H., et.al. (2010). Field-independent charge photogeneration in PCPDTBT/PC70BM solar cells. The Journal of Physical Chemistry Letters, 1(23), 3306-3310.

[80] Albrecht, S., Schäfer, S., Lange, I., et.al. (2012). Light management in PCPDTBT: PC 70 BM solar cells: A comparison of standard and inverted device structures. Organic Electronics, 13(4), 615-622.

[81] Haidari, G., Hajimahmoodzadeh, M., Fallah, H. R., et.al. (2015). Thermally evaporated Ag nanoparticle films for plasmonic enhancement in organic solar cells: effects of particle geometry. physica status solidi (RRL)-Rapid Research Letters, 9(3), 161-165.

[82] Kettle, J., Waters, H., Horie, M., & Smith, G. C. (2016). Alternative selection of processing additives to enhance the lifetime of OPVs. Journal of Physics D: Applied Physics, 49(8), 085601.

[83] Haidari, G., Hajimahmoodzadeh, M., Fallah, H. R., & Varnamkhasti, M. G. (2015). Effective medium analysis of thermally evaporated Ag nanoparticle films for plasmonic enhancement in organic solar cell. Superlattices and Microstructures, 85, 294-304.

[84] Morana, M., Wegscheider, M., Bonanni, A., et.al. (2008). Bipolar Charge Transport in PCPDTBT-PCBM Bulk-Heterojunctions for Photovoltaic Applications. Advanced Functional Materials, 18(12), 1757-1766.

[85] Mühlbacher, D., Scharber, M., Morana, M., et.al. (2006). High photovoltaic performance of a low-band gap polymer. Advanced Materials, 18(21), 2884-2889.

[86] Peet, J., Kim, J. Y., Coates, N. E., et.al. (2007). Efficiency enhancement in low-band gap polymer solar cells by processing with alkane dithiols. Nature materials, 6(7), 497-500.

[87] Lee, J. K., Ma, W. L., Brabec, C. J., et.al. (2008). Processing additives for improved efficiency from bulk heterojunction solar cells. Journal of the American Chemical Society, 130(11), 3619-3623.

[88] Dante, M., Garcia, A., & Nguyen, T. Q. (2009). Three-dimensional nanoscale organization of highly efficient low band-gap conjugated polymer bulk heterojunction solar cells. The Journal of Physical Chemistry C, 113(4), 1596-1600.

[89] Liang, Y., Xu, Z., Xia, J., et.al. (2010). For the bright future—bulk heterojunction polymer solar cells with power conversion efficiency of 7.4%. Advanced Materials, 22(20).

[90] He, Z., Zhong, C., Su, S., et.al. (2012). Enhanced power-conversion efficiency in polymer solar cells using an inverted device structure. Nature Photonics, 6(9), 591-595.

[91] Taima, T., Tanaka, J., Kuwabara, T., & Takahashi, K. (2016). Insertion of interlayers in efficient polymer-based organic solar cells for control of phase separation. Japanese Journal of Applied Physics, 55(2S), 02BF03.

[92] Li, Y., Xu, Z., Zhao, S., et.al. (2016). Enhanced carrier dynamics of PTB7: PC 71 BM based bulk heterojunction organic solar cells by the incorporation of formic acid. Organic Electronics, 28, 275-280.

[93] Wang, H., Huang, J., Xing, S., & Yu, J. (2016). Improved mobility and lifetime of carrier for highly efficient ternary polymer solar cells based on TIPS-pentacene in PTB7: PC 71 BM. Organic Electronics, 28, 11-19.

[94] He, Z., Xiao, B., Liu, F., et.al. (2015). Single-junction polymer solar cells with high efficiency and photovoltage. Nature Photonics, 9(3), 174-179.

[95] Zhou, H., Zhang, Y., Seifter, J., et.al. (2013). High-efficiency polymer solar cells enhanced by solvent treatment. Advanced Materials, 25(11), 1646-1652.

[96] Brabec, C. J., Cravino, A., Meissner, D., et.al. (2001). Origin of the open circuit voltage of plastic solar cells. Advanced Functional Materials, 11(5), 374-380.

[97] Kniepert, J., Lange, I., Heidbrink, J., et.al. (2015). Effect of solvent additive on generation, recombination, and extraction in PTB7: PCBM solar cells: A conclusive experimental and numerical simulation study. The Journal of Physical Chemistry C, 119(15), 8310-8320.

[98] Collins, B. A., Li, Z., Tumbleston, J. R., et.al. (2013). Absolute measurement of domain composition and nanoscale size distribution explains performance in PTB7: PC71BM solar cells. Advanced Energy Materials, 3(1), 65-74.

[99] Chen, J. D., Cui, C., Li, Y. Q., et.al. (2015). Single-Junction Polymer Solar Cells Exceeding 10% Power Conversion Efficiency. Advanced Materials, 27(6), 1035-1041.

[100] Zhang, J., Zhang, Y., Fang, J., et.al. (2015). Conjugated polymer–small molecule alloy leads to high efficient ternary organic solar cells. Journal of the American Chemical Society, 137(25), 8176-8183.

[101] Lu, L., Chen, W., Xu, T., & Yu, L. (2015). High-performance ternary blend polymer solar cells involving both energy transfer and hole relay processes. Nature communications, 6.

[102] Yang, L., Zhou, H., Price, S. C., & You, W. (2012). Parallel-like bulk heterojunction polymer solar cells. Journal of the American Chemical Society, 134(12), 5432-5435.

[103] Khlyabich, P. P., Burkhart, B., & Thompson, B. C. (2012). Compositional dependence of the open-circuit voltage in ternary blend bulk heterojunction solar cells based on two donor polymers. Journal of the American Chemical Society, 134(22), 9074-9077.

[104] Cha, H., Chung, D. S., Bae, S. Y., et.al. (2013). Complementary Absorbing Star-Shaped Small Molecules for the Preparation of Ternary Cascade Energy Structures in Organic Photovoltaic Cells. Advanced Functional Materials, 23(12), 1556-1565.

[105] Zuo, C., & Ding, L. (2015). Bulk heterojunctions push the photoresponse of perovskite solar cells to 970 nm. Journal of Materials Chemistry A, 3(17), 9063-9066.

[106] Zhang, S., Ye, L., Zhao, W., et.al. (2015). Realizing over 10% efficiency in polymer solar cell by device optimization. Science China Chemistry, 58(2), 248-256.

[107] Hoke, E. T., Vandewal, K., Bartelt, J. A., et.al. (2013). Recombination in Polymer: Fullerene Solar Cells with Open-Circuit Voltages Approaching and Exceeding 1.0 V. Advanced Energy Materials, 3(2), 220-230.

[108] Terao, Y., Sasabe, H., & Adachi, C. (2007). Correlation of hole mobility, exciton diffusion length, and solar cell characteristics in phthalocyanine/fullerene organic solar cells. Applied Physics Letters, 90(10).

[109] Lim, K., Jung, S., Kim, J. K., et.al. (2013). Flexible PEDOT: PSS/ITO hybrid transparent conducting electrode for organic photovoltaics. Solar Energy Materials and Solar Cells, 115, 71-78.

[110] Zhao, G., He, Y., & Li, Y. (2010). 6.5% Efficiency of polymer solar cells based on poly (3-hexylthiophene) and indene-C60 bisadduct by device optimization. Advanced Materials, 22(39), 4355-4358.

[111] Jiang, L., Li, A., Deng, X., et.al. (2013). Effects of cathode modification using spin-coated lithium acetate on the performances of polymer bulk-heterojunction solar cells. Applied Physics Letters, 102(1), 013303.

[112] Hu, Z., Zhang, J., & Zhu, Y. (2014). Effects of solvent-treated PEDOT: PSS on organic photovoltaic devices. Renewable Energy, 62, 100-105.

[113] Yang, Z., Ren, J., Zhang, Z., et.al. (2015). Recent advancement of nanostructured carbon for energy applications. Chemical reviews, 115(11), 5159-5223.

[114] Dai, L., Chang, D. W., Baek, J. B., & Lu, W. (2012). Carbon nanomaterials for advanced energy conversion and storage. small, 8(8), 1130-1166.

[115] Geim, A. K., & Novoselov, K. S. (2007). The rise of graphene. Nature materials, 6(3), 183-191.

[116] Li, S. S., Tu, K. H., Lin, C. C., et.al. (2010). Solution-processable graphene oxide as an efficient hole transport layer in polymer solar cells. ACS nano, 4(6), 3169-3174.

[117] Jeon, Y. J., Yun, J. M., Kim, D. Y., et.al. (2012). High-performance polymer solar cells with moderately reduced graphene oxide as an efficient hole transporting layer. Solar Energy Materials and Solar Cells, 105, 96-102.

[118] Valentini, L., Cardinali, M., Bon, S. B., et.al. (2010). Use of butylamine modified graphene sheets in polymer solar cells. Journal of Materials Chemistry, 20(5), 995-1000.

[119] Liu, J., Xue, Y., & Dai, L. (2012). Sulfated graphene oxide as a hole-extraction layer in high-performance polymer solar cells. The journal of physical chemistry letters, 3(14), 1928-1933.

[120] Liu, J., Kim, G. H., Xue, Y., et.al. (2014). Graphene oxide nanoribbon as hole extraction layer to enhance efficiency and stability of polymer solar cells. Advanced Materials, 26(5), 786-790.

[121] Liu, J., Xue, Y., Gao, Y., et.al. (2012). Hole and Electron Extraction Layers Based on Graphene Oxide Derivatives for High-Performance Bulk Heterojunction Solar Cells. Advanced Materials, 24(17), 2228-2233.

[122] Brennan, L. J., Byrne, M. T., Bari, M., & Gun'ko, Y. K. (2011). Carbon Nanomaterials for Dye-Sensitized Solar Cell Applications: A Bright Future. Advanced Energy Materials, 1(4), 472-485.

[123] Wang, X., Li, Q., Xie, J., et.al. (2009). Fabrication of ultralong and electrically uniform single-walled carbon nanotubes on clean substrates. Nano letters, 9(9), 3137-3141.

[124] Landi, B. J., Raffaelle, R. P., Castro, S. L., & Bailey, S. G. (2005). Single-wall carbon nanotube–polymer solar cells. Progress in photovoltaics: research and applications, 13(2), 165-172.

[125] Cataldo, S., Salice, P., Menna, E., & Pignataro, B. (2012). Carbon nanotubes and organic solar cells. Energy & Environmental Science, 5(3), 5919-5940.

[126] Zhang, H., Xu, M., Cui, R., et.al. (2013). Enhanced performance of inverted organic photovoltaic cells using CNTs–TiOX nanocomposites as electron injection layer. Nanotechnology, 24(35), 355401.

[127] Li, J., Sham, M. L., Kim, J. K., & Marom, G. (2007). Morphology and properties of UV/ozone treated graphite nanoplatelet/epoxy nanocomposites. Composites Science and Technology, 67(2), 296-305.

[128] Yan, J., Ni, T., Zou, F.,et.al. (2014). Towards optimization of functionalized single-walled carbon nanotubes adhering with poly (3-hexylthiophene) for highly efficient polymer solar cells. Diamond and Related Materials, 41, 79-83.

[129] Bindl, D. J., Safron, N. S., & Arnold, M. S. (2010). Dissociating excitons photogenerated in semiconducting carbon nanotubes at polymeric photovoltaic heterojunction interfaces. ACS nano, 4(10), 5657-5664.

[130] Lu, L., Xu, T., Chen, W.,et.al. (2013). The role of N-doped multiwall carbon nanotubes in achieving highly efficient polymer bulk heterojunction solar cells. Nano letters, 13(6), 2365-2369.

[131] He, Y., Chen, H. Y., Hou, J., & Li, Y. (2010). Indene− C60 bisadduct: a new acceptor for high-performance polymer solar cells. Journal of the American Chemical Society, 132(4), 1377-1382.

[132] Zhang, F., Zhuo, Z., Zhang, J., et.al. (2012). Influence of PC 60 BM or PC 70 BM as electron acceptor on the performance of polymer solar cells. Solar Energy Materials and Solar Cells, 97, 71-77.

[133] Pfattner, R., Rovira, C., & Mas-Torrent, M. (2015). Organic metal engineering for enhanced field-effect transistor performance. Physical Chemistry Chemical Physics, 17(40), 26545-26552.

[134] Kadem, B., & Hassan, A. (2015). The effect of fullerene derivatives ratio on P3HT-based organic solar cells. Energy Procedia, 74, 439-445.

[135] Kadem, B., Hassan, A. & Cranton W. " P3HT:PCBM-based organic solar cells: the effects of different PCBM derivatives," in Proceeding of 32nd European Photovoltaic Solar Energy Conference and Exhibition (EUPVSEC2016), Munich-Germany, 2016.

[136] He, Y., & Li, Y. (2011). Fullerene derivative acceptors for high performance polymer solar cells. Physical chemistry chemical physics, 13(6), 1970-1983.

[137] Lampande, R., Kim, G. W., Boizot, J., et.al. (2013). A highly efficient transition metal oxide layer for hole extraction and transport in inverted polymer bulk heterojunction solar cells. Journal of Materials Chemistry A, 1(23), 6895-6900.

[138] Khurelbaatar, Z., Shim, K. H., Cho, J., et.al. (2015). Temperature Dependent Current-Voltage and Capacitance-Voltage Characteristics of an Au/n-Type Si Schottky Barrier Diode Modified Using a PEDOT: PSS Interlayer. Materials Transactions, 56(1), 10-16.

[139] Guerrero, A., Marchesi, L. F., Boix, P. P., et.al. (2012). How the charge-neutrality level of interface states controls energy level alignment in cathode contacts of organic bulk-heterojunction solar cells. ACS nano, 6(4), 3453-3460.

[140] Yakuphanoglu, F., & Anand, R. S. (2010). Charge transport properties of an organic solar cell. Synthetic Metals, 160(21), 2250-2254.

[141] Lou, Y., Wang, Z., Naka, S., & Okada, H. (2012). Charge transport characteristics in P3HT: PCBM organic blends under illumination: Influence of metal work functions. Chemical Physics Letters, 529, 64-68.

[142] Qi, B., Zhou, Q., & Wang, J. (2015). Exploring the open-circuit voltage of organic solar cells under low temperature. Scientific reports, 5.

[143] Kadem, B. Y., Al-hashimi, M. K., & Hassan, A. K. (2014). The effect of solution processing on the power conversion efficiency of P3HT-based organic solar cells. Energy Procedia, 50, 237-245.

[144] Kadem, B. Y., Hassan, A. K., & Cranton, W. (2016, July). The effects of organic solvents and their co-solvents on the optical, structural, morphological of P3HT: PCBM organic solar cells. In AIP Conference Proceedings (Vol. 1758, No. 1, p. 020006). AIP Publishing.

[145] Mihailetchi, V. D., Xie, H., de Boer, B., et.al. (2006). Origin of the enhanced performance in poly (3-hexylthiophene):[6, 6]-phenyl C~ 6~ 1-butyric acid methyl ester solar cells upon slow drying of the active layer. Applied physics letters, 89(1), 12107-12107.

[146] Zhang, F., Jespersen, K. G., Björström, C., et.al. (2006). Influence of solvent mixing on the morphology and performance of solar cells based on polyfluorene copolymer/fullerene blends. Advanced Functional Materials, 16(5), 667-674.

[147] Hoth, C. N., Schilinsky, P., Choulis, S. A., & Brabec, C. J. (2008). Printing highly efficient organic solar cells. Nano letters, 8(9), 2806-2813.

[148] Morvillo, P., Grimaldi, I. A., Diana, R., et.al. (2013). Study of the microstructure of inkjet-printed P3HT: PCBM blend for photovoltaic applications. Journal of Materials Science, 48(7), 2920-2927.

[149] Motaung, D. E., Malgas, G. F., & Arendse, C. J. (2010). Comparative study: The effects of solvent on the morphology, optical and structural features of regioregular poly (3-hexylthiophene): fullerene thin films. Synthetic Metals, 160(9), 876-882.

[150] Sun, Y., Liu, J. G., & Ding, Y. (2013). Controlling the surface composition of PCBM in P3HT/PCBM blend films by using mixed solvents with different evaporation rates. Chinese Journal of Polymer Science, 31(7), 1029-1037.

[151] Jang, S. K., Gong, S. C., & Chang, H. J. (2012). Effects of various solvent addition on crystal and electrical properties of organic solar cells with P3HT: PCBM active layer. Synthetic Metals, 162(5), 426-430.

[152] Yusli, M. N., Yun, T. W., & Sulaiman, K. (2009). Solvent effect on the thin film formation of polymeric solar cells. Materials Letters, 63(30), 2691-2694.

[153] Tang, H., Lu, G., Li, L.,et.al. (2010). Precise construction of PCBM aggregates for polymer solar cells via multi-step controlled solvent vapor annealing. Journal of Materials Chemistry, 20(4), 683-688.

[154] Yip, H. L., & Jen, A. K. Y. (2012). Recent advances in solution-processed interfacial materials for efficient and stable polymer solar cells. Energy & Environmental Science, 5(3), 5994-6011.

[155] Chen, M., Pei, Z. L., Sun, C., et.al. (2001). ZAO: an attractive potential substitute for ITO in flat display panels. Materials Science and Engineering: B, 85(2), 212-217.

[156] Chen, D., Liu, F., Wang, C., et.al. (2011). Bulk heterojunction photovoltaic active layers via bilayer interdiffusion. Nano letters, 11(5), 2071-2078.

[157] Hau, S. K., O'Malley, K. M., Cheng, Y. J., et.al. (2010). Optimization of active layer and anode electrode for high-performance inverted bulk-heterojunction solar cells. IEEE Journal of Selected Topics in Quantum Electronics, 16(6), 1665-1675.

[158] Chen, C. Y., Retamal, J. R. D., Wu, I. W., et.al. (2012). Probing surface band bending of surface-engineered metal oxide nanowires. Acs Nano, 6(11), 9366-9372.

[159] Lee, J. H., Ko, K. H., & Park, B. O. (2003). Electrical and optical properties of ZnO transparent conducting films by the sol–gel method. Journal of Crystal Growth, 247(1), 119-125.

[160] Jouane, Y., Colis, S., Schmerber, G., et.al. (2011). Room temperature ZnO growth by rf magnetron sputtering on top of photoactive P3HT: PCBM for organic solar cells. Journal of Materials Chemistry, 21(6), 1953-1958.

[161] Beek, W. J., Wienk, M. M., & Janssen, R. A. (2005). Hybrid polymer solar cells based on zinc oxide. Journal of Materials chemistry, 15(29), 2985-2988.

[162] Özgür, Ü., Alivov, Y. I., Liu, C., et.al. (2005). A comprehensive review of ZnO materials and devices. Journal of applied physics, 98(4), 041301.

[163] Sazonov, A., Striakhilev, D., Lee, C. H., & Nathan, A. (2005). Low-temperature materials and thin film transistors for flexible electronics. Proceedings of the IEEE, 93(8), 1420-1428.

[164] Nam, J., Lee, Y., Choi, W., et.al. (2016). Transfer Printed Flexible and Stretchable Thin Film Solar Cells Using a Water-Soluble Sacrificial Layer. Advanced Energy Materials, 6(21).

[165] Lin, M. Y., Wu, S. H., Kang, Y. L., et.al. (2016, July). ITO-free inverted small molecule solar cells. In Active-Matrix Flatpanel Displays and Devices (AMFPD), 2016 The 23rd International Workshop on Active-Matrix Flatpanel Displays and Devices (pp. 243-245). IEEE.

[166] Gaceur, M., Dkhil, S. B., Duché, D., et.al. (2016). Ligand-Free Synthesis of Aluminum-Doped Zinc Oxide Nanocrystals and their Use as Optical Spacers in Color-Tuned Highly Efficient Organic Solar Cells. Advanced Functional Materials, 26(2), 243-253.

[167] Lin, Y., Xie, J., Wang, H., et.al. (2005). Green luminescent zinc oxide films prepared by polymer-assisted deposition with rapid thermal process. Thin Solid Films, 492(1), 101-104.

[168] Tsai, S. H., Ho, S. T., Jhuo, H. J., et.al. (2013). Toward high efficiency of inverted organic solar cells: Concurrent improvement in optical and electrical properties of electron transport layers. Applied Physics Letters, 102(25), 253111.

[169] Bekci, D. R., Karsli, A., Cakir, A. C., et.al. (2012). Comparison of ZnO interlayers in inverted bulk heterojunction solar cells. Applied energy, 96, 417-421.

[170] Lee, B. R., Jung, E. D., Nam, Y. S., et.al. (2014). Amine-Based Polar Solvent Treatment for Highly Efficient Inverted Polymer Solar Cells. Advanced Materials, 26(3), 494-500.

[171] He, Z., Zhong, C., Huang, X., et.al. (2011). Simultaneous enhancement of open-circuit voltage, short-circuit current density, and fill factor in polymer solar cells. Advanced Materials, 23(40), 4636-4643.

[172] He, Z., Zhang, C., Xu, X., et.al. (2011). Largely enhanced efficiency with a PFN/Al bilayer cathode in high efficiency bulk heterojunction photovoltaic cells with a low band gap polycarbazole donor. Advanced Materials, 23(27), 3086-3089.

[173] Liu, Z., Tian, M., & Wang, N. (2014). Influences of Alq 3 as electron extraction layer instead of Ca on the photo-stability of organic solar cells. Journal of Power Sources, 250, 105-109.

[174] Kadem, B. Y., Hassan, A. K., & Cranton, W. (2015). Enhancement of power conversion efficiency of P3HT: PCBM solar cell using solution processed Alq3 film

as electron transport layer. Journal of Materials Science: Materials in Electronics, 26(6), 3976-3983.

[175] Lassiter, B. E., Wei, G., Wang, S., et.al. (2011). Organic photovoltaics incorporating electron conducting exciton blocking layers. Applied Physics Letters, 98(24), 243307.

[176] Song, Q. L., Li, F. Y., Yang, H., et.al. (2005). Small-molecule organic solar cells with improved stability. Chemical Physics Letters, 416(1), 42-46.

[177] Liu, C., Wang, K., Du, P., et.al. (2015). Efficient Solution-Processed Bulk Heterojunction Perovskite Hybrid Solar Cells. Advanced Energy Materials, 5(12).

[178] Wei, Q., Mukaida, M., Kirihara, K., et.al. (2015). Recent Progress on PEDOT-Based Thermoelectric Materials. Materials, 8(2), 732-750.

[179] Park, T., Park, C., Kim, B., et.al. (2013). Flexible PEDOT electrodes with large thermoelectric power factors to generate electricity by the touch of fingertips. Energy & Environmental Science, 6(3), 788-792.

[180] Khan, Z. U., Bubnova, O., Jafari, M. J., et.al. (2015). Acido-basic control of the thermoelectric properties of poly (3, 4-ethylenedioxythiophene) tosylate (PEDOT-Tos) thin films. Journal of Materials Chemistry C, 3(40), 10616-10623.

[181] Sangeeth, C. S., Jaiswal, M., & Menon, R. (2009). Correlation of morphology and charge transport in poly (3, 4-ethylenedioxythiophene)–polystyrenesulfonic acid (PEDOT–PSS) films. Journal of Physics: Condensed Matter, 21(7), 072101.

[182] Murray, I. P., Lou, S. J., Cote, L. J., et.al. (2011). Graphene oxide interlayers for robust, high-efficiency organic photovoltaics. The Journal of Physical Chemistry Letters, 2(24), 3006-3012.

[183] Xia, Y., & Ouyang, J. (2011). PEDOT: PSS films with significantly enhanced conductivities induced by preferential solvation with cosolvents and their application in polymer photovoltaic cells. Journal of Materials Chemistry, 21(13), 4927-4936.

[184] Woo, S., Lyu, H. K., Han, Y. S., & Kim, Y. (2013). Effects of Hole-Collecting Buffer Layers and Electrodes on the Performance of Flexible Plastic Organic Photovoltaics. International Journal of Photoenergy, 2013.

[185] Ko, C. J., Lin, Y. K., Chen, F. C., & Chu, C. W. (2007). Modified buffer layers for polymer photovoltaic devices. Applied Physics Letters, 90(6), 063509.

[186] Hu, Z., Zhang, J., Hao, Z., & Zhao, Y. (2011). Influence of doped PEDOT: PSS on the performance of polymer solar cells. Solar Energy Materials and Solar Cells, 95(10), 2763-2767.

[187] Xiao, T., Cui, W., Anderegg, J., et.al. (2011). Simple routes for improving polythiophene: fullerene-based organic solar cells. Organic Electronics, 12(2), 257-262.

[188] Sun, K., Xia, Y., & Ouyang, J. (2012). Improvement in the photovoltaic efficiency of polymer solar cells by treating the poly (3, 4-ethylenedioxythiophene): poly (styrenesulfonate) buffer layer with co-solvents of hydrophilic organic solvents and hydrophobic 1, 2-dichlorobenzene. Solar energy materials and solar cells, 97, 89-96.

[189] Kim, G. H., Song, H. K., & Kim, J. Y. (2011). The effect of introducing a buffer layer to polymer solar cells on cell efficiency. Solar Energy Materials and Solar Cells, 95(4), 1119-1122.

[190] Gong, C., Yang, H. B., Song, Q. L., et.al. (2012). Mechanism for dimethylformamide-treatment of poly (3, 4-ethylenedioxythiophene): poly (styrene sulfonate) layer to enhance short circuit current of polymer solar cells. Solar Energy Materials and Solar Cells, 100, 115-119.

[191] Jung, J. W., Lee, J. U., & Jo, W. H. (2009). High-efficiency polymer solar cells with water-soluble and self-doped conducting polyaniline graft copolymer as hole transport layer. The Journal of Physical Chemistry C, 114(1), 633-637.

[192] Ke, W. J., Lin, G. H., Hsu, C. P., et.al. (2011). Solution processable self-doped polyaniline as hole transport layer for inverted polymer solar cells. Journal of Materials Chemistry, 21(35), 13483-13489.

[193] Zhao, W., Ye, L., Zhang, S., et.al. (2014). Ultrathin polyaniline-based buffer layer for highly efficient polymer solar cells with wide applicability. Scientific reports, 4.

[194] Ke, W. J., Lin, G. H., Hsu, C. P., et.al. (2011). Solution processable self-doped polyaniline as hole transport layer for inverted polymer solar cells. Journal of Materials Chemistry, 21(35), 13483-13489.

[195] Li, C. Y., Wen, T. C., & Guo, T. F. (2008). Sulfonated poly (diphenylamine) as a novel hole-collecting layer in polymer photovoltaic cells. Journal of Materials Chemistry, 18(37), 4478-4482.

[196] Chaudhary, S., Lu, H., Müller, A. M., et.al. (2007). Hierarchical placement and associated optoelectronic impact of carbon nanotubes in polymer-fullerene solar cells. Nano Letters, 7(7), 1973-1979.

[197] Kim, J. S., Park, J. H., Lee, J. H.,et.al. (2007). Control of the electrode work function and active layer morphology via surface modification of indium tin oxide for high efficiency organic photovoltaics. Applied Physics Letters, 91(11), 112111.

[198] Kang, B., Tan, L. W., & Silva, S. R. P. (2008). Fluoropolymer indium-tin-oxide buffer layers for improved power conversion in organic photovoltaics. Applied physics letters, 93(13), 133302.

[199] Shrotriya, V., Li, G., Yao, Y., et.al. (2006). Transition metal oxides as the buffer layer for polymer photovoltaic cells. Applied Physics Letters, 88(7), 073508.

[200] Irwin, M. D., Buchholz, D. B., Hains, A. W., et.al. (2008). p-Type semiconducting nickel oxide as an efficiency-enhancing anode interfacial layer in polymer bulk-heterojunction solar cells. Proceedings of the National Academy of Sciences, 105(8), 2783-2787.

[201] Yoon, W. J., & Berger, P. R. (2008). 4.8% efficient poly (3-hexylthiophene)-fullerene derivative (1: 0.8) bulk heterojunction photovoltaic devices with plasma treated AgOx/indium tin oxide anode modification. Applied Physics Letters, 92(1), 013306.

[202] Zhang, F., Ceder, M., & Inganäs, O. (2007). Enhancing the photovoltage of polymer solar cells by using a modified cathode. Advanced Materials, 19(14), 1835-1838.

[203] Wei, Q., Nishizawa, T., Tajima, K., & Hashimoto, K. (2008). Self-Organized Buffer Layers in Organic Solar Cells. Advanced Materials, 20(11), 2211-2216.

[204] Park, M. H., Li, J. H., Kumar, A., Li, G., & Yang, Y. (2009). Doping of the metal oxide nanostructure and its influence in organic electronics. Advanced Functional Materials, 19(8), 1241-1246.

[205] Kumar, P., & Chand, S. (2012). Recent progress and future aspects of organic solar cells. Progress in Photovoltaics: Research and applications, 20(4), 377-415.

[206] Jain, S. C., Willander, M., & Kumar, V. (2011). Conducting organic materials and devices (Vol. 81). Newnes.

[207] Motaung, D. E., Malgas, G. F., Nkosi, S. S., et.al. (2013). Comparative study: the effect of annealing conditions on the properties of P3HT: PCBM blends. Journal of Materials Science, 48(4), 1763-1778.

[208] Ho, C. S., Huang, E. L., Hsu, W. C., et.al. (2012). Thermal effect on polymer solar cells with active layer concentrations of 3–5wt%. Synthetic Metals, 162(13), 1164-1168.

[209] Bagienski, W., & Gupta, M. C. (2011). Temperature dependence of polymer/fullerene organic solar cells. Solar Energy Materials and Solar Cells, 95(3), 933-941.

[210] Motaung, D. E., Malgas, G. F., Arendse, C. J., et.al. (2009). Thermal-induced changes on the properties of spin-coated P3HT: C 60 thin films for solar cell applications. Solar energy materials and solar cells, 93(9), 1674-1680.

[211] Duda, J. C., Hopkins, P. E., Shen, Y., & Gupta, M. C. (2013). Thermal transport in organic semiconducting polymers. Applied Physics Letters, 102(25), 251912.

[212] Al-Ibrahim, M., Ambacher, O., Sensfuss, S., & Gobsch, G. (2005). Effects of solvent and annealing on the improved performance of solar cells based on poly (3-hexylthiophene): fullerene. Applied Physics Letters, 86(20), 201120.

[213] Chirvase, D., Parisi, J., Hummelen, J. C., & Dyakonov, V. (2004). Influence of nanomorphology on the photovoltaic action of polymer? fullerene composites. Nanotechnology, 15(9), 1317.

[214] Li, G., Yao, Y., Yang, H., et.al. (2007). "Solvent Annealing" Effect in Polymer Solar Cells Based on Poly (3-hexylthiophene) and Methanofullerenes. Advanced Functional Materials, 17(10), 1636-1644.

[215] Wang, J. L., Liu, K. K., Yan, J., et.al. (2016). A Series of Multifluorine Substituted Oligomers for Organic Solar Cells with Efficiency over 9% and Fill Factor of 0.77 by Combination Thermal and Solvent Vapor Annealing. Journal of the American Chemical Society.

[216] Xie, Y., Zhou, W., Yin, J., et.al. (2016). Post-annealing to recover the reduced open-circuit voltage caused by solvent annealing in organic solar cells. Journal of Materials Chemistry A, 4(16), 6158-6166.

[217] Chen, F. C., Ko, C. J., Wu, J. L., & Chen, W. C. (2010). Morphological study of P3HT: PCBM blend films prepared through solvent annealing for solar cell applications. Solar Energy Materials and Solar Cells, 94(12), 2426-2430.

[218] Shrotriya, V., Li, G., Yao, Y., et.al. (2006). Accurate measurement and characterization of organic solar cells. Advanced Functional Materials, 16(15), 2016-2023.

[219] Wu, J., Yue, G., Xiao, Y., et.al. (2010). Application of a polymer heterojunction in dye-sensitized solar cells. Electrochimica Acta, 55(20), 5798-5802.

[220] Yi, H., Im, C., An, J., et.al. (2014). Acceptor blending ratio dependence of bulk heterojunction organic photovoltaic devices. Journal of the Korean Physical Society, 64(6), 910-916.

[221] Dante, M., Peet, J., & Nguyen, T. Q. (2008). Nanoscale charge transport and internal structure of bulk heterojunction conjugated polymer/fullerene solar cells by scanning probe microscopy. The Journal of Physical Chemistry C, 112(18), 7241-7249.

[222] Li, H., Zhang, Z. G., Li, Y., & Wang, J. (2012). Tunable open-circuit voltage in ternary organic solar cells. Applied Physics Letters, 101(16), 163302.

[223] Thompson, B. C., Kim, Y. G., & Reynolds, J. R. (2005). Spectral broadening in MEH-PPV: PCBM-based photovoltaic devices via blending with a narrow band gap cyanovinylene-dioxythiophene polymer. Macromolecules, 38(13), 5359-5362.

[224] Khlyabich, P. P., Burkhart, B., & Thompson, B. C. (2011). Efficient ternary blend bulk heterojunction solar cells with tunable open-circuit voltage. Journal of the American Chemical Society, 133(37), 14534-14537.

[225] Xu, Z. X., Roy, V. A. L., Low, K. H., & Che, C. M. (2011). Bulk heterojunction photovoltaic cells based on tetra-methyl substituted copper (II) phthalocyanine: P3HT: PCBM composite. Chemical Communications, 47(34), 9654-9656.

[226] Ameri, T., Khoram, P., Min, J., & Brabec, C. J. (2013). Organic ternary solar cells: a review. Advanced Materials, 25(31), 4245-4266.

[227] Ameri, T., Min, J., Li, N., et.al. (2012). Performance Enhancement of the P3HT/PCBM Solar Cells through NIR Sensitization Using a Small-Band gap Polymer. Advanced Energy Materials, 2(10), 1198-1202.

[228] Zhang, C., Tong, S. W., Jiang, C., et.al. (2008). Efficient multilayer organic solar cells using the optical interference peak. Applied Physics Letters, 93(4), 043307.

[229] Koppe, M., Egelhaaf, H. J., Dennler, G., et.al. (2010). Near IR sensitization of organic bulk heterojunction solar cells: towards optimization of the spectral response of organic solar cells. Advanced Functional Materials, 20(2), 338-346.

[230] Hu, Z., Tang, S., Ahlvers, A., et.al. (2012). Near-infrared photoresponse sensitization of solvent additive processed poly (3-hexylthiophene)/fullerene solar cells by a low band gap polymer. Applied Physics Letters, 101(5), 053308.

[231] Ramani, R., & Alam, S. (2013). A comparative study on the influence of alkyl thiols on the structural transformations in P3HT/PCBM and P3OT/PCBM blends. Polymer, 54(25), 6785-6792.

[232] Peet, J., Wen, L., Byrne, P., et.al. (2011). Bulk heterojunction solar cells with thick active layers and high fill factors enabled by a bithiophene-co-thiazolothiazole push-pull copolymer. Applied Physics Letters, 98(4), 043301.

[233] Morvillo, P., Bobeico, E., Esposito, S., & Diana, R. (2012). Effect of the active layer thickness on the device performance of polymer solar cells having [60] PCBM and [70] PCBM as electron acceptor. Energy Procedia, 31, 69-73.

[234] Apaydın, D. H., Yıldız, D. E., Cirpan, A., & Toppare, L. (2013). Optimizing the organic solar cell efficiency: role of the active layer thickness. Solar Energy Materials and Solar Cells, 113, 100-105.

[235] Chang, J. F., Sun, B., Breiby, D. W., et.al. (2004). Enhanced mobility of poly (3-hexylthiophene) transistors by spin-coating from high-boiling-point solvents. Chemistry of materials, 16(23), 4772-4776.

[236] Sirringhaus, H., Brown, P. J., Friend, et.al. (1999). Two-dimensional charge transport in self-organized, high-mobility conjugated polymers. Nature, 401(6754), 685-688.

[237] Hauch, J. A., Schilinsky, P., Choulis, S. A., et.al. (2008). Flexible organic P3HT: PCBM bulk-heterojunction modules with more than 1 year outdoor lifetime. Solar Energy Materials and Solar Cells, 92(7), 727-731.

[238] Norrman, K., Madsen, M. V., Gevorgyan, S. A., & Krebs, F. C. (2010). Degradation patterns in water and oxygen of an inverted polymer solar cell. Journal of the American Chemical Society, 132(47), 16883-16892.

[239] Chuang, S. Y., Chen, H. L., Lee, W. H., et.al. (2009). Regioregularity effects in the chain orientation and optical anisotropy of composite polymer/fullerene films for high-efficiency, large-area organic solar cells. Journal of Materials Chemistry, 19(31), 5554-5560.

[240] Li, G., Shrotriya, V., Yao, Y., & Yang, Y. (2005). Investigation of annealing effects and film thickness dependence of polymer solar cells based on poly (3-hexylthiophene). Journal of Applied Physics, 98(4), 043704.

[241] Sun, Y., Welch, G. C., Leong, W. L., et.al. (2012). Solution-processed small-molecule solar cells with 6.7% efficiency. Nature materials, 11(1), 44-48.

[242] Wang, D. H., Pron, A., Leclerc, M., & Heeger, A. J. (2013). Additive-Free Bulk-Heterojuction Solar Cells with Enhanced Power Conversion Efficiency, Comprising a Newly Designed Selenophene-Thienopyrrolodione Copolymer. Advanced Functional Materials, 23(10), 1297-1304.

[243] Zawacka, N. K., Andersen, T. R., Andreasen, J. W., et.al. (2014). The influence of additives on the morphology and stability of roll-to-roll processed polymer solar cells studied through ex situ and in situ X-ray scattering. Journal of Materials Chemistry A, 2(43), 18644-18654.

[244] Kim, W., Kim, J. K., Kim, E., et.al. (2015). Conflicted Effects of a Solvent Additive on PTB7: PC71BM Bulk Heterojunction Solar Cells. The Journal of Physical Chemistry C, 119(11), 5954-5961.

[245] Norrman, K., Gevorgyan, S. A., & Krebs, F. C. (2008). Water-induced degradation of polymer solar cells studied by H218O labeling. ACS applied materials & interfaces, 1(1), 102-112.

[246] Ngo, E., Venkatesan, S., Galipeau, D., & Qiao, Q. (2013). Polymer photovoltaic performance and degradation on spray and spin coated electron transport layer and active layer. IEEE Transactions on Electron Devices, 60(7), 2372-2378.

[247] Lima, F. A. S., Beliatis, M. J., Roth, B., et.al. (2016). Flexible ITO-free organic solar cells applying aqueous solution-processed V2O5 hole transport layer: An outdoor stability study. APL Materials, 4(2), 026104.

[248] Vijay, P., & Sumaria, V. Advancement in P3HT PCBM solar cells, the most efficient Polymer Photovoltaic cell. In 10th Annual Session of Students' Chemical Engineering Congress, 2014.

Chapter 4: Methodologies

4.1 Materials

The main material used in the current study as an electron donor is regioregular poly (3-hexathiophine-2,5-diyl) (P3HT) which was purchased from Sigma-Aldrich. Several fullerene derivatives were used as the electron acceptors; these are [6,6]-Phenyl C_{61} butyric acid methyl ester ($PC_{61}BM$) and [6,6]-Phenyl C_{71} butyric acid methyl ester ($PC_{71}BM$) mixture of isomers which were purchased from Sigma-Aldrich while Bis(1-[3-(methoxycarbonyl)propyl]-1-phenyl)-[6,6]C_{62} ($PC_{60}BM$) and [6,6]-Phenyl-C_{71}-butyric acid methyl ester ($PC_{70}BM$) were purchased from Ossila. Poly (3,4-ethylene dioxythiophene) poly (styrene sulfonate) (PEDOT:PSS) (conductive grade 1.3%) were purchased from Sigma-Aldrich and used as a hole transport layer. Fig.4.1 shows the main materials used in the current study. Several solvents were purchased from Sigma-Aldrich and used in the preparation or cleaning procedures. These are Chlorobenzene (CB), Chloroform (CF), and dichlorobenzene (DCB) which were used as the main solvents to dissolve the active layer blends. Other solvents including acetone, 2-propanol and methanol are used for cleaning purposes. Square shape ITO-coated glass slides (2.5 × 2.5 cm) with sheet resistant of 8-12 Ω/□ as well as glass slides were purchased from Sigma-Aldrich. Different metal salts were also purchased from Sigma-Aldrich and used as dopants in the PEDOT:PSS layer in part of this research; these are $CuCl_2$ (99.99%), $CdCl_2$ (99.99%), NaCl (99.99%) and LiCl (99.99%). Additionally, tris-(8-hydroxyquinoline) Aluminium (Alq3) was used an electron transport layer after dissolving in formic acid, both of them were purchased from Sigma-Aldrich.

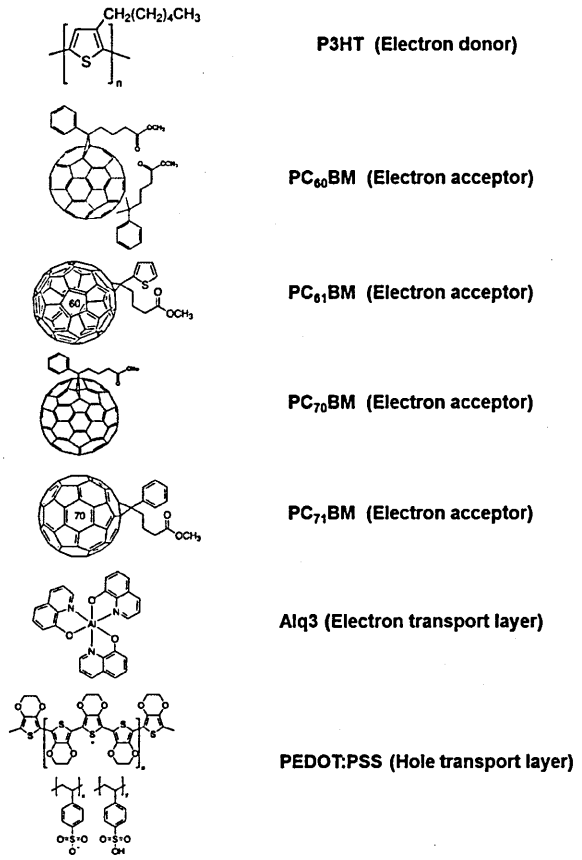

Fig.4.1: The main materials used in the current research

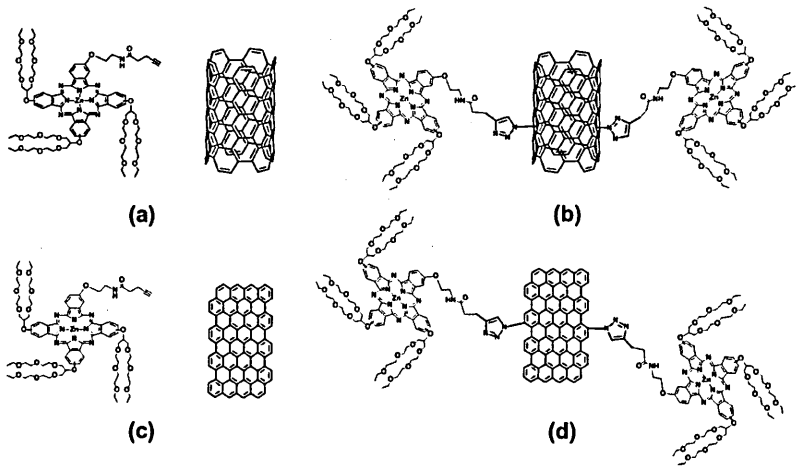

Fig.4.2: (a) ZnPc:SWCNT non-covalently bonded , (b) ZnPc:SWCNT covalently bonded, (c) ZnPc:rGO non-covalently bonded, and (d) ZnPc:rGO non-covalently bonded, hybrid materials

Furthermore, the synthesis of novel 1-[N-(2-ethoxyethyl)-4-pentynamide]-8(11),15(18),22(25)-tris-{2-[2-(2-ethoxyethoxy)ethoxy]-1-[2-((2-ethoxyethoxy)-ethoxy) methyl] ethyloxy} zinc(II) phthalocyanine (ZnPc) hybrids both as covalently and non-covalently bonded to single-wall carbon nanotubes (SWCNTs) and reduced graphene oxide (rGO) were carried out by our research collaborators from Gebza Technical University, Turkey, as described in our publication (see Fig.4.2) [1]. The characterisation analysis of hybrid materials is presented in Appendix A.

4.2 Device fabrication

The ITO coated slides as well as the glass substrates were washed in acetone, 2-propanol and DI water for 10 min each in an ultrasonic bath, respectively, and then blown dry with nitrogen gas and kept in a desiccator. PEDOT:PSS layer was spin coated on the ITO coated glass or glass substrates at 2000 rpm spin speed for 30 sec, followed by heat treatment on a hot plate at 150°C in ambient air for 10 min. P3HT:PCBM active layers in the weight ratios of 1:1 and a concentration of 14mg/ml have been dissolved in different organic solvents.
The solutions were stirred overnight at 45°C followed by filtering the P3HT:PCBM solutions through a PTFE filter with pore size of 0.45 μm. All the P3HT:PCBM active layers have been spin coated inside a nitrogen-filled glove box with different spin speeds to produce different active layer thickness and heat treated inside the nitrogen filled glove box on a hot plate at 120°C for 10 min. The active layer thickness was determined using spectroscopic ellipsometry (see section 4.3.8 for further details). To end with the device preparation, a back contact of aluminium (Al) was then thermally evaporated with a thickness of 100 nm through a shadow mask with an active area of 0.07cm^2. This process was carried out under a vacuum of about10^{-6} mbar (~10^{-4} Pa), at the deposition rate of 0.1-0.2 nm/sec. Both film thickness and deposition rate were monitored using a quartz crystal thickness monitor. Fig.4.3 shows the cross section of the studied devices with all the layers used in this project.

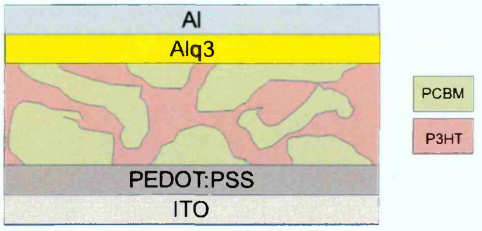

Fig.4.3: Cross section of the studied device

The first part of this research was based on employing different solvents and their co-solvents to process the P3HT:PCBM blends as the active layers of the studied OSCs. The used solvents are CB, CF and DCB and their co-solvents DCB:CF, DCB:CB and CB:CF in the volume ratios of 1:1. Moreover, the best solvent processed device was used as a reference device to prepare different active layer thickness devices. Further developments in the device structure have been carried out using different fullerene derivatives ($PC_{60}BM$, $PC_{61}BM$, $PC_{70}BM$ and $PC_{71}BM$) to study the effect of these derivatives as the acceptor materials on the electrical properties of the solar cells. All the prepared devices have been subjected to heat treatment inside the nitrogen glove box at 120°C for 10 min prior to the deposition of the back contact (Al) and left to cool down for 30 min.

Further to the initial heat treatment, post-deposition annealing has been carried out at different temperatures in the range 100 - 180°C for 10 min each following the full device fabrication in order to study the effects of these post-deposition heat treatments on the devices performance. Moreover, Alq3 has been used as a novel ETL. This material has been dissolved in formic acid at the concentration of 4mg/ml and sonicated for a few minutes. A Thin film of Alq3 layer of about 5 nm thickness was deposited between the active layer and the back electrode (Al) by spin coating. This process was carried out inside the glove box at a spin speed of 2000 rpm for 30 sec followed by annealing inside the glove box at 80 °C for 10 min. As part of this research, PEDOT:PSS was doped with different metal salts; these are $CuCl_2$, $CdCl_2$, NaCl and LiCl which were used both in powders form and in as aqueous solutions with different concentrations. 1mg of the metal salts was added separately as powders to 1ml of the PEDOT:PSS solution.

The final solutions were sonicated for 30 min to ensure good dispersion and complete solubility of the salts. In a separate method, aqueous solutions of each metal salt with the concentration of 1mg/ml were prepared in DI water. The solutions were sonicated for 30

min before mixing with PEDOT:PSS solution with the volume ratio of 0.1:1. Further sonication for 30 min was carried out for efficient dispersion after mixing the PEDOT:PSS with the aqueous salts solutions. Additional samples of LiCl in DI water were used in the concentrations of 5mg/ml and 10mg/ml in order to examine the role of dopant concentration on the electrical and optical properties of PEDOT:PSS. A complete device processed by applying the different parameters described above has been prepared and studied as a completely optimised OSC device; these included, the use of best solvents (CB:CF), choice of optimum active layer thickness (~100nm), choice of the best fullerene derivatives ($PC_{61}BM$) as the acceptor component, the use of Alq3 as ETL, the use of PEDOT:PSS treated with LiCl in the concentration of 10mg/ml and the use of best post-annealing temperature. These preparations have been carried out inside nitrogen filled glove box. Aluminium was used as the back contact with the thickness of ~100nm. Finally, novel zinc phthalocyanine (ZnPc) covalently and non-covalently bonded to SWCNTs and rGO materials have been used as additives to the P3HT:PCBM blend to prepare ternary blends.

P3HT:ZnPc-hybrids has also been prepared by mixing P3HT with ZnPc covalently bonded (ZnPc-SWCNTs-co) and non-covalently bonded (ZnPc-SWCNTs-non-co) to SWCNTs as well as ZnPc covalently bonded (ZnPc-rGO-co) and non-covalently bonded (ZnPc-rGO-non-co) to reduced graphene oxide in the weight ratio of (1:0.01) mg in CB as solvent. P3HT:PCBM blends were mixed with ZnPc functionalized carbon nanomaterials to produce a ternary active layer blends with the weight ratio of (1:1:0.01); these hybrids were dissolved in CB:CF co-solvent and the solutions were stirred overnight at 45°C. PEDOT:PSS layer was spin coated on the ITO coated glass or glass substrates at 2000 rpm spin speed for 30 sec, followed by heat treatment on a hot plate at 150°C in ambient air. The active layers were spin coated at 1500 rpm for 30 sec to obtain a thickness of ~150 nm and then heat-treated inside the glove box at 120 °C for 10 min. Another set of devices with a different active layer thickness (~100nm) has been prepared as this is the optimum thickness achieved in this study. Aluminium (Al) was thermally evaporated as a back electrode. All completed devices were subjected to further heat treatment inside the glove box at 140°C for 10 min.

4.2.1 Thermal evaporation:

4.2.1.1 Instrumentation

Edwards E306A Thermal Evaporator (Fig.4.1 5(a)) has been used to evaporate a metal film onto a substrate. The metal source to be evaporated, typically aluminium is placed in a suitable filament or crucible, in which a large current is passed. The metal melts, and evaporates onto the target substrate above the source, producing a thin film. The thickness of the metal film is monitored in-situ using a quartz crystal thickness monitor (Model Edward FTM5). Even though the turret can accommodate up to four different materials and changed via manual rotation, the most common practice was to evaporate single material during one pump-down cycle.

4.2.1.2 Evaporation procedure

Vacuum deposition via thermal evaporation includes two simple processes, evaporation and condensation. It brings to mind the familiar process by which liquid water appears on the lid of a boiling pan, but the situation and heat source are quite different. Evaporation process occurs in a vacuum, where gases other than the source material are almost completely removed before the evaporation begins. Therefore, particles can travel straight to the deposition target avoiding collision with the background gaseous molecules. Hot objects inside the evaporation chamber such as heating filaments create unwanted vapours that limit the quality of the vacuum.

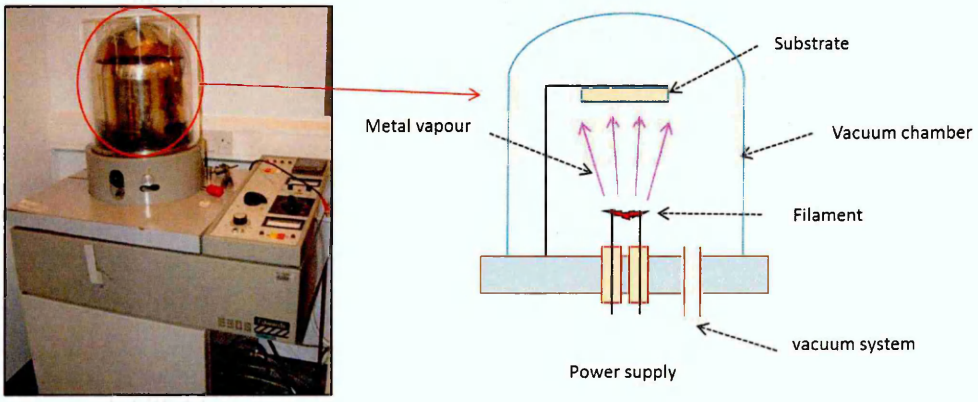

Fig.4.4: Edwards E306A thermal evaporator and a schematic illustration showing the evaporation process

Generally, other unwanted gases collide with the evaporated material may react with them. For example, if aluminium is deposited in the presence of oxygen, it will form aluminium oxide. They also reduce the amount of vapour that reaches the substrate, which makes the thickness difficult to control [2]. Fig.4.4 shows a sketch of the evaporation process.

4.2.2 Spin coating method

4.2.2.1 Instrumentation

A photoresist spinner model 4000 (Electronic Micro Systems Ltd.) has been used to spin cast the thin films used in the current study. A drop of the materials solution is deposited using adjustable micro-syringe (Eppendorf 10-100 µl) onto a rotating substrate.

4.2.2.2 Background and method

Spin coating is a fast and easy method to generate thin and homogeneous organic films out of solutions. Spin coating is a procedure used to apply uniform thin films to flat substrates. In short, an excess amount of a solution is placed on the substrate, which is then rotated at high speed in order to spread the fluid by centrifugal force. This method was first described by Emslie et al. (1958) [3] and Meyerhofer et al. (1978) [4]. In the early stages of spin coating, the rate of thinning by centrifugal forces is much larger than by evaporation. After the spin-off, the thinning of the film is just due to evaporation and occurs constantly. The transition point between the spin-off and evaporation is the point where the rate of thinning due to centrifugal forces is the same as that due to evaporation. Fig.4.5 illustrates the stages of the spin coating; film thickness at each transition point is different. The time after reaching the transition point is called drying time. The liquid film becomes supersaturated due to evaporation of the solvent. After completing the solvent's evaporation, a solid film is formed on the substrate.

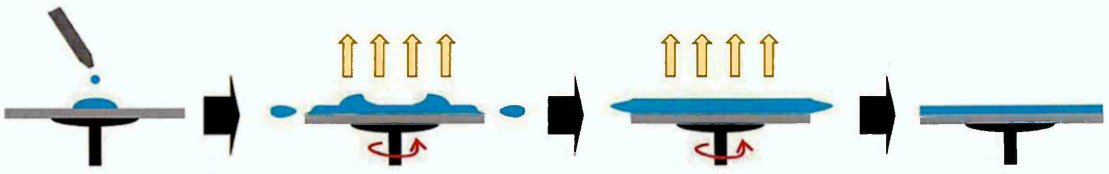

Fig.4.5: Schematic figure of spin-coating indicating the dominant process at the beginning of spin-coating (spin-off) and later after the equilibrium liquid film thickness is reached

4.3 Characterizations techniques

Several techniques were employed in this study to investigate the organic layers physical properties as well as examining the solar cell device performance. The preparation methods are mainly based on solution processing of OSC devices and spin coating was employed the film deposition method. For further details, the following sections describe the characterisation and the methods used in this research.

4.3.1 UV-visible absorption spectroscopy

4.3.1.1 Instrumentation

Varian 50 scan UV-Visible spectrophotometer (see Fig.4.7) covers the spectral range between 190 to 1100nm has been employed to investigate the absorption and the transmittance spectra of the studied layers. Generally, the spectrophotometer is designed around three fundamental parts: the light source, the monochromator, which constitutes the optical section and the detection system. These components are typically integrated into a unique framework to make the spectrophotometers [5].

Fig.4.6: Varian 50 scan UV-visible spectrophotometer

All the samples have been measured using clean glass substrate (Sigma-Aldrich) as well as quartz cuvette for the solution samples; the cleaning procedure is described in section 4.2. Firstly, the reference sample (e.g. uncoated glass slide) is measured in order to obtain the baseline; followed by the measurement of a film-coated slide. If the intensity of light source changes slightly, this can affect the output measurement. For this reason, after a number of measurements, the reference sample should be used again as a baseline for recalibration in order to make sure that the readings are accurate.

4.3.1.2 The principles of absorption spectroscopy

UV-Vis absorption spectroscopy is the measurement of light absorption by a sample in the ultraviolet-visible spectral region of the electromagnetic spectrum. The UV-Visible spectral region is divided into three sub-regions termed as near UV (185-400 nm), visible (400-700 nm) and near infrared (700-1100 nm). This absorption or attenuation can occur when light passes through a thin film or a translucent liquid sample. The difference in the incident light and the transmitted light is used to determine the actual absorbance. When an atom or molecule absorbs energy, electrons are promoted from their ground state to an excited state. Molecules can only absorb radiant energy in definite units, or quanta, which correspond to the energy difference between the ground and excited states (see Fig.4.7(a)). The energy (E) carried by any one quantum (photon) is proportional to its frequency of oscillation, that is:

$$E = h\nu = \frac{hc}{\lambda} \tag{4.1}$$

where ν is the frequency, λ is the wavelength, c is the speed of light and h is Plank's constant. The principle of absorption is the interaction of ions or molecules of the sample with the photons of an incident beam produced by a source. When a molecule interacts with a photon, this photon is absorbed and one or more of the molecule's outer electrons will capture its energy. Consequently, total electronic energy increases and promotion of an electron from the ground states (HOMO) to the excited states (LUMO) takes place. The observed transitions involve electrons engaged in σ, π or non-binding n electron orbitals which might occur according to the transitions explained in Fig.4.7(b).

When light with an intensity (I) passes through a material with thickness x and absorption coefficient α, the transmittance is the relation between the amount of light that is transmitted to the detector once it has passed through the sample (I) and the initial intensity of light (I_o) as demonstrated in Fig.4.8.

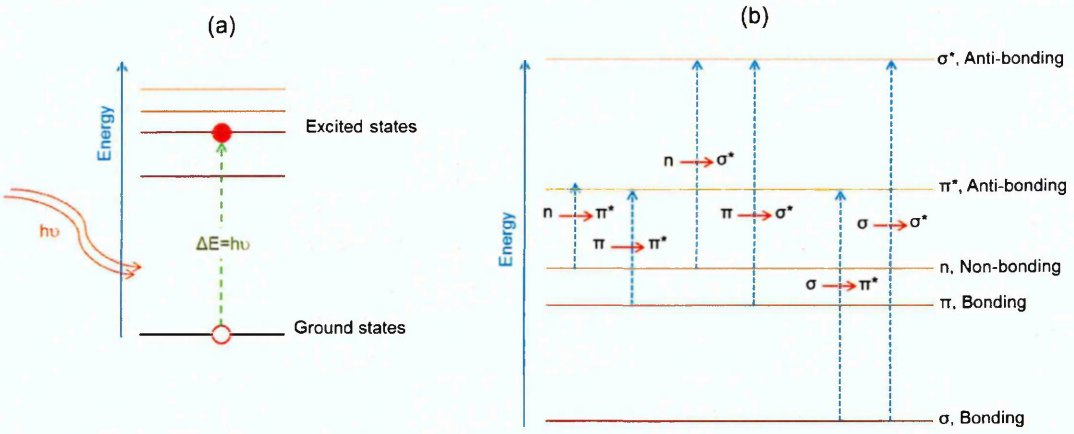

Fig.4.7: (a) Energy levels for an electron in an atom: ground state and excited states. After absorbing energy, an electron may jump from the ground state to a higher energy excited state, and (b) the possible electronic transitions in organic materials.

This could be expressed in following formula which is well-known as Lambert-Beer equation [6]:

$$I = I_0 e^{-\alpha x} \tag{4.2}$$

The transmittance (T) is defined as the ratio of the intensity of light exited from sample (I) to the initial intensity (I_o) entering the sample as given by the following equation:

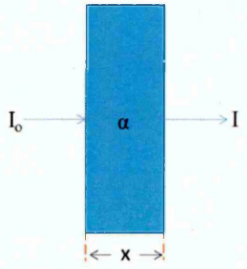

Fig.4.8: Lambert-Beer law where the light travelling through the sample with a thickness (x) and an absorption coefficient α

$$T = \frac{I}{I_o} \tag{4.3}$$

The transmittance (T) can also be related to the absorbance (A) according to the following equation:

$$A = \log_{10}\left(\frac{I_o}{I}\right) = \log_{10}\left(\frac{1}{T}\right) \quad (4.4)$$

By substituting eq. 4.3 in 4.2, the absorption coefficient (α) can be evaluated using the following equation:

$$\alpha = -\frac{\ln(T)}{x} \quad (4.5)$$

The absorption coefficient (α) is also related to the energy of incident light hυ as well as the E_g of the material according to Tauc's equation [7]:

$$(\alpha h\upsilon)^n = B(h\upsilon - E_g) \quad (4.6)$$

where n takes the value of 2 for a direct energy band gap semiconductor and $\frac{1}{2}$ for an indirect energy band gap semiconductor.

4.3.2 Electrical measurements

4.3.2.1 J-V and C-V measurements

Keithley 4200 Semiconductor Characterisation System (4200-SCS) (see Fig.4.9) has been used for the DC electrical characterization of the studied thin films as well as for the measurement of the solar cell current-voltage (I-V) characteristics. The system is specified to work in the 1pA-1A current range with the maximum voltage range of 21-210 V and 200mV-200V voltage range with the maximum current of 10.5-105mA. The 4200-SCS can automatically perform IV and CV measurements of semiconductor devices, using up to eight Source-Measure Units (SMUs). I-V measurements of the studied devices have been carried out both in the dark and under illumination conditions; an AM1.5 solar simulator source of 100mW/cm^2 has been used in the current study. Furthermore, C-V measurements have been employed to study the C-V characteristics of the studied OSCs devices using an HP4284A (20Hz-1MHz) Precision LCR meter (see Fig.4.10).

The samples capacitance versus voltage (C-V) was measured at a fixed frequency of 100 kHz over a range of applied voltage. The theoretical part of the I-V and C-V characteristics are described in details in sections chapter 2.

Fig.4.9: Keithley 4200 semiconductor characterization system

Fig.4.10: HP-4284A (20Hz-1MHz) Precision LCR meter

4.3.2.2 Conductivity measurement

According to Ohm's law, the current I (in amperes) in a sample is directly proportional to the potential difference V (in volts) across two points in this sample [8]:

$$R = \frac{V}{I} \tag{4.7}$$

where R is the sample resistance measured in ohms.

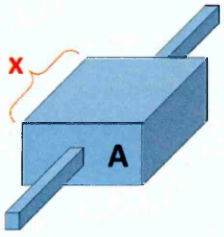

Fig.4.11: A piece of resistive material with electrical contacts at the ends

Assuming that, the current passes through a piece of material with length x (m) and a cross section area A (m^2) as shown in Fig.4.11. The electrical resistivity ρ can be defined as:

$$\rho = R\frac{A}{x} \tag{4.8}$$

where the conductivity (σ) is the inverse of the resistivity (ρ). Therefore, we can write Ohm's low in the following expression:

$$J = \sigma E \tag{4.9}$$

where J is the current density (I/A) (in ampere/cm^2) and E is the magnitude of the electric field (V/x) (in volt/m). To measure the electrical conductivity of the studied films, interdigitated platinum electrodes (IDEs), which were bought from drop sense, have been used (see Fig.4.12(a)). The dimensions of the IDEs are described in Fig.4.12(b); t is film thickness, W is the overlapping distance between the fingers (7mm), n is the number of fingers (250) and L is the space between electrodes (5μm). I/V is the gradient of plotted graphs representing the measured I-V data, the electrical conductivity is determined using the following equation [9,10]:

$$\sigma = \left(\frac{I}{V}\right)\left(\frac{L}{Wtn}\right) \tag{4.10}$$

Spin-coating method has been mainly used to deposit the organic layers; the layer's thicknesses have been determined using spectroscopic ellipsometry.

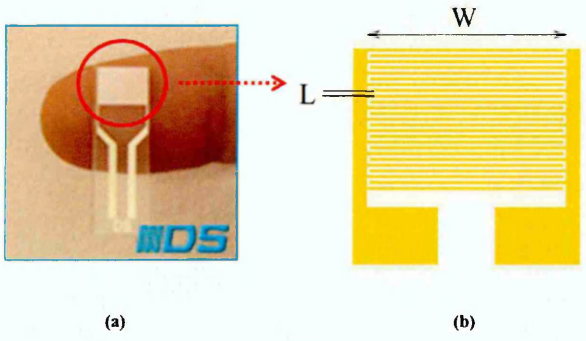

Fig.4.12: (a) Interdigitated electrodes (IDE), and (b) sketch diagram of IDE.

4.3.3 Scanning Electron Microscopy (SEM)

4.3.3.1 Instrumentation

FEI-nova nanosem 200 SEM (Fig.4.13(a)) has been used in this research. The scheme of SEM operation is shown in Fig.4.13(b), which consists of electron gun as an electron source, two condenser lenses, scanning coils, which facilitates the deflection of the electron beam in x and y directions, an objective lens, and detectors for backscattered and secondary electrons. SEM operates inside a vacuum chamber with high-energy electron source (2-25kV). The condenser lenses focus the electron beam onto a section of the examined sample of nanometer size. The reflected electrons from the sample, backscattered or secondary electrons, are collected by the detector to provide an image of the sample. In many cases, the backscattered electrons reflected from the sample are used in analytical SEM due to the relation between the intensity and the atomic number of materials [11].

In a SEM experiment, the sample is placed in a chamber, which is pumped down to create vacuum environment with the pressure of about 10^{-7} mbar. The electron gun, which is usually made of a tungsten filament, heats up to about 2400°C where it starts emitting electrons. These electrons are accelerated down the column with the help of the anode. The accelerating potential can be within the range of (1-30kV) depending on the type of material to be examined. The electrons accelerated by the anode are usually scattered, and with the help of the magnetic lenses, they are focussed in a narrow electron beam. These lenses also control the number of electrons reaching the sample. The purpose of the scanning coils is to deflect the electron beam in the x and y-directions so that the surface of the sample can be scanned. The final focusing of the electron beam is done by the objective lens, thereafter, the high-energy electron beam interacts with the sample and different signals are emitted. These signals are then collected by a relevant detector and used to create an image of the surface.

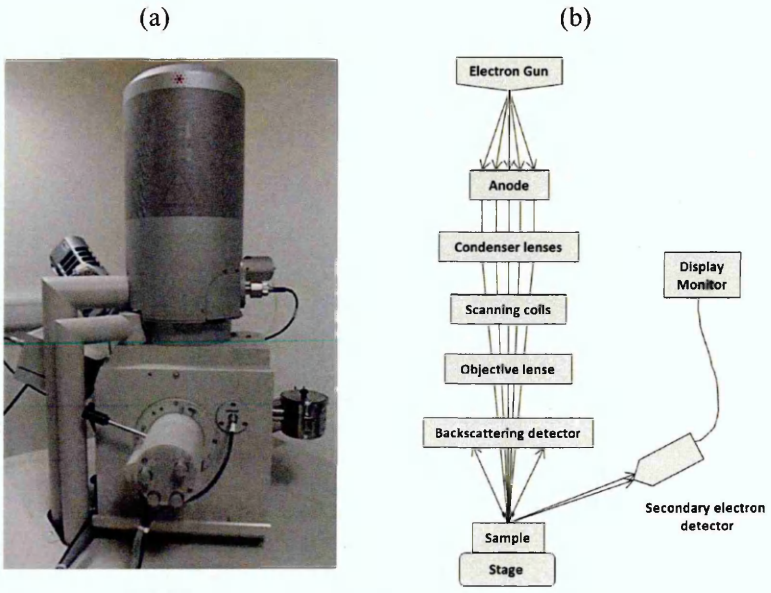

Fig.4.13: FEI-nova nanosem 200 Scanning Electron Microscope (SEM)

4.3.3.2 Secondary and backscattered electrons

Two imaging modes are available in SEM; Secondary Electron Imaging (SEI) and Backscattered Electron Imaging (BEI) as shown in Fig.4.14. In the former, low energy secondary electrons (typically < 50 eV) emitted from the interaction between the incident beam of high energy electrons with the atoms of the sample via inelastic collisions are detected and used to build an image of the surface topography of the sample. Due to the relatively low energies of these secondary electrons, only those from the surface (a very thin layer of tens of nanometres) are able to emerge from the sample. In the case of BEI, the image is derived from scattered or reflected electrons from elastic collisions of the high energy electron beam with the nuclei of the atoms at high angles approaching 180° (Fig.4.14). The yield of backscattered electrons is a function of atomic number. Heavier elements, i.e. those with a higher atomic number, reflect a greater proportion of electrons and therefore appear brighter, and lighter elements with a low atomic number reflect a lower proportion of electrons and appear darker. The contrast indicates the average atomic number of the elements present within the microstructure and is indicative of the varying elemental compositions [12].

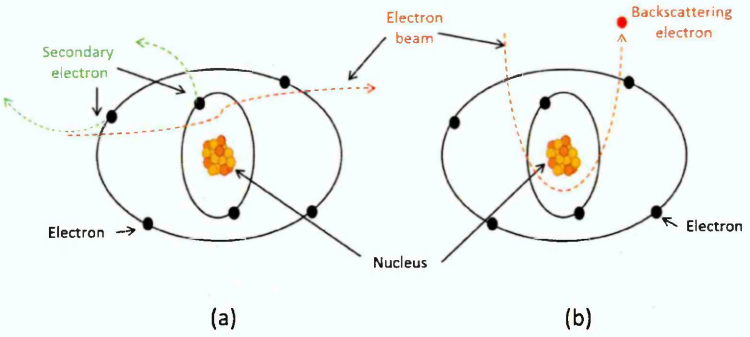

Fig.4.14: Interaction between electron beam and sample producing (a) secondary electrons and (b) backscattered electrons

4.3.4 X-Ray Diffraction (XRD)

4.3.4.1 Instrumentation

Multipurpose X`Pert Philips X-ray diffractometer (MPD) (Fig.4.15) with Cu-Kα X-ray source of wavelength 1.54 Å and with source voltage and current of 40 kV and 40 mA respectively was used to measure the X-ray diffraction patterns of thin films deposited as OSC active layers. The structure parameters of studied active layers are evaluated by fitting the maximum peaks at 2θ with one Gaussian to estimate the full width at half maximum (FWHM) or (β), the d-spacing as well as the peak position with the intensity height. The grain size (D) of the nanocrystalline films was calculated using Scherer equation where β is the FWHM at 2θ [13]:

$$D = \frac{0.94\,\lambda}{\beta \cos(\theta)} \qquad (4.11)$$

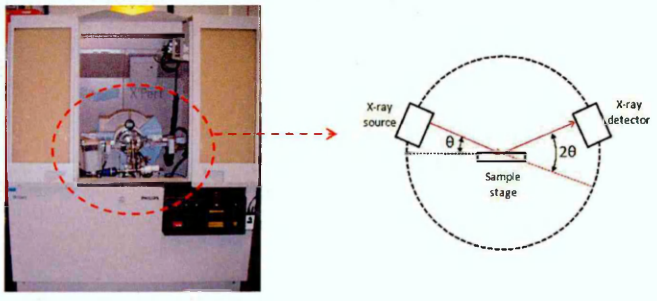

Fig.4.15: Multipurpose X`Pert Philips XRD and the outline of a diffracted ray utilising X-ray diffraction.

4.3.4.2 XRD Method

The X-ray method covers several procedures based on the scattering, emission and absorption properties of X-radiation. The most commonly used X-ray techniques involve X-ray diffraction (XRD), Energy dispersive X-ray spectroscopy (EDX) and X-ray fluorescence (XRF). These techniques are used to provide information about the crystal structure, chemical composition and physical properties of materials and thin films. In the current study, XRD has been used to study the structure of thin films to analyse their use for solar cells application. XRD is a non-destructive technique, which is used to determine the crystallographic structure, phase and crystallite size of materials. In XRD analysis, the crystalline sample is exposed to the monochromatic radiation (X-ray) generated by cathode ray tube. The incident ray interacts with the sample and produces constructive interference between diffracted rays when conditions satisfy Bragg's law. The Bragg's law states that the constructive interference occurs when the path difference between two interfering waves is equal to the whole number (n) of the wavelength (λ). The Bragg's law is given by the following equation [14]:

$$n\lambda = 2d\sin(\theta) \tag{4.12}$$

where d is the inter-atomic distance (lattice spacing) and θ is the angle between the incident beam and scattering plane. The XRD characteristics generated in the XRD analysis provides useful information about the crystal phases presented in the sample.

4.3.5 Atomic Force Microscopy (AFM)

4.3.5.1 Background

Atomic force microscopy (AFM) is a powerful surface analytical technique used to produce a high-resolution morphological image of the sample. As compared to SEM technique, AFM does not require the vacuum environment. This technique is able to create 3D-image of the surface features and also can magnify the surface of the sample up to 108 times. AFM has been invented in 1986 by Binning et. al. [15]. Like all other scanning probe microscopes, AFM utilises a sharp probe moving over the surface of a sample in a raster scan.

The probe is a tip on the end of a cantilever, which bends in response to the force between the tip and the sample. Unlike traditional microscopes, scanned-probe systems do not use lenses, so the size of the probe determines the resolution limit. In AFM the cantilever is treated as a Hookean spring, and hence a simple relationship may be assumed between the deflection of the lever, x, and the force F acting on the tip [16]:

$$F = -kx \tag{4.13}$$

The constant of proportionality k is the spring constant, which is strongly dependent on the physical dimensions of the cantilever (width, length, thickness) and the elasticity of material [17].

4.3.5.2 Instrumentation

The AFM instrument used in this study is NanoScope IIIa Multimode 8 AFM (Fig.4.16); the microscope itself rests on an anti-vibration platform, which can be spring suspended on a tripod to reduce further noise. The NanoScope IIIa Multimode 8 instrument gives the opportunity to take images of the sample surface with nanometer resolution and to determine their characteristics, such as the sample features' height and distribution. Changes in the tip-sample interaction are monitored using an optical cantilever detection system, where a laser beam is reflected back from the cantilever and collected by a position sensitive detector consisting of two closely spaced photodiodes connected to a differential amplifier. The angular displacement of the cantilever results in one photodiode collecting more light than the other photodiode, producing an output signal (the difference between the photodiode signals is normalised by their sum), which is proportional to the deflection of the cantilever. The accuracy of the detection of cantilever deflections is less than 1Å (thermal noise limited). The long beam path (several centimetres) amplifies changes in the beam angle [18].

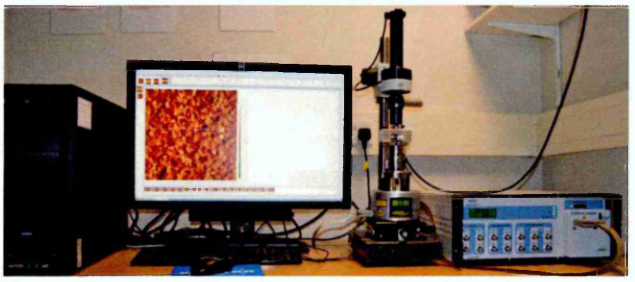

Fig.4.16: NanoScope IIIa Multimode 8 SPM system components

4.3.5.3 AFM image analysis

The software provided with this system (NanoScope Analysis 1.50) has been used to analyse the cross-section, roughness, particle size, etc., and creates virtual 2D and 3D images of the sample surface. Further analysis has been carried out using WSxM software. The latter has been used to estimate the phase contrast images and analysing these images using Fast Fourier Transform (FFT) analysis. This software also provides virtual 2D and 3D images with their phase contrast. The phase contrast images were analysed using FFT and the obtained images give assumption to the phase separation of the evaluated materials. FFT filtering was applied to AFM phase images, to transform the data in the frequency domain. Bright peaks on a dark background in the power spectra represent the intensity of spatial frequency components in the real space image. The brightest peaks present near to the origin correspond to the periodic sources of noise, and the distributed peaks far from the origin are evidence of surface periodicities [19].

4.3.5.4 Distance between sample surface and tip

Three different primary imaging modes are possible according to the distance (d) between the sample surface and the tip, contact mode ($d < 0.5$ nm), non-contact mode (0.5 nm $< d <$ 10), and tapping mode ($d \sim 0.5$-2 nm), as shown in Fig.4.17. In a contact mode, the tip scans the sample surface by being pushed against the surface. Contact mode is suitable for hard surfaces where the tip cannot damage the surface [20]. In non-contact mode, the separation of the tip from the sample surface is large, that the interaction between the tip and the sample surface is small and mostly in the range of the damping forces in ambient conditions. Therefore, the non-contact mode is appropriate for measurement mostly under vacuum, and even sub-molecular resolution could be achieved [21].

In tapping mode, the cantilever oscillates and the tip taps the surface slightly during scanning. Thus the surface is less damaged than in the case of contact mode while the lateral forces are eliminated. The feedback loop maintains constant oscillation amplitude by maintaining a constant tip-sample interaction during the scan [22].

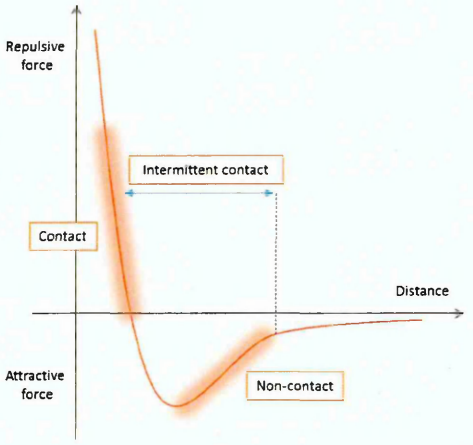

Fig.4.17: Van der Waals force against distance [15]

On the other hand, tapping mode tends to be more applicable to general imaging in air, particularly for soft surfaces, as the resolution is similar to or even better than contact mode, while the forces applied to the sample is lower. In fact, the only disadvantage of tapping mode is that the scan speed is slightly slower than in contact mode and the AFM operation is a bit more complex, but these disadvantages are outweighed by the advantages.

4.3.6 Spectroscopic Ellipsometry

4.3.6.1 Instrumentation

A commercial M2000 J. A. Woollam Spectroscopic Ellipsometry (Fig.4.18(a)) operating in the spectral range of 350−1000 nm has been used in the current study mainly to determine the film's thickness. The resulted data is represented by the two ellipsometry parameters ψ and Δ, representing, respectively, the amplitude ratio (ψ) and phase shift (Δ) between the p and s components of polarised light Fig.4.18(b).

4.3.6.2 Film's thickness determination and data fitting

In order to determine the film's thickness as well as its optical constants, data fitting is performed on the measured ψ and Δ spectra by solving Fresnel equations many times for different values of refractive index (n) and film thickness (d) and subsequently minimizing the error function of the experimental and theoretical (calculated) values of ψ and Δ using one of least square techniques. Commercial WVASE32® software is provided by J.A. Woollam Co. Inc., for this task. Data processing requires building an optical model, which corresponds to the sample under investigation. Dielectric functions of some layers (namely; BK7 glass, organic, Alq3, ITO) are known and can be selected from the WVASE software library [17]. Ellipsometry data fitting requires a great deal of experience and the outcomes depend on the selection of a physically adequate model as well as the choice of initial parameter fitting routine, i.e. the use of 'normal fit', or 'point by point fit' option, limiting the range of variable parameters, and removing 'anomalous' data points, and so on. In order to achieve reliable results, the fitting procedure needs to be repeated several times (preferably from different initial conditions) until consistent values of thickness (d), refractive index (n) and extinction coefficient (k) are achieved.

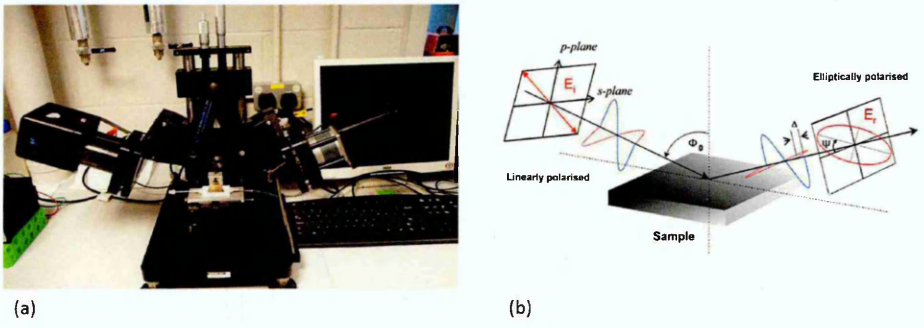

Fig.4.18: (a) J.A.Woollam M2000 Ellipsometer and (b) an illustration of the changes in the polarised light after reflected from the surface.

4.3.7 Cyclic voltammetry

4.3.7.1 Instrumentation

A Potentiostat (μStat 200) supplied from drop-sense (Fig.4.19) has been used in the current study to estimate the energy level position of some materials used in the current research

based on the oxidation and redox potentials. μStat 200 is a small portable potentiostat supported by DropView software to control the instrument and perform the analysis. Disposable screen-printed electrodes based on carbon were used in the current study as shown in Fig.4.19. These electrodes based of ceramic substrate (L33 x W10 x H0.5 mm) consisting of working electrode made of carbon (4 mm diameter), a counter electrode made of carbon and reference electrode made of silver.

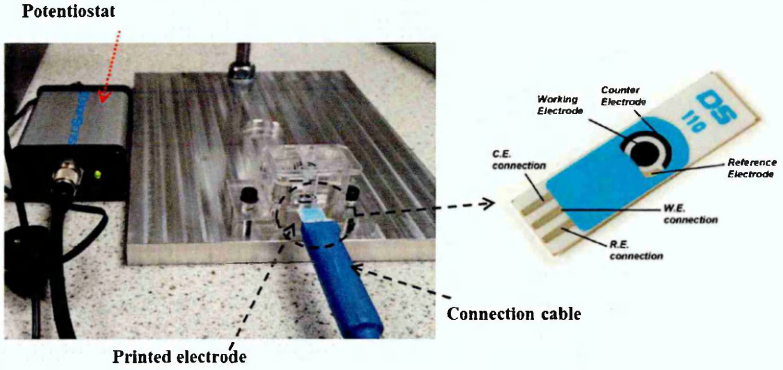

Fig.4.19: μStat 200 potentiostat and screen-printed carbon electrode purchased from drop-sense

4.3.7.2 Method

Cyclic voltammetry (CV) is a type of potentiodynamic electrochemical measurement. In a CV experiment, the working electrode potential is ramped linearly versus time. Unlike in linear sweep voltammetry, after the set potential is reached, the working electrode's potential is ramped in the opposite direction to return to the initial potential. These cycles of ramping in potential could be repeated as many times as needed. The current at the working electrode is plotted versus the applied voltage (that is, the working electrode's potential) to give the cyclic voltammogram trace. In the current study, cyclic voltammetry measurements have been carried out in the potential range from -2.0V to +2.0V in DMF solutions containing 0.1M LiCl as the supporting electrolyte. Generally, the highest occupied molecular orbital (HOMO) represents the energy required to extract an electron from a molecule (oxidation process=E_{ox}) while the lowest unoccupied molecular orbital LUMO is the energy necessary to inject an electron to a molecule (reduction process= E_{red}) [23] (see Fig.4.20). The determination of the energy levels has been carried out using the E_{ox} and E_{red} as in the following equations [24]:

$$E_{LUMO} = -(E_{red} + 4.4)eV \quad (4.14)$$

$$E_{HOMO} = -(E_{ox} + 4.4)eV \quad (4.15)$$

Therefore, the HOMO and LUMO energy levels can estimated from the respective oxidation and reduction peaks on cyclic voltammogram.

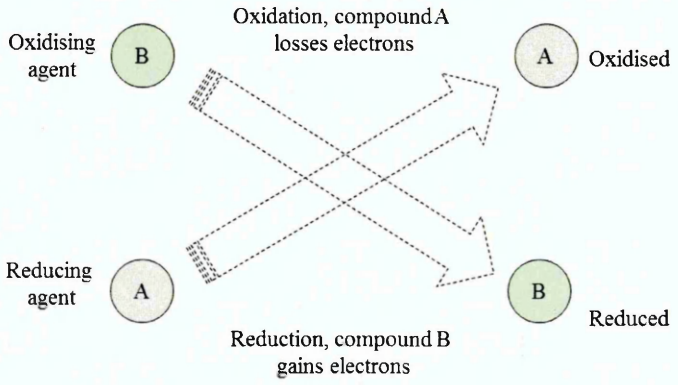

Fig.4.20: the reduction and oxidation process in a system with two compounds

Generally speaking, oxidation-reduction (redox) reactions refer to the change in oxidation state of the atoms involved; the oxidation state is changed through a loss or gain of electrons. The oxidation refers to a loss of electrons, which results in an increase of oxidation state. The reduction refers to a gain of electrons, which results in a decrease of oxidation state. The oxidation and reduction occur simultaneously.

4.3.8 Spectral response characterisation

Spectral response (R) characterisation is an important measurement in the field of solar cell research. The data obtained from the spectral response can be used to monitor the quality and to assess the performance of the fabricated solar cells. There are three types of spectral response measurements, which are used to characterise the solar cell performance. These include; spectral responsivity (R), external quantum efficiency (EQE) and internal quantum efficiency (IQE) [25].

4.3.8.1 Spectral responsivity

Spectral responsivity is defined as the ratio of the measured photocurrent (I_{ph}) to the incident light power (P_{in}) at a given wavelength (λ). In other words, the spectral responsivity is a measure of the effectiveness of the conversion of light power into electrical current. The unit of R is amperes per watt (A/W). The spectral responsivity is given by the following equation:

$$R = \frac{I_{ph}}{P_{in}} \tag{4.16}$$

External quantum efficiency (EQE) also referred to as Incident Photon to Charge Carrier Efficiency (IPCE) is defined as the ratio of the number of charge carriers collected by the solar cell to the number of photons of a given energy incident on the solar cell from outside as given by the following equation [26]:

$$EQE = \frac{\text{electron/sec}}{\text{photon/sec}} = \frac{\text{output current/charge of one electron}}{\text{total power of photons/energy of one photon}} \tag{4.17}$$

The EQE can also be given by [27]:

$$EQE = \frac{J_{ph}}{q\emptyset(\lambda)} \tag{4.18}$$

where λ is the wavelength of the incident photon, J_{ph} is the photocurrent at a given wavelength, q is the charge of the electron, $\emptyset(\lambda)$ is the number of photons per unit area per unit time per unit bandwidth of wavelength. Also, the EQE is related to the spectral responsivity (R) by [27]:

$$EQE = R\frac{hc}{q\lambda} \approx 1240\ \frac{R}{\lambda} \tag{4.19}$$

where h = 6.626×10^{-34} Js, is the Planck constant, c = 3×108 ms^{-1}, is the speed of light and q = 1.602×10^{-19} C, is the electron charge. The external quantum efficiency depends on both absorption of photons and collection of charge carriers. When photons are being absorbed

and create electron-hole pairs, these charges must be separated and directed to the external circuit before recombination. The recombination of charge carriers reduces the EQE.

4.3.8.2 Internal quantum efficiency (IQE)

IQE shows the actual number of photons absorbed by the solar cell in order to generate photocurrent. When photons are incident on the solar cell, some are absorbed, some are reflected back and the remaining part is transmitted through the solar cell. The main difference between EQE and IQE is that, in IQE, the reflected and transmitted photons should also be considered. The IQE can be expressed by the following equation, which is the modification of equ.4.19 [27]:

$$IQE = \frac{EQE}{(1-R-T)} = \frac{J_{ph}}{q\emptyset(\lambda)(1-R-T)} \tag{4.19}$$

where R and T represent the fraction of the photons reflected by and transmitted through the solar cell respectively. It should be noted that the IQE is always higher than EQE. A high IQE means that most of the charge carriers created by incident photons are separated and collected by the external circuit.

References

[1] Kadem, B., Göksel, M., Şenocak, A., et.al. (2016). Effect of covalent and non-covalent linking on the structure, optical and electrical properties of novel zinc (II) phthalocyanine functionalized carbon nanomaterials. Polyhedron, 110, 37-45.

[2] https://www.edwardsvacuum.com/Support/Reference/Documentation.aspx.

[3] Emslie, A. G., Bonner, F. T., & Peck, L. G. (1958). Flow of a viscous liquid on a rotating disk. Journal of Applied Physics, 29(5), 858-862.

[4] Meyerhofer, D. (1978). Characteristics of resist films produced by spinning. Journal of Applied Physics, 49(7), 3993-3997.

[5] Schnabel, W. (2007). Polymers and light: fundamentals and technical applications. John Wiley & Sons.

[6] Wiberley, S. E., Colthup, N. B., & Daly, L. H. (1990). Introduction to infrared and Raman Spectroscopy. ed. NB Colthup and LH Daly, Academic Press, Inc., San Diego.

[7] Rao, B. S., Kumar, B. R., Reddy, V. R., & Rao, T. S. (2011). Preparation and characterization of CdS nanoparticles by chemical co-precipitation technique. Chalcogenide Lett, 8(3), 177-185.

[8] Solymar, L., & Walsh, D. (2009). Electrical properties of materials. OUP Oxford.

[9] Skjolding, L. H. D., Spegel, C., Ribayrol, A., et.al. (2008). Characterisation of nano-interdigitated electrodes. In Journal of Physics: Conference Series (Vol. 100, No. 5, p. 052045). IOP Publishing.

[10] Kadem, B., Cranton, W., & Hassan, A. (2015). Metal salt modified PEDOT: PSS as anode buffer layer and its effect on power conversion efficiency of organic solar cells. Organic Electronics, 24, 73-79.

[11] Egerton, R. F. (2006). Physical principles of electron microscopy: an introduction to TEM, SEM, and AEM. Springer Science & Business Media.

[12] Zworykin, V. K. (1942). The Scanning Electron Microscope. Scientific American, 167, 111-113.

[13] Monshi, A., Foroughi, M. R., & Monshi, M. R. (2012). Modified Scherrer equation to estimate more accurately nano-crystallite size using XRD. World Journal of Nano Science and Engineering, 2(03), 154.

[14] Cherry, P., & Duxbury, A. (Eds.). (2009). Practical radiotherapy: Physics and equipment. John Wiley & Sons.

[15] B. Corporation, Multimode 8 with Scan Asyst Instruction Manual 004-1033-000, UK: Bruker, 2009, 2010, 2011.

[16] Binnig, G., Quate, C. F., & Gerber, C. (1986). Atomic force microscope. Physical review letters, 56(9), 930.

[17] Vickerman, J. C., & Gilmore, I. S. (Eds.). (1997). Surface analysis: the principal techniques (Vol. 1). Chichester, UK: Wiley.

[18] Tsargorodska, A., & Sheffield Hallam University. (2007). Research and Development in Optical Biosensors for Determination of Toxic Environmental Pollutants.

[19] Bkakri, R., Kusmartseva, O. E., Kusmartsev, F. V., et.al. (2015). Degree of phase separation effects on the charge transfer properties of P3HT: Graphene nanocomposites. Journal of Luminescence, 161, 264-270.

[20] Schmitz, I., Schreiner, M., Friedbacher, G., & Grasserbauer, M. (1997). Tapping-mode AFM in comparison to contact-mode AFM as a tool for in situ investigations of surface reactions with reference to glass corrosion. Analytical chemistry, 69(6), 1012-1018.

[21] Pawlak, R., Kawai, S., Fremy, S., et.al. (2012). High-resolution imaging of C60 molecules using tuning-fork-based non-contact atomic force microscopy. Journal of Physics: Condensed Matter, 24(8), 084005.

[22] Ghani, F. (2013). Nucleation and growth of unsubstituted metal phthalocyanine films from solution on planar substrates. PhD thesis, Max plank institute of colloid and interfaces.

[23] Freitas, A.R., Silva, M., Ramos, M.L., et.al. (2015). Synthesis, structure, and spectral and electrochemical properties of chromium (III) tris-(8-hydroxyquinolinate). Dalton Transactions, 44(25), 11491-11503.

[24] Lohrman, J., Zhang, C., Zhang, W., & Ren, S. (2012). Semiconducting carbon nanotube and covalent organic polyhedron–C 60 nanohybrids for light harvesting. Chemical Communications, 48(67), 8377-8379.

[25] Hartman, J. S., & Lind, M. A. (1982). Spectral response measurements for solar cells. Solar Cells, 7(1), 147-157.

[26] Sze, S. M., & Ng, K. K. (2006). Physics of semiconductor devices. John wiley & sons.

[27] Solanki, C. S. (2015). Solar photovoltaics: fundamentals, technologies and applications. PHI Learning Pvt. Ltd.

Chapter 5: Optimisation of P3HT:PCBM-based OSCs

5.1 Introduction

The blend morphology and structures are considered as one of the main issues which affect the performance of the OSCs. These properties can be significantly influenced by the used solvents [1-6]. It has been invariably shown that BHJ layers require a nanoscale interpenetrated network structure, which is favourable for charge separation and transportation [7]. In a P3HT:PCBM blend, the crystallisation of P3HT occurs faster than the aggregation of PCBM [8]. Mono-solvents and co-solvents have been used to control the morphology of P3HT:PCBM by controlling the film formation process with different evaporation rates of different used solvents in the preparation of PV active layers [9]. Chlorinated solvents including CB, CF, DCB and their co-solvents are used to dissolve P3HT:PCBM blends in the volume ratio of 1:1. Moreover, adjusting the active layer thickness has the potential to influence the device performance by improving charge collection rate and reducing the recombination rate [10].

The surface morphology provides different interface properties between the P3HT:PCBM and the Al contact. Fig.5.1 shows the variation in the metal/organic interface due to the surface morphology variation with different energy level alignments for both P3HT and PCBM with respect to Al contact. The film's thickness has shown to influence the contact resistance as well as charge transport mechanism within the solar cell active layer. Fig.5.2 shows a schematic representation of the effect of the active layer thickness on charge carriers generation and collection. Although, a thicker film is more desirable for absorbing more light compared to thinner films, thicker film however could increase the series resistance (R_s) and reduce the charge carriers' mobility [11]. Thinner films on the other hand are capable of showing nearly 100% conversions of absorbed photons into charge carriers [12]. Among several other parameters, it has frequently been shown that OSCs performance is determined by the electrical characteristics of the organic semiconductor/metal interface [13].

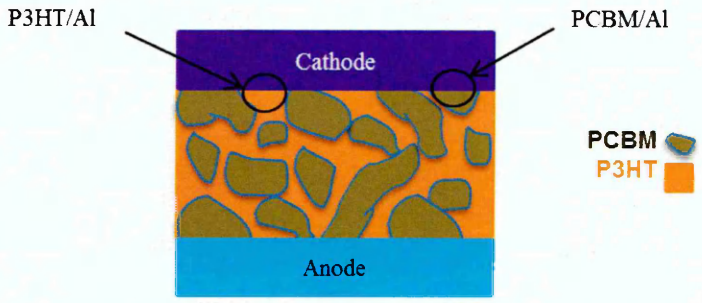

(a)

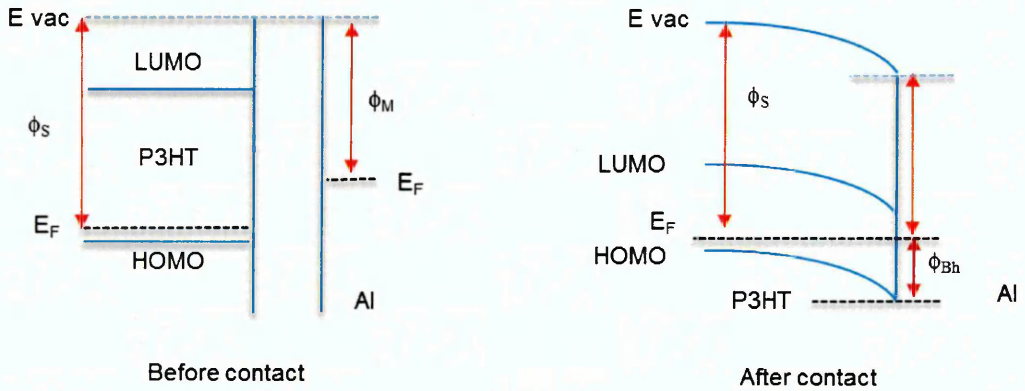

(b)

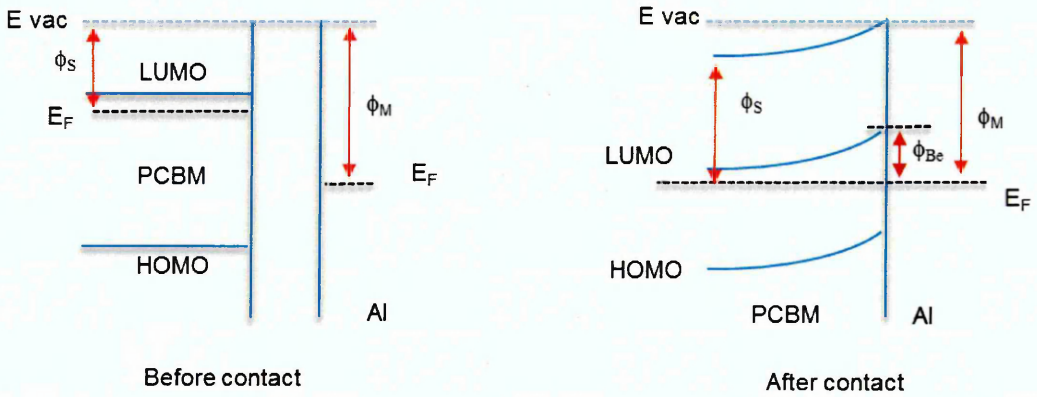

(c)

Fig.5.1: (a) P3HT:PCBM blends with different cathode interface. The energy level alignment and the interface before and after contact with (b) P3HT/Al and (c) PCBM/Al

The study of these characteristics could provide valuable information to help to improve the shape of the solar cell output. Ideality factor (n), Schottky barrier height (ϕ_B) and series resistance (R_s) are the main parameters that can be altered by the nature of this interface. Yakuphanoglu and co-workers [14] have studied the inhomogeneity of Schottky barrier in organic solar cells where higher ideality factor has been ascribed to series resistance and interface state properties. The interfacial states at the organic/metal interface affect the barrier height, charge extraction and the charge transport inside the acceptor/donor blends, which therefore determine the overall performance of the OSCs [15].

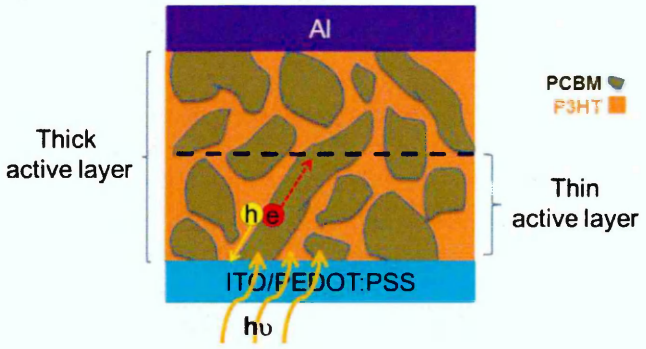

Fig.5.2: P3HT:PCBM organic solar cell sketch illustrating the role of the active layer thickness

The organic/metal barrier height varies with the BHJ blend arrangement, depending on which fullerene is used, leading to the formation of different cathode/PCBM interface properties [16] (see Fig.5.1(c)). In general, the surface disorder of the active layer induces extra energy levels into the band gap, where this is thought to control the charge transport properties in the organic blend [17]. However, further consideration of the interface properties such as the understanding of their effect on charge transport in organic layers by space-charge limited current (SCLC) is required [18]. Therefore, using different fullerene derivatives with different HOMO and LUMO positions to prepare P3HT:PCBM- based OSCs has also been carried out to increase the open circuit voltage (V_{oc}) and the built-in potential (V_{bi}) of the studied OSCs [19]. A complete understanding of the organic device physics, in particular, P3HT:PCBM solar cells is an essential requirement for optimising device and materials performance [20].

These are mainly determined by parameters such as active layer morphology and interface properties within the layer, both are largely affected by the thermal treatment of the layer (both pre-annealing and post-annealing). As it has been mentioned earlier, one of the main factors that influence the P3HT:PCBM performance is the morphology of donor and acceptor regions and their phase distribution within the active layer (see Fig.5.1(a, b and c)). Due to the low exciton diffusion length in organic materials, it is essential that efficient distribution for both phases is obtained which leads to increased interfacial area within the active layer blend [1] The conditions of heat-treatment could be one of the main parameters that determine the Quasi-Fermi level energy position (E_F) and thus the semiconductor/metal junction properties [21] and the semiconductor properties [20]. To investigate the effect of heat treatment, OSCs have been examined by applying several thermal annealing strategies; Oklobia and co-authors have studied the development of PCBM aggregates in P3HT:PCBM thin films; it was shown that vertical segregation of PCBM was formed upon thermal annealing and the maximum PCE of 3.84% was recorded after heat treatment at 150°C for 10min [22]. Padinger and co-workers have reported that post production heat treatment at 75°C for 5 min and subjecting the device to an external electric field by applying 2.7V have resulted in improving the PCE of P3HT:PCBM solar cells from 0.4% to 3.5% [23]. Furthermore, the thermal treatment has a direct effect on the morphology and conductivity of the P3HT:PCBM blends [24]. It has been found that the annealing treatment up to 140℃ for 30 min can alter the structure order of P3HT:PCBM blend. Large PCBM aggregates have been observed, leading PCE to improve from around 1% to 2.3%. After the annealing time was increased up to 60 min at the same temperature, PCE has deteriorated to reach a value of 0.81% [25].

5.2 Results and discussions

5.2.1 UV-visible absorption spectra

Fig.5.3(a) shows the absorption spectra of P3HT:PCBM blended films using different solvents and their co-solvents. Generally, the absorption spectra at the wavelength range 400-640nm are attributed to the P3HT absorption with three different bands (A, B, and C) [10], while the absorption band D is related to the absorption of PCBM [26].

The maximum absorption peak C is found to be around 485nm for thin films prepared using CF and DCB:CF solvents. Using high boiling point solvents (DCB and CB) to prepare the P3HT:PCBM blends have resulted in a red shift in the maximum absorption peak from ~485nm to ~500nm.

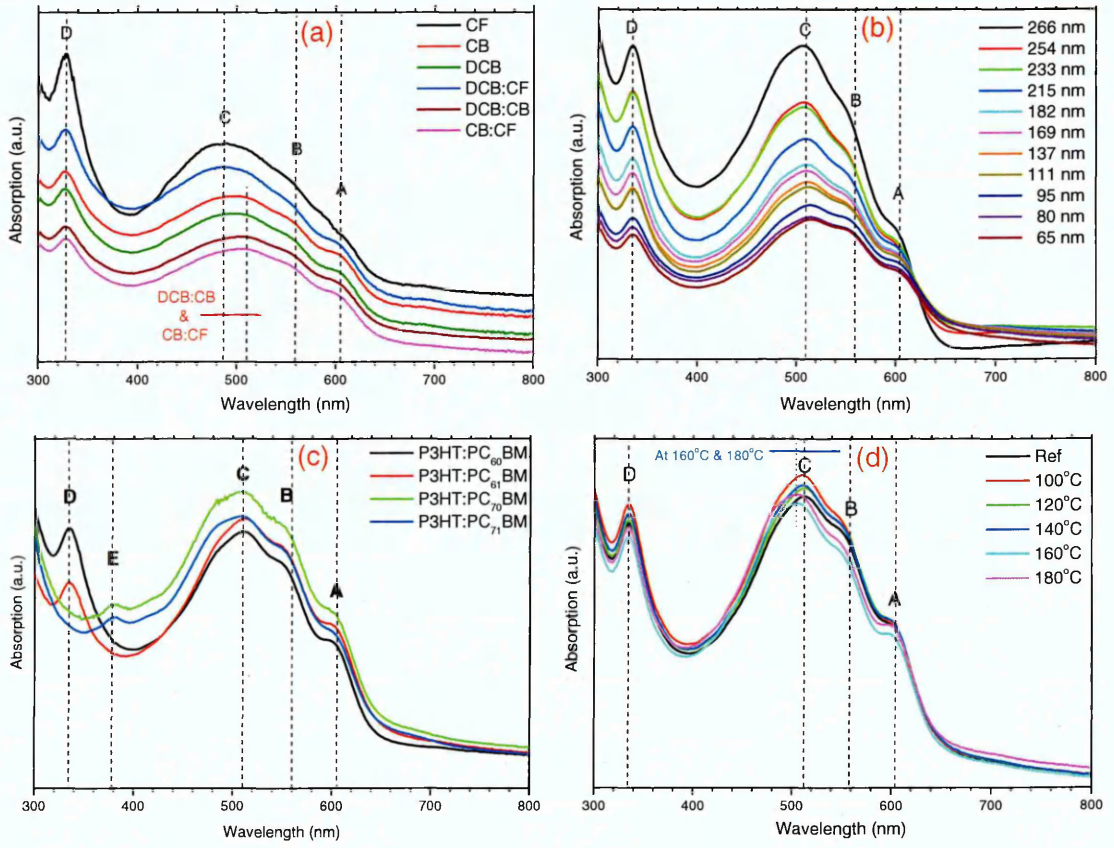

Fig.5.3:UV-visible absorption spectra for the P3HT:PCBM based films using (a) different solvents, (b) different active layer thickness, (c) different fullerene derivatives and (d) different temperature treatment.

Using co-solvents (DCB:CB and CB:CF) have resulted in a further red shift in the maximum peak to about 510nm. The different absorption intensities have been attributed to different film's thickness; the low boiling point of CF results in relatively thicker films than the other used solvents [27]. All the maximum absorption peaks were attributed to the π-π^* electronic transition in the P3HT [28]. The co-solvents based films have demonstrated more pronounced shoulders (A and B) around 605nm and 560nm, respectively.

Band A is attributed to the absorption of the interchain stacking of P3HT whereas band B is ascribed to the extended conjugated polymer [29]. Bands A and B are pronounced clearly when the high boiling point solvent was used which indicate that P3HT chains have not packed well in the case of using low boiling point solvent through blending with PCBM molecules. This has assisted in forming interchain crystalline environment by the aid of using co-solvents. At the same time, the two pronounced shoulders A and B are a strong evidence of improved P3HT interchain packing [9]. The high boiling point solvents facilitate the P3HT:PCBM blends in a favourable structure and better P3HT chain orientation [30]. The P3HT structure arrangement is mainly defined due to the Head-Tail arrangement, rather than a Head-Head arrangement. Pronounced shoulders in the A and B bands indicate a good packing of P3HT stacking planes [31]. Brown and co-authors have argued that the performance of OSC could be enhanced by improving the optical absorption properties of the active layer and the charge carriers' transport which are mainly affected by P3HT chains orientation [32]. The red shift in absorption band A suggests that the use of CF has demonstrated a low degree of P3HT orientation with Head-Head alignment of P3HT monomers while the high boiling point solvents and co-solvents suggest the favourable Head-Tail alignment which affects the optical properties of P3HT [32,33]. The optical bandgap of P3HT:PCBM blended films using different solvents has been determined using Tauc equation (see eqn. 4.6) [34]. Fig.5.4 shows the bandgap estimation for the P3HT:PCBM films, the latter have demonstrated a decrease in the optical bandgap from around 1.9eV in the CF-based film to around 1.8eV in CF:CB-based film. Lee and co-authors have argued that tuning the energy band gap is important for solar cell applications [35]. Therefore, using co-solvents such as CB:CF is found to make the best solvent to produce thin films from P3HT:PCBM blends, however using other co-solvents such as DCB:CB or even CB alone are still well considered [36,37]. Although, thicker films absorb more light compared to thinner films, thicker films however could also increase the series resistance (R_s) and reduce the charge carrier's mobility [11]. Thinner films however are capable of showing nearly 100% conversion of absorbed photons into collected carriers [12] as organic semiconductors are known to have fairly strong absorption coefficients ($10^{5}cm^{-1}$) resulting in high light absorption in films even thinner than 100nm [38].

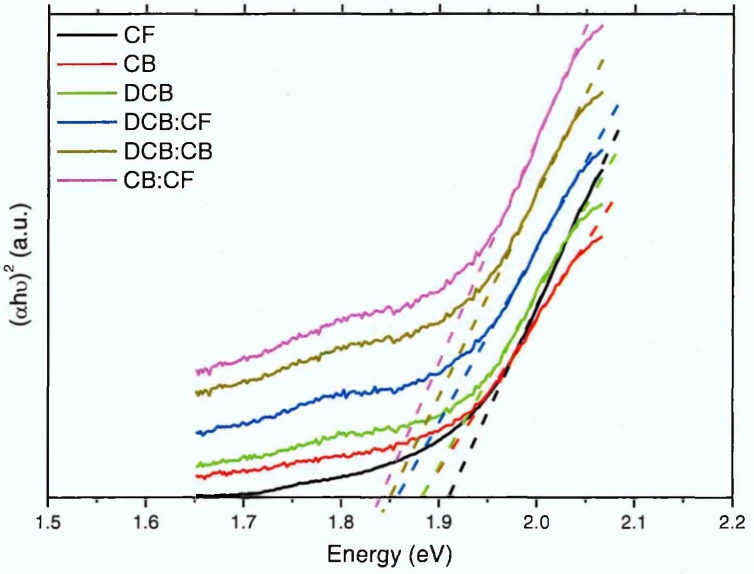

Fig.5.4: The energy bandgap determination for the P3HT:PCBM based films prepared by different solvents and their co-solvents

Fig.5.3(b) shows the absorption spectra of P3HT:PCBM active layers prepared with different thicknesses in the range of 65-266nm using CB:CF co-solvent. The absorption intensity has noticeably varied with the variation in the active layer thickness. No change in the position of the maximum peak (C) as well as bands A and B has been observed due to variations in films' thickness; however band D has exhibited a red-shift of about 6nm. Moreover, using different PCBM derivatives in the P3HT:PCBM blend has resulted in different PCBM absorption peak position as shown in Fig.5.3(c). PCBM absorption spectra have shown two different bands (D and E), $PC_{60}BM$ and $PC_{61}BM$ have exhibited an absorption peak (band D) around 340nm while $PC_{70}BM$ and $PC_{71}BM$ have shown an absorption peak (band E) at around 380nm [39]. Nicolaidis and co-workers have stated that an increase of about 13% in generated photocurrent could be attributed to light absorption by the fullerene molecules within the P3HT:PCBM blends [40]. This means that the photo-generated current due to light absorption by the fullerene component needs to be taken into account in the performance of OSCs systems containing PCBM [39]. $PC_{70}BM$ and $PC_{71}BM$ have shown broader and weaker peaks compared to $PC_{60}BM$ and $PC_{61}BM$ which have shown stronger peaks.

In order to further improve the optical properties of the P3HT:PCBM-based films which were prepared using ~100nm thick films with $PC_{61}BM$ as the acceptor and employing CB:CF as the solvent, these films were subjected to heat treatment at different temperatures as shown in Fig.5.3(d). Upon heat treatment, the active layers have changed their colours from orange/brown to purple/red, as it has already been shown by Manceau and co-authors [41]. All the spectra of P3HT:PCBM active layers have exhibited typical absorption spectra that are identified into four different bands (A, B, C and D). After subjecting the active layer to a heat treatment above 140°C, the maximum absorption peak (C) has exhibited a blue shift to around 500nm which could be attributed to the change in the orientation for the P3HT chain ordering as a result of excessive heat treatment [30]. However, bands A and B have shown no change due to the further heat treatment as well as the absorption band below 400 nm (D), which has not shown any noticeable shift.

5.2.2 XRD results

It is well known that P3HT chain structure has the ability to facilitate their self-orientation into two-dimensional sheets by means of interchain stacking and therefore shows highly crystalline features [33]. This could be controlled by adjusting the films' growth as well as the drying time [30]. Fig.5.5(a) shows the XRD patterns of P3HT:PCBM-based films using different solvents and their mixtures. A single diffraction peak at $2\theta=5.5\pm0.2^{\circ}$ was observed and attributed to the (100) plane. Generally, all the observed peaks are ascribed to the lamella structure of P3HT component of the P3HT:PCBM blend, which suggests a high degree of crystallinity. P3HT lamella stacks could occur either parallel to the substrate (face-on orientation) or perpendicular to the substrate (edge-on orientation); a mixed orientation might also occur, especially in the non-annealed films [42]. The shortest distance between P3HT layers is known as the π-π stacking distance or the d-spacing [43]. The P3HT crystallinity is further improved when high boiling point solvents are used indicating that P3HT chains have exhibited edge-on orientation at the (100) plane, and all the observed peaks are attributed to the P3HT interchain spacing associated with the Interdigitated alkyl chains [44,45].

On the other hand, PCBM is an amorphous environment, which could interrupt P3HT crystalline growth. The high boiling point solvents are thought to give PCBM molecules more time to aggregate and diffuse within the P3HT matrix as described earlier in Fig.3.12 [5, 9]. Using high boiling point solvents could assist the PCBM molecules to move slowly in a vertical direction with the solvent molecules during the wetting time and therefore better homogeneity is expected to occur [9]. The measured XRD patterns were then fitted with one Gaussian peak to calculate the peaks' width and the lattice constants. The grain size of the crystalline structure of the P3HT:PCBM blends were calculated using Scherer equation as mentioned in chapter 4 [46]. However the variation in d-spacing values is not significant, co-solvents-based films have exhibited lower d-spacing values compared to mono-solvents-based films, which suggest a well-packed stacking. The full width at half maximum (FWHM) of (100) phase gives an idea about the degree of crystallisation and the grain size (crystal size). The d-spacing of the CF-based device is found to be ~1.75nm; after using high boiling point solvents such as CB or DCB, this value has reduced to ~1.6nm which is attributed to the good packing of the P3HT stacks as was suggested by the UV-visible spectra. Further increase in the P3HT ordering is demonstrated using co-solvents which result in lower d-spacing values compared to mono-solvents based films. Improving the crystallinity of the organic films can play a key role in obtaining high current densities by enhancing the charge carrier transport properties [47].

Mainly, the d-spacing is representing the distance between P3HT planes or in other words the π-π stacking, therefore, the smaller the d-spacing is further enhanced electrical conductivity [48]. It has been proposed that the π-π stacking of P3HT chains permits hole delocalization between the chains and facilitates a transport route along the interchain direction, rather than only transport along the backbone direction [49]. Among the two transport procedures, charge transport along the backbone is significantly easier than that along the π-π stacking direction [48]. The grain size of the prepared films has demonstrated different values based on the used solvents. While CF-based films have exhibited grain size of ~11nm, the use of high boiling point has considerably increased the grain size to ~14nm and ~15nm in CB and DCB-based films, respectively. The increase in grain size is ascribed to the longer time taken for the P3HT to crystallise [50].

Similar results have been observed by Kekuda and co-authors [47], who have shown that using low boiling point solvent (CF) to process the P3HT:PCBM film has resulted in a smaller grain size of ~8nm, whereas using high boiling point solvent such as Trichlorobenzene (TCB) has resulted in larger grain size of about 19nm [47].

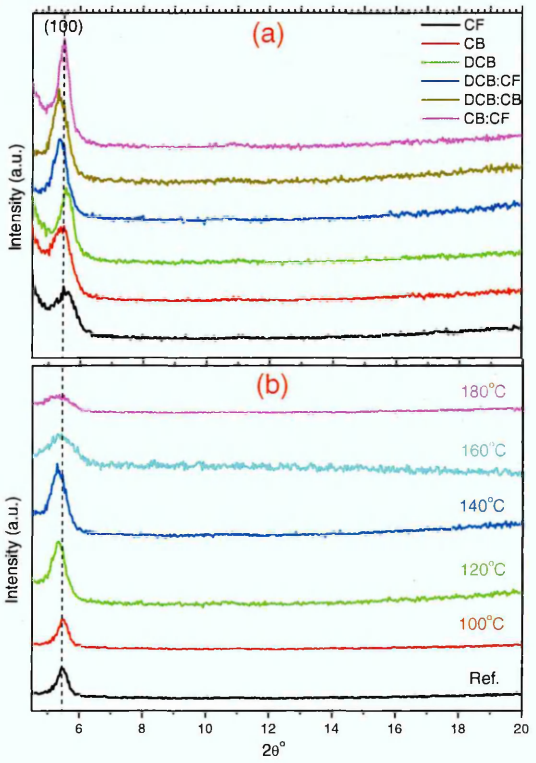

Fig.5.5: XRD patterns for P3HT:PCBM blended in a mono-solvent and co-solvents

Generally, smaller domain size is critical for efficient exciton diffusion in BHJ OSCs; however, efficient charge transport requires high conductivity of the donor material. Therefore, for crystalline donor polymers such as P3HT, high crystallinity and aggregation are desired [50]. Further increase in the grain size has been observed using co-solvents; as an example in CB:CF-based film, where the grain size reached ~21nm. It is well known that the temperature treatment is an essential parameter to improve the organic thin film crystallinity and morphology [51]. Therefore, P3HT:PCBM-based films using CB:CF have been subjected to post-deposition treatment at different temperatures and the XRD results are shown in Fig.5.5(b).

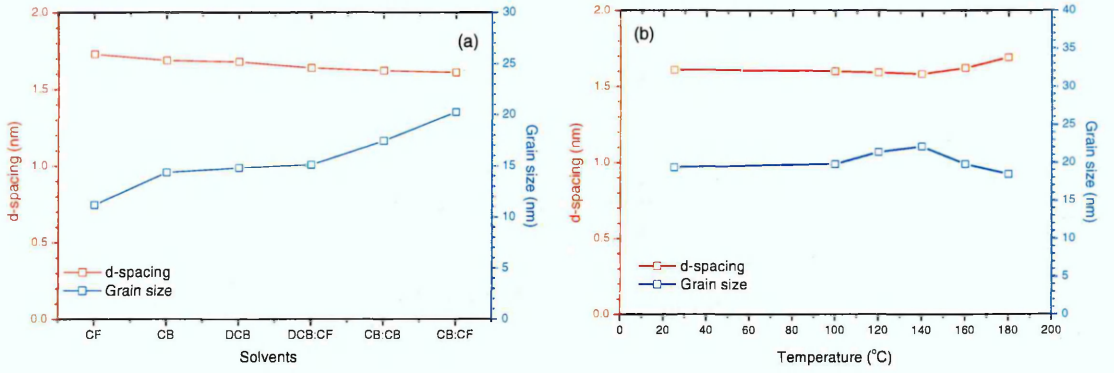

Fig.5.6: Grain size and d-spacing variation for P3HT:PCBM based films prepared using (a) different solvents and (b) treated at different temperatures

No significant change in the peak position has been observed for all the P3HT:PCBM active layers after the heat treatment process. Increasing the post-deposition treatment temperature to 100°C for 10min has demonstrated no significant variation in d-spacing and the grain size (see Fig.5.6). Further heat treatment to 120°C as well as 140°C has resulted in larger grain size and smaller d-spacing. The post-deposition treatment at 140°C has demonstrated the optimum grain size of ~22nm and the lowest d-spacing of about 1.6nm. This indicates that this temperature has resulted in the optimum degree of P3HT crystallinity and well packing of the corresponding planes, which is favourable for efficient charge transport when the delocalized states are oriented in the transport direction. Subjecting the film to further heat treatment at 160°C and 180°C has resulted in deterioration the P3HT:PCBM crystallinity, where the d-spacing increases to approximately1.7nm and the grain size reduced to about18nm.

5.2.3 Morphological study

The variation in the surface morphology of P3HT:PCBM films as a function of different solvents and different post-annealing treatment have been carried out using both AFM and SEM techniques.

5.2.3.1 Morphological analysis using AFM

Fig.5.7 shows the variation in the surface morphology of P3HT:PCBM BHJ films prepared using different chlorinated solvents. CF-based film has revealed a smooth surface with rms roughness of 1.33nm correlating with noticeable pinholes. On the other hand, DCB and CB-based films have demonstrated higher surface roughness with rms values of 3.09nm and 2.04nm, respectively. Mainly, the brighter regions are associated with the PCBM domains while the darker regions are related to the P3HT domains [52].

The diffusion of PCBM molecules within the P3HT main matrix has demonstrated different behaviour as affected by the boiling point of the used solvent. This has influenced the phase separation between the D/A domains. To evaluate the phase separation of the D/A within P3HT:PCBM blends, Qualitative phase analysis was carried out using two-dimensional Fast Fourier Transformation (2D-FFT) analysis. A reduction in the phase separation within the P3HT:PCBM blends prepared in high boiling point solvents (DCB and CB) is observed compared to CF-based films because the 2D-FFT analysis shows an increase in the darker background. The decrease in the phase separation within the P3HT:PCBM blend leads to an enhancement of the dissociation rate of the photo-generated excitons [53]. Further enhancement in the surface morphology has been observed using co-solvents to prepare P3HT:PCBM blend films (see Fig.5.8), which was attributed to the further improvement in the diffusion and distribution of PCBM within the P3HTmain matrix which in turn has resulted in a good interpenetrating network. Surface roughness with the rms values of 3.33nm, 2.34nm and 2.37nm were obtained for DCB:CF, DCB:CB and CB:CF-based films, respectively. The improvement in the interpenetrating network could facilitate charge carrier transport, and hence improved solar cell performance. The phase analysis has revealed a better phase separation between P3HT and PCBM within the P3HT:PCBM blends in the co-solvents based films compared to the mono-solvents based films. The darker region is higher in the case of co-solvents based films, which suggests that the phase separation has become less resulting in improved dissociation rate of the photo-generated excitons [54].

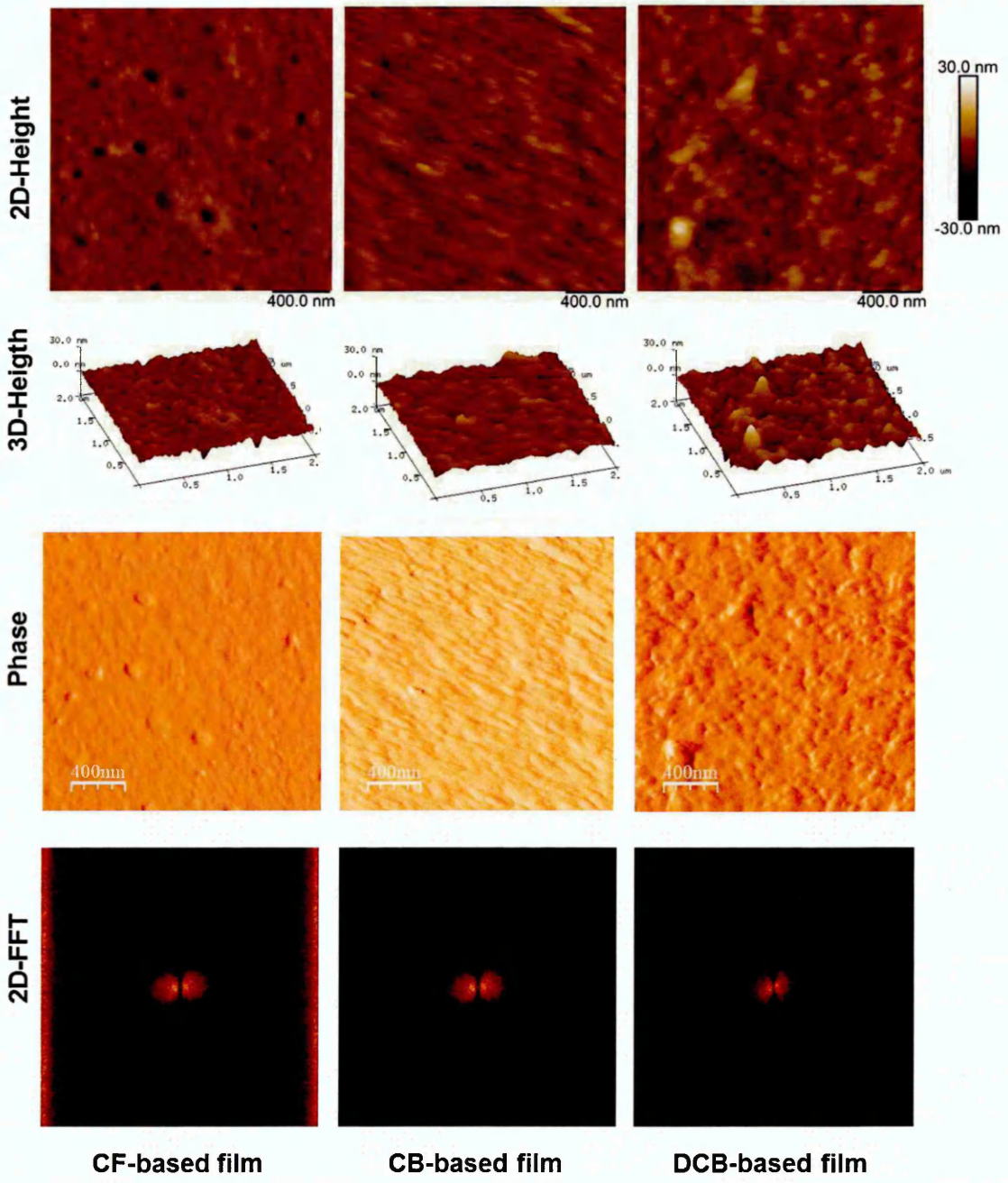

Fig.5.7: 2D and 3D AFM images and phase analysis of the P3HT:PCBM blends prepared by different chlorinated solvents

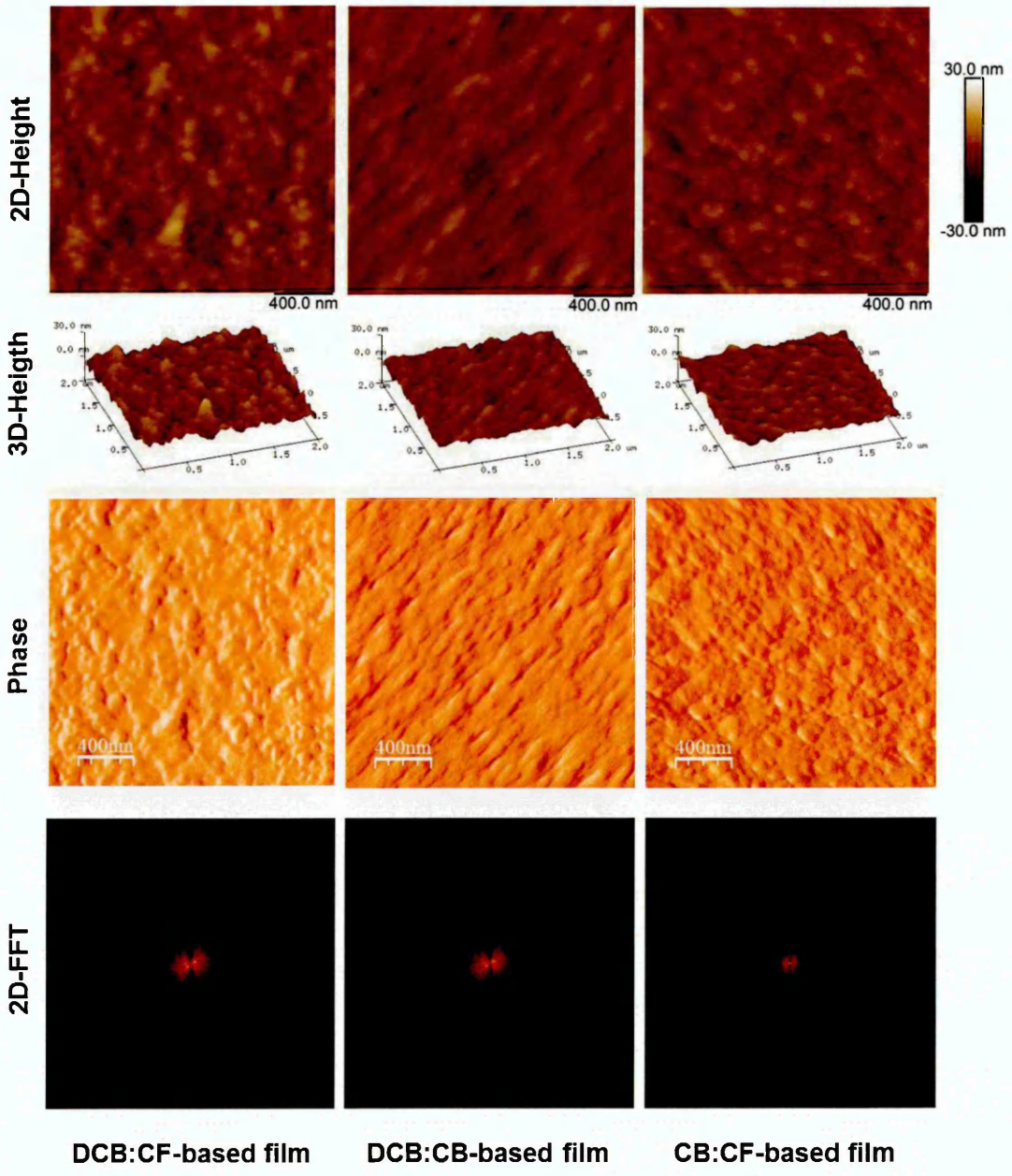

Fig.5.8: 2D and 3D AFM images and phase analysis for P3HT:PCBM blends prepared by different co-solvents

Etxebarria et. al. [55] have identified three different morphologies in the polymer:fullerene blends as shown in Fig.5.9. An illustration of the different distributions of PCBM within P3HT main matrix has been demonstrated in this figure, which leads to three different domain sizes within the final blend. In the case of small domain size (see Fig.5.9(a)) where the PCBM domains are not linked with each other, higher charge carrier's recombination is thought to occur. In large domain size as shown in Fig.5.9(b), there is a scarcity of interface areas within the BHJ, which results in low excitons' separation. A critical balance between the two domains is necessary in order to have moderate domain size as shown in Fig.5.9(c). This is advantageous for higher charge dissociation and improved network for charge transport [55]. Therefore, it is worthwhile mentioning that:

(a) Small domains with a large number of interfaces: Large charge generation yield (high J_{sc}) but non-efficient charge transport (low FF) due to high recombination rate.
(b) Excessively large domains with a lower interface area between the donor and acceptor: Low charge generation yield (low J_{sc}) but good charge transport (high FF).
(c) Intermediate domain size with an optimised interface area: Large charge generation yield (high J_{sc}) and good charge transport (high FF).

In the current study, it has been shown that the co-solvents based films have exhibited the best morphology as compared to the mono solvents. Further treatment to the P3HT:PCBM based films prepared using CB:CF co-solvents was carried out under different post-deposition treatment temperatures and the results are shown in Fig.5.10 and Fig.5.11. AFM images show different surface roughness; the reference P3HT:PCBM film has exhibited a smooth surface morphology with rms of 1.2nm. Subjecting the P3HT:PCBM films to the heat treatment has resulted in rougher film surface. As an example, an rms of 3.3nm has been evaluated for the P3HT:PCBM film when treated at 140°C. The increase in surface roughness is thought to be useful for increasing the contact area between the film and the top metal contact, therefore enhancing J_{sc} [51]. Further increase in the temperature of the post-deposionit heat treatment has resulted in clear phase segregation corresponding to a rougher surface of P3HT:PCBM, where the brighter regions of the surface represent PCBM rich domains [52].

As it has been mentioned earlier, three different nano-morphologies could exist in polymer:fullerene blends, small, intermediate and large nano-morphology domains.

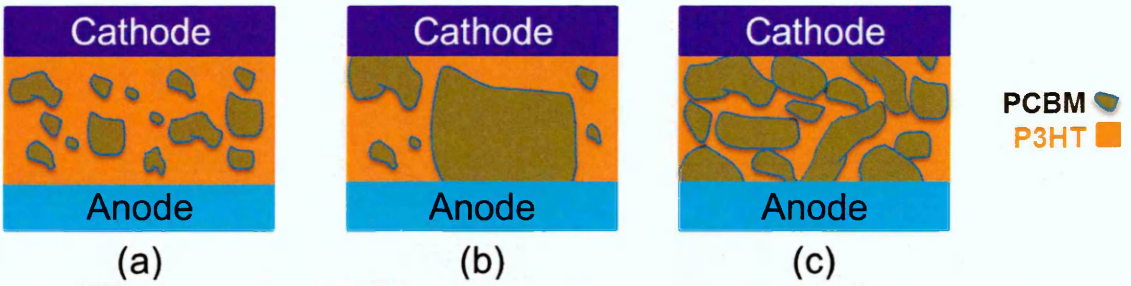

Fig.5.9: Different domain size for P3HT:PCBM blends; (a) small, (b) large and (c) intermediate domain size.

The current results suggest that the P3HT:PCBM films heat-treated at temperatures up to 140°C have exhibited intermediate domains within the blend. This is thought to enhance the interface area and thus result in improved charge generation (larger J_{sc}) and charge transport (larger FF) [55]. Phase analysis of these blends has shown that P3HT:PCBM films heat-treated at a temperature below 140°C have demonstrated less phase separation; the dark region in the 2D-FFT images has increased which suggests an improvement in the film morphology. On the other hand, increasing the temperature above 140°C has shown a decrease in the dark region of the 2D-FFT image. Reducing the phase separation is the key factor for improving the dissociation rate of the photo-generated excitons which therefore results in higher efficiency [54].

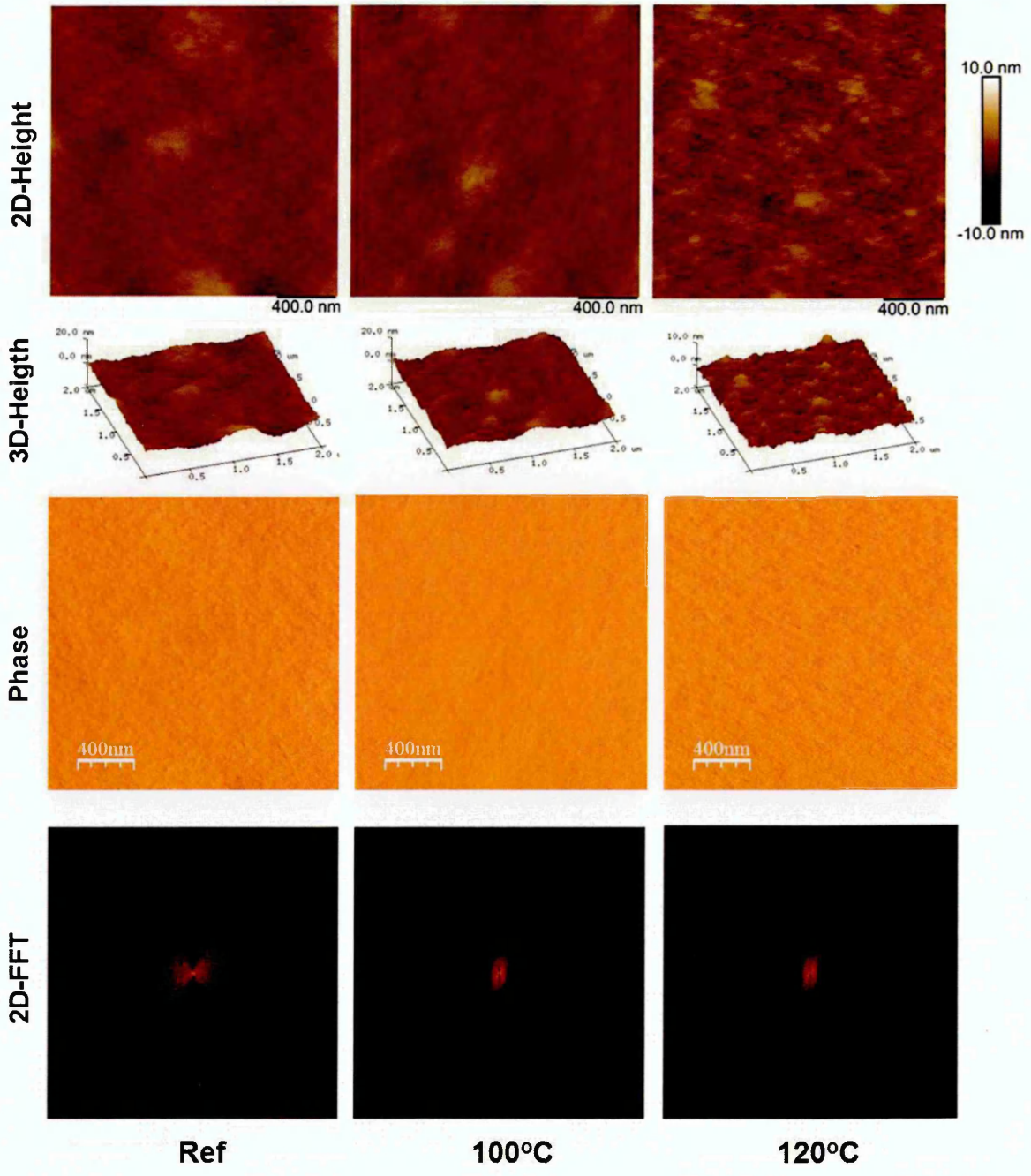

Fig.5.10: 2D and 3D AFM images and phase analysis of un-treated P3HT:PCBM (Ref.) active layers and heat-treated one at 100°C and 120°C

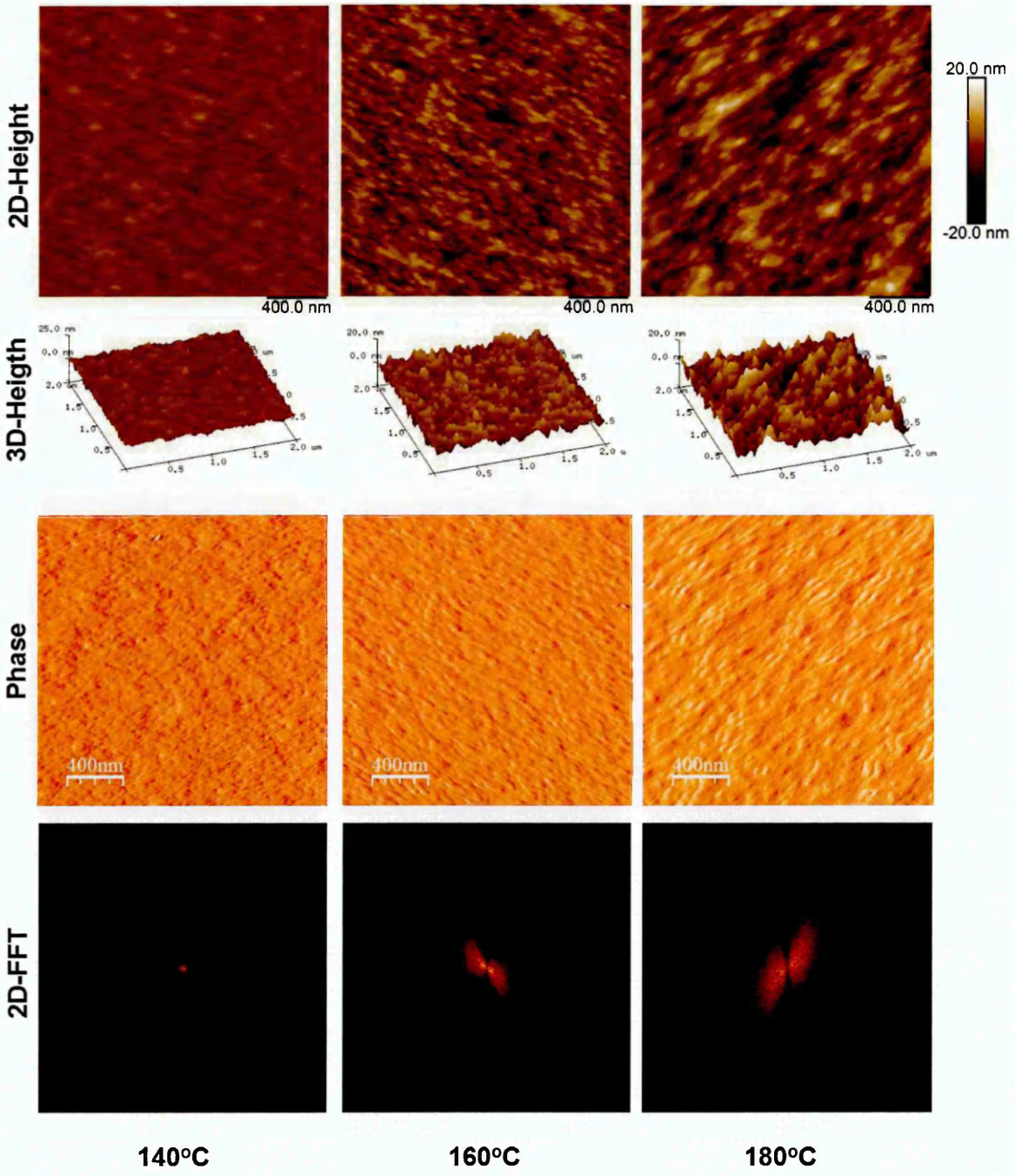

Fig.5.11: 2D and 3D AFM images and phase analysis of P3HT:PCBM active layers heat-treated at 140°C,160°C and 180°C

5.2.3.2 Morphological analysis using SEM

Further details about the P3HT:PCBM-based films' morphology using different solvents have been investigated using scanning electron microscopy (SEM) as shown in Fig.5.12 Generally, the darker regions are attributed to the P3HT domains whereas the lighter regions are related to the PCBM domains [29]. The CF-based film has shown clear pinholes and bubbles like features while the CB-based film has shown a small aggregation of PCBM on the surface. The diffusion of PCBM within the P3HT matrix is varied due to the solvent type and different PCBM clusters and aggregates have been observed on the surface of the mono-solvent-based films compared to the better network for both P3HT and PCBM in the case of co-solvents-based films. The latter observation has suggested that the co-solvents based films have demonstrated intermediate domains [55]. These aggregations have increased in the DCB-based film. On the other hand, using co-solvents have shown the ability of creation better interpenetrating networks; this can easily facilitate the charge carrier' transportation within the blend.

Oklobia and Shafia [22] have pointed out that controlling the formation of PCBM aggregates within the P3HT:PCBM blends is a key factor in maximising PCEs. Several reports have specified that there are no significant variations in the PCBM part upon thermal annealing at around 120-140°C [56,57]. It has been proposed that annealing temperatures above 150°C could result in a significant phase separation which in particular affects the photocurrent generation [22]. It can be stressed here that the use of co-solvents, specifically CB:CF, assists the film drying process and therefore leads to better spatial distribution of linked donor and acceptor domains in the order of exciton diffusion length which ensures effective charge separation and transport as demonstrated in Fig.5.13 [36].

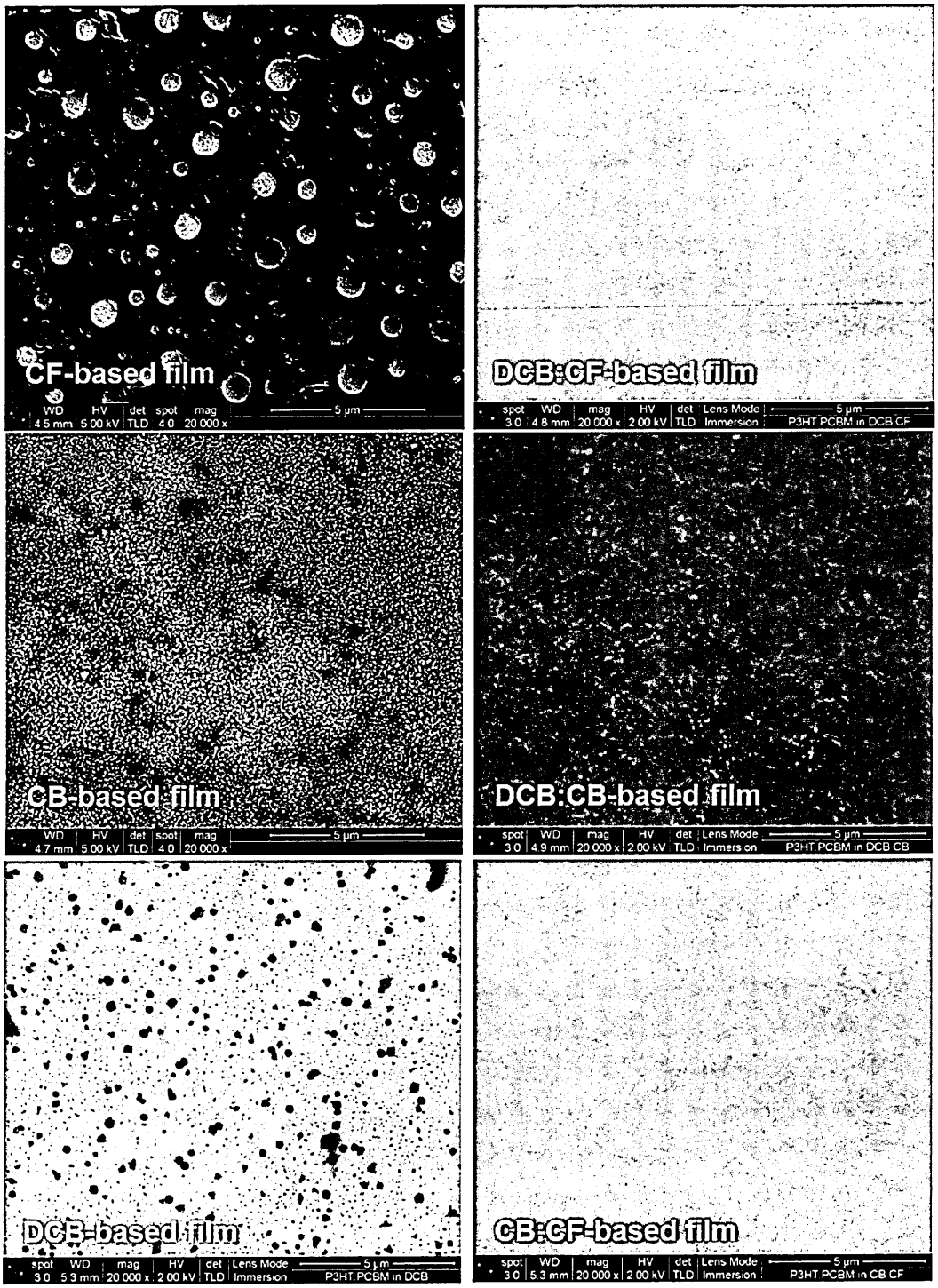

Fig.5.12: SEM images of P3HT:PCBM hybrid films prepared by different solvents and their co-solvents

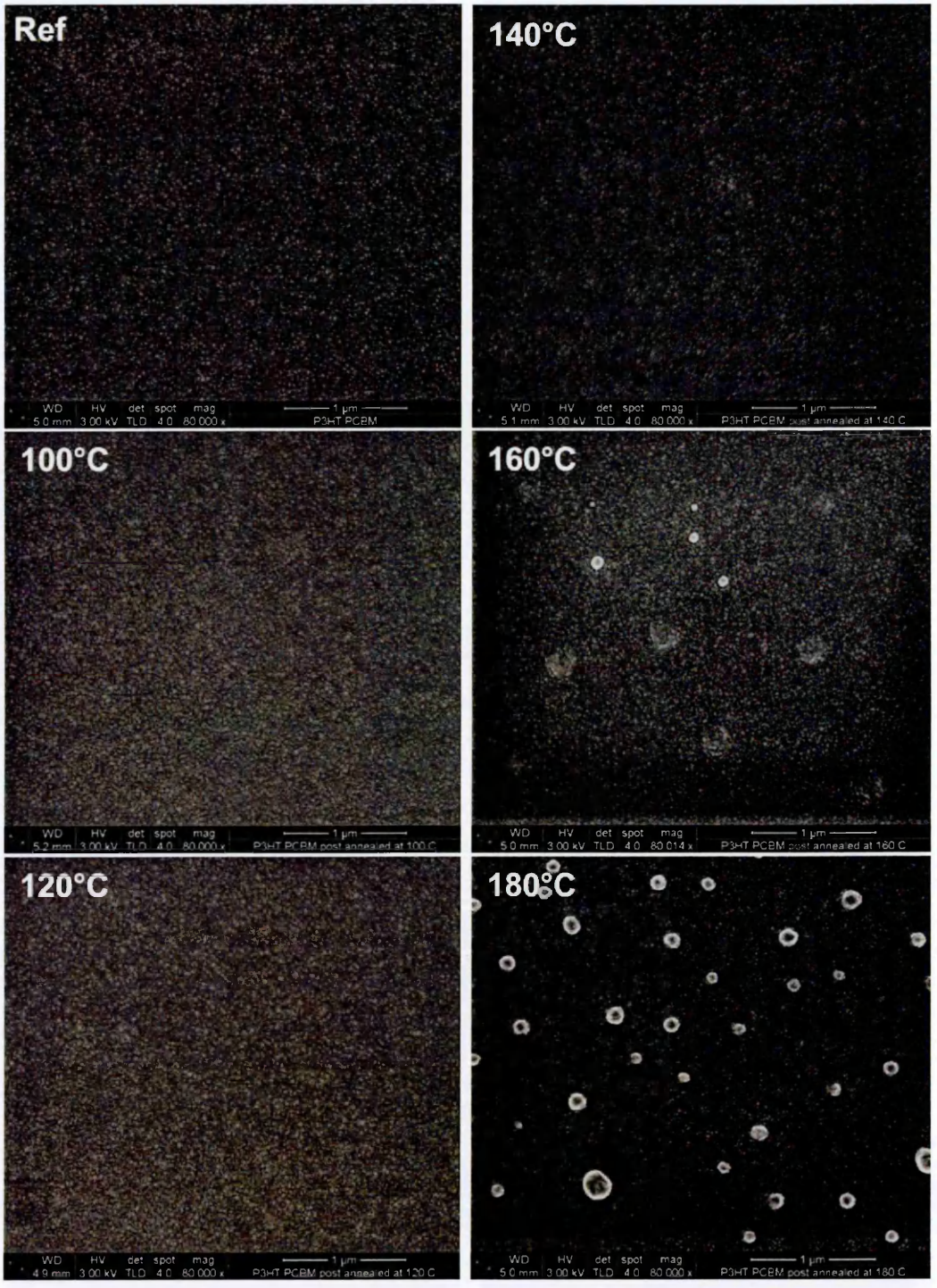

Fig.5.13: SEM images of P3HT:PCBM hybrid films heat treated at different temperatures

After applying heat treatment to the P3HT:PCBM-based films, the morphology of pure P3HT:PCBM films has exhibited smooth surface features with nanoscale morphology. No obvious changes were observed in film morphology as a result of heat-treatment up to 140°C. P3HT:PCBM-based films heat-treated at 160°C have exhibited spherical-like features which were attributed to the formation of PCBM aggregates. Such aggregations could form due to phase separation as a result of heat-treatment at higher temperatures. These aggregates are thought to interrupt charge transport and thus resulting in reducing device performance [58]. Heat-treatment of the P3HT:PCBM-based films has resulted in a significant density of spherical-like nano-scale PCBM aggregations. This could reduce the interface between P3HT and PCBM and therefore reduce the connected domains. In this case, most of the generated charges will recombine before reaching the electrodes and will not contribute to the photocurrent [55].

5.2.4 Electrical conductivity measurements

The electrical conductivity of P3HT:PCBM layers was measured using Interdigitated electrode (IDE) as described earlier in chapter 4. Fig.5.14 shows the variation in the electrical conductivity as a result of using different solvents to process P3HT:PCBM active layer. It is clear that the conductivity has increased significantly in films produced from co-solvents in comparison with films produced by mono-solvents. This increase could be ascribed to the diffusion of PCBM molecules in the P3HT matrix aided by the second solvent as suggested by the XRD and morphological results [48, 49] which is expected to result in reducing charge hopping distance between these molecules and thus enhance films' conductivity [36]. Furthermore, the enhancement in the conductivity of the studied active layers could also be ascribed to the well-ordered structures and the enhancement in the π-π stacking order using co-solvents which result in smaller d-spacing in favour of increasing the films' conductivity [48].

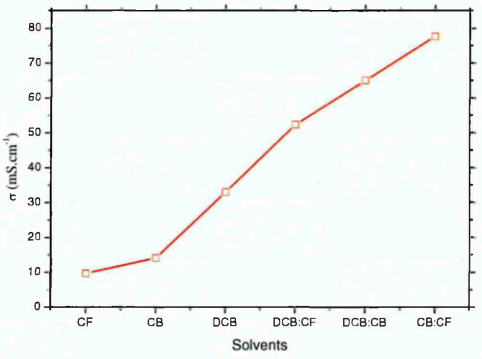

Fig.5.14: The electrical conductivity of P3HT:PCBM active layer as a function of different solvents

5.2.5 Dark current measurements

The electrical characteristics of the studied devices were measured in the dark using current –voltage (I-V) and capacitance-voltage (C-V) measurements. The latter can provide useful information about the diode parameters of the studied solar cells.

5.2.5.1 Extraction of device series resistance (R_s)

It is well established that series resistance (R_s) has a significant impact on the solar cell performance, as it directly affects the FF and consequently PCE of the solar cell [59]. The R_s of the OSCs produced using different solvents have been estimated using dark J-V characteristics as was described in chapter 2 [60]. The CF-based device has exhibited high R_s compared to co-solvents-based devices as shown in Fig.5.15(a). The main reason for this high series resistance in the CF-based device is thought to be the clear presence of pinholes. A high series resistance results in low FF and therefore reduced solar cell efficiency; improved contact properties between the active layer and the back (Al) electrode will result in low series resistance due to the stronger interfacial adhesion [60]. Series resistance is also shown to be reduced by the aid of using high boiling point solvents and co-solvents to process the active layer. The inset of Fig.5.15(a) shows the variation in the series resistance as a function of different solvents. The lowest Rs value was obtained for the DCB:CB and CB:CF-processed devices with the values of 67Ω and 54Ω, respectively. The film thickness, on the other hand, can play a significant role in determining the series resistance [61].

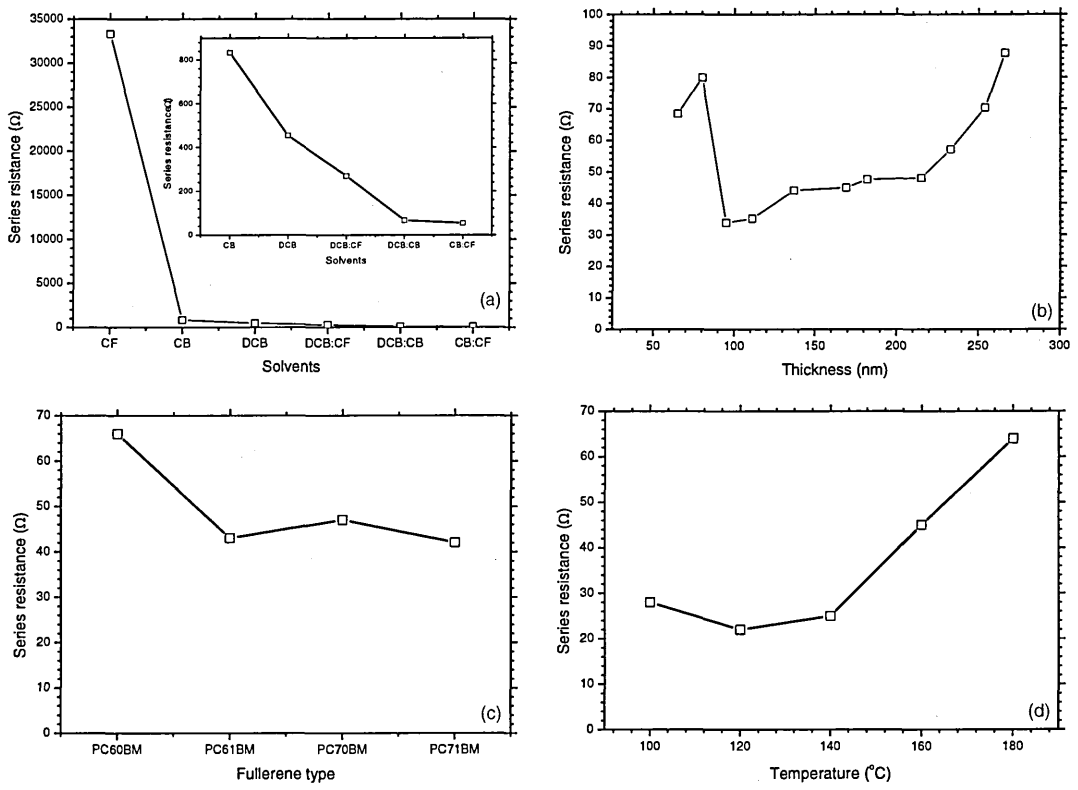

Fig.5.15: Series resistance as a function of, (a) different solvents, (b) different active layer thickness, (c) different fullerenes and (d) different post-annealing temperatures

The P3HT:PCBM solar cells with different active layer thickness have revealed a decrease in R_s with decreasing the active layer thickness as demonstrated in Fig.5.15(b). The highest R_s has been found for the thicker film of 266nm, while the optimum thickness of 95 nm is associated with the lowest R_s. This could be attributed to the carrier diffusion length which will be affected by thicker layer leading to increased possibility of recombination and therefore higher R_s [60]. Further increase in R_s was observed on decreasing active layer thickness below 95nm. The R_s has also been shown to vary using different fullerene types; R_s was found to exhibit a decrease in its value from the value of 93Ω for P3HT:PC_{60}BM-based device to 25Ω for the P3HT:PC_{61}BM-based device as presented in Fig.5.15 (c). Studies have also shown that the formation of metal-polymer bonds (C–Al or C–O–Al bonds) [62,63] as well as Al diffusion could also contribute to the decrease in contact resistance due to thermal annealing. R_s has decreased from ~30Ω in the reference device to ~22Ω for devices heat-treated at 120°C and to 24Ω for devices heat-treated at 140°C as

illustrated in Fig.5.15(d). Further heat-treatment up to 180°C has resulted in a significant increase in R_s to about 64Ω. The observed improvement in R_s values as described above may be attributed to lower interfacial barriers.

5.2.5.2 Evaluation of charge carriers' mobility

In the P3HT:PCBM solar cell, both charge carriers are transported through the percolation pathways; the holes are travelled through the P3HT and the electrons through the PCBM components of the hybrid networks [64]. Shen and co-authors [60] have stated that the transport properties of these charge carriers are limited by their own mobility. The total current is therefore limited by the material with the lower mobility, which is P3HT in this case. Generally speaking, charge carrier mobility in the organic polymers is very low, which mainly related to structural disorder [60]. In π-conjugated polymers, electrical conduction occurs mainly by the process of charge hopping between localised states [65]. However, the interaction between P3HT and PCBM molecules could occur. The electrons and holes recombination is very likely to happen during the two separated transport processes [60]. The charge carrier mobility was determined using SCLC theory as represented by the J-V characteristics of the PEDOT:PSS/P3HT:PCBM/Al device plotted on a double log scale and shown in Fig.5.16. Generally, all the curves have demonstrated a power law dependence of the form $J\alpha V^m$ where m is the gradient of the linear regions of the logJ-logV curves over different applied voltage regions. Once the carriers are injected from the metal to the active layer, their transport through the active layer toward the opposite electrode is determined by the conduction properties of the active layer. The transport properties in a BHJ is mainly described by Ohm's law at low applied voltages due to thermally excited carriers hopping from one isolated state to the next. SCLC on the other hand is due to injected charge carriers into the active layer from the contacts [66]; such contacts are referred to as ohmic contacts. With an ohmic contact, the J-V characteristics often exhibit an ohmic behaviour at low applied voltages up to a certain value since the field due to the injected carriers is negligible compared to that due to the applied voltage. This is manifested by the linear relation with the slope of ~1 displayed on the double log plot.

To calculate the charge carriers' mobility, SCLC theory has been applied to the measured I-V characteristics obtained in this work. Fig.5.17 shows the charge carriers' mobility as a function of different treatment. Fig.5.16 (a) shows the dark J-V characteristics in a double log scale for the P3HT:PCBM-based devices prepared by different solvents and their co-solvents. Different regions of different slopes have been identified in the measured logJ-logV characteristics. Detailed analysis of charge transport as inferred from these regions has resulted in the estimation of charge carrier mobility for the BHJ devices produced using different solvents.

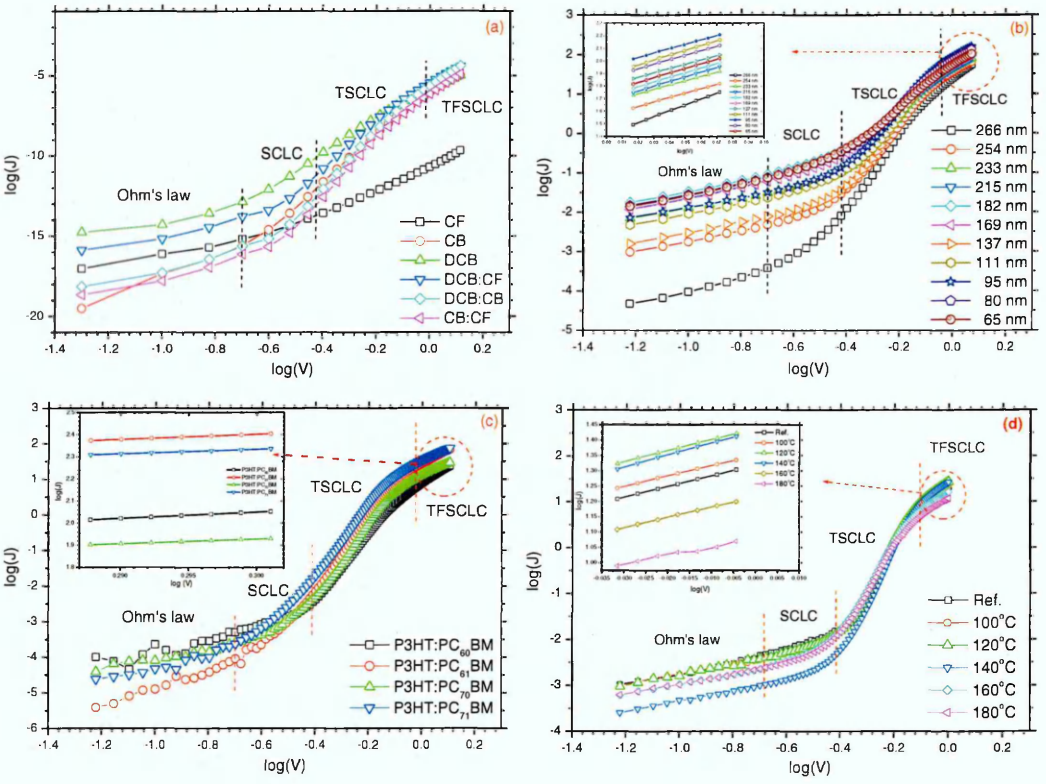

Fig.5.16: J-V characteristics plotted on a double log scale for the determination of charge carriers' mobility of P3HT:PCBM blend treated at different conditions: (a) using different solvents, (b) different active layer thickness, (c) using different fullerenes and (d) post-deposition heat treatment at different temperatures

Devices produced using co-solvents such as DCB:CB and CB:CF have resulted in higher charge carriers' mobility compared to the CF-based device as shown in Fig.5.17(a). This could be attributed to the improved interpenetrating networks of the D/A within the blend, which is believed to facilitate the charge carriers' pathways through preferential direction. Furthermore, the well-ordered π-π stacking in the P3HT:PCBM blend as well as improved electrical conductivity are in among several reasons behind this increase in the charge carriers' mobility [67]. Changing the active layer thickness is thought to play a key role in determining the charge carriers' mobility as it directly affects the diffusion length and the series resistance of the examined devices [60]. Fig.5.16(b) shows the double log J-V plot for the P3HT:PCBM-based devices prepared by using different active layer thicknesses. The charge carrier mobility was found to increase with decreasing layer thickness (see Fig.5.16(b)); the maximum recorded mobility of 1.37×10^{-5} $cm^2.V^{-1}.s^{-1}$ was found for a device with an active layer thickness of 95nm, with smaller values were estimated for thicknesses both above and below 95nm.

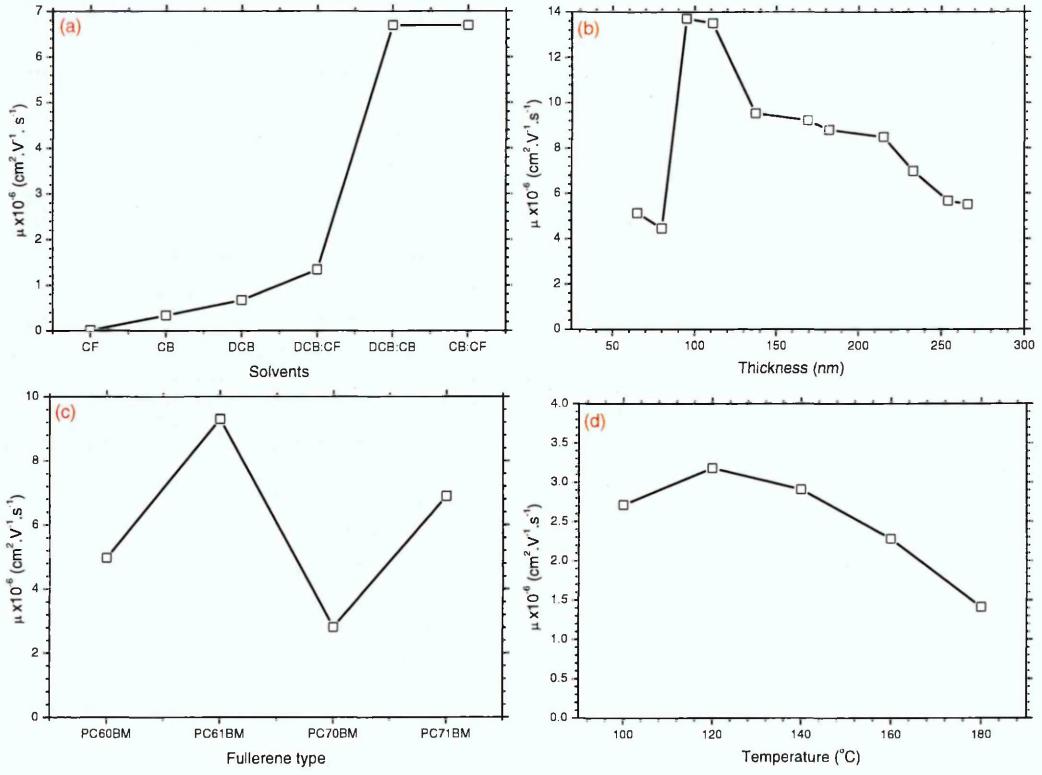

Fig.5.17:Charge carriers' mobility as a function of (a) different solvents, (b) different active layer thickness, (c) different fullerenes and (d) different post-annealing temperatures

The decreased charge carrier mobility for thicker films was ascribed to increasing bulk resistivity of the active layer [68], as well as decreasing electric field (at constant applied voltage) leading to reduced separation rate of excitons, hence decreasing charge carrier mobility [69]. On the other hand, using different fullerenes has shown no significant change in the J-V characteristics as shown in Fig.5.16(c). Different fullerenes have resulted in different charge carriers' mobility of the P3HT-based devices as shown in Fig.5.17(c). The maximum value of mobility of $9.3x10^{-6}$ $cm^2V^{-1}s^{-1}$ was attained for the P3HT:PC_{61}BM-based device whereas the other PCBMs have shown lower charge carriers mobilities. Furthermore, subjecting the P3HT:PCBM based device to different post-deposition heat treatment has affected their charge carriers' mobility as demonstrated in Fig.5.16(d) and Fig.5.17(d). Usually, charge carrier mobility in organic layers is very low, mainly due to structural disorder in the films [60]. The charge carrier mobility was found to increase with increasing temperature of post-deposition heat treatment. Devices subjected to higher treatment temperatures above 140°C have exhibited lower mobility. This could be ascribed to a significant change in the film morphology correlated with the increase in phase separation that results in disturbing the percolation pathways and therefore decreasing the charge carrier mobility. This decrease in mobility might be ascribed to the change in fullerene distribution within the blend which may lead to reduced exciton dissociation specifically above 140°C, which can compromise the OSC performance [70].

5.2.5.3 Metal-semiconductor interface properties

In general, two basic charge transport processes control the J-V characteristics of OSCs; the charge carrier's injection in the BHJ layer by the electrodes and charge transport in the BHJ layer [21]. Carriers injected by the metal electrode into the HOMO and LUMO levels of the polymer have to overcome or tunnel through the barrier of the Schottky junctions formed at the metal-organic interface [60]. Small barriers are formed at the PEDOT:PSS/P3HT interface and the PCBM/Al interfaces [60]. Therefore, the estimation of Schottky barrier height is needed in order to evaluate the difference between the differently produced devices. Fig.5.18(a) shows the plots of LnJ versus the applied voltage for P3HT:PCBM–based devices using different solvents.

The ideality factor and Schottky barrier heights have been calculated from these curves as described in chapter 2 (equ. 2.13 and 2.14) and the results are shown in Fig.5.18(b). Using different solvents has resulted in different dark J-V characteristics with different rectification; the CF-based device has revealed almost symmetric behaviour, which suggests that the device has exhibited the lowest rectification behaviour compared to the other devices. The ideality factor for the CF-based device is found to be 5.9 which suggests high recombination rate in such device. This high value might be attributed to the morphological disorder of the CF-based device which shows clear pinholes and interrupted networks [55]. Using high boiling point solvents has resulted in a decreased recombination rate as demonstrated by the decreasing ideality factor to reach 2.3 and 2.2 in DCB and CB-based devices, respectively. Moreover, the use of co-solvents has shown a further improvement in device quality, again as shown by the lower ideality factor values.

Devices processed by DCB:CF, DCB:CB and CB:CF have demonstrated ideality factors with the values of 2.2, 2 and 2, respectively. This enhancement has been attributed to the improved distribution of PCBM within P3HT matrix and thus improved films' morphology which facilitate the charge carriers' transportation by creating percolation pathways for both charges and hence a decrease in the recombination rate [55]. On the other hand, ϕ_B has demonstrated different values based on the used solvents. CF-based device has shown the lowest ϕ_B with the value of 0.7eV, whereas the DCB and CB-based devices have shown ϕ_B of 0.72eV and 0.75eV, respectively. The increase in ϕ_B has been ascribed to the morphological enhancement which has a significant impact on the interface properties of the BHJ layers. Moreover, the use of co-solvents to prepare the P3HT:PCBM active layers has noticeably increased ϕ_B to reach 0.85eV in CB:CF-based device. Further improvement in the interface properties has been achieved using different fullerene derivatives which have resulted in different energy level alignments. This is so because different PCBM derivatives have different HOMO and LUMO positions (see Fig.5.19), which therefore results in different dark J-V characteristics. Fig.5.20(a) shows the LnJ versus applied voltage for P3HT:PCBM-based devices prepared using different fullerene derivatives.

$PC_{60}BM$-based device has exhibited the lowest ϕ_B with the value of 0.84eV, whereas $PC_{61}BM$ device, has shown the highest ϕ_B value of 0.9eV. This increase in ϕ_B is correlated with a decrease in the ideality factor from 2.39 in the $PC_{60}BM$-based device to 1.68 in the $PC_{61}BM$-based device. Such a decrease in the ideality factor indicates a lower recombination rate; results are demonstrated in Fig.5.20(b).

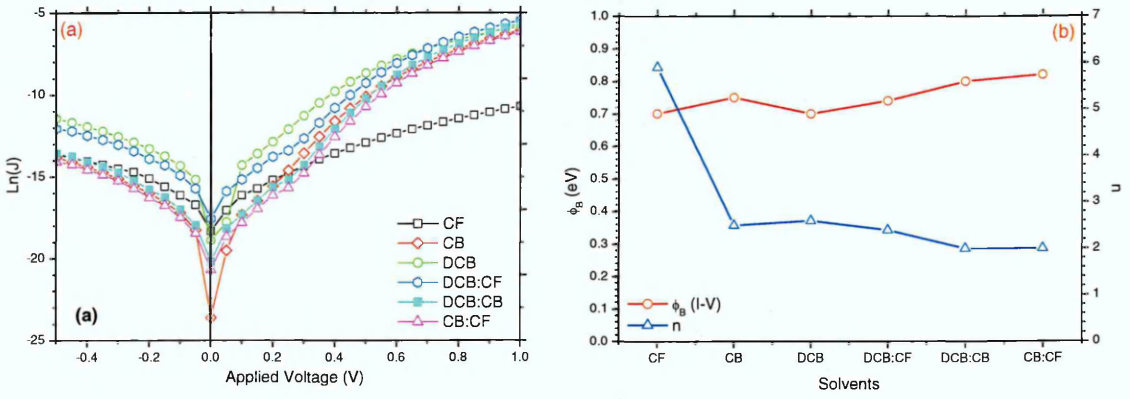

Fig.5.18: (a) Ln(J) versus applied voltage for the P3HT:PCBM-based devices prepared with different solvents under dark condition and (b) The barrier height and the ideality factor versus different solvents

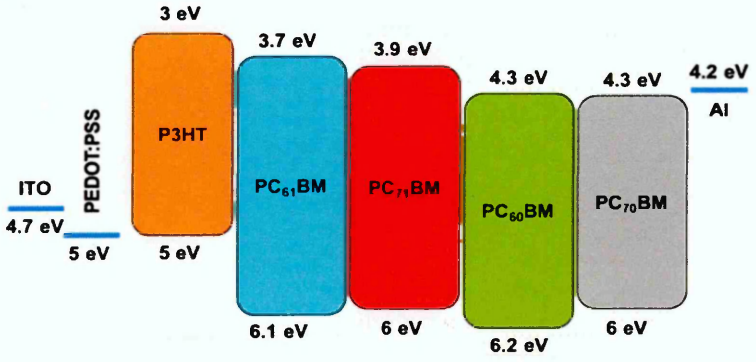

Fig.5.19: The energy level alignment between P3HT and the fullerene derivatives ($PC_{71}BM$, $PC_{61}BM$, $PC_{60}BM$ AND $PC_{70}BM$)

At the PCBM/Al interface, no barrier is created due to the position of PCBM LUMO level with respect to the Al work function [60]. $PC_{70}BM$ and $PC_{60}BM$ have demonstrated the lowest ϕ_B compared to $PC_{61}BM$; the higher ϕ_B results in smaller reverse saturation current density (J_o), therefore, higher open circuit voltage could be resulted from high barrier device as represented by the following equation [71]:

$$V_{oc} = \frac{nkT}{q} \ln\left(\frac{J_L}{J_o} + 1\right) \tag{5.1}$$

Additionally, ϕ_B was estimated using Mott-Schottky analysis of the device C-V characteristics as shown in Fig.5.20(c); the extrapolation of the linear part of the plot of $1/C^2$ versus applied voltage intersects with the voltage axis giving an estimated value of the built-in potential (V_{bi}) [72]. The barrier height values estimated from the C-V measurements have shown good agreement with ϕ_B values extracted from the J-V measurements (see Fig.5.20(b)). The small variation in the built-in potential values estimated from the two measurements could be attributed to the excess capacitance and inhomogeneity of barrier heights [73]. On the other hand, V_{bi} has demonstrated different values due to different fullerene types. The highest V_{bi} has been observed for the $PC_{61}BM$ based device with a value of 0.64V whereas $PC_{60}BM$-based device has demonstrated 0.57V as shown in Fig.5.20(d). It has been reported that the fullerene molecular energy levels play a significant role in determining V_{oc} and V_{bi} in OSCs as it depends on the energy level alignments as described earlier [74]. Because of the constant amount of P3HT in the four blends and different fullerene energy levels, hence the cathode interfaces is different; this may be the main reason for having different V_{bi}, ϕ_B as well as V_{oc} [17]. Another important parameter is the Fermi level position (E_F) within the band gap; this parameter was estimated from the C-V measurements and its values presented in Fig.5.20 (d). No significant change in the E_F position has been observed as a result of changing the fullerene type used as the acceptor. The P3HT:PCBM based devices have been subjected to different post-deposition heat treatment; the results of the dark J-V characteristics in the form of LnJ-V are shown in Fig.5.21(a), and obtained values of n and ϕ_B are presented in Fig.5.21(b). ϕ_B has demonstrated an increase with increased heat treatment temperature up to 140°C and then started to decrease as a result of further heat treatment at higher temperatures which might be due to induced phase separation.

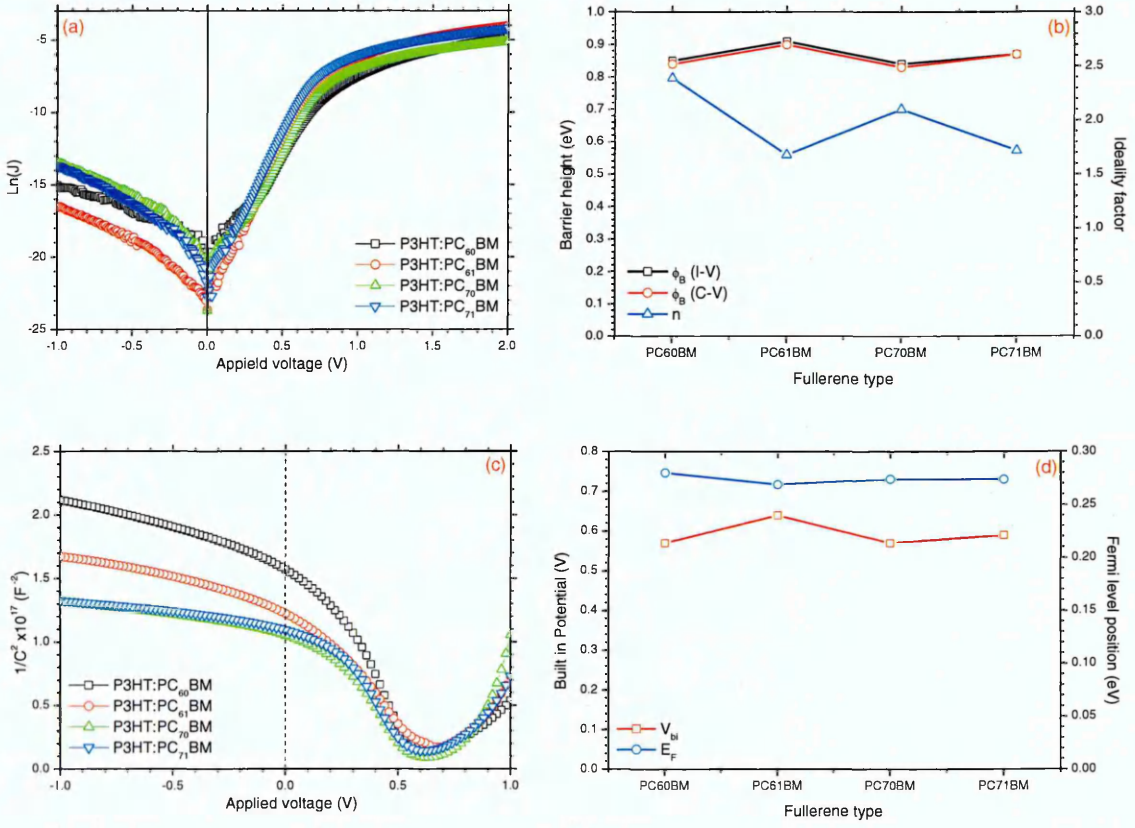

Fig.5.20: (a) Ln(J) versus applied voltage for the P3HT:PCBM-based devices prepared with different fullerene derivatives under dark conditions; (b) The barrier height and the ideality factor versus different fullerene derivatives; (c) Mott-Schottky plot ($1/C^2$ versus Voltage) characteristics for P3HT:PCBM-based devices prepared using different fullerene derivatives and (d) the built-in potential and the Fermi level position versus different fullerene derivatives

It can be assumed that the surface of the blend is made up of P3HT as well as PCBM domains; therefore, the nature of the metal (Al in this case)/semiconductor interface varies due to different energy level alignment across the surface. Fig.5.1 shows an illustration and thus estimations of the energy levels of both contacts occurring on the surface (P3HT/Al and PCBM/Al), where the two domains could exhibit different types of barriers. In the case of Al/P3HT contact (see Fig.5.1(b)) and since $\phi_S > \phi_M$ (ϕ_S and ϕ_M are the semiconductor and metal work functions respectively), Al/P3HT contact will effectively act as a hole blocking contact, whereas Al/PCBM contact (see Fig.5.1(c)) is expected to exhibit a lower

potential barrier (where $\phi_S<\phi_M$) and electrons are thus injected from the LUMO of PCBM to the electrode (Al) [21]. Potscavage and co-authors [75] have reported the relation between V_{oc} and J_o at different temperatures for heterojunction devices. They have found that the reverse saturation current density (J_o) could be thermally activated and the activation energy (barrier height) is related to the HOMO and LUMO positions. Furthermore, a hole only test device (ITO/PEDOT:PSS/P3HT/Al) was produced to help estimate the barrier height and other parameters on heat-treatment at 140°C.

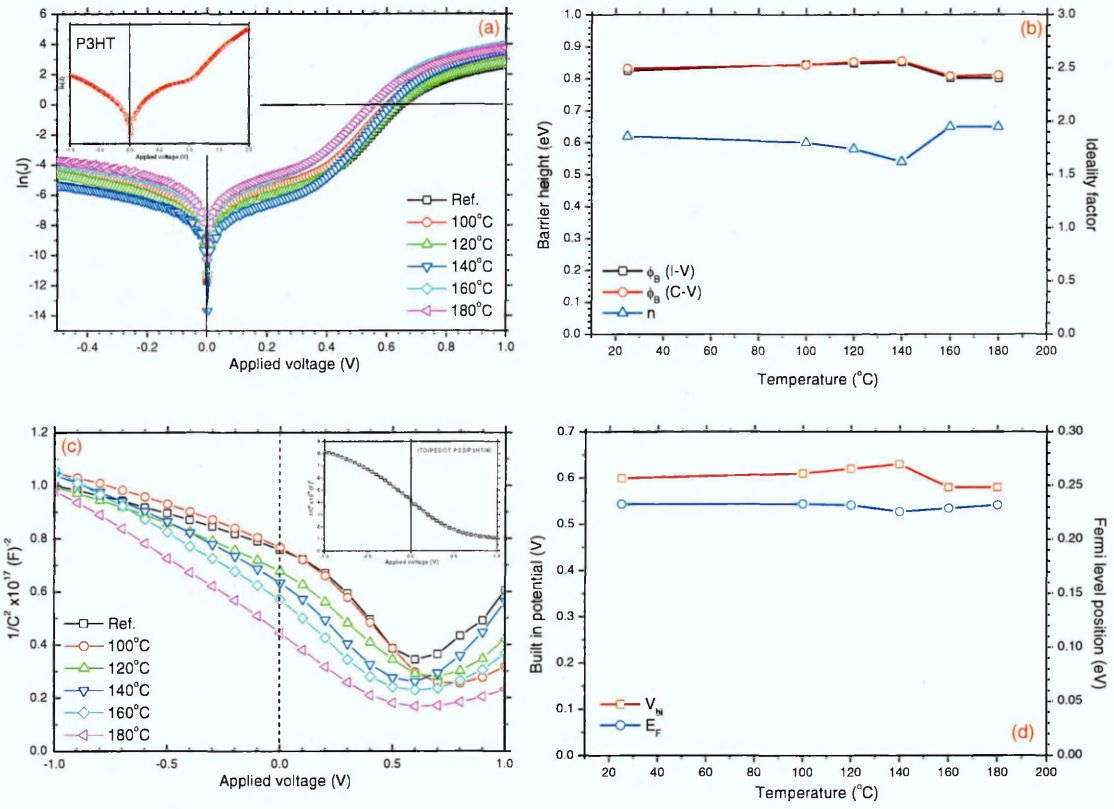

Fig.5.21: (a) Ln(J) versus applied voltage for the P3HT:PCBM-based devices prepared with different post-deposition annealing temperatures under dark condition, (b) The barrier height and the ideality factor versus different post-annealing temperatures (c) Mott-Schottky plot ($1/C^2$ versus Voltage) for P3HT:PCBM-based devices prepared using different post-deposition annealing temperatures and (d) the built-in potential and the Fermi level position versus different post-deposition annealing temperatures

The barrier height for the latter device was found to be in a good agreement with the estimated barrier height for the P3HT:PCBM-based device treated at 140°C; the inset of Fig.5.21(a) shows the ln(J) versus V for the P3HT-based device. A combined bulk- and electrode-limited conduction has been observed in OSCs devices when Al contact was used as an electrode [15]. Moreover, the variation in the barrier height with post-deposition heat treatment at different temperatures could be ascribed to recombination [76]. The ideality factor was found to decrease as a result of heat-treatment up to 140°C reaching 1.62, which implies a lower recombination rate within the device treated at 140°C. On the other side of the device, PEDOT:PSS layer plays an important role in controlling the flow of holes to the ITO electrode. Fig.5.21(c) shows a plot of the Mott-Schottky analysis of C-V measurements carried out for the devices treated under different post-deposition annealing temperatures; the results are shown in in Fig.5.21(d). V_{bi} has exhibited different values with the highest value of 0.63V for P3HT:PCBM-based device treated at 140°C. ϕ_B on the other hand, has shown similar trend whereas E_F has shown no significant change with reference to the LUMO level of P-type material. A good correlation in the results from the J-V and C-V measurements has been observed. Furthermore, the reference (P3HT-based) device has shown ϕ_B of 0.86eV, V_{bi} of 0.63V and similar E_F position.

5.2.6 Solar cell performance:

P3HT:PCBM-based organic solar cells subjected to different treatments have been investigated under illumination. Firstly, the use of different solvents and their co-solvents to control the active layer morphology and structure has resulted in different solar cell performances as shown in Fig.5.22(a). The CF-based device has exhibited the poorest performance with PCE=0.83%, FF=31% and J_{sc}=4.4mA.cm^{-2} correlating with low carriers mobility, low electrical conductivity as well as high series resistance. The highest performance was observed for OSCs processed using the co-solvents CF:CB-based device with PCE=2.73%, FF=53% and J_{sc}=8.3mA.cm^{-2} associated with improved charge carriers' mobility and higher electrical conductivity as well as lower series resistance. Table 5.1 summarised the PV parameters for P3HT:PCBM-based devices prepared using different solvents and their co-solvents. The clear increase in the FF has been attributed to the enhancement of the device resistance, both series and shunt resistances.

The creation of a shunt path has enhanced the shunt resistance and decreased the device leakage current [52]. The enhancement in the blend morphology and the reduced recombination rate using co-solvents compared to CF-based device with clear pinholes are the main reasons for enhancing the FF [77]. The use of co-solvents to process the OSCs has also resulted in an increase in the measured current of these devices; the increase in J_{sc} has been ascribed to the increase in the charge carriers' mobility and the electrical conductivity due to the improved layer structure and the good interpenetrating network [30]. V_{oc}, on the other hand, has remained unchanged for the produced devices; V_{oc} is mainly determined by the difference between the HOMO of the donor and the LUMO of the acceptor [52]. The obvious increase in J_{sc} has resulted in improved PCE by more than 3 times for devices produced in co-solvents. In order to examine the PV performance as a function of different active layer thickness, another set of devices have been prepared using the CB:CF-based device as a reference device, and the results are presented in Fig.5.22(b). As the solar cells performance is mainly characterised by their short-circuit current density (J_{sc}), fill factor (FF) and the open circuit voltage (V_{oc}), a higher PCE is therefore ascribed to higher values of these parameters [78].

Table 5.1: The J-V characteristics for the P3HT:PCBM based devices under illumination

Solvents	V_{oc} (V)	J_{sc} (mA.cm^{-2})	FF (%)	PCE (%)
CF-Based device	0.62	4.4	31	0.83
CB-Based device	0.62	5	49	1.52
DCB-Based device	0.62	5.6	50	1.72
DCB:CF-Based device	0.62	6.6	52	2.12
DCB:CB-Based device	0.62	7.4	53	2.44
CB:CF-Based device	0.62	8.3	53	2.73

Improved OSC performance could only take place once the photo-generated carriers are extracted with lower recombination loss; hence the fill factor of the solar cell is limited by the carriers' diffusion length (L_d) according to the following relation [51]:

$$L_d = \mu\tau E \qquad (5.2)$$

where τ is the carrier recombination lifetime and E is the electrical field. Therefore, to prevent charge recombination L_d must be higher than the active layer thickness; higher mobility or thinner active layer is very important for charge carrier extraction. PCE and other performance parameters were found to increase with decreasing the active layer thickness until reaching an optimum thickness of 95nm; this thickness was shown to exhibit a PCE of 3.84% with J_{sc} 12.6mA.cm^{-2} and FF 50% as summarised in Table 5.2. The V_{oc}, on the other hand, was found to be constant within the range 0.6-0.62V. Devices with active layer thickness larger than 95nm have demonstrated a deteriorated performance compared to those with the optimum film thickness. In general, PCE of organic solar cells are limited by two factors; low carrier mobility and short exciton diffusion lengths [68]. The current density was found to decrease when the photoactive layer thickness increased. The increase in the series resistance could be the main reason for the decreased FF in thicker films based devices as well as the devices with the active layer thickness below 95nm [16]. Further enhancement in the solar cell performance was carried out using different fullerene derivatives as shown in Fig.5.22(c). It has been shown that different PCBM types with different HOMO and LUMO positions have a significant impact on the organic solar cells properties such as V_{oc} [19]. P3HT:PC_{61}BM-based device has exhibited the highest device performance as shown in Table 5.3 with PCE reaching 4.2% corresponding to FF of 62%, V_{oc} of 0.65V and J_{sc} of 10.4mA.cm^{-2}. On the other hand P3HT:PC_{60}BM-based device has shown lowest performance with PCE of 2.6%, FF of 52%, V_{oc} of 0.61V and J_{sc} of 8.2mA.cm^{-2}. Moreover, P3HT:PC_{70}BM-based device has shown PCE of 3%, FF of 52%, V_{oc} of 0.62V and J_{sc} of 9.3mA.cm^{-2} and P3HT:PC_{71}BM based device has shown PCE of 3.9%, FF of 58%, V_{oc} of 0.64V and J_{sc} of 10.4mA.cm^{-2}. It could be pointed out that V_{oc} has exhibited different values depending on the used fullerene type, all of which are of sufficiently high values. It has been reported that high V_{oc} could be ascribed to sufficiently low leakage current density in the solar cell devices [71,79]. FF of the studied devices has also exhibited higher values in P3HT:PC_{61}BM compared to other devices, which could be attributed to the low series resistance (R_s) [80]. The increase in J_{sc} could be related to the higher charge carrier mobility as well as the lower recombination rate leading to high FF. Furthermore, higher V_{oc} could also contribute in increasing the overall power conversion efficiency.

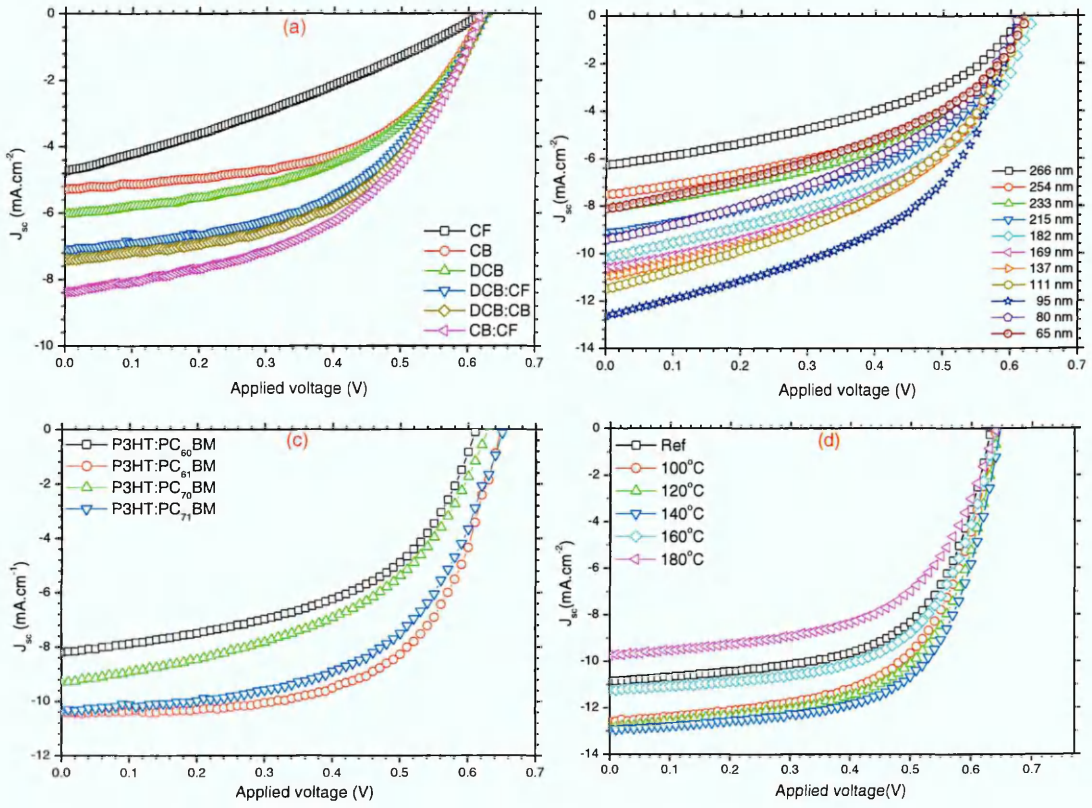

Fig.5.22: J-V characteristics for P3HT:PCBM-based devices under AM 1.5 solar simulator source of 100mW.cm^{-2}: (a) Using different solvents, (b) using different active layer thickness, (c) using different fullerene derivatives and (d) using different post-annealing heat treatment

Controlling the device parameters is essential to obtain good device performance. Further improvement in the device characteristics and efficiency is required. The next section will cover the post-deposition heat treatment for the devices based on the optimum solvents; optimum active layer thickness and optimum fullerene derivatives all combined in one device and treated with different post- deposition heat treatment temperatures. Fig.5.22(d) shows the J-V characteristics of P3HT:PCBM devices subjected to different post-deposition heat treatment under illumination and the calculated parameters are summarised in Table 5.4.

Table 5.2: Performance parameters of the P3HT:PCBM-based devices produced with different active layer thickness

Active layer thickness (nm)	V_{oc} (V)	J_{sc} (mA.cm^{-2})	FF %	PCE %
266	0.61	6.27	44	1.68
254	0.62	7.53	49	2.30
233	0.62	8.1	48	2.40
215	0.62	9.1	47	2.64
182	0.63	10	47	2.98
169	0.62	10.6	47	3.10
137	0.62	11	48	3.24
111	0.61	11.5	48	3.36
95	0.61	12.6	50	3.84
80	0.61	9.4	44	2.53
65	0.62	8.1	44	2.20

Table 5. 3: Solar cell parameters for P3HT:PCBM-based devices with different fullerene derivatives

Devices based on fullerene	V_{oc} (V)	J_{sc} (mA.cm^{-2})	FF %	PCE %
$PC_{60}BM$-Based device	0.61	8.2	52	2.6
$PC_{61}BM$-Based device	0.65	10.4	62	4.2
$PC_{70}BM$-Based device	0.62	9.3	52	3
$PC_{71}BM$-Based device	0.64	10.4	58	3.9

The best PV performance was demonstrated by P3HT:PCBM device heat-treated at 140°C with PCE=5.5%, J_{sc}=12.9mA.cm^{-2}, FF=65.6% and V_{oc}=0.65V, whereas the reference P3HT:PCBM device has exhibited PCE=4.3%, J_{sc}=10.86mA.cm^{-2}, FF=62.8% and V_{oc}=0.63V. Upon heat treatment at higher temperatures up to 180°C, the PCE has degraded to reach 3.6% with J_{sc}=9.74mA.cm^{-2}, FF=57.8% and V_{oc}=0.62V. The improvement in J_{sc} in devices subjected to heat-treatment at 140 °C could be ascribed to the enhancement in the film morphology which facilitates more charge carrier percolation pathways and hence increased J_{sc} [55, 70]. Due to the nano-morphology and the difference between electron and hole mobilities, BHJ organic solar cells generally exhibit lower FF than the inorganic solar cells. Additionally, the interface between the active layer and metal contact plays a significant role in defining the FF value of the OSCs [81]. FF has improved from 62.8% to 65.5% when devices were subjected to heat-treatment at temperatures up to 140°C; this treatment has also been shown to reduce R_s. The latter is one of several reasons leading to improvement in FF as well as the control of P3HT:PCBM blends morphology which is essential to restrain recombination [59].

Table 5. 4 P3HT:PCBM organic solar cell parameters as a function of different post-deposition treatment temperature.

Devices based on temp.	V_{oc} (V)	J_{sc} (mA.cm^{-2})	FF (%)	PCE(%)
P3HT:PCBM (Ref.)	0.63	10.86	62.8	4.3
P3HT:PCBM (100°C)	0.64	12.56	62.2	5
P3HT:PCBM (120°C)	0.64	12.8	62.8	5.15
P3HT:PCBM (140°C)	0.65	12.9	65.6	5.5
P3HT:PCBM (160°C)	0.64	11.23	62.6	4.5
P3HT:PCBM (180°C)	0.64	9.74	57.8	3.6

5.2.7 OSCs Stability

OSCs' long-term stability is one of the main objectives of the current research programme as well as other researchers worldwide. Device stability study in the current work has been carried out to understand the device performance over extended periods of time; Fig.5.23 shows the stability of the P3HT:PCBM-based devices after optimisation of the active layer thickness for a period of 41 days. The device PCE has shown a decrease of about 71% from 3.84% to 1.12% after this period, while, FF has reduced in about 40% from 50% to 30%. Moreover, J_{sc} has shown a decrease of about 50% from 12.6mA.cm^{-2} to 6.24mA.cm^{-2}, while V_{oc} has exhibited no significant change in the value of 0.605±0.05V. It could be argued that controlling the active layer thickness is crucial to achieve high device characteristics with good stability. However, 41days test period is not sufficient to prove the required stability for such devices. Degradation of the studied OSCs mainly happens due to the decrease in J_{sc} and FF. The decrease in the FF is correlated with the increase in the R_s while the decrease in J_{sc} is attributed to the change in the blend morphology over the prolonged test period, which is thought to impact on the optical properties of the blend [83]. OSC devices that have been optimised through post annealing treatment have demonstrated better stability over a longer period of time as shown in Fig.5.24.

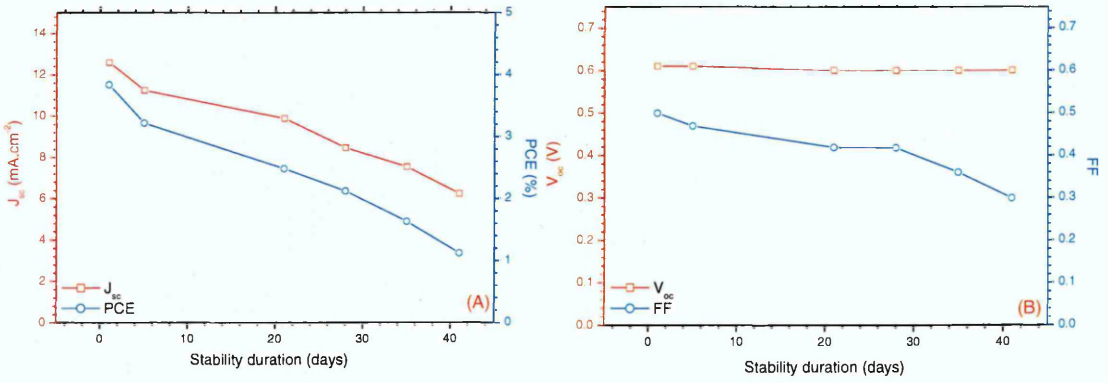

Fig.5.23: Stability of the P3HT:PCBM-based device after optimisation of the active layer thickness

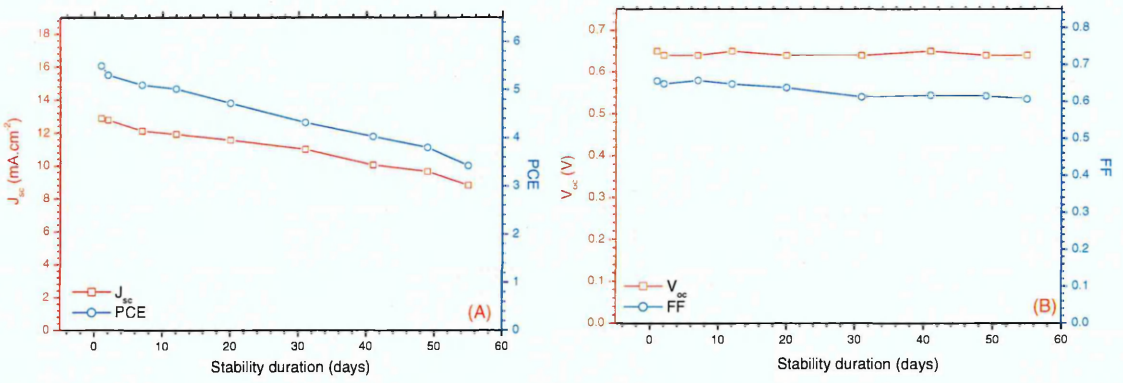

Fig.5.24: Stability of the P3HT:PCBM-based device optimised in post deposition heat treatment

Although the degradation of the PCE is about 38% by decreasing from 5.5% to 3.42% after 55 days, which is close to the level of the degradation of devices optimised in thickness but over longer testing time. This therefore shows that the post deposition heat treatment has enhanced the duration of device stability and also the resistance of the devices as the FF has exhibited a decrease of about 8% from 66% to 61% over the 55 days of testing. This improvement has been attributed to the enhancement in the device series resistance (R_s) as well as the interface properties after post annealing treatment. Voroshazi and co-authors [83] have shown that the FF can be altered by engineering the interface properties of the cathode/organic interfaces. Moreover, V_{oc} has remained almost with no significant change and the J_{sc} has shown a decrease in about 32% from 12.9mA.cm^{-2} to 8.81mA.cm^{-2}.

5.3 Summary

Different strategies were carried out in order to improve the performance of P3HT:PCBM-based solar cells; these are employing different solvents and their co-solvents, preparing different active layer thickness, selecting the optimum PCBM among different PCBM's derivatives and finally post-annealing treatments for the optimum combined devices. Firstly, the morphology and crystallinity of polymer blends have presented significant improvement as a result of using mixed solvents. OSCs devices produced in co-solvents CB:CF has demonstrated a noticeable increase in its performance with improved PCE from 0.83% in the CF-based device to 2.73% in CB:CF-based device. Using the optimum solvent (CB:CF), P3HT:PCBM solar cells were fabricated with a different active layer thickness in the range 65-266nm. The main aim of this part of the study is to study the thickness dependence of the charge carriers' mobility using SCLC theory; the mobility was found to decrease with increasing film thickness. The PV performance was evaluated for these devices as a function of active layer thickness and the maximum PCE of 3.84% was recorded for the device with 95nm active layer thickness. In addition, OSCs based on P3HT blended with different fullerene have been investigated using the optimum solvents (CF:CB) and the optimum active layer thickness (95nm). The main purpose was to improve the open circuit voltage by using different HOMO and LUMO level for different PCBM derivatives. Optimum device performance was associated with $PC_{61}BM$ as the acceptor material with higher LUMO energy level which has resulted in improving open circuit voltage. PCE of 4.2% and fill factor of 62% have been obtained for such blends with J_{sc} and V_{oc} of 10.4 $mA.cm^{-2}$ and 0.65V, respectively. Finally, the effect of post deposition annealing (at different temperatures in the range 100-180°C) on the charge transport as well as PV properties of P3HT:PCBM bulk heterojunction (BHJ) thin films was investigated using the above mentioned parameters. The heat-treatment has shown to result in significant impact on the morphology of the BHJ films. Samples heat-treated at 140°C have exhibited significantly improved PV performance with PCE reaching 5.5%, and FF approaching 66%. Furthermore, the device has shown a good stability for about 55 days with a decrease in PCE in about 35%, FF in about 8% and J_{sc} in about 32% while V_{oc} has remained almost unchanged.

References

[1] Mihailetchi, V. D., Xie, H., de Boer, B., et.al. (2006). Origin of the enhanced performance in poly (3-hexylthiophene):[6, 6]-phenyl C 61-butyric acid methyl ester solar cells upon slow drying of the active layer. Applied physics letters, 89(1), 012107.

[2] Zhang, F., Jespersen, K. G., Björström, C., Svensson, M., Andersson, M. R., Sundström, V., ... & Inganäs, O. (2006). Influence of solvent mixing on the morphology and performance of solar cells based on polyfluorene copolymer/fullerene blends. Advanced Functional Materials, 16(5), 667-674.

[3] Hoth, C. N., Schilinsky, P., Choulis, S. A., & Brabec, C. J. (2008). Printing highly efficient organic solar cells. Nano letters, 8(9), 2806-2813.

[4] Eom, S. H., Park, H., Mujawar, S. H., et.al. (2010). High efficiency polymer solar cells via sequential inkjet-printing of PEDOT: PSS and P3HT: PCBM inks with additives. Organic Electronics, 11(9), 1516-1522.

[5] Reisdorffer, F., Haas, O., Le Rendu, P., & Nguyen, T. P. (2012). Co-solvent effects on the morphology of P3HT: PCBM thin films. Synthetic Metals, 161(23), 2544-2548.

[6] Morvillo, P., Grimaldi, I. A., Diana, R., et.al. (2013). Study of the microstructure of inkjet-printed P3HT: PCBM blend for photovoltaic applications. Journal of Materials Science, 48(7), 2920-2927.

[7] Liu, J., Shao, S., Wang, H., et.al. (2010). The mechanisms for introduction of n-dodecylthiol to modify the P3HT/PCBM morphology. Organic Electronics, 11(5), 775-783.

[8] Wang, T., Pearson, A. J., Lidzey, D. G., & Jones, R. A. (2011). Evolution of structure, optoelectronic properties, and device performance of polythiophene: fullerene solar cells during thermal annealing. Advanced Functional Materials, 21(8), 1383-1390.

[9] Sun, Y., Liu, J. G., Ding, Y., & Han, Y. C. (2013). Controlling the surface composition of PCBM in P3HT/PCBM blend films by using mixed solvents with different evaporation rates. Chinese Journal of Polymer Science, 31(7), 1029-1037.

[10] Ramani, R., & Alam, S. (2013). A comparative study on the influence of alkyl thiols on the structural transformations in P3HT/PCBM and P3OT/PCBM blends. Polymer, 54(25), 6785-6792.

[11] Peet, J., Wen, L., Byrne, P., et.al. (2011). Bulk heterojunction solar cells with thick active layers and high fill factors enabled by a bithiophene-co-thiazolothiazole push-pull copolymer. Applied Physics Letters, 98(4), 15.

[12] Park, S. H., Roy, A., Beaupré, S.,et.al. (2009). Bulk heterojunction solar cells with internal quantum efficiency approaching 100%. Nature photonics, 3(5), 297-302.

[13] Pfattner, R., Rovira, C., & Mas-Torrent, M. (2015). Organic metal engineering for enhanced field-effect transistor performance. Physical Chemistry Chemical Physics, 17(40), 26545-26552.

[14] Yakuphanoglu, F., & Anand, R. S. (2010). Charge transport properties of an organic solar cell. Synthetic Metals, 160(21), 2250-2254.

[15] Lou, Y., Wang, Z., Naka, S., & Okada, H. (2012). Charge transport characteristics in P3HT: PCBM organic blends under illumination: Influence of metal work functions. Chemical Physics Letters, 529, 64-68.

[16] Guerrero, A., Marchesi, L. F., Boix, P. P., et.al. (2012). How the charge-neutrality level of interface states controls energy level alignment in cathode contacts of organic bulk-heterojunction solar cells. ACS nano, 6(4), 3453-3460.

[17] Qi, B., Zhou, Q., & Wang, J. (2015). Exploring the open-circuit voltage of organic solar cells under low temperature. Scientific reports, 5.

[18] Montero, J. M., Bisquert, J., Garcia-Belmonte, G., et.al. (2009). Trap-limited mobility in space-charge limited current in organic layers. Organic Electronics, 10(2), 305-312.

[19] Li, H., Zhang, Z. G., Li, Y., & Wang, J. (2012). Tunable open-circuit voltage in ternary organic solar cells. Applied Physics Letters, 101(16), 163302.

[20] Kirchartz, T., Gong, W., Hawks, S. A., et.al. (2012). Sensitivity of the Mott–Schottky analysis in organic solar cells. The Journal of Physical Chemistry C, 116(14), 7672-7680.

[21] S. S.M., Semiconductor Devices Physics and Technology, 2nd ed., New York: Wiley, 2001.

[22] Oklobia, O., & Shafai, T. S. (2013). A quantitative study of the formation of PCBM clusters upon thermal annealing of P3HT/PCBM bulk heterojunction solar cell. Solar Energy Materials and Solar Cells, 117, 1-8.

[23] Padinger, F., Rittberger, R. S., & Sariciftci, N. S. (2003). Effects of postproduction treatment on plastic solar cells. Advanced Functional Materials, 13(1), 85-88.

[24] Duda, J. C., Hopkins, P. E., Shen, Y., & Gupta, M. C. (2013). Thermal transport in organic semiconducting polymers. Applied Physics Letters, 102(25), 251912.

[25] Huang, Y. C., Liao, Y. C., Li, S. S., et.al. (2009). Study of the effect of annealing process on the performance of P3HT/PCBM photovoltaic devices using scanning-probe microscopy. Solar energy materials and Solar Cells, 93(6), 888-892.

[26] Cook, S., Ohkita, H., Kim, Y., et.al. (2007). A photophysical study of PCBM thin films. Chemical Physics Letters, 445(4), 276-280.

[27] Burkhard, G. F., Hoke, E. T., & McGehee, M. D. (2010). Accounting for interference, scattering, and electrode absorption to make accurate internal quantum efficiency measurements in organic and other thin solar cells. Advanced Materials, 22(30), 3293-3297.

[28] Erb, T., Zhokhavets, U., Hoppe, H., et.al. (2006). Absorption and crystallinity of poly (3-hexylthiophene)/fullerene blends in dependence on annealing temperature. Thin Solid Films, 511, 483-485.

[29] Kadem, B. Y., Al-hashimi, M. K., & Hassan, A. K. (2014). The effect of solution processing on the power conversion efficiency of P3HT-based organic solar cells. Energy Procedia, 50, 237-245.

[30] Al-Ibrahim, M., Ambacher, O., Sensfuss, S., & Gobsch, G. (2005). Effects of solvent and annealing on the improved performance of solar cells based on poly (3-hexylthiophene): fullerene. Applied Physics Letters, 86(20), 201120.

[31] Chuang, S. Y., Chen, H. L., Lee, W. H., et.al. (2009). Regioregularity effects in the chain orientation and optical anisotropy of composite polymer/fullerene films for high-efficiency, large-area organic solar cells. Journal of Materials Chemistry, 19(31), 5554-5560.

[32] Brown, P. J., Thomas, D. S., Köhler, A., et.al. (2003). Effect of interchain interactions on the absorption and emission of poly (3-hexylthiophene). Physical Review B, 67(6), 064203.

[33] Kim, Y., Cook, S., Tuladhar, S. M.,et.al. (2006). A strong regioregularity effect in self-organizing conjugated polymer films and high-efficiency polythiophene: fullerene solar cells. nature materials, 5(3), 197-203.

[34] Rao, B. S., Kumar, B. R., Reddy, V. R., & Rao, T. S. (2011). Preparation and characterization of CdS nanoparticles by chemical co-precipitation technique. Chalcogenide Lett, 8(3), 177-185.

[35] Lee, C. H., Podraza, N. J., Zhu, Y., et.al. (2013). Effect of reduced dimensionality on the optical band gap of SrTiO3. Applied Physics Letters, 102(12), 122901.

[36] Kim, Y. S., Lee, Y., Kim, J. K., et.al. (2010). Effect of solvents on the performance and morphology of polymer photovoltaic devices. Current Applied Physics, 10(4), 985-989.

[37] Jang, S. K., Gong, S. C., & Chang, H. J. (2012). Effects of various solvent addition on crystal and electrical properties of organic solar cells with P3HT: PCBM active layer. Synthetic Metals, 162(5), 426-430.

[38] Hoppe, H., & Sariciftci, N. S. (2004). Organic solar cells: An overview. J. Mater. Res, 19(7), 1924-1945.

[39] Zhang, F., Zhuo, Z., Zhang, J., et.al. (2012). Influence of PC60BM or PC70BM as electron acceptor on the performance of polymer solar cells. Solar Energy Materials and Solar Cells, 97, 71-77.

[40] Nicolaidis, N. C., Routley, B. S., Holdsworth, J. L., et.al. (2011). Fullerene contribution to photocurrent generation in organic photovoltaic cells. The Journal of Physical Chemistry C, 115(15), 7801-7805.

[41] Manceau, M., Chambon, S., Rivaton, A., et.al. (2010). Effects of long-term UV–visible light irradiation in the absence of oxygen on P3HT and P3HT: PCBM blend. Solar Energy Materials and Solar Cells, 94(10), 1572-1577.

[42] Kurta, R. P., Grodd, L., Mikayelyan, E., et.al. (2015). Local structure of semicrystalline P3HT films probed by nanofocused coherent X-rays. Physical Chemistry Chemical Physics, 17(11), 7404-7410.

[43] Kanimozhi, C., Yaacobi-Gross, N., Burnett, E. K., et.sl. (2014). Use of side-chain for rational design of n-type diketopyrrolopyrrole-based conjugated polymers: what did we find out?. Physical Chemistry Chemical Physics, 16(32), 17253-17265.

[44] Zhokhavets, U., Erb, T., Hoppe, H., et.al. (2006). Effect of annealing of poly (3-hexylthiophene)/fullerene bulk heterojunction composites on structural and optical properties. Thin Solid Films, 496(2), 679-682.

[45] Park, J. H., Kim, J. S., Lee, J. H., et.al. (2009). Effect of annealing solvent solubility on the performance of poly (3-hexylthiophene)/methanofullerene solar cells. The Journal of Physical Chemistry C, 113(40), 17579-17584.

[46] Monshi, A., Foroughi, M. R., & Monshi, M. R. (2012). Modified Scherrer equation to estimate more accurately nano-crystallite size using XRD. World Journal of Nano Science and Engineering, 2(03), 154.

[47] Kekuda, D., Lin, H. S., Wu, M. C., et.al. (2011). The effect of solvent induced crystallinity of polymer layer on poly (3-hexylthiophene)/C 70 bilayer solar cells. Solar Energy Materials and Solar Cells, 95(2), 419-422.

[48] Ye, Z., Yang, X., Cui, H., & Qiu, F. (2014). Nanowires with unusual packing of poly (3-hexylthiophene) s induced by electric fields. Journal of Materials Chemistry C, 2(33), 6773-6780.

[49] Street, R. A., Northrup, J. E., & Salleo, A. (2005). Transport in polycrystalline polymer thin-film transistors. Physical Review B, 71(16), 165202.

[50] Reinspach, J. A., Diao, Y., Giri, G., et.al. (2016). Tuning the Morphology of Solution-Sheared P3HT: PCBM Films. ACS applied materials & interfaces, 8(3), 1742-1751.

[51] Ma, W., Yang, C., Gong, X., et.al. (2005). Thermally stable, efficient polymer solar cells with nanoscale control of the interpenetrating network morphology. Advanced Functional Materials, 15(10), 1617-1622.

[52] Parlak, E. A. (2012). The blend ratio effect on the photovoltaic performance and stability of poly (3-hexylthiophene):[6, 6]-phenyl-C 61 butyric acid methyl ester (PCBM) and poly (3-octylthiophene): PCBM solar cells. Solar Energy Materials and Solar Cells, 100, 174-184.

[53] Bkakri, R., Chehata, N., Ltaief, A., et.al. (2015). Effects of the graphene content on the conversion efficiency of P3HT: Graphene based organic solar cells. Journal of Physics and Chemistry of Solids, 85, 206-211.

[54] Bkakri, R., Kusmartseva, O. E., Kusmartsev, F. V., et.al. (2015). Degree of phase separation effects on the charge transfer properties of P3HT: Graphene nanocomposites. Journal of Luminescence, 161, 264-270.

[55] Etxebarria, I., Ajuria, J., & Pacios, R. (2015). Solution-processable polymeric solar cells: a review on materials, strategies and cell architectures to overcome 10%. Organic Electronics, 19, 34-60.

[56] Kim, H., So, W., & Moon, S. (2006). Effect of thermal annealing on the performance of P3HT/PCBM polymer photovoltaic cells. Journal of the Korean Physical Society, 48(3), 441-445.

[57] Jung, J. W., & Jo, W. H. (2010). Annealing-Free High Efficiency and Large Area Polymer Solar Cells Fabricated by a Roller Painting Process. Advanced Functional Materials, 20(14), 2355-2363.

[58] Lu, Y., Wang, Y., Feng, Z., et.al. (2012). Temperature-dependent morphology evolution of P3HT: PCBM blend solar cells during annealing processes. Synthetic Metals, 162(23), 2039-2046.

[59] Yang, X., & Uddin, A. (2014). RETRACTED: Effect of thermal annealing on P3HT: PCBM bulk-heterojunction organic solar cells: A critical review. Renewable and Sustainable Energy Reviews, 30, 324-336.

[60] Shen, Y., Li, K., Majumdar, N., et.al. (2011). Bulk and contact resistance in P3HT: PCBM heterojunction solar cells. Solar Energy Materials and Solar Cells, 95(8), 2314-2317.

[61] Fong, K. C., McIntosh, K. R., & Blakers, A. W. (2013). Accurate series resistance measurement of solar cells. Progress in Photovoltaics: Research and Applications, 21(4), 490-499.

[62] Lögdlund, M., & Bredas, J. L. (1994). Theoretical studies of the interaction between aluminum and poly (p-phenylenevinylene) and derivatives. The Journal of chemical physics, 101(5), 4357-4364.

[63] Birgerson, J., Fahlman, M., Bröms, P., & Salaneck, W. R. (1996). Conjugated polymer surfaces and interfaces: a mini-review and some new results. Synthetic metals, 80(2), 125-130.

[64] Kumar, P., Jain, S. C., Kumar, V., et.al. (2009). A model for the J-V characteristics of P3HT: PCBM solar cells. Journal of Applied Physics, 105(10), 104507.

[65] Asadi, K., Kronemeijer, A. J., Cramer, T., et.al. (2013). Polaron hopping mediated by nuclear tunnelling in semiconducting polymers at high carrier density. Nature communications, 4, 1710.

[66] Kapoor, A. K., Annapoorni, S., & Kumar, V. (2008). Conduction mechanisms in poly (3-hexylthiophene) thin-film sandwiched structures. Semiconductor Science and Technology, 23(3), 035008.

[67] Shaheen, S. E., Brabec, C. J., Sariciftci, N. S., et.al. (2001). 2.5% efficient organic plastic solar cells. Applied Physics Letters, 78(6), 841-843.

[68] Li, G., Shrotriya, V., Yao, Y., & Yang, Y. (2005). Investigation of annealing effects and film thickness dependence of polymer solar cells based on poly (3-hexylthiophene). Journal of Applied Physics, 98(4), 043704.

[69] Nam, Y. M., Huh, J., & Jo, W. H. (2010). Optimization of thickness and morphology of active layer for high performance of bulk-heterojunction organic solar cells. Solar Energy Materials and Solar Cells, 94(6), 1118-1124.

[70] Oklobia, O., & Shafai, T. S. (2014). Correlation between charge carriers mobility and nanomorphology in a blend of P3HT/PCBM bulk heterojunction solar cell: Impact on recombination mechanisms. Solar Energy Materials and Solar Cells, 122, 158-163.

[71] Elumalai, N. K., & Uddin, A. (2016). Open circuit voltage of organic solar cells: an in-depth review. Energy & Environmental Science, 9(2), 391-410.

[72] Şimşir, N., Şafak, H., Yüksel, Ö. F., & Kuş, M. (2012). Investigation of current–voltage and capacitance–voltage characteristics of Ag/perylene-monoimide/n-GaAs Schottky diode. Current Applied Physics, 12(6), 1510-1514.

[73] Khurelbaatar, Z., Shim, K. H., Cho, J., et.al. (2015). Temperature Dependent Current-Voltage and Capacitance-Voltage Characteristics of an Au/n-Type Si Schottky Barrier Diode Modified Using a PEDOT: PSS Interlayer. Materials Transactions, 56(1), 10-16.

[74] Uhrich, C., Wynands, D., Olthof, S., et.al. (2008). Origin of open circuit voltage in planar and bulk heterojunction organic thin-film photovoltaics depending on doped transport layers. Journal of Applied Physics, 104(4), 043107.

[75] Potscavage Jr, W. J., Yoo, S., & Kippelen, B. (2008). Origin of the open-circuit voltage in multilayer heterojunction organic solar cells. Applied physics letters, 93(19), 413.

[76] Shrotriya, V., & Yang, Y. (2005). Capacitance–voltage characterization of polymer light-emitting diodes. Journal of Applied Physics, 97(5), 054504.

[77] Zhao, D. W., Kyaw, A. K. K., & Sun, X. W. (2011). Organic Solar Cells with Inverted and Tandem Structures. In Energy Efficiency and Renewable Energy Through Nanotechnology (pp. 115-170). Springer London.

[78] Yue, G., Wu, J., Xiao, Y.,et.al. (2011). Flexible dye-sensitized solar cell based on PCBM/P3HT heterojunction. Chinese Science Bulletin, 56(3), 325-330.

[79] Thakur, A. K., Wantz, G., Garcia-Belmonte, G., et.al. (2011). Temperature dependence of open-circuit voltage and recombination processes in polymer–fullerene based solar cells. Solar Energy Materials and Solar Cells, 95(8), 2131-2135.

[80] Qi, B., & Wang, J. (2013). Fill factor in organic solar cells. Physical Chemistry Chemical Physics, 15(23), 8972-8982.

[81] Gupta, D., Mukhopadhyay, S., & Narayan, K. S. (2010). Fill factor in organic solar cells. Solar Energy Materials and solar cells, 94(8), 1309-1313.

[82] Voroshazi, E., Verreet, B., Aernouts, T., & Heremans, P. (2011). Long-term operational lifetime and degradation analysis of P3HT: PCBM photovoltaic cells. Solar Energy Materials and Solar Cells, 95(5), 1303-1307.

Chapter 6: Improved OSC performance with modified electrodes

6.1 Introduction

As it has been mentioned earlier, highly efficient OSCs could be achieved by controlling the active layer morphology [1-3]. This property has revealed an efficient dependency on the orientation of the organic molecules and chains within the blend, which directly impacts on the charge carriers' mobility [4]. On the other hand, the interface properties of the organic solar cells could play an important role in determining the final destination of the generated carriers [5]. The type of the junction at the metal-semiconductor (organic) contact as well as the energy level offset between the donor and the acceptor are other essential parameters, which strongly influence the final efficiency of the solar cell. An intensive research has been carried out both in the current work and elsewhere to investigate P3HT:PCBM as an organic system for OSC applications by applying different layer treatments including, employing different solvents to process the active layer [6, 7], investigating different active layer thicknesses [8], using different fullerene derivatives [9] and by subjecting the films to different post deposition heat treatment to the complete solar cell device [10]. The nature of contacts on both sides of the active layer is considered as an essential feature to determine the device performance [11]. In the current chapter, all the different layer treatments to optimise the OSC performance are combined in a single device as well as employing a soluble Alq3 as an electron transport layer (ETL) [12] whereas PEDOT:PSS spun layers doped with different metal salts are employed as a hole transporting layer [11]. Power conversion efficiency is considered as the main performance OSCs parameter, which inherently depends on several parameters including light harvesting properties of the active layer, generation rate of excitons, excitons diffusion and separation, and charge transportation and collection by the cell electrodes [13]. However, the modification of both contacts has been demonstrated to play significant role in the enhancing of charge collection (electrons and holes), which largely impacts on device efficiency [14].

Organic metal complexes have been established as electron transporting layers (ETL) in organic light emitting diodes (OLED) and as buffer layers in OSCs [15]. Among these complexes, tris-(8-hydroxyquinoline)Aluminium (Alq3) is considered as one of the most commonly used complexes in OFETs, OLEDs and OPVs due to its remarkable characteristics such as the low lying highest occupied molecular orbital (HOMO) level and good thermal stability [16]. Alq3 has high internal quantum yield and stable electrical conductivity and it is considered to be an excellent electron transporting as well as green light emitting material in OLEDs [17]. Usually, Alq3 has been prepared by vacuum thermal deposition and it has been successfully applied as a thin buffer layer between the organic active layer and the metal electrode [16].

In the current work Alq3 has been prepared by spin coating method, which is expected to lead to a significant improvement in OSCs performance. Furthermore, contrary to inorganic ETL such as ZnO, the use of Alq3 layer does not require high temperature treatment of the fully produced OSC devices. On the other hand, the energy level offset between donor and acceptor in BHJs, as well as the device electrodes are critical factors in determining the overall voltage of the BHJs. Therefore, it is essential to form ohmic contacts at the electrodes for effective charge extraction, which could be quite challenging for organic/metal interfaces [18]. On the other hand, PEDOT:PSS dispersed in water can easily form a transparent film with high conductivity by spin coating, thus producing a low sheet resistance film [19]. The optimised combination of conductivity and surface morphology is essential for numerous applications of PEDOT:PSS thin films; these could be influenced by a variety of factors during the drying process including the fraction of solid content, particle size, proportion of PSS and the solution viscosity which could lead to different morphological and electrical properties [20]. Up to date, several treatments have been carried out to modify the properties of the PEDOT:PSS layer, such as using different organic solvents. Among those solvents are ethanol, dimethylsulfoxide, acetonitrile, and tetra-hydrofuran which have resulted in a considerable improvement of PEDOT:PSS layer conductivity [21]. A significant reduce in the sheet resistance of PEDOT:PSS thin film from 7 MΩ/□ to 40 kΩ/□ has been observed as a result using hexafluoroacetone (HFA) as solvent [22].

In the present study, the effect of metal salts, both in powder form and as aqueous solutions on the PEDOT:PSS films' properties such as conductivity, transmittance and morphology were investigated. The modified PEDOT:PSS layers were adopted as anode buffer layer to study their effects on P3HT:PCBM OSCs performance and thus on device PCE. Afterward, the use of the Alq3 as well as the PEDOT:PSS doped with the best metal salts were combined in a fully modified (complete) device as shown in Fig.6.1

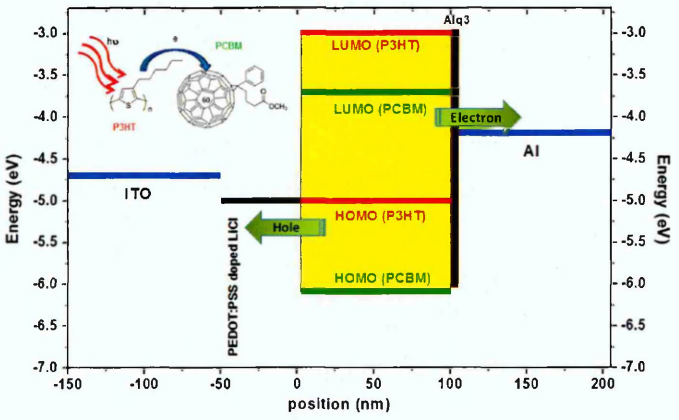

Fig.6.1: the energy level alignments of the complete device structure

6.2 Results and discussion

6.2.1 Electrical conductivity measurement

Fig.6.2 illustrates the variation in the electrical conductivity of the PEDOT:PSS layer as a result of treatment with different metal chlorides (see Fig.6.2(a)), as well as the effect of concentration of the chloride aqueous solutions (see Fig.6.2(b)). A maximum conductivity of 0.41 $S.cm^{-1}$ was obtained for the LiCl treated film when the metal salt was added in powder form while a conductivity of 0.43 $S.cm^{-1}$ was obtained for the same salt in aqueous solution form (see Fig.6.2(a)). Further treatment was carried out to examine the effect of $CdCl_2$ and LiCl concentrations on PEDOT:PSS conductivity. Fig.6.2 (b) shows the increase in films' conductivity with increased concentration of the aqueous solution added to the PEDOT:PSS. The LiCl treated film with the concentration of $10mg.ml^{-1}$ shows the highest conductivity of 0.485 $S.cm^{-1}$ while the $CdCl_2$ treated with the concentration of $10mg.ml^{-1}$ films exhibited slightly lower conductivity of 0.48 $S.cm^{-1}$.

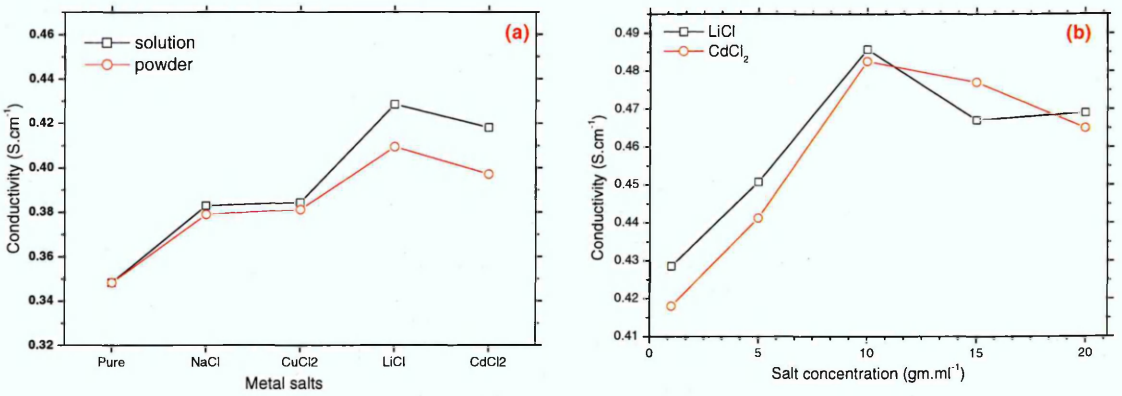

Fig.6.2: (a) The conductivity of PEDOT:PSS variation with different metal salts treatment and (b) dependence of conductivity on LiCl and CdC_2 solution concentration

It has been shown that doping the PEDOT:PSS layer with different metal salts has the ability to change the PEDOT:PSS structure by binding the metal ions to the PSS anions of PEDOT:PSS layer, which therefore results in noticeable increase in the electrical conductivity of the PEDOT:PSS layer [23]. This mechanism is illustrated in the schematic diagram given in Fig.6.3. This could be further understood as the result of dissociation of the metal salts where the higher dissociation contributes higher ions concentration which significantly reduces the columbic attraction between the PEDOT and PSS chains, thus more loss of PSS chains from the PEDOT:PSS film via the salt treatment [24]. It has been established that conduction in PEDPOT:PSS films is due to charge transport across the PEDOT chains via hopping, and that it remains unchanged after the addition of the metal salt impurities [23].

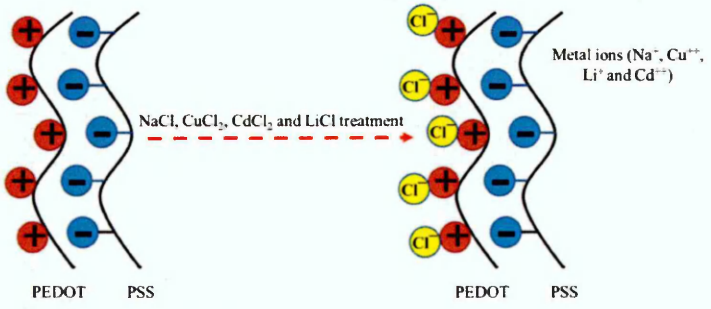

Fig.6.3: Modifying the PEDOT:PSS with different metal salts treatment and the dissociation of the metal ions and the Cl^- within the PEDOT:PSS

6.2.2 Surface morphology

The morphology of the hole and electron transport layers were investigated using SEM and AFM techniques. Fig.6.4 shows the SEM images of the PEDOT:PSS films treated with different metal salts in aqueous solution forms. The doped films have exhibited rough morphologies compared to the pure PEDOT:PSS film which were attributed to the persence of the metal salts as demonstrated by the white spots on the films' surface. In order to investegate the effect of higher concentrations of metal salts impurities on the surface morphology of PEDOT:PSS layer, aqueous solutions with higher concentrations of LiCl (1, 5 and 10mg.ml^{-1}) were examined as shown in Fig.6.5. Phase seperation between the conductive site (PEDOT) and the insulating site (PSS) might be occurred within the PEDOT:PSS layer which results in seperating both domains thus leading to a change in the PEDOT:PSS morphology [23]. The films have exhibited rougher surface with increased LiCl solution concentrations. The surface morphology of PEDOT:PSS layer was further studied using AFM imaging and to further confirm the phase separation between the PEDOT and the PSS regions using phase analysis, as shown in Fig.6.6. The pure PEDOT:PSS film has exhibited smooth surface with rms of 1.25nm while rougher surface morphologies (rms of 3.38nm) were clearly evident in the LiCl (10mg.ml^{-1} aqueous solution) doped PEDOT:PSS.

Generally speaking the brighter regions observed in the AFM images could be associated with the PEDOT whereas the darker regions are related to the less conductive PSS regions [25]. This increase in the surface roughness may be ascribed to the increase in grain size after metal chloride treatment. It has recently been shown that surface roughness and grain size of inorganic CdS layer has increased as a result of $CdCl_2$ treatment [26]. At the same time, the group VII element (Cl) has also acted as a p-type dopant when it produces complexes with un-known native defects within the inorganic layer [26]. It can be assumed here that Cl^- ions play a similar role when organic layers of PEDOT:PSS are treated with metal chlorides.

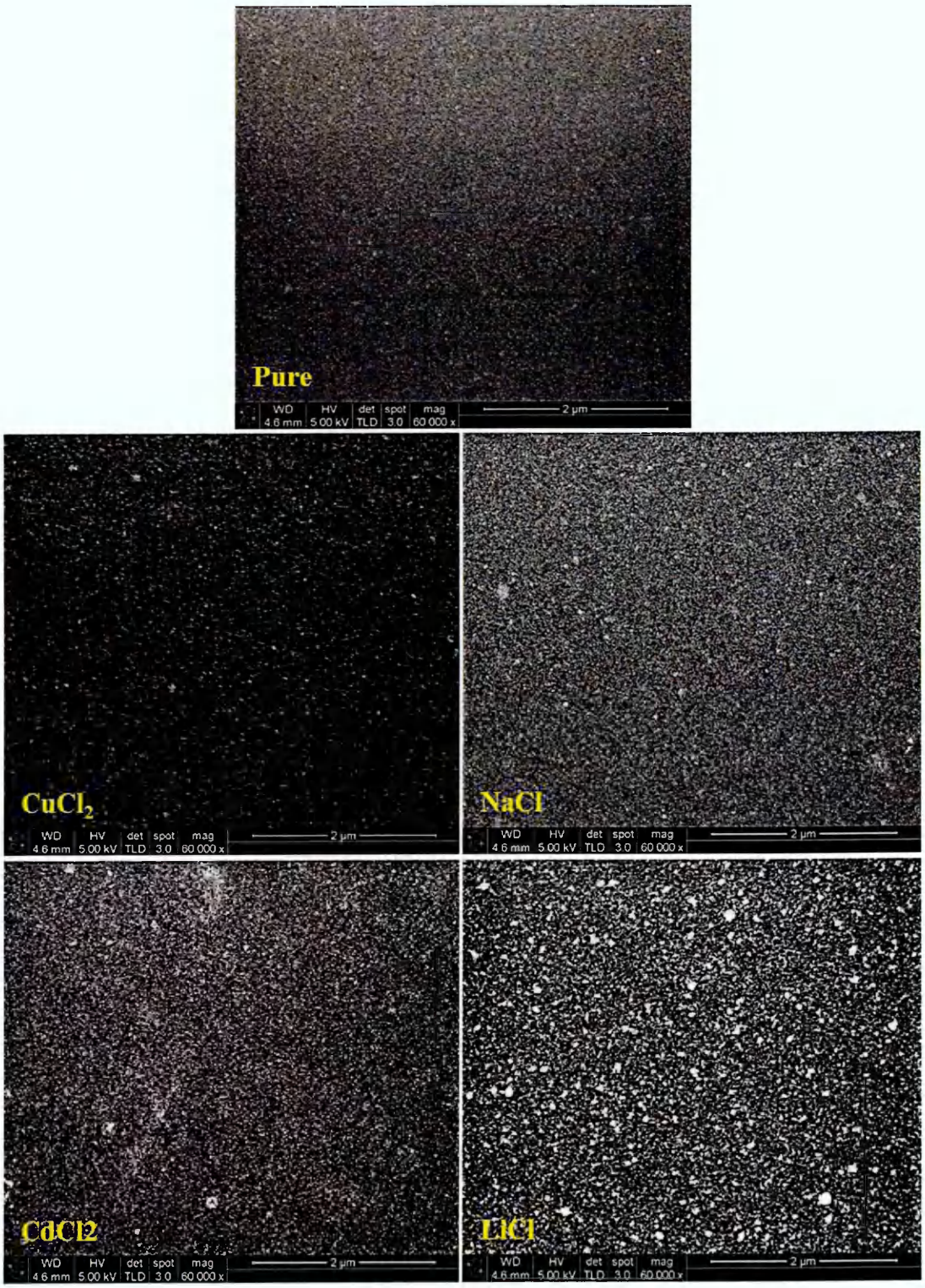

Fig.6.4: SEM images for PEDOT:PSS films treated with different metal salts in aqueous solution forms

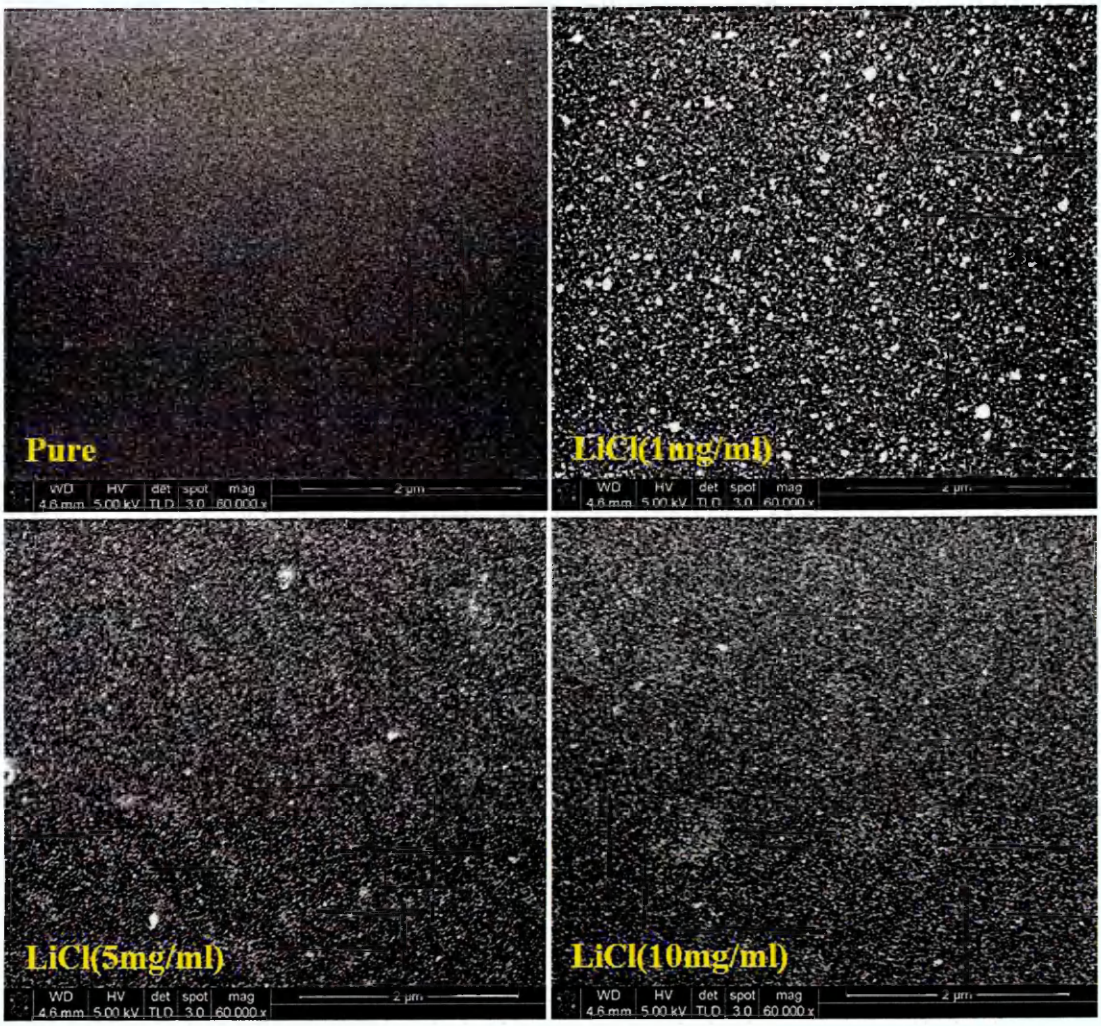

Fig.6.5: SEM images for PEDOT:PSS films treated with different concentrations of aqueous LiCl solution

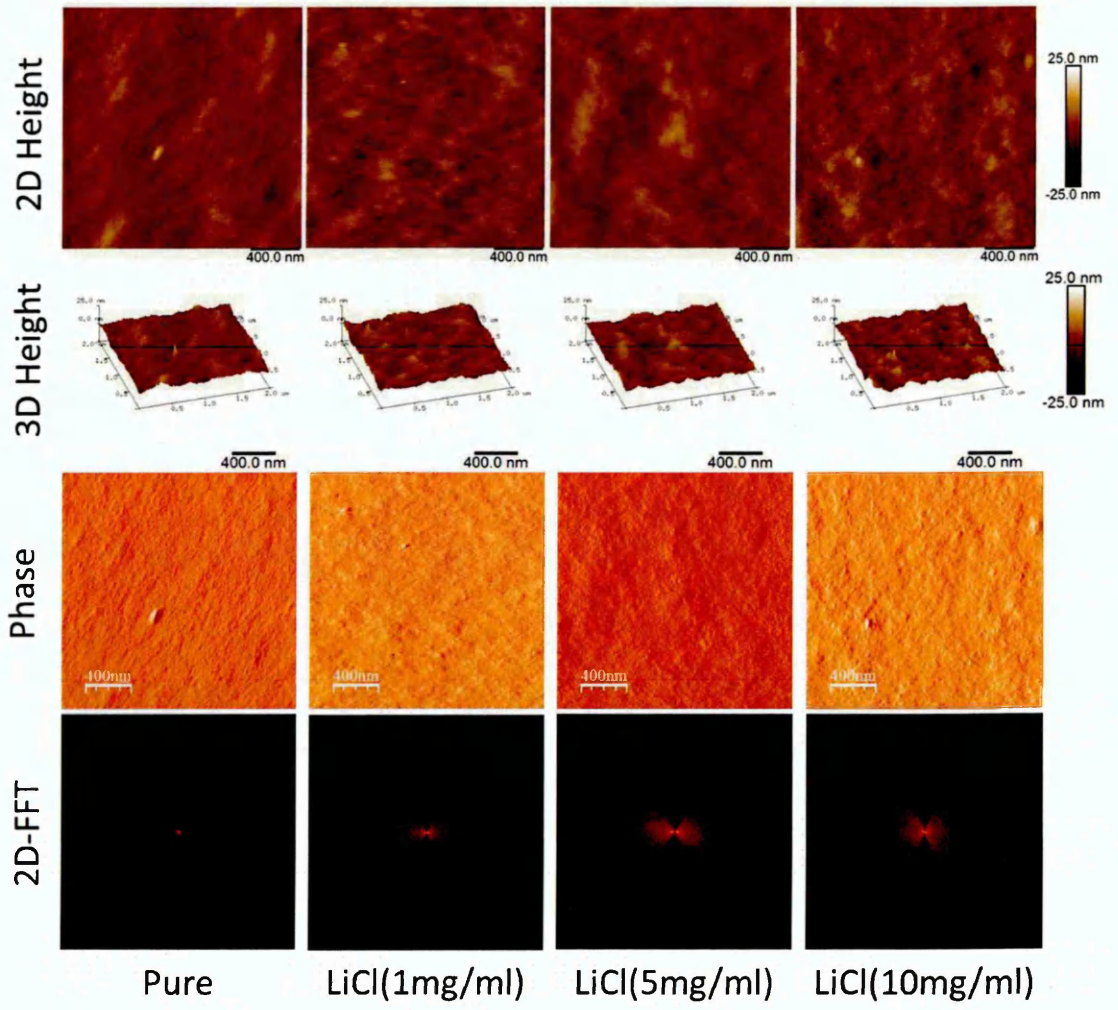

Fig.6.6: AFM images of pure and LiCl aqueous solution treated PEDOT:PSS layers of concentrations 1 $mg.ml^{-1}$, 5 $mg.ml^{-1}$ and 10 $mg.ml^{-1}$ respectively

As it has been shown earlier in Fig.6.3, the PSS could be removed by the metal ions (cations) leaving the Cl (anion) to act as a dopant impurity to improve the PEDOT conductivity and change its surface roughness. Therefore, an improvement in the light scattering might be ascribed to such surface roughness which is though to improve the light harvesting by the active layer as well as decreasing the contact resistance of the interfacial layer, hence increasing the short circuit current density (J_{sc}). To study the phase separation between the PEDOT and the PSS as suggested earlier, phase analysis has been carried out.

Clear phase separation has been observed in the 2D-FFT analysis where the darker region has decreased in the PEDOT:PSS film treated by LiCl with different concentrations [27]. However, increasing the LiCl concentration has resulted in higher separation. On the other hand, the solution based Alq3 layer has resulted a smooth surface with ripples like features of rms=1.2nm as shown in Fig.6.7.

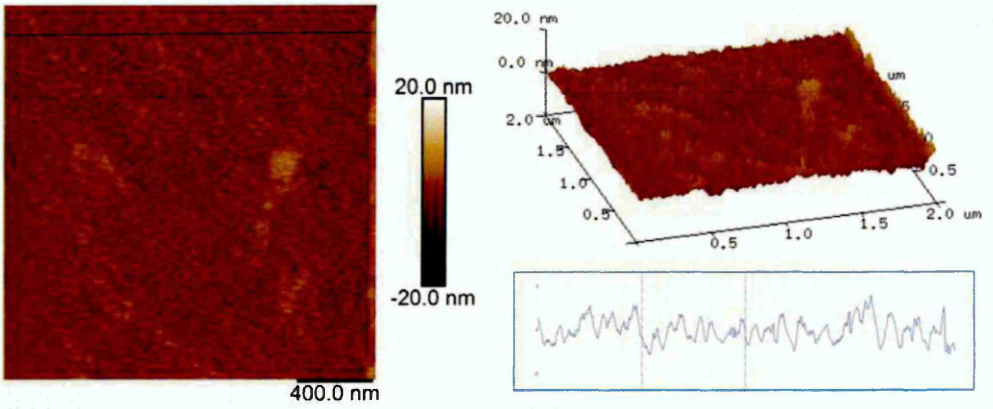

Fig.6.7: AFM image of the Alq3 film with 3D view and cross section

6.2.3 Films' optical properties

Fig.6.8 shows the absorption spectrum of the solution processed thin films of Alq3. The spectrum has demonstrated a maximum peak in the UV region around 380 nm which is attributed to the π–π^* electronic transitions. The Alq3 π-system is mainly localized in the HOMO band and the π^*-system is mainly localized in the LUMO band [28]. The inset to Fig.6.8 shows the band gap (E_g) of 2.83 eV of Alq3 as estimated using Tauc equation, which is found in good agreement with the published values [29]. The transmittance spectra of metal salts treated PEDOT:PSS films as well as those of films prepared from as pristine PEDOT:PSS are illustrated in Fig.6.9. PEDOT:PSS films doped with metal salts have exhibited higher transmittance as compared to pure PEDOT:PSS films. Aqueous solution-treated PEDOT:PSS films however have demonstrated even higher transmittance than those treated with metal salt powders. In both cases, the metal chloride treated PEDOT:PSS layers are found to be useful for solar cells specifically for materials employed as a window layers.

The maximum transmittance of pure PEDOT:PSS film was in the range 88-91% within the wavelength range (400–650 nm), while transmittance of powder salts treated-PEDOT:PSS films has increased up to 93%. Aqueous solution (1mg.ml^{-1}) of metal salts treated PEDOT:PSS films have however exhibited further increase in transmittance, reaching 94%. The PEDOT;PSS films treated with LiCl and $CdCl_2$ were shown to demonstrate maximum transmittance in both cases of treatment, in powder and in aqueous solutions.

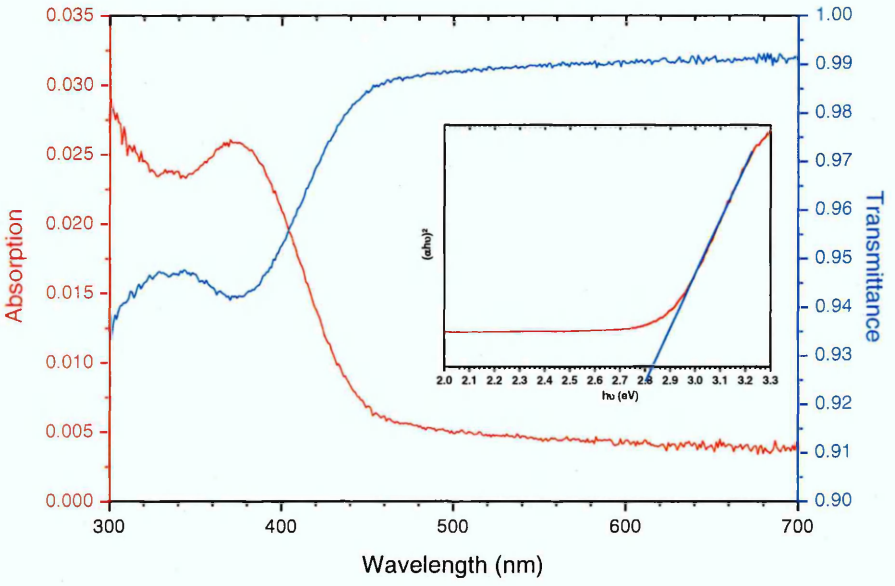

Fig.6.8: UV-visible absorption and transmittance spectra of Alq3 films; the inset represents the E_g determination using Tauc equation.

Moreover, an increase in the aqueouse solution concetration of LiCl and $CdCl_2$ has led to further improvement in the trasmittance of PEDOT:PSS films. These films have demonstrated lower transmittance in the NIR region compared to the visible region which might be related to the absorption of the PEDOT:PSS layer within this region. Gasiorowski and co-authors have argued that PEDOT:PSS layer has a small absorption coefficient in the UV and visible regions, while it has higher absorption coefficient in the NIR region of the spectra [30].

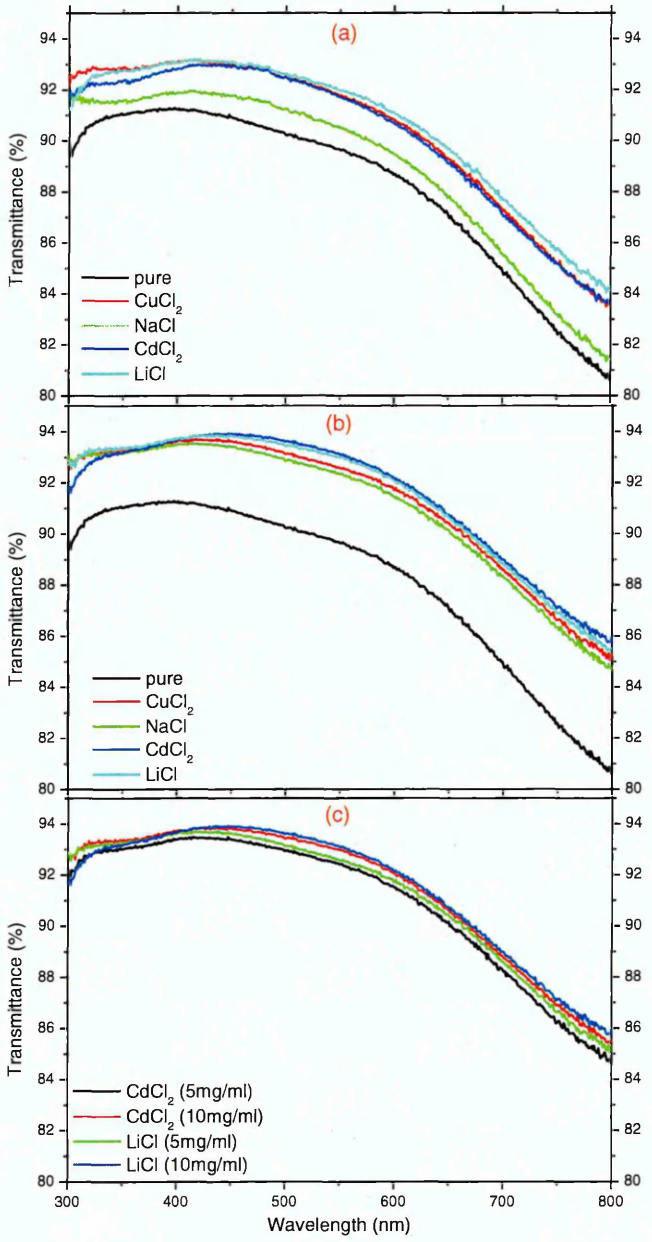

Fig.6.9: Transmittance spectra of PEDOT:PSS films: (a) on treatment with NaCl, $CuCl_2$, $CdCl_2$ and LiCl in powder forms; (b) on treatment with aqueous solutions of NaCl, $CuCl_2$, $CdCl_2$ and LiCl in DI water with the concentration $1mg.ml^{-1}$; (c) on treatment with aqueous solutions of LiCl and $CdCl_2$ with the concentrations $5mg.ml^{-1}$ and $10mg.ml^{-1}$.

On the other hand, P3HT:PCBM active layer has exhibited 4 different bands (A, B, C and D) as shown in Fig.6.10; bands A, B and C were attributed to the P3HT absorption spectra, while the band D was ascribed to the PCBM molecules, as discussed in more details in Chapter 5 [31]. Similar spectra were observed for the complete device (where the PEDOT:PSS layer treated with LiCl "10mg.ml^{-1}" and Alq3 layer were used as hole and electron transport layers, respectively) correlated with an increase in the absorption intensity over the investigated range and a clear absorption enhancement in the NIR region (above 800nm) as well as near the UV region (below 350nm), as shown in Fig.6.10. The absorption enhancement in the NIR region might be attributed to two possibilities; the contribution of the absorption of the PEDOT:PSS layer within the complete device [30] and/or the light scattering and trapping within the complete device [32].

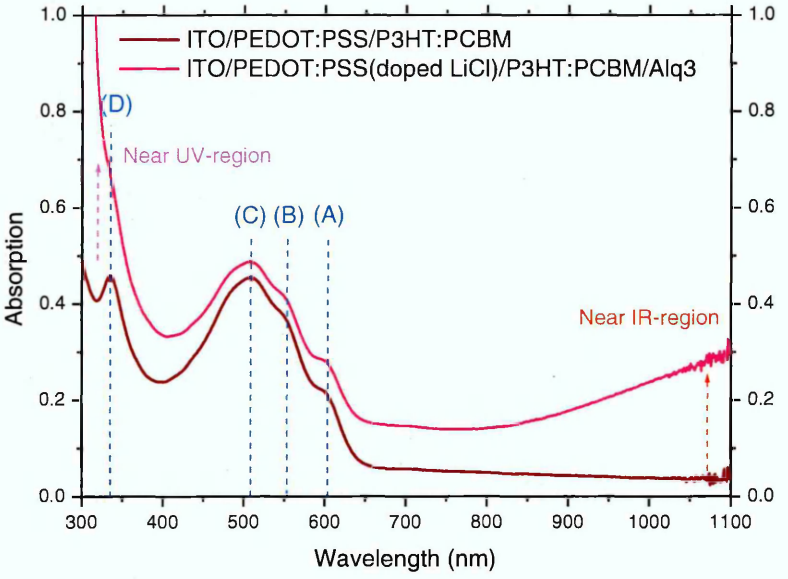

Fig.6. 10: UV-visible absorption spectra of the OSC layers under investigation

The roughness of ITO/PEDOT:PSS-LiCl doped surface might results in light scattering, therefore it may contribute in longer light propagation pathway within the P3HT:PCBM active layer and may result in light trapping. Generally, light trapping occurs due to total internal reflection, absorption, and surface plasmon [33]. Increasing the optical path length of a device with 100nm thickness by light trapping assists the light to bounce back and forth within the cell about 50 times [34].

Fig.6.11 shows an illustration of the scattered light from the ITO/PEDOT:PSS-LiCl doped rough surface. Basically, light trapping is achieved by altering the angle at which light propagates through the solar cell depending on the surface roughness and therefore giving a longer optical path distance than the physical active layer thickness. The light scattering and trapping within the complete device is thought to assist in increasing the current density through enhancing light-harvesting efficiency and thus improving the device efficiency [32,35].

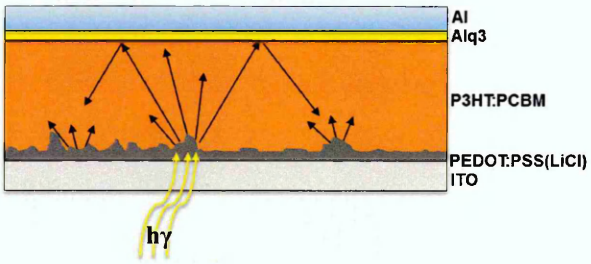

Fig.6.11: A schematic illustration of the scattered light from the ITO/PEDOT:PSS(LiCl) rough surface into the P3HT:PCBM layer within the OSCs device

Petoukhoff and co-workers [36] have stated that the roughness of the absorber layer assists the light scattering. This is thought to contribute in increasing the absorption and therefore the current density, which is essential for PV performance improvement. They have also demonstrated a total absorption enhancement as large as 12% in organic semiconductor layers with diffident metal surfaces. It has also been verified that total absorption might be further improved by minimising reflection losses when the polymer/fullerene active layer incorporated into a complete device which incorporates charge transport layers on both sides of the device as well as an anti-reflection layer [36]. Another possibility of enhancing light propagation through the device is through the reflected light from the randomly textured organometallic/metal electrode (Alq3/Al) to the P3HT:PCBM active layer, as defined by the Lambertian limit, where the reflected light exhibits prolonged optical path [37]. Randomising the direction of light may assist the reflected light to be totally internally reflected (TIR), where in the present case, the light reaching the Alq3/Al surface at an angle higher than the critical angle will be totally reflected towards the active layer, leading to a significant improvement in light absorption [37-39].

6.2.4 Dark I-V characteristics

The dark DC I-V measurements were carried out in order to determine the various electronic parameters of the studied OSC devices, including series resistance, charge carrier mobility, ideality factor and the barrier height.

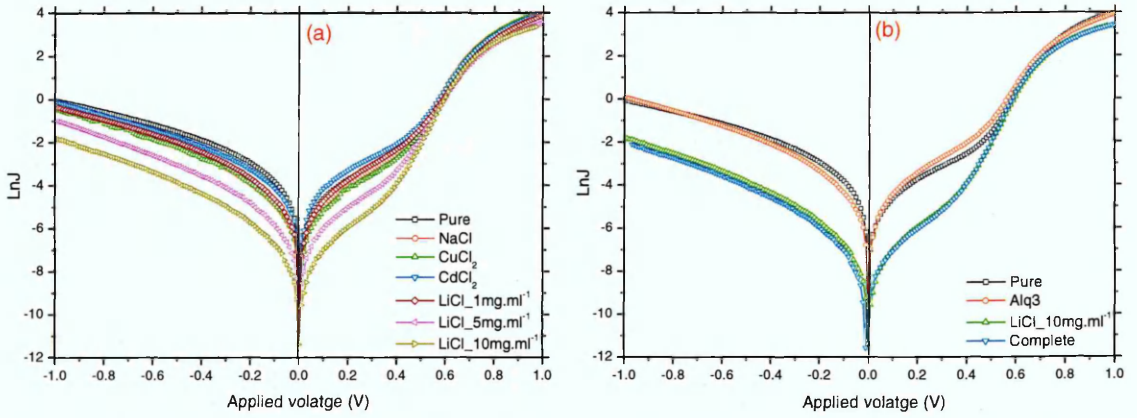

Fig.6.12: LnJ versus applied voltage of (a) devices based on different PEDOT:PSS layer treated with different metal salts, and (b) devices with and without different modifications layers (HTL, ETL and complete device)

Modifying the electrodes with either ETL or HTL or both have resulted in decreasing the series resistance in comparison to the reference device as demonstrated in Table 6.1. As an example, using Alq3 as ETL layer has reduced the R_s by about 7%, whereas the doping of PDOT:PSS layer with different metal salts has resulted in decreasing the R_s by about 14-15%. On the other hand, using different concentrations of the LiCl salt has shown no significant change in the R_s with an average value of 47Ω. The improvement in R_s could be a key factor among others towards achieving efficient electrode properties and therefore better device performance [11]. To study the properties of the organic/metal interface of the studied device, dark J-V characteristics were employed to determine the barrier height (ϕ_B) as well as the ideality factor (n) of the OSCs studied here [43]. Using the data shown in Fig.6.12 to extract the ideality factor and the barrier height, the reference device has shown an ideality factor of 2.21, which has decreased by using Alq3 as an ETL to 2.09; this decrease in device ideality factor is assigned to a lower recombination rate within the device. However the lower recombination rate may be ascribed to effective charge

collection from the selective electrodes by employing efficient hole and electron transport layers [11, 12], the latter is thought to contribute in the higher FF of the examined devices [44]. It is well known that the solar cell FF represents the efficiency of charge collection before they recombine inside the active layer of the cell, which in turn depends on the charge carrier's mobility, the built in potential and the charge carrier recombination rate [45]. Moreover, using different metal salts has further reduced the ideality factor to reach a value as low as 1.81 in the LiCl (10mg.ml^{-1}) doped PEDOT:PSS-based device.

Table 6. 1: The OSC electronic characteristics derived from the dark DC I(V) measurements

Devices	n	ϕ_B (eV)	R_s (Ω)	$\mu \times 10^{-6}$ ($cm^2V^{-1}s^{-1}$)
ITO/PEDOT:PSS/P3HT:PCBM/Al	2.21	0.80	55.2	1.11
ITO/PEDOT:PSS/P3HT:PCBM/Alq3/Al	2.09	0.81	51.5	1.67
ITO/PEDOT:PSS(NaCl)/P3HT:PCBM/Al	2.08	0.81	49.3	1.09
ITO/PEDOT:PSS(CuCl2)/P3HT:PCBM/Al	2.13	0.85	47.2	2.17
ITO/PEDOT:PSS($CdCl_2$)/P3HT:PCBM/Al	2.06	0.84	49.8	2.25
ITO/PEDOT:PSS(LiCl_1mg.ml^{-1})/P3HT:PCBM/Al	2.07	0.85	46.7	2.35
ITO/PEDOT:PSS(LiCl_5mg.ml^{-1})/P3HT:PCBM/Al	1.94	0.85	47.6	2.35
ITO/PEDOT:PSS(LiCl_10mg.ml^{-1})/P3HT:PCBM /Al	1.81	0.86	47.5	2.41
ITO/PEDOT:PSS(LiCl_10mg.ml^{-1})/P3HT:PCBM/Alq3/Al	1.6	0.86	45	2.42

Further decrease in the recombination rate was observed when both electrodes have been modified with ETL (Alq3) and HTL (PEDOT:PSS_10mg.ml^{-1}); the ideality factor has reached a value of 1.6 which suggests that efficient charge collection has occurred within the complete device as the recombination rate has reduced and therefore high solar cell parameters are expected. It was reported that many non-interactive interfaces could form between the organic layer and the metal interface, which therefore allow the injection barrier to follow Schottky-Mott limitation [46]. The latter occurs when the metal work function (ϕ_M) falls between two energy levels of both semiconductors ($P3HT_{LUMO}$ and

$PCBM_{HOMO}$) [46]. In this work the estimated barrier height has shown a slight increase from 0.8eV in the reference device to 0.86 in the complete device, which might be attributed to the inhomogeneity of the barrier across the organic/metal interface. Yakuphanoglu and co-workers [47] have investigated the inhomogeneity of Schottky barrier in OSCs where higher ideality factor has been attributed to series resistance and interface state properties. The interfacial states at the organic/metal interface affect the barrier height, charge extraction and the carrier transport inside the acceptor/donor blends, which therefore determine the overall performance of OSCs [48].

The effect of the interface properties and the barrier height on the charge transport properties has been investigated using space-charge limited conduction (SCLC) theory [49] as shown in Fig.6.13. All the J-V curves have obeyed the power law $J\alpha V^m$ with different gradient (m) values of the log(J) versus log(V) curves over the studied applied voltage range. As was discussed in chapter 5, as soon as the carriers are injected from the metal electrode into the active layer, their transport through the active layer toward the opposite electrode is controlled by the conduction properties of the active layer itself. The transport properties in a BHJ is mainly defined using Ohm's law at low applied voltages due to the hopping of the thermally excited carriers and the space-charge-limited conduction is due to the carriers injected into the active layer from the contacts [50]; such a contact is referred to as an ohmic contact. With an ohmic contact, the J-V characteristic has often exhibited an ohmic behaviour at low applied voltages up to a certain value since the field due to the injected carriers is negligible compared to that due to the applied voltage. This can be seen through the linear relation with the slope of ~1in the double log plot. To calculate the charge carriers' mobility, space charge limited conduction (SCLC) theory has been applied.

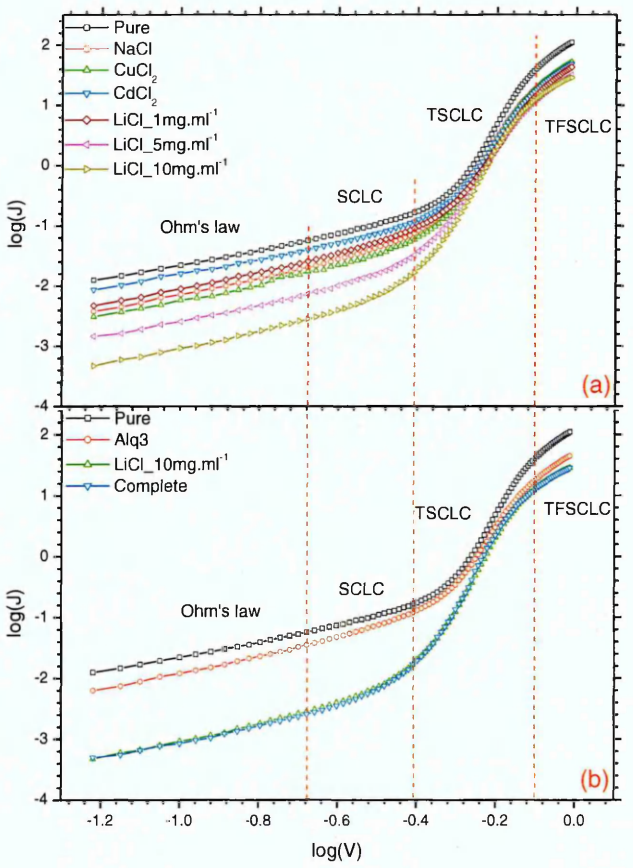

Fig.6. 13: LogJ versus logV plots of (a) devices based on different metal salts treatment, and (b) devices using modified ETL, HTL and a complete device with both electrodes modified

The reference device has shown charge carrier mobility of the value of 1.11×10^{-6} $cm^2V^{-1}s^{-1}$, while the charge carrier mobility has increased slightly to reach 1.67×10^{-6} $cm^2V^{-1}s^{-1}$ as a result of adding the electron transport layer (ETL). Using different metal salts to modify the PEDOT:PSS layer has resulted in further enhancement in the charge carriers mobility to reach a value as high as 2.41×10^{-6} in PEDOT:PSS(LiCl_10mg.ml^{-1})-based device. Moreover, no significant increase in the charge carriers' mobility has been observed after employing both ETL (Alq3) and HTL (PEDOT:PSS(LiCl_10mg.ml^{-1}) in a complete device. In these logJ-logV plots no significant change was observed in the value of the transition voltage from ohmic to SCLC regimes.

6.2.5 Photovoltaic measurements

J-V characteristics has been carried out under illumination in order to determine the PV properties of P3HT:PCBM-based solar cells which has undergone different modifications, as discussed in the previous sections. Fig.6.14. shows the J-V curves of the investigated OSCs with different metal salts treated-PEDOT:PSS layers. Devices with untreated PEDOT:PSS layer (pure) have exhibited lower PV performance with V_{oc}=0.62V, J_{sc}=11.9 mA.cm^{-1}, FF=53% and PCE of 3.92%. These are in line with values frequently reported in the literature [51]. However, devices having PEDOT:PSS layers doped with metal salt in powder form have demonstrated significant improvement in all PV parameters as shown in Fig.6.14(a), and results summarised in Table 6.2. The highest PCE of 5.6% and J_{sc} of 16.1 mA.cm^{-1} were achieved when PEDOT:PSS layer was doped with $LiCl_2$ powder. The device FF has demonstrated no change for all devices treated with metal salts, whereas V_{oc} in the region of 0.605±0.015V was recorded for those devices.

When the PEDOT:PSS layers were doped with the same metal salts in aqueous form, the PCE and J_{sc} of the studied OSC devices have reached values of about 6% and 17.4 mA.cm^{-1}, respectively, in the case of using LiCl as the dopant with the concentration of 1mg.ml^{-1} (see Fig.6.14(b)). Once again, V_{oc} and FF have remained more or less unchanged for all metal salts studied in this work (see Table 6.2). The substantial increase in J_{sc} could be ascribed to the improved electrical conductivity of PEDOT:PSS layers as a result of metal salt treatment while the enhanced PCE could be associated with the increased films' transmittance and surface roughness, as discussed earlier. V_{oc} maintained its value since it is mainly determined by the difference between the donor's higher occupied molecular orbital ($HOMO_{donor}$) and the lower unoccupied molecular orbital of the acceptor ($LUMO_{acceptor}$) [52]. Furthermore, the metal salt treatment of PEDOT:PSS layers seems to solve the wetting problem between the active layer, which is hydrophobic in nature and the hydrophilic PEDOT:PSS [53]. Such film processing method would be more suitable for the fabrication of inverted OSC structure. Electrical properties of the OSCs were further improved when the concentration of LiCl in aqueous solution was increased to 5 and 10mg.ml^{-1} as demonstrated in Fig.6.14(c).

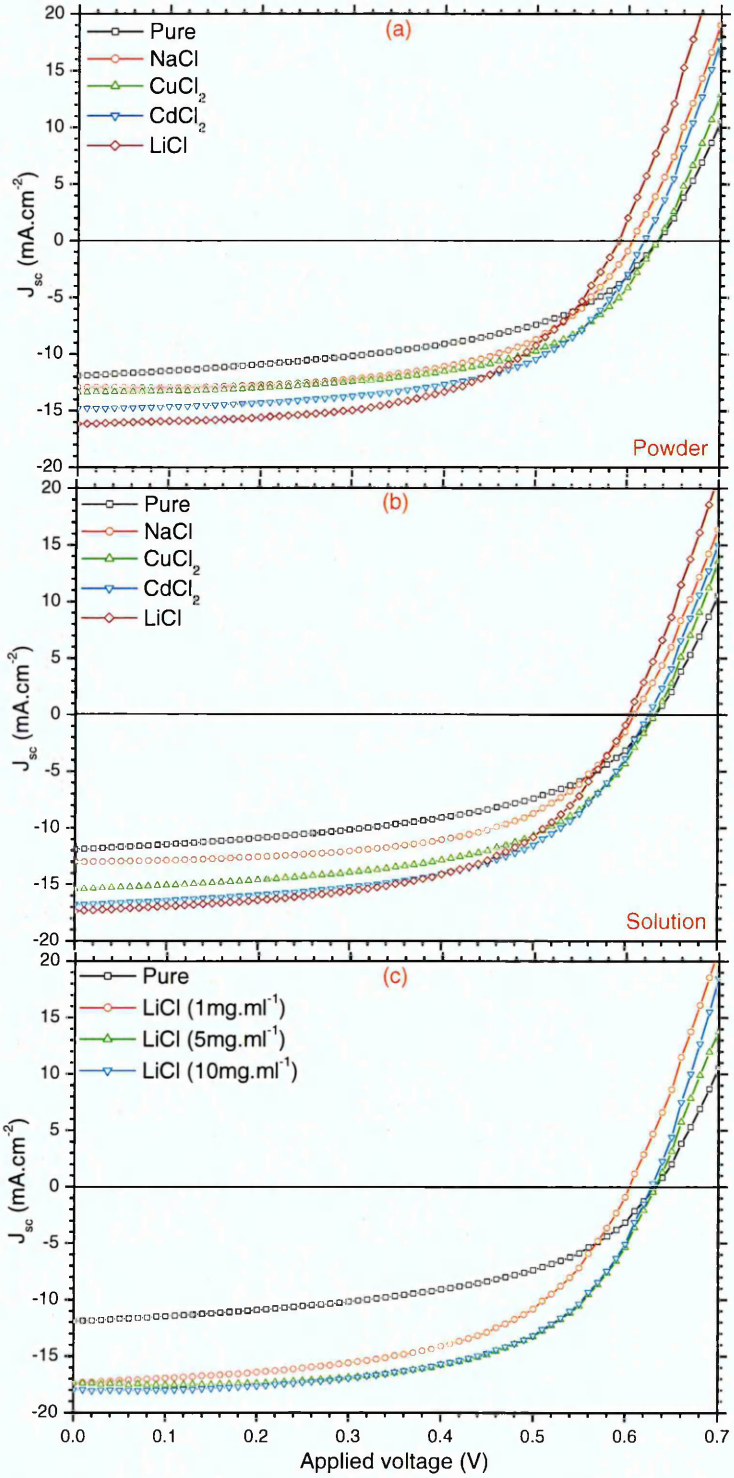

Fig.6. 14: P3HT:PCBM-based OSCs of devices having PEDOT:PSS layer treated with metal salts in (a) powder form, (b) solution form, and (c) $LiCl_2$ solution with different concentrations

A summary of the electrical parameters of the OSCs treated with those solutions is given in Table 6.3. PCE as high as 6.82% associated with FF=61%, J_{sc} of 17.97 mA.cm^{-2} and V_{oc}=0.62 V have been recorded for LiCl treated devices using a higher concentration of 10mg.ml^{-1}. Treatment of PEDOT:PSS with metal salts of concentrations higher than 10mg.ml^{-1} has not shown any further improvement in device performance. The above reported efficiency of 6.82% is found to be repeatable and on comparing this value with PCE values obtained for other metal salts treatment (see Table 6.3) it can be confirmed that these results are very reliable. The optimization of the PEDOT:PSS layer with different treatment is found to be key processing conditions to achieve good device performance [25, 54, 55].

Table 6.2: PV parameters of devices with PEDOT:PSS layer treated with metal salts as powder and aqueous solutions with the concentration of 1mg.ml^{-1}

		Powder				Solution			
	Pure	$CuCl_2$	NaCl	$CdCl_2$	LiCl	$CuCl_2$	Nacl	$CdCl_2$	LiCl
V_{oc} (V)	0.62	0.62	0.6	0.62	0.59	0.63	0.61	0.62	0.6
J_{sc} (mA.cm^{-2})	11.9	13.37	12.92	14.8	16.1	15.4	13	16.77	17.37
FF %	53	59	59	59	59	57	59	59	58
PCE %	3.92	5	4.6	5.4	5.6	5.52	4.7	6.1	6

Table 6.3: PV parameters of devices with PEDOT:PSS layer treated with different concentrations of aqueous solutions of metal salts (LiCl)

		Solution with different concentrations		
	Pure	LiCl (1mg.ml^{-1})	LiCl (5 mg.ml^{-1})	LiCl (10 mg.ml^{-1})
V_{oc} (V)	0.62	0.6	0.62	0.62
J_{sc} (mA.cm^{-2})	11.9	17.37	17.3	17.97
FF %	53	58	63	61
PCE %	3.92	6	6.77	6.82

It has been revealed that the electrical conductivity of pure PEDOT:PSS prepared from its aqueous solution can be significantly improved by adding organic compounds such as high-boiling point polar organic solvents, ionic liquids and surfactants or using post-treatment of PEDOT:PSS films with organic compounds, including high-boiling point polar solvents, salts, zwitterions, co-solvents, organic and inorganic acids [23]. On the other hand, the modification of electron transport layer in P3HT:PCBM-based OSC has revealed an improvement in the cells' PCE as compared to device without ETL as shown in Fig.6.15, with PCE reaching 4.25%, J_{sc} of 12.4mA.cm^{-2}, FF of 55% and V_{oc} of 0.63V (see Table 6.4). Using the optimised processing parameters of the P3HT:PCBM active layer and adding Alq3 layer as electron transport layer (ETL) prior to depositing the back contact (Al) has improved the performance of the device by assisting the charge collection and therefore increase J_{sc} which subsequently has caused an increase in the device efficiency. The improved FF has indicated a good resistance in the device, which may be attributed to the nice moulding between the Al electrode and the Alq3 surface during Al film evaporation. Similar characteristics have been reported for Alq3/Au interface [56].

It could be assumed that the organic-organic interface between Alq3 layer and the photoactive layer could be more favourable for charge transport in comparison with the organic-metal interface [57]. Although, there is a mismatching in the energy level between the active layer and Alq3 layer, electron transport can happen through damage induced trap states created by the evaporation of hot metal atoms onto the Alq3 surface [58]. Song and co-workers [59] have ascribed the improved performance in OSC devices using Alq3 layer to its effect as a blocking layer, which prevents the cathode atoms from diffusing into the active layer during the evaporation process. The insertion of Alq3 layer prepared by thermal evaporation and doped with magnesium has led to PCE enhancement in the PV performance of ZnPc/Mg:Alq3 OSCs [60]. This improvement was ascribed to the lowering of the potential barrier for electrons injection in the organic devices. Dey and co-workers have stated that the use of evaporated Alq3 layer could improve the PCE of the solar cell by up to 40%, where a maximum PCE of 3.9% has been reported by combining both Alq3 and novel zinc-benzothiazole complexes in OSC devices as a double buffer layer [61]. A similar performance has been reported in the present work using solution-processed Alq3 rather than evaporated.

Table 6.4: PV parameters of devices with different electrode modifications

	Pure	Alq3	LiCl (10 mg.ml^{-1})	Complete
V_{oc} (V)	0.62	0.63	0.62	0.61
J_{sc} (mA.cm^{-2})	11.9	12.4	17.97	16.26
FF %	53	0.55	61	0.71
PCE %	3.92	4.25	6.82	7

In addition, the modification of both, ETL and HTL layers has resulted in further enhancement in the device performance as shown in Fig.6.15; a PCE of 7% with a FF of 71%, J_{sc} of 16.26mA.cm^{-2} and V_{oc} of 0.61V have been confirmed. It could be argued that one of the main factors that affect the device PCE is the current density where the large stated value of 16.2mA.cm^{-2} may be attributed to the increased light absorption capability of the film especially at the higher wavelengths as demonstrated earlier by the UV-visible absorption spectra. Chu and co-authors [62] have verified that controlling the polymer nanoscale and increasing the crystallinity of P3HT:PCBM active layer has resulted in improving J_{sc} and FF. This was ascribed to the increased light absorption in the red region and improved charge transfer properties. Furthermore, the IPCE measurements were carried out to investigate the photo response and to confirm the increase in the current density as shown in Fig.6.16. A clear increase in the photocurrent has been observed after modifying the P3HT:PCBM-based device with ETL and HTL (complete device) with a maximum IPCE of 60% compared to a maximum IPCE of around 40% in the case of pristine device. A very useful parameter for defining the photo conversion efficiency of PV devices is the IPCE, which ideally should reach 100% every incident photon will generate an electron-hole pair. Nevertheless, practically, IPCE is usually less than 100% due to the losses caused by the reflection of incident photons, deficient absorption by the semiconductor, and recombination of charge carriers within the semiconductor [63]. Pangdam and co-authors [64] have demonstrated that the use of urchin-like gold nanothorns within the PEDOT:PSS layer has resulted in increasing the IPCE of the organic solar cells. These gold nanothorns are resulted in enhancing the light accumulation by acting as light-trapping materials.

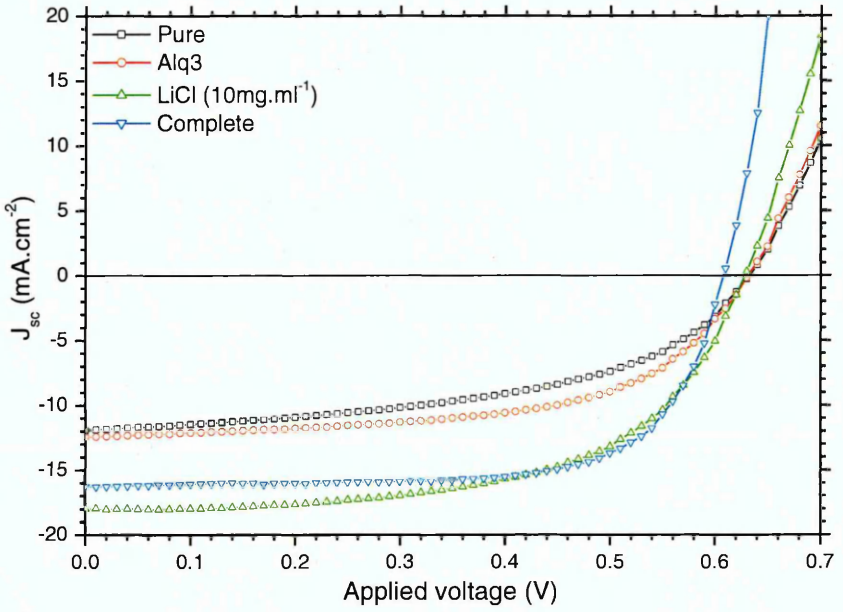

Fig.6. 15:P3HT:PCBM-based OSCs with different modification layers, device without any modification layer (pure), device with Alq3 as ETL, device with PEDOT:PSS treated LiCl (10mg.ml^{-1}) as HTL and a complete device with both ETL and HTL

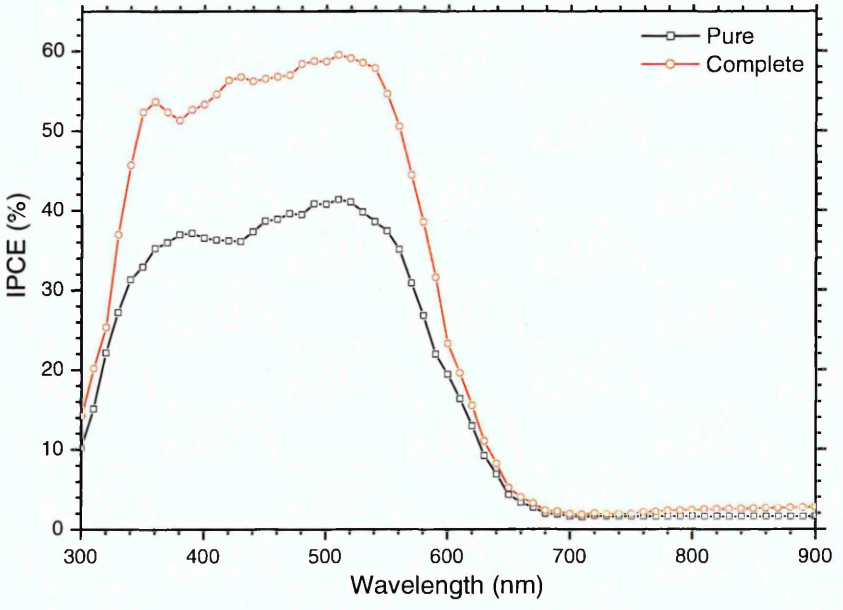

Fig.6. 16: IPCE of the P3HT:PCBM-based OSCs before and after modifying the two electrodes (complete device) with holes and electrons transport layers

6.2.6 Stability

The device stability of the P3HT:PCBM-based OSCs has been investigated after modifying the PEDOT:PSS with different metal salts as shown in Fig.6.17. The devices with best achieved performance (PEDOT:PSS-LiCl(10mg.ml^{-1})) have shown a degradation in the PCE from 6.82% to around 1% after 96 days. This huge degradation might be attributed to the fact that PEDOT:PSS is a highly acidic suspension (pH~1), which can erode the ITO electrode and cause indium migration into the P3HT:PCBM layer; furthermore, water molecules are easily penetrated into the hygroscopic PEDOT:PSS layer, resulting in degraded device performance. Besides, LiCl salt solution is basically neutral due to the following reactions between water and LiCl which results in both strong acids and bases:

$$Li^+ + H_2O \Longrightarrow LiOH + H^+$$

$$Cl^- + H_2O \Longrightarrow HCl + OH^-$$

It is well known that PEDOT:PSS has several problems including high acidity, hygroscopic properties, and inhomogeneous electrical properties, resulting in poor long-term stability [65]. Generally, all the solar cell parameters are influenced by the long-term usage; FF has shown a decrease of about 50% after 96 days, while degradation in J_{sc} has led to a similar trend in the device PCE. On the other hand, V_{oc} has exhibited no significant change. The degradation in the studied OSCs is thought to be due to the degradation in FF as well as the clear reduction in the J_{sc} value due to the morphological changes within the active layer [66].

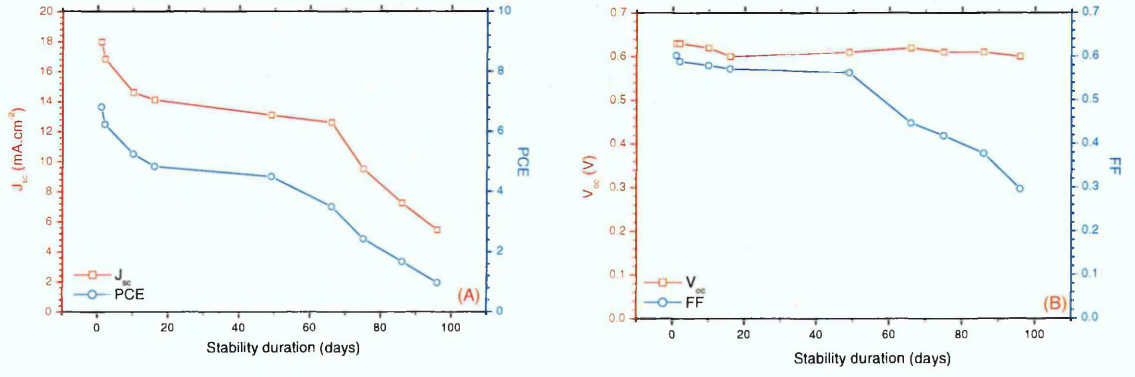

Fig.6. 17: Stability of the P3HT:PCBM-based devices after modifying the PEDOT:PSS with different metal salts

6.3 Summary

In this chapter, the effects of the hole and electron transport layers have been investigated. Using PEDOT:PSS as a typical hole transport layer has shown PCE of 3.92; this value has increased to 6.82 as a result of doping this layer with LiCl metal salts in aqueous solutions of the concentration of $10mg.ml^{-1}$. The latter device has shown good stability for a period of 45 days then degraded dramatically when tested after 96 days to reach a PCE of around 1%. Furthermore, the use of a solution processed electron transport layer of Alq3 has shown an improved device performance with PCE reaching 4.25% compared to the reference device without modifying the PEDOT:PSS layer. On the other hand, when these two layers modifications have been applied in one device (complete device) the PCE has increased to 7% with a FF of 71% which are of the highest reported parameters for OSCs using P3HT:PCBM blend.

References

[1] Reisdorffer, F., Haas, O., Le Rendu, P., & Nguyen, T. P. (2012). Co-solvent effects on the morphology of P3HT: PCBM thin films. Synthetic Metals, 161(23), 2544-2548.

[2] Mihailetchi, V. D., Xie, H., de Boer, B., et.al. (2006). Origin of the enhanced performance in poly (3-hexylthiophene):[6, 6]-phenyl C 61-butyric acid methyl ester solar cells upon slow drying of the active layer. Applied physics letters, 89(1), 012107.

[3] Motaung, D. E., Malgas, G. F., & Arendse, C. J. (2010). Comparative study: The effects of solvent on the morphology, optical and structural features of regioregular poly (3-hexylthiophene): fullerene thin films. Synthetic Metals, 160(9), 876-882.

[4] Kekuda, D., Lin, H. S., Wu, M. C., et.al. (2011). The effect of solvent induced crystallinity of polymer layer on poly (3-hexylthiophene)/C 70 bilayer solar cells. Solar Energy Materials and Solar Cells, 95(2), 419-422.

[5] Shen, Y., Li, K., Majumdar, N., et.al. (2011). Bulk and contact resistance in P3HT: PCBM heterojunction solar cells. Solar Energy Materials and Solar Cells, 95(8), 2314-2317.

[6] Kadem, B. Y., Al-hashimi, M. K., & Hassan, A. K. (2014). The effect of solution processing on the power conversion efficiency of P3HT-based organic solar cells. Energy Procedia, 50, 237-245.

[7] Kadem, B. Y., Hassan, A. K., & Cranton, W. (2016, July). The effects of organic solvents and their co-solvents on the optical, structural, morphological of P3HT: PCBM organic solar cells. In M. Aillerie, C. T. Salame, & P. Papageorgas (Eds.), AIP Conference Proceedings (Vol. 1758, No. 1, p. 020006). AIP Publishing.

[8] Kadem, B., Hassan, A., & Cranton, W. Performance optimization of P3HT: PCBM solar cells by controlling active layer thickness. In Proceedings of the 31st European photovoltaic solar energy conference and exhibition, EUPVSEC (2015, Hamburg, Germany).

[9] Kadem, B., Hassan, A., & Cranton, W. P3HT: PCBM-based organic solar cells: the effects of different PCBM derivatives. In Proceedings of the 32nd European photovoltaic solar energy conference and exhibition, EUPVSEC (2016, Munich, Germany).

[10] Kadem, B., Hassan, A., & Cranton, W. (2016). Efficient P3HT: PCBM bulk heterojunction organic solar cells; effect of post deposition thermal treatment. Journal of Materials Science: Materials in Electronics, 27(7), 7038-7048.

[11] Kadem, B., Cranton, W., & Hassan, A. (2015). Metal salt modified PEDOT: PSS as anode buffer layer and its effect on power conversion efficiency of organic solar cells. Organic Electronics, 24, 73-79.

[12] Kadem, B. Y., Hassan, A. K., & Cranton, W. (2015). Enhancement of power conversion efficiency of P3HT: PCBM solar cell using solution processed Alq3 film

as electron transport layer. Journal of Materials Science: Materials in Electronics, 26(6), 3976-3983.

[13] Han, H. C., Tseng, C. A., Du, C. Y., et.al. (2012). Enhancing efficiency with fluorinated interlayers in small molecule organic solar cells. Journal of Materials Chemistry, 22(43), 22899-22905.

[14] Steim, R., Kogler, F. R., & Brabec, C. J. (2010). Interface materials for organic solar cells. Journal of Materials Chemistry, 20(13), 2499-2512.

[15] Kulkarni, A. P., Tonzola, C. J., Babel, A., & Jenekhe, S. A. (2004). Electron transport materials for organic light-emitting diodes. Chemistry of materials, 16(23), 4556-4573.

[16] Dey, S., Vivo, P., Efimov, A., & Lemmetyinen, H. (2011). Enhanced performance and stability of inverted organic solar cells by using novel zinc-benzothiazole complexes as anode buffer layers. Journal of Materials Chemistry, 21(39), 15587-15592.

[17] Hoshi, T., Kumagai, K. I., Inoue, K., et.al. (2008). Electronic absorption and emission spectra of Alq 3 in solution with special attention to a delayed fluorescence. Journal of Luminescence, 128(8), 1353-1358.

[18] Chen, L. M., Xu, Z., Hong, Z., & Yang, Y. (2010). Interface investigation and engineering–achieving high performance polymer photovoltaic devices. Journal of Materials Chemistry, 20(13), 2575-2598.

[19] Jönsson, S. K. M., Birgerson, J., Crispin, X., et.al. (2003). The effects of solvents on the morphology and sheet resistance in poly (3, 4-ethylenedioxythiophene)–polystyrenesulfonic acid (PEDOT–PSS) films. Synthetic Metals, 139(1), 1-10.

[20] Sangeeth, C. S., Jaiswal, M., & Menon, R. (2009). Correlation of morphology and charge transport in poly (3, 4-ethylenedioxythiophene)–polystyrenesulfonic acid (PEDOT–PSS) films. Journal of Physics: Condensed Matter, 21(7), 072101.

[21] Xia, Y., & Ouyang, J. (2011). PEDOT: PSS films with significantly enhanced conductivities induced by preferential solvation with cosolvents and their application in polymer photovoltaic cells. Journal of Materials Chemistry, 21(13), 4927-4936.

[22] Yamamoto, N. A., Lima, L. F., Perdomo, R. E., et.al. (2013). Modification of PEDOT: PSS anode buffer layer with HFA for flexible polymer solar cells. Chemical Physics Letters, 572, 73-77.

[23] Ouyang, J. (2013). "Secondary doping" methods to significantly enhance the conductivity of PEDOT: PSS for its application as transparent electrode of optoelectronic devices. Displays, 34(5), 423-436.

[24] Xia, Y., & Ouyang, J. (2010). Anion effect on salt-induced conductivity enhancement of poly (3, 4-ethylenedioxythiophene): poly (styrenesulfonate) films. Organic Electronics, 11(6), 1129-1135.

[25] Badre, C., Marquant, L., Alsayed, A. M., & Hough, L. A. (2012). Highly Conductive Poly (3, 4-ethylenedioxythiophene): Poly (styrenesulfonate) Films Using 1-Ethyl-3-

methylimidazolium Tetracyanoborate Ionic Liquid. Advanced Functional Materials, 22(13), 2723-2727.

[26] Dharmadasa, I. M. (2014). Review of the CdCl2 treatment used in CdS/CdTe thin film solar cell development and new evidence towards improved understanding. Coatings, 4(2), 282-307.

[27] Bkakri, R., Kusmartseva, O. E., Kusmartsev, F. V., et.al. (2015). Degree of phase separation effects on the charge transfer properties of P3HT: Graphene nanocomposites. Journal of Luminescence, 161, 264-270.

[28] Shi, Y. W., Shi, M. M., Huang, J. C., et.al. (2006). Fluorinated Alq3 derivatives with tunable optical properties. Chemical communications, (18), 1941-1943.

[29] Dalasiński, P., Łukasiak, Z., Wojdyła, M., et.al. (2006). Study of optical properties of TRIS (8-hydroxyquinoline) aluminum (III). Optical Materials, 28(1), 98-101.

[30] Gasiorowski, J., Menon, R., Hingerl, K., et.al. (2013). Surface morphology, optical properties and conductivity changes of poly (3, 4-ethylenedioxythiophene): poly (styrenesulfonate) by using additives. Thin Solid Films, 536, 211-215.

[31] Cook, S., Ohkita, H., Kim, Y., et.al. (2007). A photophysical study of PCBM thin films. Chemical Physics Letters, 445(4), 276-280.

[32] Chao, Y. C., Lin, Y. H., Lin, C. Y., et.al. (2014). Improved light trapping in polymer solar cells by light diffusion ink. Journal of Physics D: Applied Physics, 47(10), 105102.

[33] Brückner, R., Lyssenko, V. G., Hofmann, S., & Leo, K. (2014). Lasing of Tamm states in highly efficient organic devices based on small-molecule organic semiconductors. Faraday discussions, 174, 183-201.

[34] Ferry, V. E., Verschuuren, M. A., Li, H. B., et.al. (2010). Light trapping in ultrathin plasmonic solar cells. Optics express, 18(102), A237-A245.

[35] Zeng, L., Bermel, P., Yi, Y., et.al. (2008). Demonstration of enhanced absorption in thin film Si solar cells with textured photonic crystal back reflector. Applied Physics Letters, 93(22), 221105.

[36] Petoukhoff, C. E., & O'Carroll, D. M. (2015). Absorption-induced scattering and surface plasmon out-coupling from absorber-coated plasmonic metasurfaces. Nature communications, 6.

[37] Hua, B., Lin, Q., Zhang, Q., & Fan, Z. (2013). Efficient photon management with nanostructures for photovoltaics. Nanoscale, 5(15), 6627-6640.

[38] Yablonovitch, E., & Cody, G. D. (1982). Intensity enhancement in textured optical sheets for solar cells. IEEE Transactions on Electron Devices, 29(2), 300-305.

[39] Petrova, P. K., Tomova, R. L., & Stoycheva-Topalova, R. T. (2011). Organic Light Emitting Diodes Based on Novel Zn and Al Complexes. INTECH Open Access Publisher.

[40] Arwin, H., Poksinski, M., & Johansen, K. (2004). Total internal reflection ellipsometry: principles and applications. Applied optics, 43(15), 3028-3036.

[41] Nabok, A. V., Tsargorodskaya, A., Hassan, A. K., & Starodub, N. F. (2005). Total internal reflection ellipsometry and SPR detection of low molecular weight environmental toxins. Applied surface science, 246(4), 381-386.

[42] Baba, A., Aoki, N., Shinbo, K., et.al. (2011). Grating-coupled surface plasmon enhanced short-circuit current in organic thin-film photovoltaic cells. ACS applied materials & interfaces, 3(6), 2080-2084.

[43] Güllü, Ö., Aydoğan, Ş., & Türüt, A. (2012). High barrier Schottky diode with organic interlayer. Solid State Communications, 152(5), 381-385.

[44] Ma, W., Yang, C., Gong, X., et.al. (2005). Thermally stable, efficient polymer solar cells with nanoscale control of the interpenetrating network morphology. Advanced Functional Materials, 15(10), 1617-1622.

[45] Ray, B., & Alam, M. A. (2013). Achieving fill factor above 80% in organic solar cells by charged interface. IEEE Journal of Photovoltaics, 3(1), 310-317.

[46] Liu, C., Xu, Y., & Noh, Y. Y. (2015). Contact engineering in organic field-effect transistors. Materials today, 18(2), 79-96.

[47] Yakuphanoglu, F., & Anand, R. S. (2010). Charge transport properties of an organic solar cell. Synthetic Metals, 160(21), 2250-2254.

[48] Lou, Y., Wang, Z., Naka, S., & Okada, H. (2012). Charge transport characteristics in P3HT: PCBM organic blends under illumination: Influence of metal work functions. Chemical Physics Letters, 529, 64-68.

[49] Montero, J. M., Bisquert, J., Garcia-Belmonte, G., et.al. (2009). Trap-limited mobility in space-charge limited current in organic layers. Organic Electronics, 10(2), 305-312.

[50] Kapoor, A. K., Annapoorni, S., & Kumar, V. (2008). Conduction mechanisms in poly (3-hexylthiophene) thin-film sandwiched structures. Semiconductor Science and Technology, 23(3), 035008.

[51] Mbule, P. S., Swart, H. C., & Ntwaeaborwa, O. M. (2014). Effects of thermal treatment and depth profiling analysis of solution processed bulk-heterojunction organic photovoltaic cells. Journal of colloid and interface science, 436, 9-15.

[52] Rauh, D., Wagenpfahl, A., Deibel, C., & Dyakonov, V. (2011). Relation of open circuit voltage to charge carrier density in organic bulk heterojunction solar cells. Applied Physics Letters, 98(13), 69.

[53] Lin, Y., Li, Y., & Zhan, X. (2012). Small molecule semiconductors for high-efficiency organic photovoltaics. Chemical Society Reviews, 41(11), 4245-4272.

[54] Sun, K., Xia, Y., & Ouyang, J. (2012). Improvement in the photovoltaic efficiency of polymer solar cells by treating the poly (3, 4-ethylenedioxythiophene): poly (styrenesulfonate) buffer layer with co-solvents of hydrophilic organic solvents and hydrophobic 1, 2-dichlorobenzene. Solar energy materials and solar cells, 97, 89-96.

[55] Fan, B., Mei, X., & Ouyang, J. (2008). Significant conductivity enhancement of conductive poly (3, 4-ethylenedioxythiophene): poly (styrenesulfonate) films by adding anionic surfactants into polymer solution.

[56] Vivo, P., Jukola, J., Ojala, M., et.al. (2008). Influence of Alq 3/Au cathode on stability and efficiency of a layered organic solar cell in air. Solar energy materials and solar cells, 92(11), 1416-1420.

[57] Liu, Z., Tian, M., & Wang, N. (2014). Influences of Alq 3 as electron extraction layer instead of Ca on the photo-stability of organic solar cells. Journal of Power Sources, 250, 105-109.

[58] Lassiter, B. E., Wei, G., Wang, S., et.al. (2011). Organic photovoltaics incorporating electron conducting exciton blocking layers. Applied Physics Letters, 98(24), 112.

[59] Song, Q. L., Li, F. Y., Yang, H., et.al. (2005). Small-molecule organic solar cells with improved stability. Chemical Physics Letters, 416(1), 42-46.

[60] Chou, C. T., Lin, C. H., Wu, M. H., et.al. (2011). Tuning open-circuit voltage in organic solar cells by magnesium modified Alq3. Journal of applied physics, 110(8), 083104.

[61] Qi, B., & Wang, J. (2012). Open-circuit voltage in organic solar cells. Journal of Materials Chemistry, 22(46), 24315-24325.

[62] Chu, C. W., Yang, H., Hou, W. J., Huang, J., et.al. (2008). Control of the nanoscale crystallinity and phase separation in polymer solar cells. Applied Physics Letters, 92(10), 86.

[63] Kim, C. H., Cha, S. H., Kim, S. C., et.al. (2011). Silver nanowire embedded in P3HT: PCBM for high-efficiency hybrid photovoltaic device applications. ACS nano, 5(4), 3319-3325.

[64] Pangdam, A., Nootchanat, S., Ishikawa, R., et.al. (2016). Effect of urchin-like gold nanoparticles in organic thin-film solar cells. Physical Chemistry Chemical Physics, 18(27), 18500-18506.

[65] Yun, J. M., Yeo, J. S., Kim, J., et.al. (2011). Solution-Processable Reduced Graphene Oxide as a Novel Alternative to PEDOT: PSS Hole Transport Layers for Highly Efficient and Stable Polymer Solar Cells. Advanced Materials, 23(42), 4923-4928.

[66] Voroshazi, E., Verreet, B., Aernouts, T., & Heremans, P. (2011). Long-term operational lifetime and degradation analysis of P3HT: PCBM photovoltaic cells. Solar Energy Materials and Solar Cells, 95(5), 1303-1307.

Chapter 7: Ternary blend organic solar cells

7.1 Introduction

Due to the rapid development in materials' technology, hybrid and composite materials have been addressed as significant candidates in several optoelectronic device applications regarding their effects on the electrical, optical and mechanical properties [1-3]. Among several others, carbon-based materials such as carbon nanotubes (CNTs) and graphene are the most attractive candidates. Graphene is a two dimensional single layer of carbon atoms bonded together in a honeycomb lattice; this material demonstrates unique mechanical, thermal and electrical characteristics [4]. Graphene has semiconducting properties with zero band gap, with electrons act as massless particles which suggests less power consumption and improved performance due to increased carrier velocities [5]. Graphene has considerable electrical conductivity; charges can transfer up to micrometers on the graphene sheet without being scattered. On the other hand, CNTs have ballistic charge transport with free paths of the order of micrometres as well [6]. CNTs' diameters can be in the range of <1 nm for single-wall carbon nanotubes (SWCNTs) and up to tens of nanometres for multi-walled carbon nanotubes (MWCNTs). Despite the fact that SWCNTs can be either metallic or semiconducting, MWCNTs are mostly metallic [5]. CNTs also exhibit strong chemical and mechanical stability with very high thermal conductivity [7]. Metallo phthalocyanines is another class of materials with great range of interesting properties, which have been employed in several optoelectronic applications due to their strong absorption peaks in the visible and near infra-red region of their UV-visible spectra [8]. The integration of CNTs or graphene with the metal phthalocyanines has been shown to enhance the optoelectronic [1] as well as the sensing properties of these compounds [3]. Kaya and co-authors [9] have demonstrated an effective interaction between SWCNTs and pyrene-substituents on the ZnPc ring. In a fundamental study it has been revealed that π-π interaction is formed within non-covalently bonded hybrids of copper phthalocyanine-3,4',4",4"'-tetrasulfonic acid tetrasodium salt (TSCuPc) and graphene [10].

Karousis and co-authors [4] have developed electron donor-acceptor system based on (2-aminoethoxy)(tri-tert-butyl) zinc phthalocyanine (ZnPc)-graphene hybrid material by exfoliating graphene sheets in ortho-dichlorobenzene (oDCB) using sonication technique followed by covalently attaching ZnPc onto the exfoliated graphene. These hybrids have been used to fabricate photo-electrochemical cell where the hybrid films have exhibited prompt, stable, and reproducible photocurrent. Moreover, these hybrid materials having graphene and photoactive moieties were proposed as promising materials for solar cell applications [4]. In this work, the comparative study of single walled carbon nanotubes (SWCNTs) and reduced graphene oxide (rGO) covalently and non-covalently functionalized with the novel 1-[N-(2-ethoxyethyl)-4-pentynamide]-8(11),15(18),22(25)-tris-{2-[2-(2-ethoxyethoxy) ethoxy]-1-[2-((2-ethoxyethoxy)-ethoxy)methyl]ethyloxy} zinc(II) phthalocyanine has been carried out. The target SWCNTs and rGO hybrid materials covalently functionalized with phthalocyanine moieties were prepared by the reaction of azido substituted SWCNTs or rGO with the asymmetrically substituted zinc(II) phthalocyanine (ZnPc) containing a terminal alkyne group via "Click" reaction (see Fig.7.1). The effects of the covalent and non-covalent linking on the chemical properties of these materials and the some of their characterisation are presented in Appendix A. In order to achieve a higher solar cell performance, it is crucial that nanoscale interpenetrated network of the blend is formed in the active layer. Such nanoscale network is frequently shown to facilitate charge carriers separation and transportation, with exciton diffusion length in the range 10-20 nm [11]. Using these novel hybrids within the P3HT:PCBM blend to form a ternary blend has been investigated. It is worth stating that the ternary blend is an encouraging concept to improve OSCs performance by either incorporation of complementary optical material or a material with higher charge carrier mobility or both. There are however two main restrictions in designing the ternary blends; these are the alignment of the energy levels of the donor and acceptor materials in the blend and the distribution of the dopants within the blend [12]. The band gap and the energy level alignment of the D/A within P3HT:PCBM blends could also lead to enhanced light absorption [13]. Functional materials such as SWCNTs with ballistic charge transport, high flexibility, and excellent mechanical and chemical stability are promising materials for ternary blend composites [14].

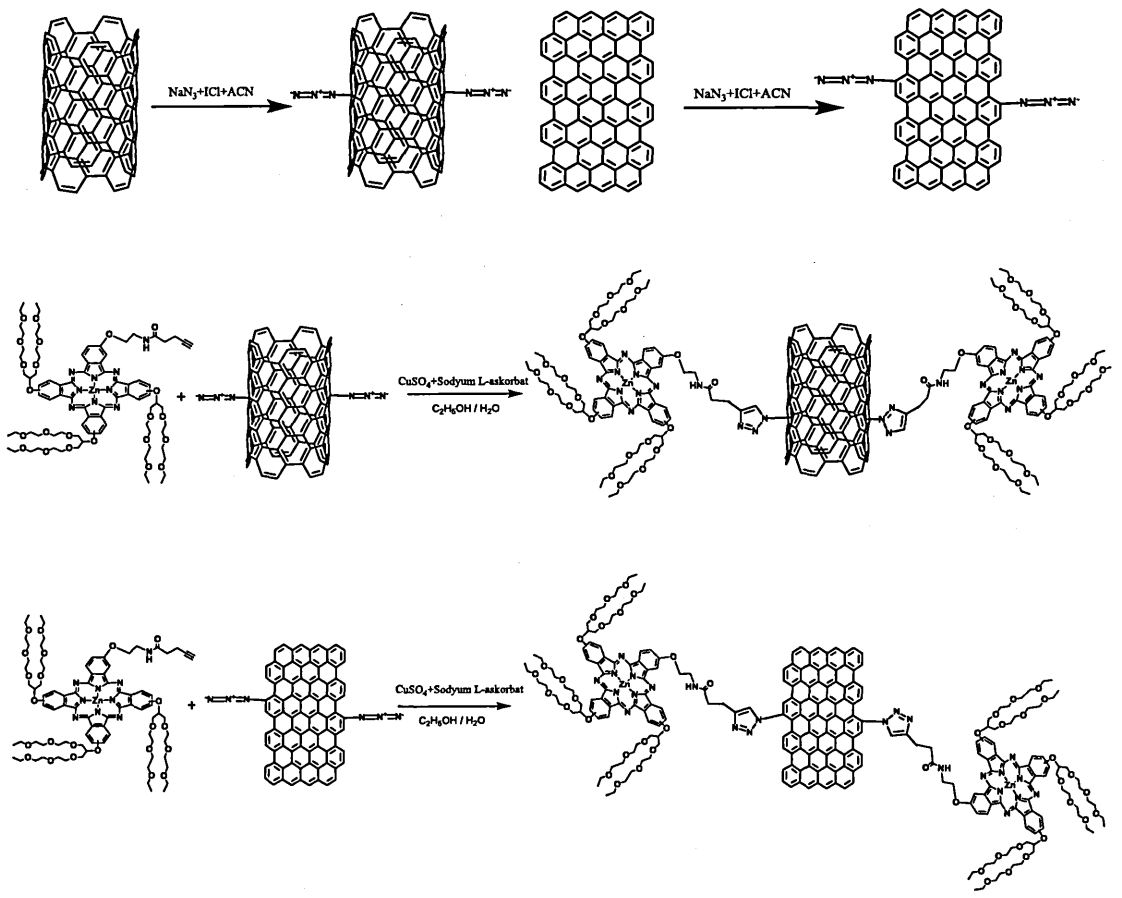

Fig.7.1: Click reaction method; The target azido substituted hybrid materials covalently functionalized with the asymmetrical zinc(II) phthalocyanine (ZnPc) containing a terminal alkyne group

Additionally, reduced graphene oxide (rGO) or graphene are usually used as transparent electrodes [15] or as novel alternatives to PEDOT:PSS hole transport layers [16] as well as an acceptor within the organic solar cell blends [17]. On the other hand, zinc phthalocyanine is an organic semiconductor material which has shown a promising application in organic solar cells with the potential of further enhancing the light harvesting properties of the blends due to its wide absorption bands in the near red region [18]. The use of functional materials such as SWCNTs and rGO might have some disadvantages in this respect due to their possible contribution in compromising the device shunt resistance, as well as acting as charge recombination centres [19].

Optimisation of carbon-based functional materials used in OSCs could however be achieved when small proportions of these materials are included in a controlled manner in these hybrids [12].

7.2 Results and discussion

7.2.1 UV-visible absorption spectra

Pristine asymmetrically substituted ZnPc, covalently and non-covalently bonded ZnPc:SWCNTs and ZnPc:rGO hybrid materials were dispersed in DMF with the concentration of 0.25 $mg.mL^{-1}$; 20 μL from each solution was added to 3 mL DMF for absorption m easurements. ZnPc is soluble in DMF while the hybrids have exhibited good dispersion in this solvent as shown in Fig.7.2. UV–visible absorption spectra of ZnPc and its hybrid materials are shown in Fig.7.3. The spectrum of the ZnPc shows a characteristic absorption in the Q band region at 683 nm. Absorption in this region represents the vibration levels referring to the first and second excited electronic states. Moreover, a Soret band (B-band) was observed at around 345 nm, which is related to a group of electronic transitions with different spins and dipole moments [20]. The ZnPc:SWCNTs and ZnPc:rGO hybrids on the other hand have exhibited lower absorption intensities, with absorption bands appeared broadened and extended throughout the UV region. Similar absorption spectra were observed by Karousis and co-workers for ZnPc/Graphene composite [4]. They have revealed that such spectra give obvious indication of ground-state electronic interactions between ZnPc and graphene within the hybrid materials. Such broad coverage of the absorption spectra over the UV-vis-NIR regions could result in improved light-harvesting properties when such hybrids are employed for solar cell applications [21]. Furthermore, the hybrid solutions exhibited a blue shift of about 10 nm in the B-band. Simultaneously, the shoulder peak of the Q-band of ZnPc ascribed to ZnPc dimers has slightly disappeared, especially in ZnPc:rGO-co hybrids. This can be ascribed to the strong π-π interaction between ZnPc and SWCNTs or rGO [22]. Energy band gaps (E_g) of ZnPc and its hybrids with rGO or SWCNTs were estimated using UV-visible absorption spectra. Generally, ZnPc has a band gap in the region of 1.8eV [23].

In the current study, similarly to [23], Tauc equation has been used for estimation of E_g, and band gap E_g =1.7 eV was found for ZnPc as shown in Fig.7.4. On the other hand, smaller values of E_g have been obtained for the hybrids with values of 1.68 eV and 1.62 eV for the ZnPc:rGO-non-co and ZnPc:rGO-co hybrids respectively while values of 1.69 eV and 1.64 eV were obtained for ZnPc:SWCNTs-non-co and ZnPc:SWCNTs-co hybrids, respectively. This reduction in E_g could be ascribed to the π-π interaction within the hybrids and it could be a useful factor for optoelectronic device applications as in solar cells [24].

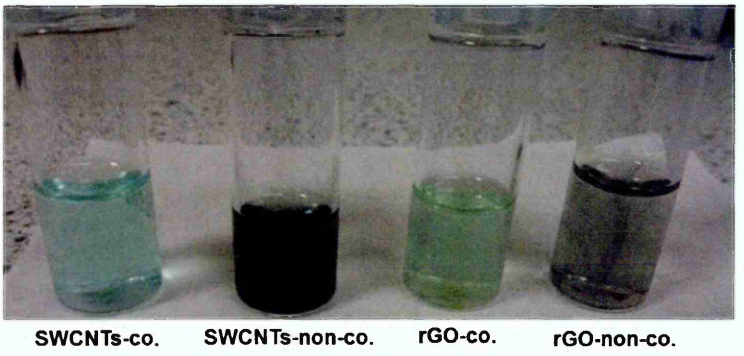

Fig.7.2: ZnPc-based hybrids suspended in DMF solution

The absorption spectra of P3HT:PCBM active layer with and without adding a small amount of ZnPc hybrids to the blend are shown in Fig.7.5. Basically, the absorption spectra for P3HT:PCBM blend are characterised by 3 absorption bands (A, B, and C) as demonstrated earlier in chapter 5, which are related to the P3HT absorption whereas the forth band (D) is related to absorption by PCBM molecules [25]. Similar spectra have been observed after adding small amount of these hybrids to the P3HT:PCBM with a slight red shift in band (C) of ZnPc:rGO-based films. On the other hand, the absorption intensity has increased after adding these hybrids (the film's thicknesses was controlled to be 150±5nm as were determined by spectroscopic ellipsometry). Salim and co-authors [12] have argued that the slight increase in absorbance is thought to enhance the photon harvesting which may contribute to improved charge carrier generation.

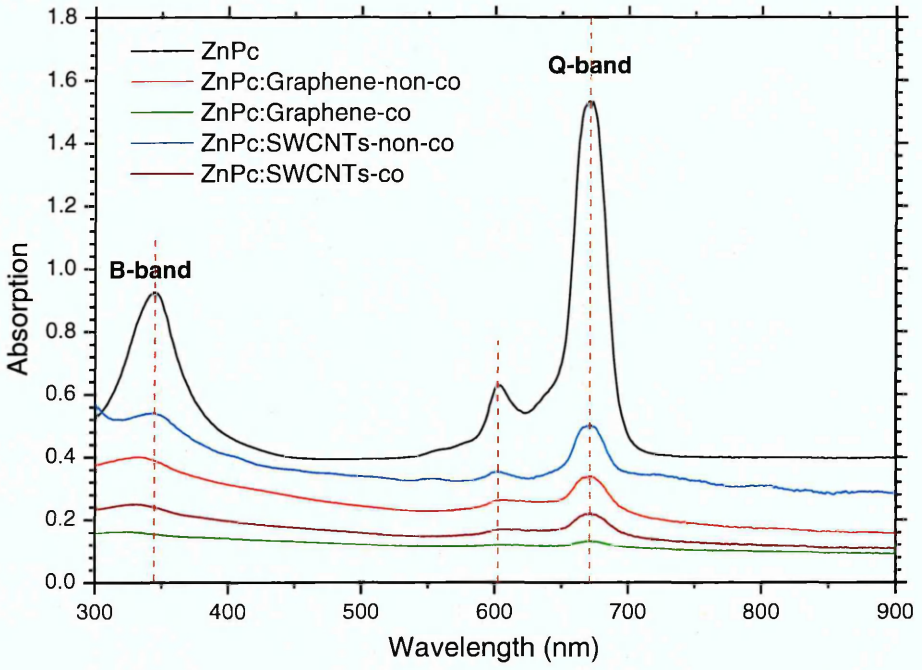

Fig.7.3: UV–visible absorption spectra of ZnPc and its hybrid materials (ZnPc:SWCNTs and ZnPc:rGO) dispersed in DMF

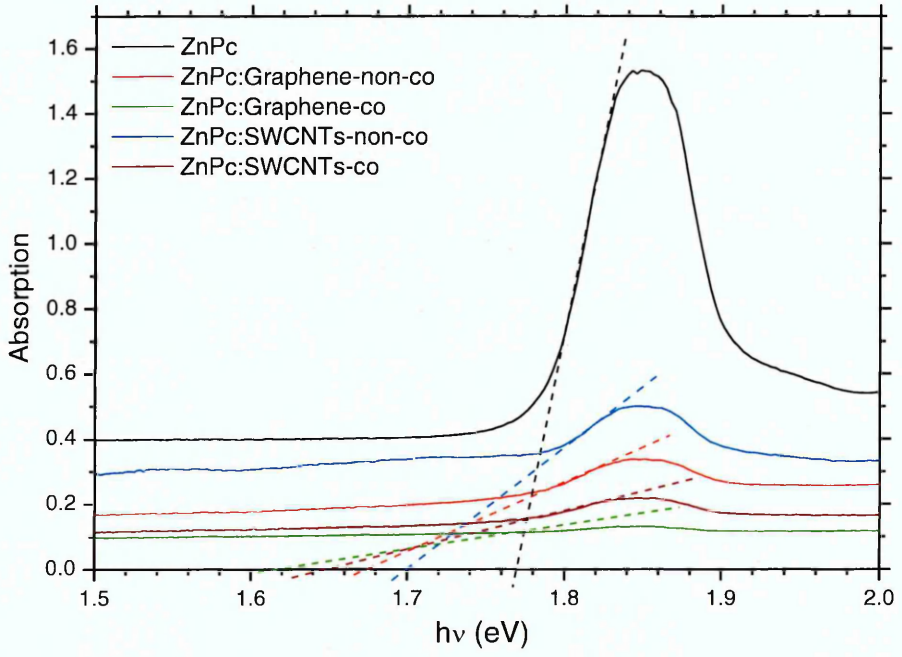

Fig.7.4: Energy band gap determination using Tauc equation for the hybrids under study

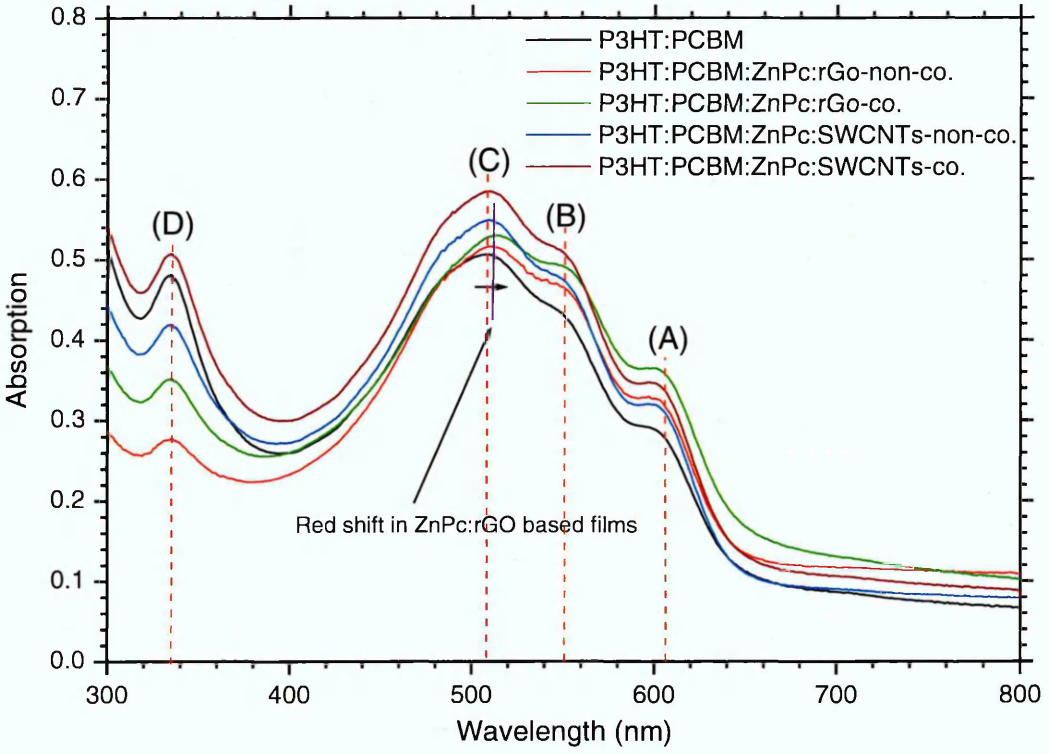

Fig.7.5: UV–visible absorption spectra of P3HT:PCBM before and after addition of small amount of ZnPc hybrid materials (ZnPc:SWCNTs and ZnPc:rGO)

7.2.2 Cyclic voltammetry

Cyclic voltammetry is one of the most useful methods to estimate positions of the energy of the highest occupied molecular orbital (HOMO) and the energy of lowest unoccupied molecular orbital (LUMO) of organic semiconductors and to help estimating their energy band gap (E_g) [26]. The latter is basically the energy difference between the LUMO and the HOMO, where the HOMO represents the energy required to extract an electron from a molecule (oxidation process=E_{ox}) while LUMO is the energy necessary to inject an electron to a molecule (reduction process= E_{red}) [27]. The latter processes can be determined using cyclic voltammetry by measuring the E_{ox} and E_{red} potentials and using equations 4.14 and 4.15, given in Chapter 4. In this study, the obtained voltammogram measured for the studied hybrids are presented in Fig.7.6. This was carried out using screen printed carbon electrodes in DMF solution containing 0.1 M LiCl [28] at a scan rate of 50 mV s^{-1}.

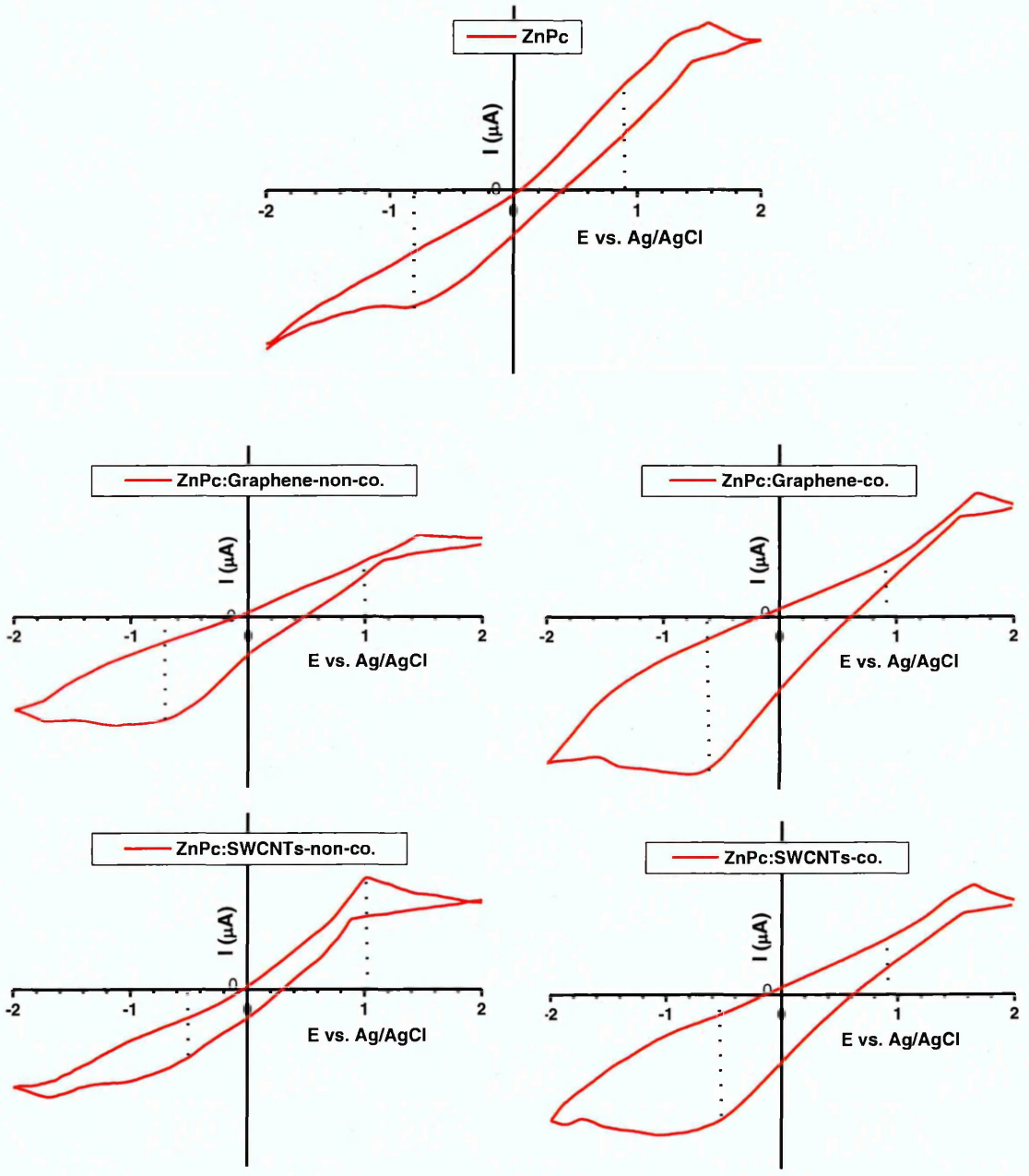

Fig.7.6: Cyclic voltammogram of pristine ZnPc as well as ZnPc, both covalently and non-covalently bonded to SWCNTs and rGO suspended in DMF solution in the presence of 0.1M LiCl.

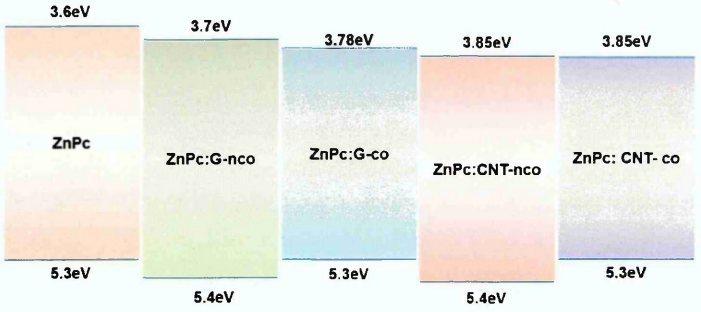

Fig.7.7: Molecular energy levels of the ZnPc and its hybrids

The HOMO and LUMO energy levels of the studied materials were calculated and presented in Table 7.1. Different oxidation and reduction peaks were observed for the different hybrids in the scanned electrochemical window. ZnPc bonded covalently with SWCNTs or rGO has exhibited broadened redox peaks, which were attributed to the low solubility and strong aggregation in the solution [29]. As has been described in chapter 4 (eq. 2.14 and 2.15), the positions of the HOMO and LUMO energy levels were estimated from oxidation and reduction peaks in Fig.7.6 which appear occasionally as shoulders on CV curves, E_g values were therefore calculated. The first oxidation/reduction peaks of the hybrids were considered for the calculations of the HOMO and LUMO positions. Table 7.1 shows that these values are in good agreement with the E_g values obtained using UV-visible absorption spectroscopy in DMF solutions. The energy levels alignment of the ZnPc and its hybrids are presented in Fig.7.7.

Table 7. 1: The HOMO and LUMO energy levels and the energy band gap (eV) of the hybrids determined from cyclic voltammetry and optical absorption spectroscopy

	ZnPc	ZnPc: rGO-non-co	ZnPc: rGO-co	ZnPc: SWCNTs-non-co	ZnPc: SWCNTs-co
E_{HOMO}	5.3	5.4	5.3	5.4	5.3
E_{LUMO}	3.6	3.7	3.78	3.85	3.85
E_g (cyclic)	1.7	1.7	1.52	1.55	1.45
E_g (optical)	1.7	1.68	1.62	1.69	1.64

7.2.3 Morphological properties

The morphological features of the hybrids under study were examined using SEM and AFM techniques, and the results are shown in Fig.7.8 and Fig.7.9 respectively. Fig.7.8 shows the SEM images of the studied hybrids, which clearly shows that ZnPc film exhibits smooth surface texture with small crystalline features. On the other hand, functionalized rGO and SWCNTs with ZnPc have demonstrated different surface topographies depending on the type of bonding. SWCNTs based hybrids have exhibited clear features of ZnPc attached to the SWCNTs; however, the non-covalently bonded hybrids have demonstrated clear nanotube features on the surface, while the covalently bonded hybrids have exhibited more homogeneous distribution of both materials. rGO-based hybrids however have demonstrated different features in keeping with the two dimensional nature of graphene nanomaterials. ZnPc:rGO-co hybrids show stacks-like features while the ZnPc:rGO-non-co exhibited flakes-like structure. Further confirmation of the surface topographies of these hybrids has been revealed by AFM images as shown in Fig.7.9.

AFM images have demonstrated similar surface morphologies to those shown using SEM measurements for the same studied hybrids. The hybrid films were prepared for AFM measurements using chloroform-based solution and casting method. 2D AFM images of these hybrids show that the surface roughness of the ZnPc film is found to vary due to the clearly shown small round grain features. ZnPc:rGO-co bonded film shows clear ZnPc:rGO sheets arranged laterally with respect to the substrate, whereas the ZnPc:rGO:non-co bonded shows randomly distributed flacks of ZnPc and rGO sheets. Furthermore, ZnPc:SWCNTs-co bonded hybrid shows better homogeneity compared to ZnPc:SWCNTs-non-co bonded film. The 3D AFM images demonstrate a good view to the surface morphology based on the features and the surface roughness for each film. On blending the ZnPc:carbon-based hybrids with the P3HT:PCBM blend for solar cell applications, the morphological features of P3HT:PCBM blend have exhibited nanoscale networks as demonstrated in the SEM images shown in Fig.7.10.

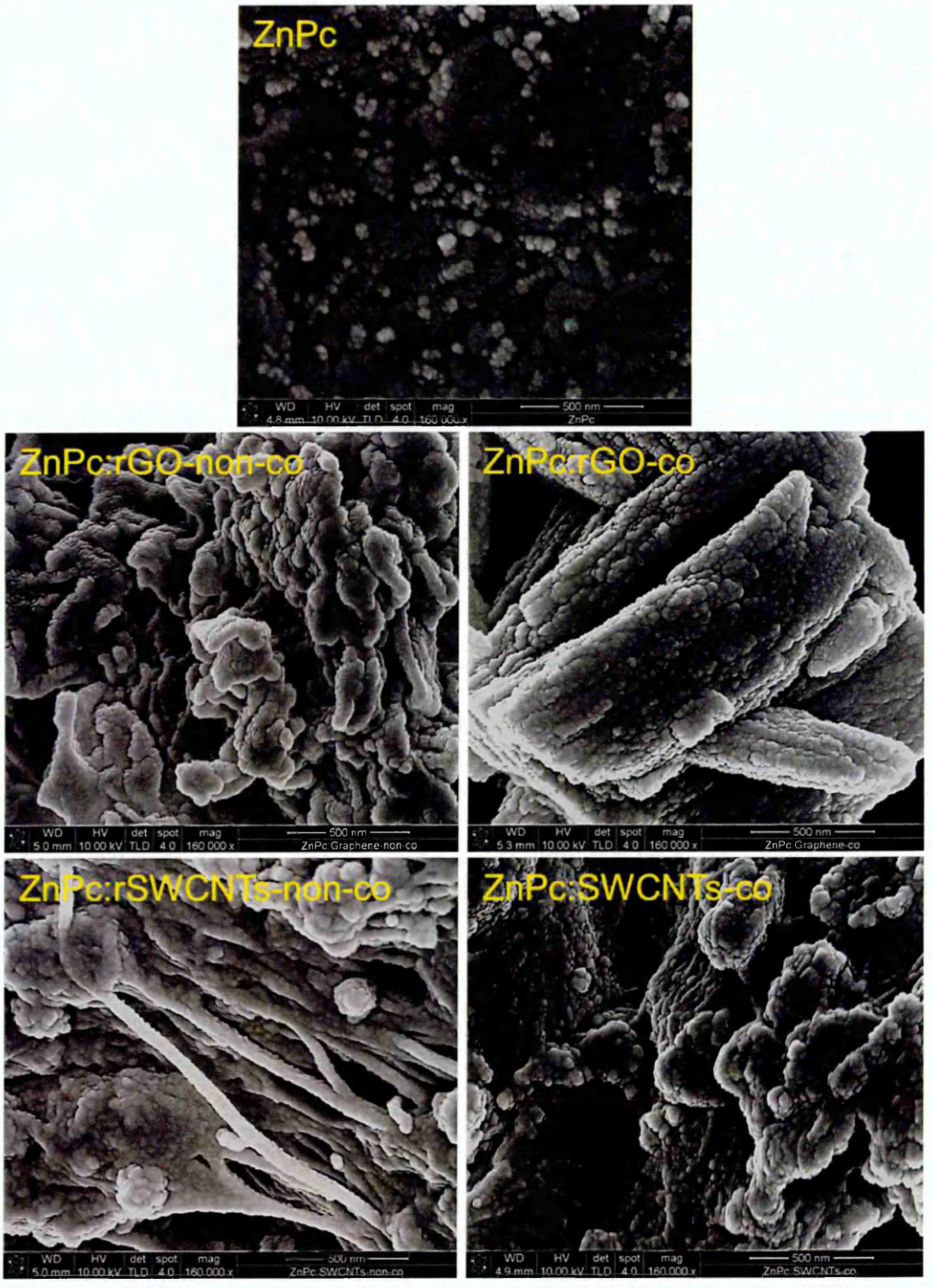

Fig.7.8: SEM images of pristine ZnPc, and its hybrids both, covalently and non-covalently functionalized with rGO or SWCNTs

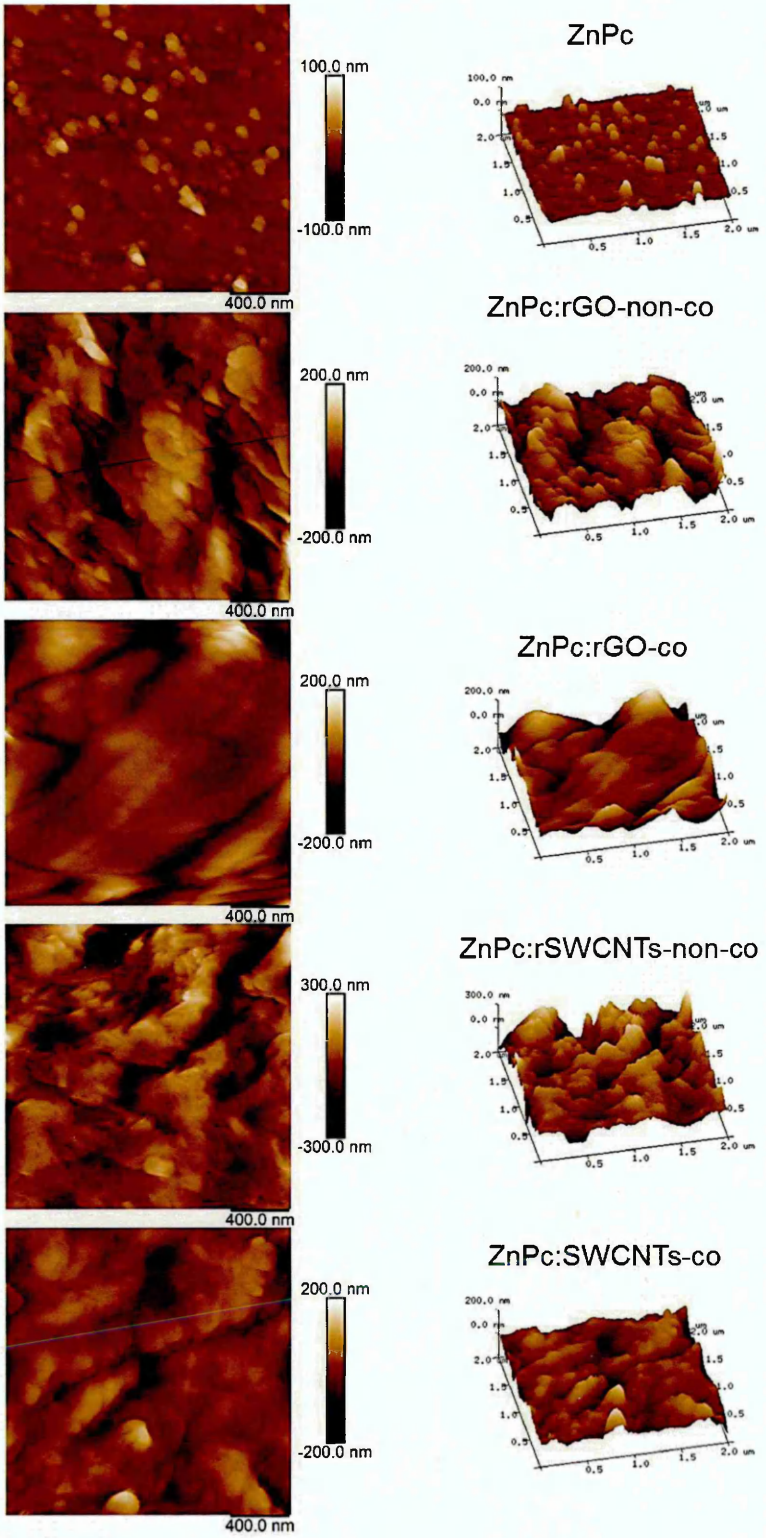

Fig.7.9: AFM images of pristine ZnPc, and its hybrids both, covalently and non-covalently functionalized with rGO or SWCNTs

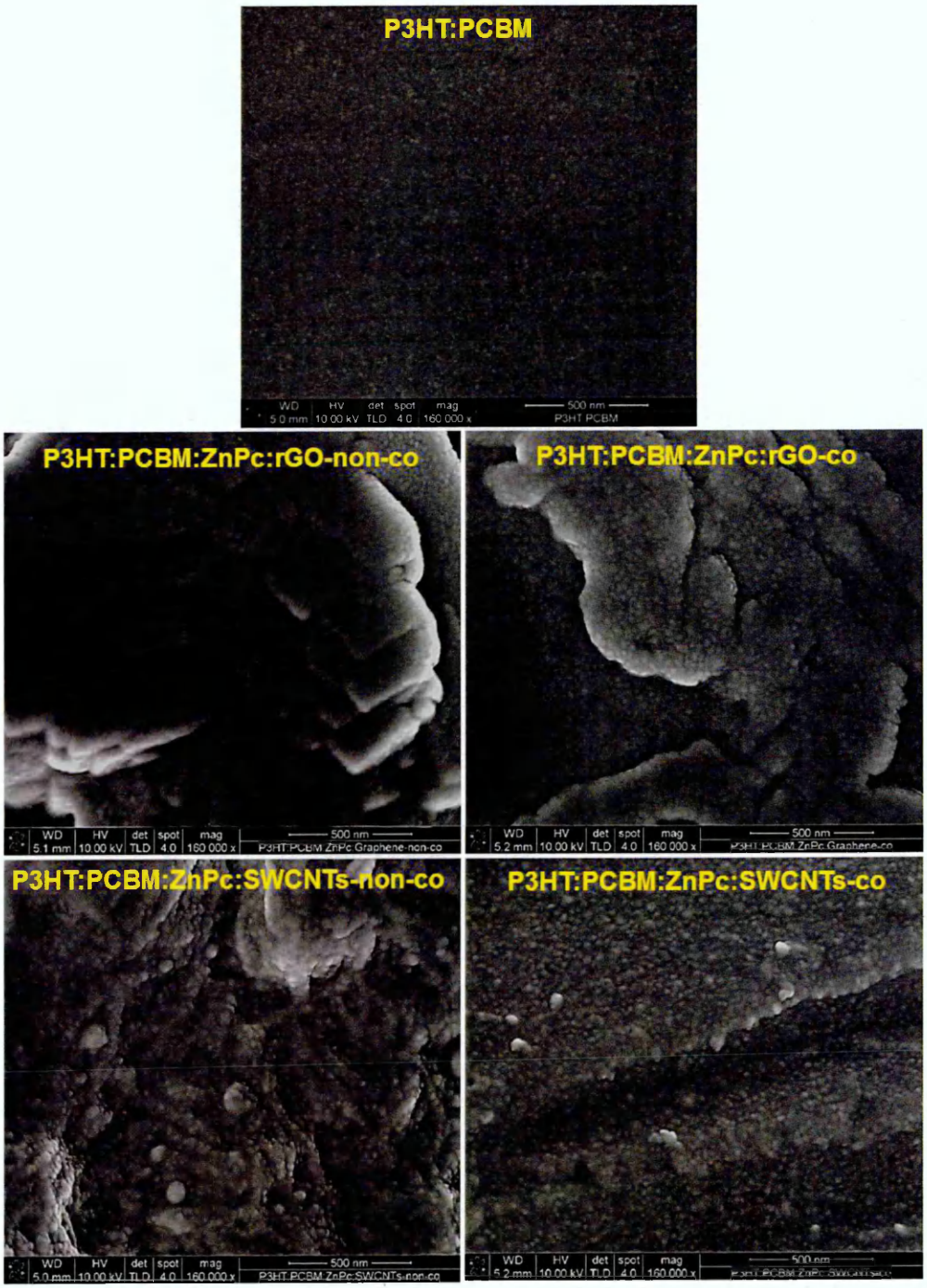

Fig.7.10: SEM images of P3HT:PCBM and P3HT:PCBM:ZnPc-hybrid films

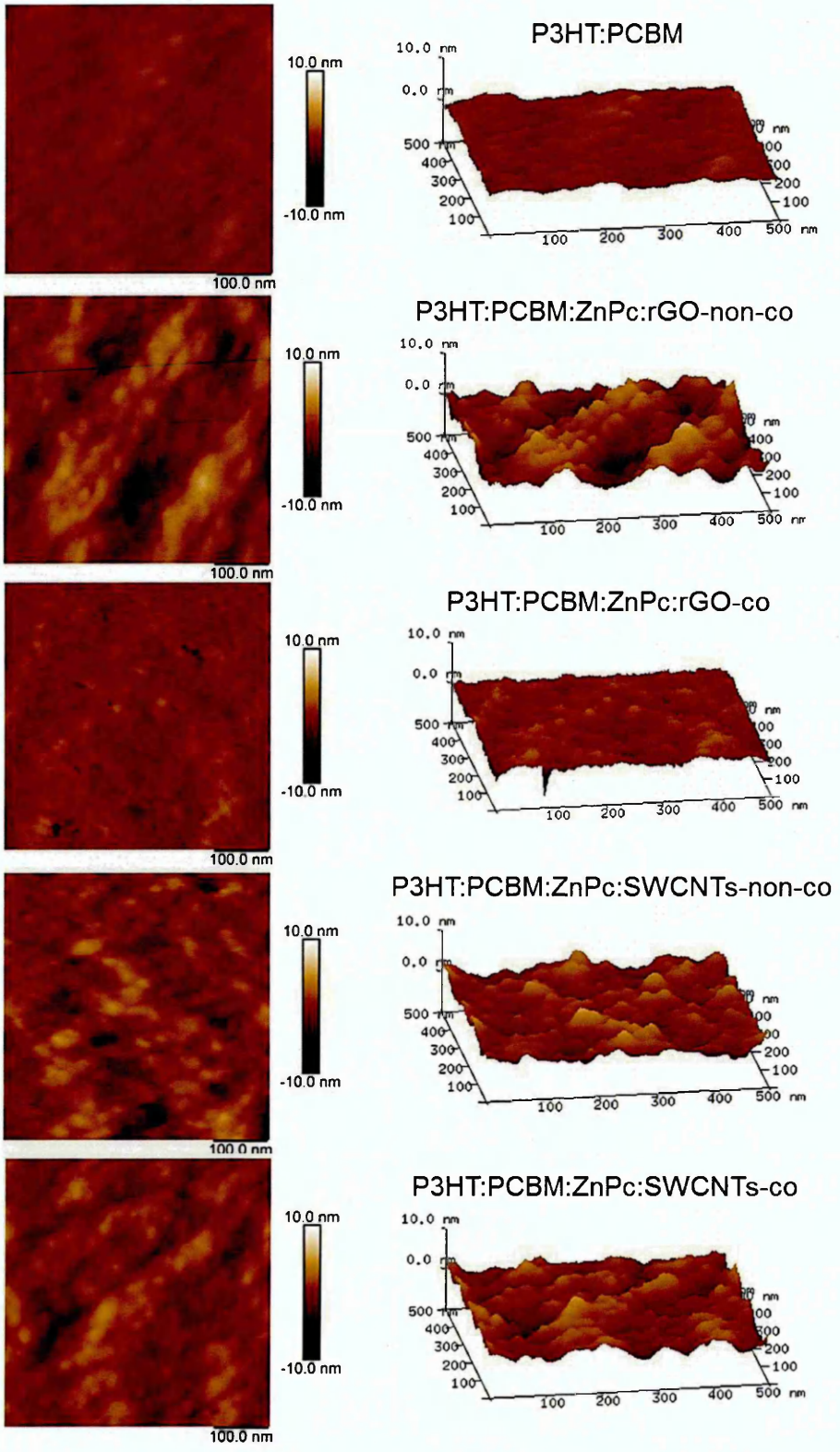

Fig.7.11: AFM images of P3HT:PCBM, and P3HT:PCBM:ZnPc-hybrid films

P3HT:PCBM:ZnPc-SWCNTs-non-co film has shown clear CNT features while P3HT:PCBM:ZnPc-SWCNT-co films have exhibited different surface topography which suggests higher homogeneity in the case of covalently bonded hybrids. On the other hand, rGO-based films have exhibited different morphologies which are attributed to the two dimensional nature of graphene itself. P3HT:PCBM blends involving rGO-based hybrids have exhibited flakes-like features on the film surface [30]. Fig.7.11 shows AFM images of the P3HT:PCBM:ZnPc-hybrids; P3HT:PCBM film has revealed a smooth surface with rms of 1.2nm whereas introducing ZnPc:hybrids within P3HT:PCBM blends is shown to lead to rougher surface morphologies due to the nature of these hybrids was established using SEM measurements. P3HT:PCBM:ZnPc:SWCNTs-non-co blend has shown slightly higher surface roughness with rms value of about 2.36 nm whereas P3HT:PCBM:ZnPc:SWCNTs-co blend has exhibited roughness of 2.3 nm. On the other hand, P3HT:PCBM:ZnPc:rGO-non-co and P3HT:PCBM:ZnPc:rGO-co bonded blends have displayed surface roughness of 2.4 nm and 2 nm, respectively. It could be claimed that the formation of rougher surface as a result of adding these hybrids to P3HT:PCBM blend could increase the contact area with the back electrode and therefore increases the current density and charge carrier collection [31].

7.2.4 XRD results

The structural properties of P3HT:PCBM:ZnPc-hybrid layers were also studied using XRD, and the obtained patterns are shown in Fig.7.12. Generally, P3HT chains facilitate their self-orientation into two-dimensional sheets by means of inter-chain stacking and therefore demonstrate highly crystalline property [11]. The presence of ZnPc hybrids within P3HT:PCBM shows no significant effect on the structural properties and the films remain almost unchanged showing same peak intensity of the same (100) orientation without observing any shifting or the appearance of any new peaks. A single diffraction peak at $2\theta=5.5\pm0.1^{o}$ for (100) preferential orientation was observed and was ascribed to the edge-on orientation of the P3HT polymer. This corresponds to the in-plane π-π stacking of the conjugated polymer rings and out of plane stacking of the alkyl groups perpendicular to the substrate.

The reflection peak in all studied films is attributed to the P3HT lamella structure which suggests higher degree of crystallinity [32]. The addition of small proportions of ZnPc-hybrids to the P3HT:PCBM blend has resulted in no significant change in the P3HT crystallinity. The diffraction peaks width however have shown a slight change, specifically in the P3HT:PCB:ZnPc-SWCNT-co which suggests that this hybrid has demonstrated a lower d-spacing and higher π-π stacking. Salim and co-authors [12] have shown that higher concentrations of SWCNTs disturb the orientation of P3HT, and the edge-on orientation partially changed into face-on orientation. Therefore, a low concentration of the studied hybrids has been used in this work in order to avoid significant structural disorder as well as reducing chances of device short circuit occurrence. Similar diffraction peaks are observed in the case of P3HT:PCBM:ZnPc-hybrid films, and are attributed to the edge-on orientation of P3HT main polymer.

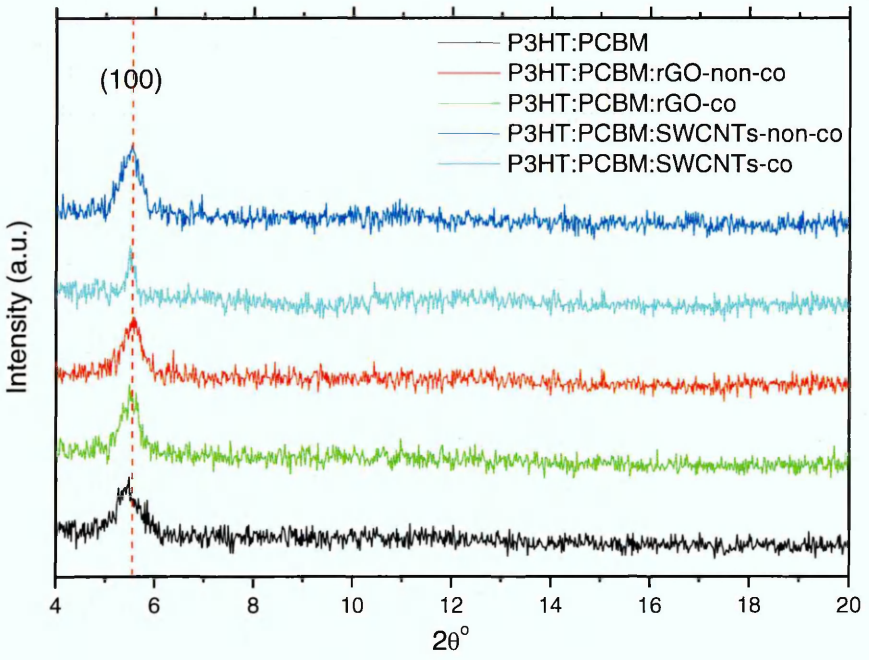

Fig.7.12: XRD patterns of thin films of P3HT:PCBM and its blends with ZnPc-hybrids

7.2.5 Electrical conductivity

Electrical conductivity measurements of rGO and SWCNTs covalently and non-covalently functionalized with ZnPc hybrid thin films were carried out using interdigitated electrodes as substrates. Keithley 4200 Semiconductor Characterisation System (4200-SCS) was used to measure the DC current as a function of applied voltage of the studied films, as discussed in more details in Chapter 4. The pure ZnPc film has demonstrated an electrical conductivity of 11.4mS.cm^{-1}. This value has noticeably increased to 51mS.cm^{-1} when rGO was covalently and non-covalently bonded with ZnPc. On the other hand, SWCNTs has significantly increased the conductivity for both covalently and non-covalently bonded ZnPc film to 218.6mS.cm^{-1} and 140mS.cm^{-1}, respectively. Fig.7.13 (A) shows the variation of the films' electrical conductivity as a function of different hybrid forms; this enhancement in the electrical conductivity upon adding SWCNTs or rGO was thought to be useful for photovoltaic device application. Research on SWCNTs:organic based solar cells has been directed towards developing alternative, lightweight, and flexible devices for space power applications [33]. Likewise, an increase in conductivity of the P3HT:PCBM blend has been observed after the addition of these hybrids to the blend (see Fig.7.13(B)).

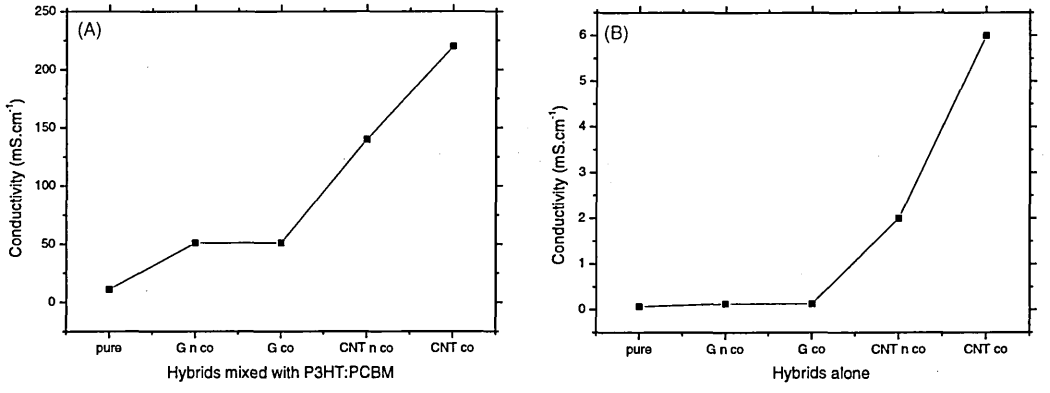

Fig.7.13: The electrical conductivity of (A) ZnPc hybrids alone, and (B) ZnPc hybrids mixed with P3HT:PCBM

Thin films of undoped P3HT:PCBM blend has demonstrated an electrical conductivity of 0.07mS.cm^{-1}; this value has increased to 0.13 mS.m^{-1} as a result of adding ZnPc:rGO both covalently and non-covalently bonded to the P3HT:PCBM blend. This can be ascribed to the well-distributed ZnPc-hybrids within the P3HT:PCBM blend as shown in the SEM and AFM images (see Fig.7.10 and Fig.7.11) as well as the efficient charge transfer between the blend molecules [33, 34]. Moreover, the conductivity of P3HT:PCBM blend has increased to around 4 mS.m^{-1} and 6 mS.m^{-1} as results of adding ZnPc:SWCNTs both as non-covalently and covalently bonded. The significant increase in the electrical conductivity is thought to be the result of efficient charge transfer between ZnPc and SWCNTs or rGO hybrids, which suggest that nanoscale interpenetrated network has been achieved [30]. This nanoscale structure as well as the improved charge transfer would also contribute in preventing charge carriers' recombination and thus improving the PCE of the OSCs [35]. These improvements in active layers' electrical conduction could also contribute in enhancing the shunt resistance by creating percolation pathways which facilitate charge carriers' transport and thus enhance the short circuit current density [36].

7.2.6 Dark I-V characteristics

Dark J-V measurements have been used to estimate some important parameters including charge carriers mobility (μ), series resistance (R_s), shunt resistance (R_{sh}) and ideality factor (n) of the studied OSC devices. The J-V characteristics in the form of double log scale are shown in Fig.7.14; the data in this plot has been used to determine the charge carrier's mobility using space charge limited conduction theory. Generally, all the curves have exhibited power law dependency of the form $J\alpha V^m$, where m is the gradient of the log-log plot, which has different values over different applied voltage regions [37]. Four distinct regions were demonstrated in the logJ-logV curves; at low applied voltage where $m\approx1$, charge transport is governed by ohm's law. This occurs when the background carrier density within the active layer is higher than the injected carrier's density. Once the applied voltage is increased, more carriers are injected to the active layer and the amount of the injected carriers is higher than the background carrier density; the slope of this region is changed to approximately 2.

Charge transport in this region is attributed to trap-controlled space charge limited conduction (SCLC) with traps located at a single energy level inside the band gap [38]. A much steeper gradient has been obtained at higher applied voltages in the third region with m taking values ~9. This region of the logJ-logV dependence can be related to trap-filling limit beyond which trap-filled SCLC mechanism occurs [38]. The latter mechanism is evident by the onset of trap-free space charge limited conduction (TFCLC), with m taking on a value of ≈ 2 and the J-V dependence in this region can be described by Child's law [39] (see the inset of Fig.7.14). The data in the square law region (TFCLC) has been used to estimate the charge carriers' mobility. The obtained charge carriers' mobility values are summarised in Table 7.2. The charge carrier mobility has nearly doubled in P3HT:PCBM:ZnPc-SWCNTs-co based device compared to P3HT:PCBM as a reference device. This increase in mobility could be attributed to the formation of percolation pathways, which facilitate the charge carrier transport through the blends. The increase in the charge carriers' mobility is thought to be a key factor in increasing the current and reducing the charge carriers' recombination. Moreover, the nanostructured morphology with the well-distributed components of the blends is thought to reduce the hopping distance and increase the charge carriers' mobility. In order to determine the recombination rate within the active layer of the solar cell devices, the dark J-V characteristics are re-plotted in the form of LnJ versus applied voltage as shown in Fig.7.15. The obtained values of n from the gradient of the linear part of the LnJ-V curves are summarised in Table 7.2. P3HT:PCBM reference device has exhibited higher recombination rate as indicated by the device ideality factor of 2.52. The estimated ideality factor has shown a good agreement within experimental error with those derived using transient techniques for OSC based on P3HT:PCBM [40]. The lowest ideality factor of 1.99 was obtained for P3HT:PCBM:ZnPc:SWCNTs-co based devices indicating the lowest recombination rate in these blends.

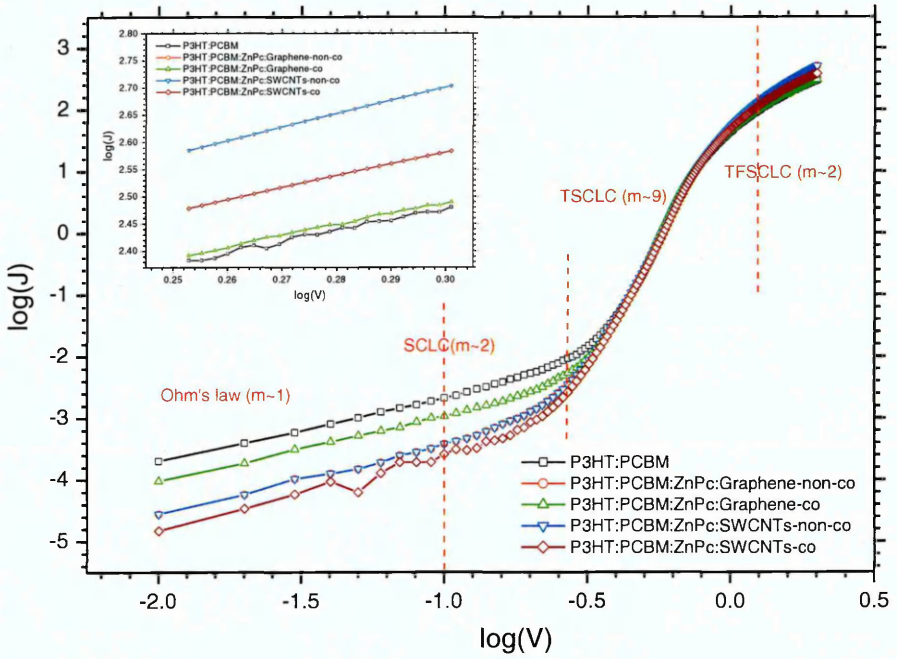

Fig.7.14: Dark J-V characteristics in the form of double log scale of the studied P3HT:PCBM blend-based solar cells; the inset represents the TFSCLC region

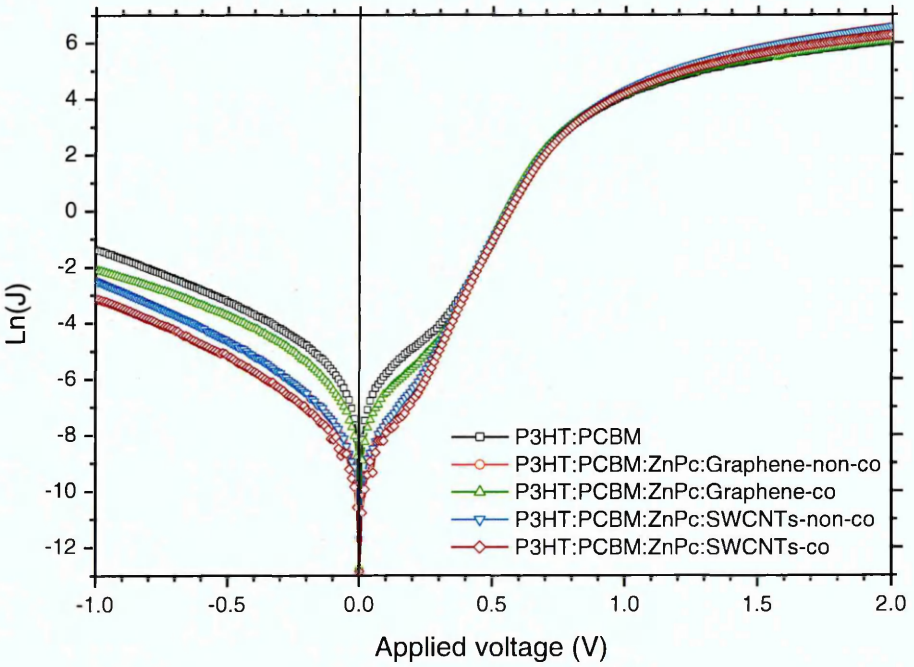

Fig.7.15: Dark J-V characteristics in the form of LnJ vs. applied voltage of the studied P3HT:PCBM blend-based solar cells

Table 7.2: Dark J-V characteristics of the studied P3HT:PCBM blend-based solar cells

Devices	R_s (Ω)	R_{sh}(MΩ)	μ ($cm^2.V^{-1}.s^{-1}$)	n
P3HT:PCBM	48.3	0.5	4.65	2.52
P3HT:PCBM:ZnPc:rGO-non-co	47.8	1.25	4.72	2.07
P3HT:PCBM: ZnPc:rGO--co	24.8	3.33	9.1	2.05
P3HT:PCBM: ZnPc:SWCNTs-non-co	36.2	2.5	6.19	2.04
P3HT:PCBM: ZnPc:SWCNTs-co	24.8	3.33	9.34	1.99

7.2.7 Solar cell performance

P3HT:PCBM as well as P3HT:PCBM:ZnPc-hybrids solar cells have been investigated under illumination of 100mW.cm^{-2} and the J-V characteristics of the hybrid OSCs are presented in Fig.7.16 (A for thick film and B for thin film). Solar cell devices prepared with P3HT:PCBM:ZnPc-hybrids as active layers have exhibited significantly improved PCE with values at least 35% higher in comparison with the reference P3HT:PCBM-based device as shown in Table 7.3. The highest performance was observed for P3HT:PCBM:ZnPc-SWCNTs-co based device with PCE of 5.3% and FF of 68%. This increase in the device performance could be assigned to the ZnPc-hybrids inducing the nanostructured P3HT:PCBM blends in enhancing photon harvesting as well as improving charge carriers transport. The latter could be attributed to the efficient charge transfer between the P3HT:PCBM and ZnPc-SWCNTs-co hybrids with the new blends. Fig.7.17(A) shows the energy level alignment of the materials under study; the band bending of the P3HT:PCBM:ZnPc-SWCNTs-co is demonstrated as an example in Fig.7.17(B), showing the charge transport through this blend. The obtained higher FF could be ascribed to the lower recombination rate in these devices as demonstrated by the lower ideality factor values as well as low R_s and high R_{sh} as shown in Table 7.2; FF represents the efficiency of charge collection before they recombine inside the cell, which basically depends on the charge carriers' mobility, V_{bi} and the charge carriers' recombination rate [41] as well as the improvement in the series resistance (R_s) [42].

As revealed in Fig.7.17(B), it could be alleged that electrons could easily be injected from the LUMO of PCBM to the respective electrode (Al) whereas the holes transfer takes place from the HOMO level of the P3HT or ZnPc-hybrids to the respective electrode which is the PEDOT:PSS/ITO front. This could be attributed to the difference in the work functions at the metal/organic semiconductor interface [43]. It has also been shown that ZnPc-hybrids energy levels are located between the HOMO and the LUMO of both the donor and acceptor materials. Several reports have demonstrated that changes in the active layers' morphology are unlikely to have significant effect on the value of V_{oc} [44, 45].

The enhancement in OSC device performance after doping P3HT:PCBM blends with ZnPc-hybrids could be ascribed to the enhancement in the electrical conductivity of the new blends as well as the increase in charge carriers' mobility, which in turn improves the short circuit current density. The effect of the distribution of ZnPc-hybrids within the P3HT:PCBM blend (nanoscale interpenetrated networks) as demonstrated by the morphological analysis could increase the interface area within the blend, and thus result in improved charge carriers generation (larger J_{sc}) and charge transport (larger FF) [46]. Films of lower thickness of about 100 nm have been examined (see Fig.7.17(B)), where such thickness was earlier shown to be an optimum active layer thickness that was associated with improved OSC performance [47]. However, the thinner films have shown slightly smaller PCE but much improved FF. The smaller values of J_{sc} could be attributed to the thinner active layer, which is thought to provide lower photons absorption intensity compared to the thicker one; the V_{oc} has demonstrated no significant change. These results provide further confirmation of the reproducibility of these devices.

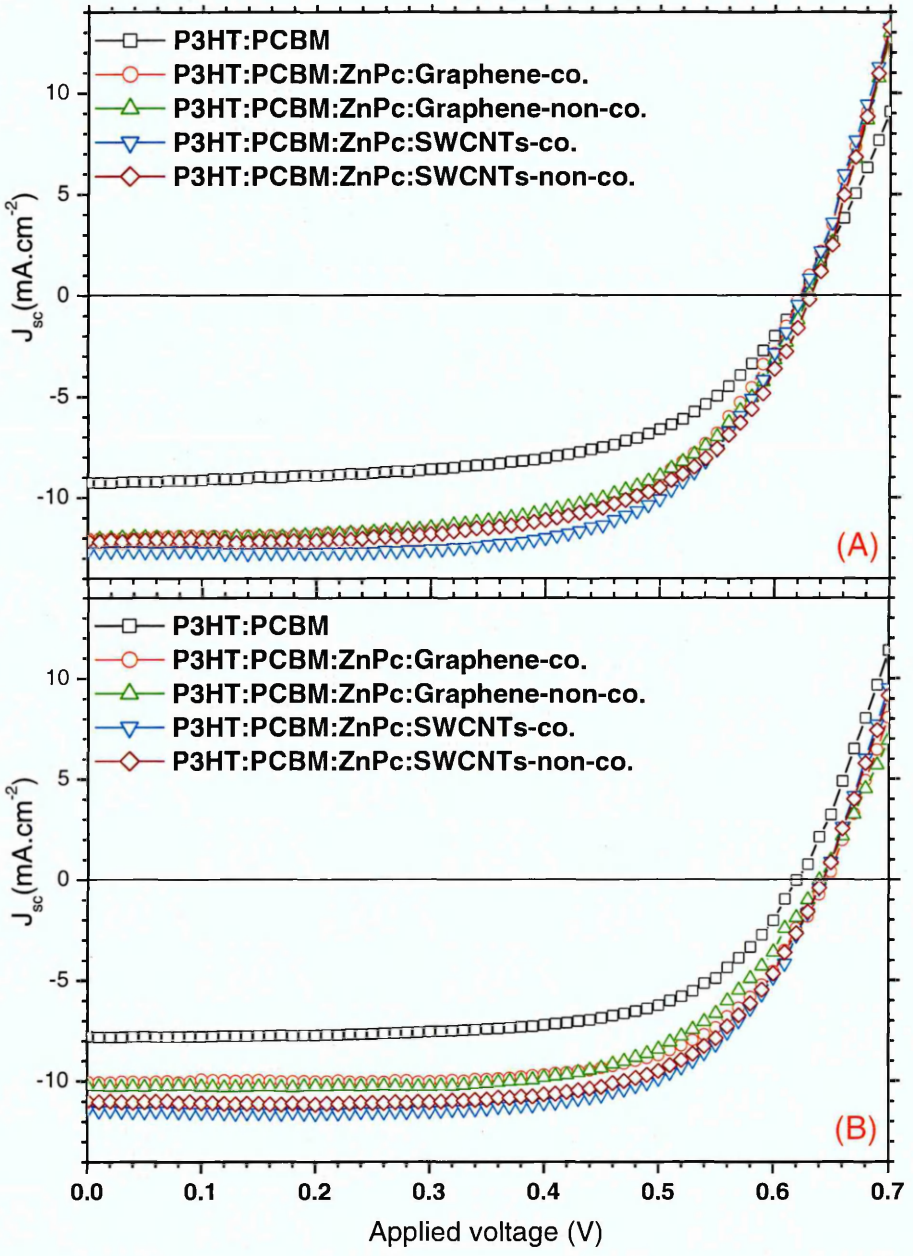

Fig.7.16: Solar cells characteristics of P3HT:PCBM and P3HT:PCBM:ZnPc-hybrids films; (A) Thick active layer of ~150nm and (B) Thin active layer of ~100nm

Table 7. 3: Photovoltaic parameters of P3HT:PCBM and P3HT:PCBM:ZnPc-Hybrids films

	Thicker active layer (~150nm) (Fig.7.16(A))				Thinner active layer (~100nm) (Fig.7.16 (B))			
P3HT:PCBM -based Devices	J_{sc} ($mA.cm^{-2}$)	V_{oc} (V)	FF	PCE (%)	J_{sc} ($mA.cm^{-2}$)	V_{oc} (V)	FF	PCE (%)
Reference	9.3	0.62	0.60	3.46	7.8	0.62	0.65	3.15
ZnPc:rGO-non-co	12	0.63	0.62	4.7	10.2	0.64	0.66	4.3
ZnPc:rGO--co	12	0.62	0.63	4.7	10	0.64	0.69	4.4
ZnPc:SWCNTs-non-co	12	0.63	0.65	4.9	9.5	0.64	0.68	4.15
ZnPc:SWCNTs-co	12.6	0.62	0.68	5.3	10.3	0.64	0.71	4.65

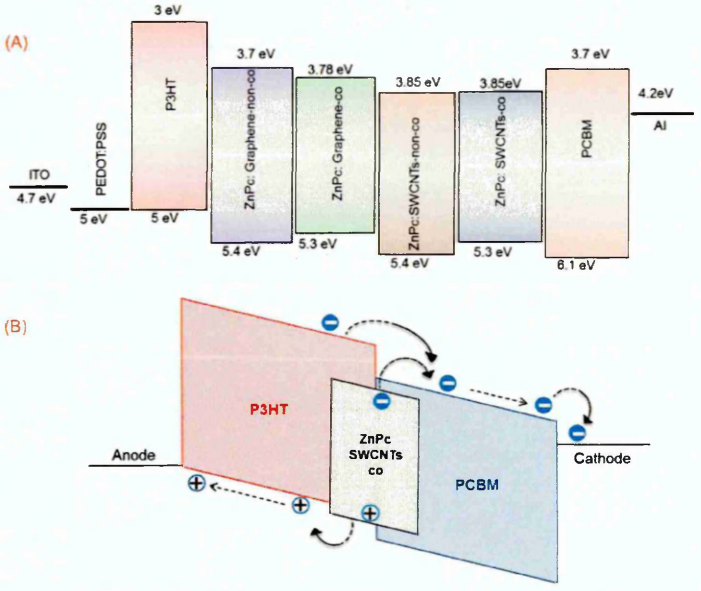

Fig.7.17: (A) Energy level alignment for the materials under study, where only one of the ZnPc-hybrids is involved at a time; (B) proposed band diagram for the P3HT:PCBM:ZnPc-SWCNTs-co based device as an example for the energy levels position and the flow direction of both charge carriers

7.3 Summary

The effect of using novel ZnPc hybrids covalently and non-covalently bonded to SWCNTs or rGO within the P3HT:PCBM active layer as ternary blends has been investigated using different measurement techniques. The electrical conductivity of such hybrids are shown to be high and their effects on the P3HT:PCBM blend's conductivity is clear. Light absorption of these ternary blends has demonstrated red shift in the case of adding rGO hybrids to the P3HT:PCBM blend, however, the energy band gap estimation has shown that the band gap of P3HT:PCBM has decreased after being doped with these hybrids separately. The morphological study has shown that addition of these hybrids has induced a better distribution of the materials involved within the active layer and that was thought to assist in the formation of an interpenetrating network that can facilitate the charge carriers' transport. Besides, the charge carriers' mobility has exhibited an increase in its value, which is believed to result in higher J_{sc} in the studied solar cell. The overall device performance has shown a significant improvement with an increase of about 35% in the PCE after doping the active layer of P3HT:PCBM blend with ZnPc-SWCNTs-co hybrid compared to the basic (reference) device made of an active layer of undoped P3HT:PCBM blend.

References

[1] Hahn, U., Engmann, S., Oelsner, C., et.al. (2010). Immobilizing Water-Soluble Dendritic Electron Donors and Electron Acceptors Phthalocyanines and Perylenediimides onto Single Wall Carbon Nanotubes. Journal of the American Chemical Society, 132(18), 6392-6401.

[2] Mugadza, T., & Nyokong, T. (2010). Synthesis, characterization and the electrocatalytic behaviour of nickel (II) tetraamino-phthalocyanine chemically linked to single walled carbon nanotubes. Electrochimica Acta, 55(20), 6049-6057.

[3] Moraes, F. C., Golinelli, D. L., Mascaro, L. H., & Machado, S. A. (2010). Determination of epinephrine in urine using multi-walled carbon nanotube modified with cobalt phthalocyanine in a paraffin composite electrode. Sensors and Actuators B: Chemical, 148(2), 492-497.

[4] Karousis, N., Ortiz, J., Ohkubo, K., et.al. (2012). Zinc phthalocyanine–graphene hybrid material for energy conversion: synthesis, characterization, photophysics, and photoelectrochemical cell preparation. The Journal of Physical Chemistry C, 116(38), 20564-20573.

[5] Soldano, C., Talapatra, S., & Kar, S. (2013). Carbon nanotubes and graphene nanoribbons: potentials for nanoscale electrical interconnects. Electronics, 2(3), 280-314.

[6] Charlier, J. C., Blase, X., & Roche, S. (2007). Electronic and transport properties of nanotubes. Reviews of modern physics, 79(2), 677.

[7] Choi, T. Y., Poulikakos, D., Tharian, J., & Sennhauser, U. (2006). Measurement of the thermal conductivity of individual carbon nanotubes by the four-point three-ω method. Nano letters, 6(8), 1589-1593.

[8] D'Souza, S., Moeno, S., Antunes, E., & Nyokong, T. (2013). Effects of gold nanoparticle shape on the aggregation and fluorescence behaviour of water soluble zinc phthalocyanines. New Journal of Chemistry, 37(7), 1950-1958.

[9] Kaya, E. N., Tuncel, S., Basova, T. V., et.al. (2014). Effect of pyrene substitution on the formation and sensor properties of phthalocyanine-single walled carbon nanotube hybrids. Sensors and Actuators B: Chemical, 199, 277-283.

[10] Mensing, J. P., Kerdcharoen, T., Sriprachuabwong, C., et.al. (2012). Facile preparation of graphene–metal phthalocyanine hybrid material by electrolytic exfoliation. Journal of Materials Chemistry, 22(33), 17094-17099.

[11] Kim, Y. S., Lee, Y., Kim, J. K., et.al. (2010). Effect of solvents on the performance and morphology of polymer photovoltaic devices. Current Applied Physics, 10(4), 985-989.

[12] Salim, T., Lee, H. W., Wong, L. H.,et.al. (2016). Semiconducting carbon nanotubes for improved efficiency and thermal stability of polymer–fullerene solar cells. Advanced Functional Materials, 26(1), 51-65.

[13] Sun, Y., Liu, J., Ding, Y., & Han, Y. (2013). Decreasing the aggregation of PCBM in P3HT/PCBM blend films by cooling the solution. Colloids and Surfaces A: Physicochemical and Engineering Aspects, 421, 135-141.

[14] De Volder, M. F., Tawfick, S. H., Baughman, R. H., & Hart, A. J. (2013). Carbon nanotubes: present and future commercial applications. science, 339(6119), 535-539.

[15] Wu, J., Becerril, H. A., Bao, Z., et.al. (2008). Organic solar cells with solution-processed graphene transparent electrodes. Applied Physics Letters, 92(26), 237.

[16] Yun, J. M., Yeo, J. S., Kim, J., et.al. (2011). Solution-Processable Reduced Graphene Oxide as a Novel Alternative to PEDOT: PSS Hole Transport Layers for Highly Efficient and Stable Polymer Solar Cells. Advanced Materials, 23(42), 4923-4928.

[17] Liu, Q., Liu, Z., Zhang, X., et.al. (2008). Organic photovoltaic cells based on an acceptor of soluble graphene. Applied Physics Letters, 92(22), 195.

[18] Maruhashi, H., Oku, T., Suzuki, A., et.al. (2015, February). Fabrication and characterization of P3HT: PCBM-based thin film organic solar cells with zinc phthalocyanine. In A. Sandhu, H. Okada, M. Boutchich, S. Maenosono, & R. Wadhwa (Eds.), AIP Conference Proceedings (Vol. 1649, No. 1, pp. 89-95). AIP.

[19] Holt, J. M., Ferguson, A. J., Kopidakis, N., et.al. (2010). Prolonging charge separation in P3HT− SWNT composites using highly enriched semiconducting nanotubes. Nano letters, 10(11), 4627-4633.

[20] Sibata, M. N., Tedesco, A. C., & Marchetti, J. M. (2004). Photophysicals and photochemicals studies of zinc (II) phthalocyanine in long time circulation micelles for photodynamic therapy use. European journal of pharmaceutical sciences, 23(2), 131-138.

[21] Ren, B., Zhu, L., Cui, G., et.al. (2013). Zinc phthalocyanine π-conjugately linked with electron-withdrawing benzothiadiazole towards broad absorption. Tetrahedron Letters, 54(45), 5953-5955.

[22] Banimuslem, H., Hassan, A., Basova, T., et.al. (2015). Copper phthalocyanine functionalized single-walled carbon nanotubes: thin films for optical detection. Journal of nanoscience and nanotechnology, 15(3), 2157-2167.

[23] Senthilarasu, S., Sathyamoorthy, R., Lalitha, S., et.al. (2004). Thermally evaporated ZnPc thin films—band gap dependence on thickness. Solar energy materials and solar cells, 82(1), 179-186.

[24] Lee, C. H., Podraza, N. J., Zhu, Y., et.al. (2013). Effect of reduced dimensionality on the optical band gap of SrTiO3. Applied Physics Letters, 102(12), 122901.

[25] Ramani, R., & Alam, S. (2013). A comparative study on the influence of alkyl thiols on the structural transformations in P3HT/PCBM and P3OT/PCBM blends. Polymer, 54(25), 6785-6792.

[26] Leonat, L., Sbârcea, G., & Branzoi, I. V. (2013). Cyclic voltammetry for energy levels estimation of organic materials. UPB Sci Bull Ser B, 75, 111-118.

[27] Freitas, A. R., Silva, M., Ramos, M. L., et.al. (2015). Synthesis, structure, and spectral and electrochemical properties of chromium (III) tris-(8-hydroxyquinolinate). Dalton Transactions, 44(25), 11491-11503.

[28] Touaiti, S., Hajri, A., Kahwech, M S., & Jamoussi, B. (2013). Optoelectronic properties of New Synthesized phtalocyanine, International Journal of Materials Science and Applications, 2, 179-184.

[29] Ahmida, M. M., & Eichhorn, S. H. (2010). Measurements and prediction of electronic properties of discotic liquid crystalline triphenylenes and phthalocyanines. ECS Transactions, 25(26), 1-10.

[30] Kadem, B., Göksel, M., Şenocak, A., et.al. (2016). Effect of covalent and non-covalent linking on the structure, optical and electrical properties of novel zinc (II) phthalocyanine functionalized carbon nanomaterials. Polyhedron, 110, 37-45.

[31] Geethu, R., Kartha, C. S., & Vijayakumar, K. P. (2015). Improving the performance of ITO/ZnO/P3HT: PCBM/Ag solar cells by tuning the surface roughness of sprayed ZnO. Solar Energy, 120, 65-71.

[32] Park, J. H., Kim, J. S., Lee, J. H., et.al. (2009). Effect of annealing solvent solubility on the performance of poly (3-hexylthiophene)/methanofullerene solar cells. The Journal of Physical Chemistry C, 113(40), 17579-17584.

[33] Alturaif, H. A., ALOthman, Z. A., Shapter, J. G., & Wabaidur, S. M. (2014). Use of carbon nanotubes (CNTs) with polymers in solar cells. Molecules, 19(11), 17329-17344.

[34] Najeeb, C. K., Lee, J. H., Chang, J., & Kim, J. H. (2010). The effect of surface modifications of carbon nanotubes on the electrical properties of inkjet-printed SWNT/PEDOT–PSS composite line patterns. Nanotechnology, 21(38), 385302.

[35] Robaeys, P., Bonaccorso, F., Bourgeois, E., et.al. (2014). Enhanced performance of polymer: fullerene bulk heterojunction solar cells upon graphene addition. Applied Physics Letters, 105(8), 136_1.

[36] Derbal-Habak, H., Bergeret, C., Cousseau, J., & Nunzi, J. M. (2011). Improving the current density J sc of organic solar cells P3HT: PCBM by structuring the photoactive layer with functionalized SWCNTs. Solar Energy Materials and Solar Cells, 95, S53-S56.

[37] Gunduz, B., Yahia, I. S., & Yakuphanoglu, F. (2012). Electrical and photoconductivity properties of p-Si/P3HT/Al and p-Si/P3HT: MEH-PPV/Al organic devices: Comparison study. Microelectronic Engineering, 98, 41-57.

[38] Oklobia, O., & Shafai, T. S. (2014). Correlation between charge carriers mobility and nanomorphology in a blend of P3HT/PCBM bulk heterojunction solar cell: Impact on recombination mechanisms. Solar Energy Materials and Solar Cells, 122, 158-163.

[39] Apaydın, D. H., Yıldız, D. E., Cirpan, A., & Toppare, L. (2013). Optimizing the organic solar cell efficiency: role of the active layer thickness. Solar Energy Materials and Solar Cells, 113, 100-105.

[40] Foertig, A., Rauh, J., Dyakonov, V., & Deibel, C. (2012). Shockley equation parameters of P3HT: PCBM solar cells determined by transient techniques. Physical Review B, 86(11), 115302.

[41] Ray, B., & Alam, M. A. (2013). Achieving fill factor above 80% in organic solar cells by charged interface. IEEE Journal of Photovoltaics, 3(1), 310-317.

[42] Zhao, D. W., Kyaw, A. K. K., & Sun, X. W. (2011). Organic Solar Cells with Inverted and Tandem Structures. In Energy Efficiency and Renewable Energy Through Nanotechnology (pp. 115-170). Springer London.

[43] Sze, S. M., and Kwok K. Ng. Physics of semiconductor devices. John wiley & sons, 2006.

[44] Ray, B., Lundstrom, M. S., & Alam, M. A. (2012). Can morphology tailoring improve the open circuit voltage of organic solar cells?. Applied Physics Letters, 100(1), 7.

[45] Ray, B., & Alam, M. A. (2012). Random vs regularized OPV: Limits of performance gain of organic bulk heterojunction solar cells by morphology engineering. Solar Energy Materials and Solar Cells, 99, 204-212.

[46] Etxebarria, I., Ajuria, J., & Pacios, R. (2015). Solution-processable polymeric solar cells: a review on materials, strategies and cell architectures to overcome 10%. Organic Electronics, 19, 34-60.

[47] Kadem, B., Hassan, A., & Cranton, W. Performance optimization of P3HT: PCBM solar cells by controlling active layer thickness. In Proceedings of the 31st European photovoltaic solar energy conference and exhibition, EUPVSEC (2015, Hamburg, Germany).

Chapter 8: Conclusion and future work

8.1 Conclusion

This thesis has presented the development and characterisation of low-cost, high efficiency OSCs based on BHJ of P3HT:PCBM blends. The research programme is firstly focussed on investigating P3HT:PCBM blend properties such as the blend morphology as well as electron transport properties pertained to the interface properties within the blend itself as well as those related to the metallic charge collecting electrodes. Different strategies were carried out in order to improve the performance of P3HT:PCBM-based solar cells; these are employing different solvents and their co-solvents, preparing different active layer thickness, selecting the optimum PCBM among different PCBM's derivatives and finally post-annealing treatments for the optimum combined devices. In a separate chapter, the effects of the hole and electron transport layers have been investigated. Finally, The effect of using novel ZnPc hybrids covalently and non-covalently bonded to SWCNTs or rGO within the P3HT:PCBM active layer as ternary blends has been investigated.

Firstly, using mixed solvents has resulted in significant improvements in the P3HT:PCBM morphology and crystallinity. The co-solvents CB:CF has revealed a noticeable increase in its performance with improved PCE from 0.83% in the CF-based device to 2.73%. This was ascribed to the improvement in the interpenetrating network, which facilitates charge carriers' transport properties, and hence improved solar cell performance. Moreover, thickness dependence of the charge carriers' mobility using SCLC theory was carried out to estimate the charge carriers' mobility; the mobility was found to decrease with increasing film thickness. The photovoltaic performance was evaluated for these devices as a function of active layer thickness and the maximum PCE of 3.84% was evaluated for the device with 95nm active layer thickness. In addition, using different PCBM derivatives with different HOMO and LUMO positions has resulted in improving the open circuit voltage.

Optimum device performance was associated with $PC_{61}BM$ as the acceptor material with higher LUMO energy level with PCE of 4.2%. Further treatment were carried out by subjecting the P3HT:PCBM-based devices to post deposition annealing at different temperatures in the range 100-180°C. The heat-treatment has shown to result in significant improvement in the PV performance with PCE reaching 5.5%. This was attributed to the significant impact on R_s as well as the morphology of the BHJ which facilitates the charge carriers' percolation pathways and hence increased J_{sc}.

Additionally, the effects of the hole and electron transport layers have been studied. Typically, the device based on the typical hole transport layer (PEDOT:PSS) has shown PCE of 3.92; this value has improved to 6.82 as a result of doping the PEDOT:PSS layer with LiCl metal salts in aqueous solutions of the concentration of $10mg.ml^{-1}$. On the other hand, using solution processed electron transport layer (Alq3) has resulted in enhancing PCE reaching 4.25% compared to the reference device without modifying the PEDOT:PSS layer. Using these two modifications layers as a complete device has increased PCE to 7% with a FF of 71% which are of the highest reported parameter for P3HT:PCBM-based OSCs.

The effect of using novel carbon based materials (ZnPc covalently and non-covalently bonded to SWCNTs or rGO) within the P3HT:PCBM active layer as ternary blends has been carried out. The electrical conductivity of such hybrids are shown to be high and their effects on the P3HT:PCBM blend's conductivity is clear. The overall device performance has shown a significant improvement with an increase of about 35% in the PCE after doping the active layer of P3HT:PCBM blend with ZnPc-SWCNTs-co hybrid compared to the basic (reference) device made of an active layer of undoped P3HT:PCBM blend.

8.2 Future work

The current study has focused on P3HT:PCBM-based OSCs. The efficiency of the solar cells is mainly determined by three parameters; V_{oc}, J_{sc} and FF of the device. Therefore various factors can affect these parameters during the fabrication process. In the following section, few recommendations are suggested to improve the efficiency of the OSCs.

1. Spray coating method is considered as one of the commercial method to be used in organic solar cells, the use of the optimum parameters in spray coated OSCs is highly recommended.
2. Using low band gap polymers to improve the absorption properties of the active layer; this improvement is a key factor to enhance the final performance of the solar cell.
3. Using Aluminium doped zinc oxide (AZO) as an alternative to ITO with ZnO as an ETL in an inverted structure is thought to increase the device stability and efficiency.
4. Employing different polymers, such as (PVA and PMMA), to be used as capsulation layer instead of epoxy which is currently used with some degradation issues.
5. Using hybrid solar cells based on organic and perovskite materials could significantly improve the solar cell efficiency; the main challenge of this research is the stability.

Appendix A: Preparation and characterisations of the ZnPc-Hybrids

I. Materials

All the reagents and solvents were of reagent grade quality and obtained from commercial suppliers. 4-pentynoic acid and sodium L-ascorbate were purchased from Alfa Aeser. SWCNT was purchased from Aldrich. Sodium azide and copper(II) sulphate pentahydrate were supplied from Merck. Reduced graphene oxide (rGO) was obtained from Hazerfen Chemistry and Materials Company, Turkey and it was used as graphene nanomaterial. The surface area of this rGO was 565 m^2/gram and ratio of C:O was 4.77. The number of layers was in the range of 4-7 sheets. 1-{[2-aminoethoxy]ethoxy}–8(11),15(18),22(25)-tris-{2-[2-(2-ethoxyethoxy) ethoxy]-1-[2-((2-ethoxyethoxy) ethoxymethyl] ethyloxy} phthalocyaninato zinc(II) (1) was synthesized and purified according to published procedure [1].

II. Preparation of 1-[N-(2-ethoxyethyl)-4-pentynamide]-8(11),15(18),22(25)-tris-{2-[2-(2-ethoxyethoxy)ethoxy]-1-[2-((2-ethoxyethoxy)-ethoxy)methyl]ethyloxy} phthalocyaninato zinc(II) (ZnPc)

The solution of compound 1 (50 mg, 0.031 mmol) in 1 mL dimethylformamide (DMF) was added to 6.1 mg (0.062 mmol) 4-pentynoic acid and stirred 48 h at room temperature. The resulting mixture was treated for three times using 30 mL portions of ethyl acetate and water; the obtained organic phase was separated by liquid-liquid extraction. Ethyl acetate phase was dried with anhydrous Na_2SO_4, filtered off followed by removing the solvent under reduced pressure; the desired product (ZnPc) was dried under vacuum. Yield: 44 mg (85%). FT-IR (ν_{max}/cm^{-1}): 3281 (NH), 3259 (C≡CH), 3070 (Aromatic CH), 2973-2863 (Aliphatic CH), 2027 (C≡CH), 1652 (C=O), 1607 (C=C), 1486 (NH), 1337 (Aliphatic CH), 1218 (Aromatic CH), 1089 (C-O-C); UV–Vis (DMSO): λ_{max} nm (log ε) 357 (4.57), 616 (4.52), 683 (5.12); ^{1}H NMR (DMF-d_7): δ (ppm) = 9.26-9.12 (m, 4H, ArCH), 9.01-8.87 (m,

4H, ArCH), 8.85-8.75 (m, 4H, ArCH), 8.12 (bs, 1H, NH), 5.49 (m, 3H, CH), 5.18-5.07 (m, 2H, CH_2N), 4.80-4.72 (m, 2H, $CH_2C=O$), 4.13-3.95 (m, 24H, OCH_2), 3.92-3.80 (m, 24H, OCH_2), 3.75-3.67 (td, 24H, OCH_2), 3.65-3.60 (dd, 2H, OCH_2), 3.03-2.92 (t, 2H, $CH_2C\equiv C$), 2.84 (s, 1H, $C\equiv CH$), 1.14-0.97 (m, 18H, CH_3); Elemental analysis, Calcd. for $C_{84}H_{115}N_9O_{23}Zn$: 59.90 C, 6.88 H, 7.48 N%, Found: 59.52 C, 6.75 H, 7.68 N%; MS (MALDI-TOF) m/z: Calc. for $C_{84}H_{115}N_9O_{23}Zn$: 1684.24; Found: 1684.42 $[M]^+$.

III. Synthesis of SWCNT-N3 and rGO-N3

SWCNT-N_3 and rGO-N_3 were synthesized via modified method given in the literature [2]. 250 mg (3.84 mmol) NaN_3 and 165 mg (1.01 mmol) iodine monochloride were dissolved in 25 mL of acetonitrile (ACN) under nitrogen atmosphere. This mixture was magnetically stirred for 15 min at 0°C followed by adding 20 mg SWCNTs or graphene to the solution; the reaction was stirred at room temperature for 24 hours and filtered off. The solid products were washed with DMF and ethanol to remove excess unreacted compounds and dried under vacuum.

IV. Preparation of covalently bonded ZnPc-SWCNTs (ZnPc:SWCNTs-co) or ZnPc-rGO (ZnPc:rGO-co) hybrids

20 mg (0.012 mmol) of zinc(II) phthalocyanine (ZnPc) was dissolved in 2 mL DMF and then sonicated for 15 min at room temperature. On the other side, 5 mg SWCNT-N_3 (or rGO-N_3) was suspended separately in 2 mL DMF and sonicated for 30 min at room temperature; ZnPc solutions were then added to SWCNT-N_3 (or rGO-N_3) suspension by drop wise. To this suspension, 1.0 mol% copper(II) sulphate pentahydrate and 5.0 mol% sodium L-ascorbate were added as catalysts at room temperature and resulting mixture kept in the microwave oven (400 W) at 60°C for 2 hours. Finally, the reaction mixture was centrifuged twice with water, ethanol and dichloromethane in sequence and dried in vacuum. ZnPc:SWCNTs: FT-IR (ν_{max}/cm^{-1}): 3281 (NH), 3250 (Triazole ring CH), 3070 (Aromatic CH), 2973-2863 (Aliphatic CH), 1650 (C=O), 1576 (C=C), 1472 (NH), 1337 (Aliphatic CH), 1228 (Aromatic CH), 1089 (C-O-C). ZnPc:rGO: FT-IR (ν_{max}/cm^{-1}): 3305 (NH), 3283 (Triazole ring CH), 3070 (Aromatic CH), 2975-2862 (Aliphatic CH), 1645 (C=O), 1580 (C=C), 1486 (NH), 1348 (Aliphatic CH), 1240 (Aromatic CH), 1079 (C-O-C).

V. Preparation of non-covalently bonded ZnPc:SWCNTs (ZnPc:SWCNTs-non-co) or ZnPc:rGO (ZnPc:rGO-non-co) hybrids

20 mg (0.012 mmol) of zinc(II) phthalocyanine (ZnPc) was dissolved in 2 mL DMF and then sonicated for 15 min at room temperature. On the other side, 5 mg SWCNT-N_3 (or rGO-N_3) was suspended separately in 2 mL DMF and sonicated for 30 min at room temperature. After sonication, the solution of zinc(II) phthalocyanine (ZnPc) was added separately to SWCNT-N_3 (or rGO-N_3) suspension by drop wise. Zinc(II) phthalocyanine (ZnPc) which was green in colour became colourless after the addition of SWCNT-N_3 (or rGO-N_3) suspension in DMF due to adsorption of phthalocyanine onto the SWCNT-N_3 (or rGO-N_3). Then, the solution was stirred for further 1 h. The obtained solid product was washed several times with DMF, centrifuged and dried in the vacuum [3].

VI. Results and discussion

The novel asymmetrical zinc(II) phthalocyanine (ZnPc) containing three {2-[2-(2-ethoxyethoxy)ethoxy]-1-[2-((2-ethoxyethoxy)-ethoxy)methyl]ethyloxy} and one N-(2-ethoxyethyl)-4-pentynamide groups were used for the preparation of hybrid materials. It was synthesized by the reaction of mono amino functionalized zinc(II) phthalocyanine (1) [1] with 4-pentynoic acid in DMF (Scheme 1). SWCNTs and rGO bearing azido groups were synthesized by the reaction of SWCNTs or rGO with sodium azide in the presence of iodine monochloride in acetonitrile (Scheme 2). The target SWCNTs and rGO hybrid materials covalently bonded phthalocyanine moieties were also prepared by the reaction of azido substituted SWCNTs or rGO with newly synthesized asymmetrical zinc(II) phthalocyanine (ZnPc) via "Click" reaction in DMF using copper(II) sulphate pentahydrate and sodium L-ascorbate as catalysts (Scheme 3). The non-covalently bonded ZnPc:SWCNTs or ZnPc:rGO materials were prepared by mixing SWCNTs or rGO with asymmetrical zinc(II) phthalocyanine (ZnPc) in ultrasonic bath.

VI.1 1H NMR spectrum

^{1}H NMR spectrum of phthalocyanine (ZnPc) showed good resolved bands as revealed in Fig.1. However, some signals were observed as multiplets due to formation of isomer mixture. The aromatic protons belonging to phthalocyanine ring were observed in the range of 9.26-9.12, 9.01-8.87 and 8.85-8.75 ppm integrating four protons for each peaks. These

protons were observed as multiplet peaks due to formation of isomer mixture. The NH proton was observed at 8.12 ppm as a broad singlet. The CH protons on the polyoxy substituents were observed at 5.49 ppm as a multiplet integrating three protons. The signals belonging to CH_2 protons were observed in the ranges of 5.18-5.07 ppm for CH_2N integrating two protons, 4.80-4.72 ppm for $CH_2C{=}O$ integrating two protons, 4.13-3.95 ppm for OCH_2 integrating twenty four protons, 3.92-3.80 ppm for OCH_2 integrating twenty four protons, 3.75-3.67 ppm for OCH_2 integrating twenty four protons, 3.65-3.60 ppm for OCH_2 integrating two protons and 3.03-2.92 for $CH_2C{\equiv}C$ integrating two protons. The terminal alkyne proton was observed at 2.84 ppm as a singlet peak integrating one proton. The methyl protons were observed at between 1.14-0.97 ppm as a multiplet peak integrating eighteen protons.

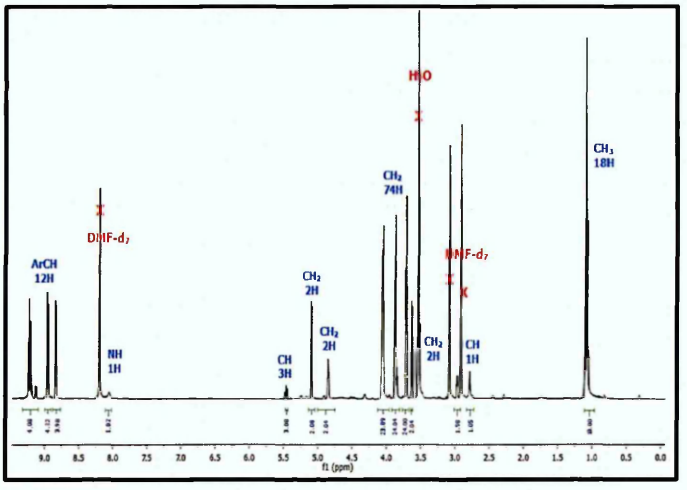

Fig.1. The NMR spectrum of phthalocyanine compound (ZnPc).

VI.2 MALDI-TOF mass spectrum

The MALDI-TOF mass spectrum of the ZnPc showed molecular ion peak at m/z = 1684.42 as $[M]^+$ supporting the proposed structure of this compound (Fig.2). The elemental analysis results were also consistent with the predicted structure of asymmetrically substituted phthalocyanine (ZnPc) shown in Scheme 1.

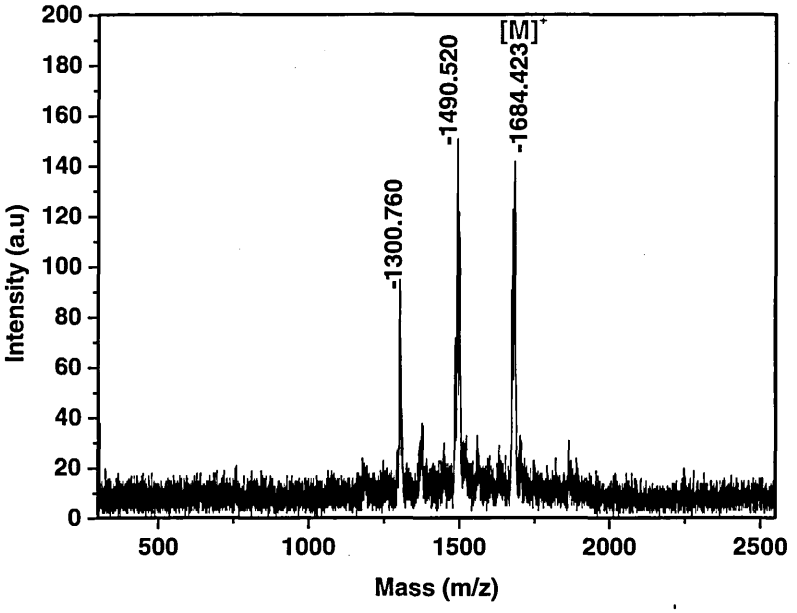

Fig.2. The MALDI mass spectrum of phthalocyanine compound (ZnPc).

VI.3 FT-IR spectra

Fig. 3 shows FT-IR spectra of free ZnPc, SWCNT-N_3 and covalently bonded SWCNTs with ZnPc hybrid (ZnPc:SWCNTs-co). This figure also shows rGO-N_3 and covalently bonded rGO with ZnPc hybrid (ZnPc:rGO-co). The phthalocyanine compound (ZnPc) exhibited vibration peaks at 3281, 3259 and 1652 cm^{-1} assigned to NH, ≡CH and C=O stretching vibrations. On the other hand, the addition of N_3 groups to SWCNTs or rGO was identified with observation of a peak at 2100 cm^{-1} for -N=N=N^+ (azide) vibration in the FT-IR spectra of SWCNTs-N_3 and rGO-N_3. The ≡CH peak in the FT-IR spectrum of ZnPc and N_3 peaks for SWCNT-N_3 or rGO-N_3 compounds were disappeared after bonding this phthalocyanine to SWCNT-N_3 or rGO-N_3 (Fig.3). Additionally, the vibration peak for CH stretching of triazole ring observed at 3250 cm^{-1} was another proof for the functionalization of SWCNTs or rGO with phthalocyanine compound (ZnPc).

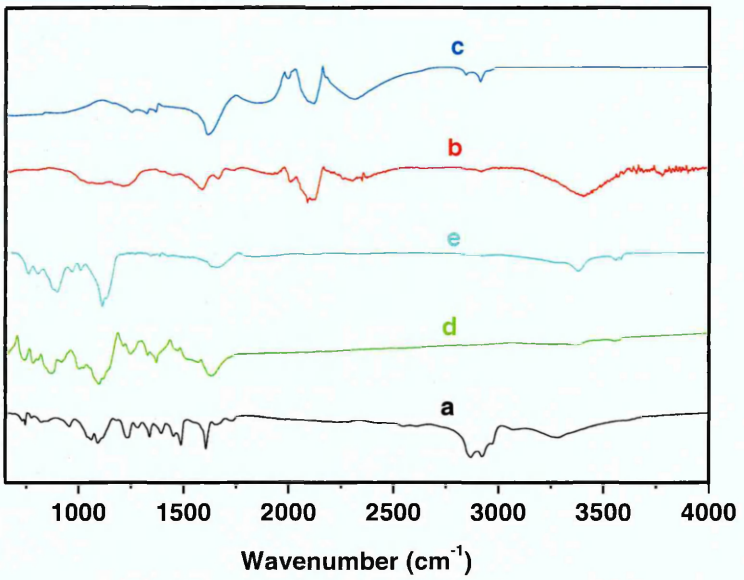

Fig.3. FT-IR spectra of free ZnPc (a), rGO-N3 (b), SWCNTs-N3 (c), ZnPc:rGO-co (d) and ZnPc-SWCNTs-co (e).

VI.4 Raman spectra

The non-covalent adsorption and covalent functionalisation of SWCNT with ZnPc confirmed by Raman spectroscopy and spectra were shown in Fig.4. The Raman spectra of rGO and its hybrids obtained by covalent and non-covalent attachment of ZnPc were presented in Fig.5. The spectra of both pristine SWCNT and hybrids (Fig.4) contain the following characteristic peaks: the D band located at about 1340 cm^{-1} (disorder mode) [4-6] and the G band (tangential mode) centred at 1590 cm^{-1} [7]. Comparing SWCNTs (Fig.4-a) and ZnPc:SWCNTs-non-co (Fig.4-b) spectra, only small variation of the ratio of the D band to the G band (I_D/I_G) could be observed which suggests that ZnPc derivative was attached to the surface of SWCNT through a non-covalent modification. The I_D/I_G ratio had a value of 0.044 in the spectrum of pure SWCNT, while the value of 0.052 was obtained from the spectra of ZnPc:SWCNTs-non-co. In the case of ZnPc:SWCNTs-co (Fig.4-c) the ratio I_D/I_G was much higher and equal to 0.077. The inset of Fig.5 shows an enlarged section of the spectrum from 70 to 1200 cm^{-1}. The intensities of characteristic vibrations of phthalocyanine macrocycle were very low in the spectrum of ZnPc:SWCNTs-non-co (Fig.4-b, inset), while the bands corresponding the ZnPc vibrations were more noticeable in the spectrum of ZnPc:SWCNTs-co (Fig.4-c, inset). A comparison of the hybrid spectra

with those of pure ZnPc (Fig.5-d) shows that some characteristic vibrations of phthalocyanine macrocycle were shifted noticeably due to interaction with SWCNT. The RBMs of SWCNT in the range 158-304 cm^{-1} (Fig.4-a) were ascribed to a distribution of diameters in the SWCNTs [8,9], which corresponds to nanotube diameters in the range 0.7 to 1.4 nm. The RBMs at 158, 179, 200, 225 cm^{-1} of SWCNT were shifted to 160, 184, 203, 227 cm^{-1} after the adsorption of ZnPc (Fig.4-b, inset). The π-π stacking interaction between SWCNTs and the phthalocyanine macrocycles gives rise to a higher frequency RBM shift due to a "hardening effect" [10]. In particular, the higher frequency shift indicates that SWCNTs becomes stiffer when they are coated with aromatic cores. The more noticeable changes were observed with the range of RBM modes in the case of ZnPc:SWCNTs-co (Fig.4-c, inset). In this case, the intensities of the most RBMs decreased and only one band at 207 cm^{-1} remained pronounced in this spectral region. rGO sample displayed two characteristic peaks at 1358 cm^{-1} and 1598 cm^{-1} corresponding to D band and G band, respectively (Fig.5-a). Both bands were broadened and the intensity of D band increased substantially in comparison with those of graphene [11] because of the significant reduction in size of the in-plane sp^2 domains and functional groups [12]. In contrast to the case of graphite, the G and D bands of ZnPc:rGO-co and ZnPc:rGO-non-co appeared at 1585 and 1353 cm^{-1}, respectively. The low-frequency peak shift could be assigned to electron transfer interaction between the donor molecules (ZnPc) and the acceptor molecules (rGO) in the hybrid systems [13,14] and the increased abundance of charge carriers [15,16] provided by the ZnPc molecules on the rGO plane. The variation of I_D/I_G ratio provide further indication of graphene nanomaterials modification [4]. The I_D/I_G intensity ratios of rGO (1.46) and ZnPc:rGO-non-co (1.52) showed no significant difference, which is indicating that the conjugations of rGO was not destroyed, and demonstrated the non-covalent modification. However I_D/I_G ratio visibly changed to 2.31 in the case of ZnPc:rGO-co. In comparison with ZnPc (Fig.5-d), characteristic vibrational peaks of ZnPc were also evident in the ZnPc:rGO-co hybrid spectrum (Fig.5-c), thus indicating that ZnPc has indeed bound to rGO.

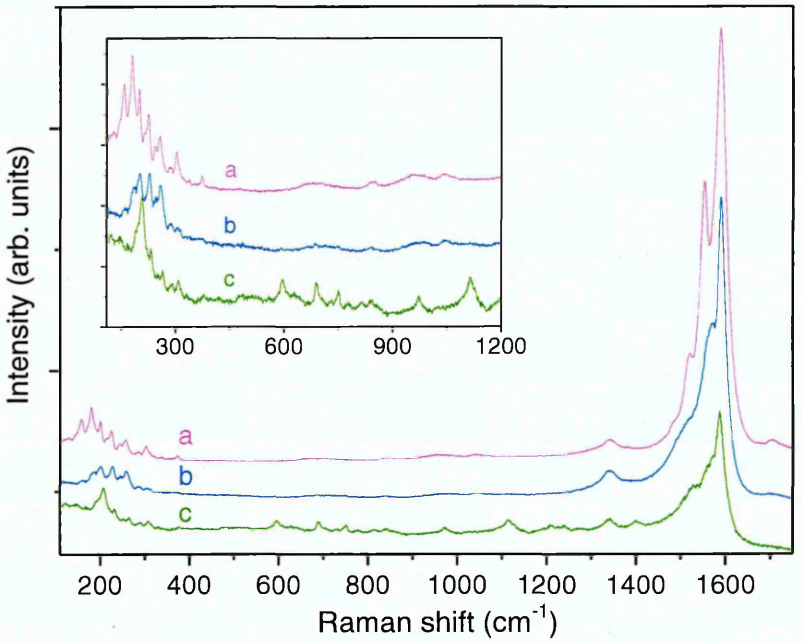

Fig.4. Raman spectra of (a) SWCNTs and their ZnPc hybrids obtained by (b) non-covalent and (c) covalent functionalization.

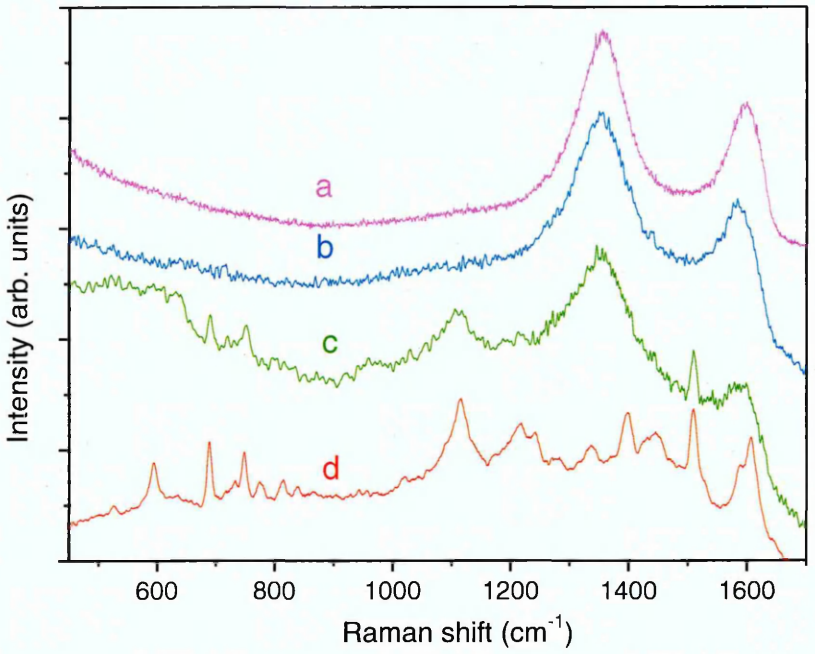

Fig.5. Raman spectra of (a) rGO, and their ZnPc hybrids obtained by (b) non-covalent and (c) covalent functionalization and (d) pure ZnPc.

References

[1] M. Göksel, M. Durmuş, D. Atilla, J. Photochem. Photobiol. A-Chem. 266 (2013) 37-46.

[2] L. Jing, C. Liang, X. Shi, S. Ye, Y. Xian, Analyst 17 (2012) 1718-1722.

[3] E.N. Kaya, S. Tuncel, T.V. Basova, H. Banimuslem, A. Hassan, A.G. Gürek, V. Ahsen, M. Durmuş, Sensor Actuat. B-Chem. 99 (2014) 277-283.

[4] T-Y. Choi, D. Poulikakos, J. Tharian, U. Sennhauser, Nano Lett. 6 (2006) 1589-1593.

[5] B. Ballesteros, G. de la Torre, C. Ehli, G.M.A. Rahman, F. Agullo-Rueda, D.M. Guldi, T. Torres, J. Am. Chem. Soc. 129 (2007) 5061-5068.

[6] C. Casiraghi, A. Hartschuh, H. Qian, S. Pliscanec, C. Georgia, A. Fasoli, K.S. Novoselov, D.M. Basko, A.C. Ferrari, Nano Lett. 9 (2009) 1433-1441.

[7] C.A. Dyke, J.M. Tour, Nano Lett. 9 (2003) 1215-1218.

[8] L. Alvarez, A. Righi, S. Rols, E. Anglaret, J.L. Sauvajol, E. Munoz, W.K. Maser, A.M. Benito, M.T. Martinez, G.F. de La Fuente, Phys. Rev. B 63 (2001) 153401.

[9] D. Huo, L. Yang, C. Hou, H. Fa, X. Luo, Y. Lu, X. Zheng, J. Yang, L. Yang, Spectrochim. Acta. A 74 (2009) 336-343.

[10] Y. Zhang, J. Zhang, H. Son, J. Kong, Z. Liu, J. Am. Chem. Soc. 127 (2005) 17156-17157.

[11] J. Yang, Y. Gao, W. Zhang, P. Tang, J. Tan, A. Lu, D. Ma, J. Phys. Chem. C 117 (2013) 3785-3788.

[12] M.B.M. Krishna, N. Venkatramaiah, R. Venkatesan, D. N. Rao, J. Mater. Chem. 22 (2012) 3059-3068.

[13] J.H. Zhu, Y.X. Li, Y. Chen, J. Wang, B. Zhang, J.J. Zhang, W.J. Blau, Carbon 49 (2011) 1900–1905.

[14] A. Chunder, T. Pal, S.I. Khondaker, L. Zhai, J. Phys. Chem. C 114 (2010) 15129–15135.

[15] H.J. Shin, S.M. Kim, S.M. Yoon, A. Benayad, K.K. Kim, S.J. Kim, H. Park, J.Y. Choi, Y.H. Lee, J. Am. Chem. Soc. 130 (2008) 2062–2066.

[16] V.Z. Poenitzsch, D.C. Winters, H. Xie, G.R. Dieckmann, A.B. Dalton, I.H. Musselman, J. Am. Chem. Soc. 129 (2007) 14724–14732.